



**HAL**  
open science

# Synthesis and optical spectroscopy of thick-shell semiconductor nanoparticles: applications to biological imaging

Michel Nasilowski

► **To cite this version:**

Michel Nasilowski. Synthesis and optical spectroscopy of thick-shell semiconductor nanoparticles: applications to biological imaging. Material chemistry. Université Pierre et Marie Curie - Paris VI, 2015. English. NNT: 2015PA066432 . tel-01612544

**HAL Id: tel-01612544**

**<https://theses.hal.science/tel-01612544>**

Submitted on 7 Oct 2017

**HAL** is a multi-disciplinary open access archive for the deposit and dissemination of scientific research documents, whether they are published or not. The documents may come from teaching and research institutions in France or abroad, or from public or private research centers.

L'archive ouverte pluridisciplinaire **HAL**, est destinée au dépôt et à la diffusion de documents scientifiques de niveau recherche, publiés ou non, émanant des établissements d'enseignement et de recherche français ou étrangers, des laboratoires publics ou privés.



**THESE DE DOCTORAT  
DE L'UNIVERSITE PIERRE ET MARIE CURIE**

Spécialité  
Physico-Chimie des Matériaux (ED397)

Réalisée au  
Laboratoire de Physique et d'Etude des Matériaux, ESPCI ParisTech

Présentée par  
**Michel NASILOWSKI**

Pour obtenir le grade de  
**Docteur de l'Université Pierre et Marie Curie**

**Synthesis and Optical Spectroscopy of Thick-Shell  
Semiconductor Nanoparticles. Applications to Biological Imaging.**

Soutenue le 5 octobre 2015

Devant le jury composé de

M.	Sergio BROVELLI	Rapporteur
M.	Fabien DELPECH	Rapporteur
M.	Jean-Louis BESSEREAU	Examineur
M.	Alexander EFROS	Examineur
M <sup>me</sup>	Agnès MAITRE	Examinatrice
M.	Benoît DUBERTRET	Directeur de thèse





**THESE DE DOCTORAT  
DE L'UNIVERSITE PIERRE ET MARIE CURIE**

Spécialité  
Physico-Chimie des Matériaux (ED397)

Réalisée au  
Laboratoire de Physique et d'Etude des Matériaux, ESPCI ParisTech

Présentée par  
**Michel NASILOWSKI**

Pour obtenir le grade de  
**Docteur de l'Université Pierre et Marie Curie**

**Synthesis and Optical Spectroscopy of Thick-Shell  
Semiconductor Nanoparticles. Applications to Biological Imaging.**

Soutenue le 5 octobre 2015

Devant le jury composé de

M.	Sergio BROVELLI	Rapporteur
M.	Fabien DELPECH	Rapporteur
M.	Jean-Louis BESSEREAU	Examineur
M.	Alexander EFROS	Examineur
M <sup>me</sup>	Agnès MAITRE	Examinatrice
M.	Benoît DUBERTRET	Directeur de thèse





## Table of Contents

<b>Table of Contents.....</b>	<b>4</b>
<b>List of Abbreviations .....</b>	<b>12</b>
<b>Introduction.....</b>	<b>15</b>
<b>Chapter I. Colloidal semiconductor nanocrystals – Physics and chemistry of Quantum Dots .....</b>	<b>19</b>
<b>I.1. Introduction.....</b>	<b>19</b>
I.1.1. Description .....	19
I.1.2. Crystallinity .....	20
I.1.3. Historical background.....	20
<b>I.2. Electronic properties of Quantum Dots.....</b>	<b>22</b>
I.2.1. Bulk material.....	22
I.2.2. Quantum confinement theory .....	23
I.2.2.1. Different confinement regimes.....	23
I.2.2.2. Particle-in-a-sphere model.....	24
I.2.2.3. Optimization of the model.....	26
I.2.3. First excited state : $1S_e - 1S_{3/2}$ .....	27
I.2.3.1. Degeneracy of first excited state.....	27
I.2.3.2. Dark and bright excitons.....	28
<b>I.3. Optical properties of Quantum Dots .....</b>	<b>29</b>
I.3.1. On an ensemble of Quantum Dots .....	29
I.3.1.1. Absorption .....	29
I.3.1.2. Fluorescence Emission .....	30
I.3.2. On a single Quantum Dot .....	31
I.3.2.1. Creation of an exciton and thermal relaxation of charge carriers .....	31
I.3.2.2. Exciton recombination and lifetime .....	32

---

I.3.2.3. Auger recombination .....	33
I.3.2.4. Quantum yield .....	34
<b>I.4. Synthesis of colloidal semiconductor nanocrystals .....</b>	<b>34</b>
I.4.1. Nucleation-growth – LaMer theory .....	35
I.4.2. Ostwald ripening.....	36
I.4.3. Mechanistic approach .....	36
I.4.4. Core/shell system.....	38
I.4.4.1. Advantages of a core/shell system .....	38
I.4.4.2. Different types of core/shell structures.....	39
I.4.4.3. Band-gap engineering .....	40
I.4.5. Synthesis methods .....	40
I.4.5.1. Synthesis of the cores – with precursor injection .....	40
I.4.5.2. Synthesis of the cores – one pot .....	41
I.4.5.3. Synthesis of the shell – SILAR .....	42
I.4.5.4. Synthesis of the shell – dropwise addition .....	42
<b>I.5. Blinking of the Quantum Dots emission.....</b>	<b>42</b>
I.5.1. The blinking phenomenon .....	42
I.5.2. Quantum Dots blinking .....	43
I.5.2.1. Characterization of blinking .....	43
I.5.2.2. Causes of blinking.....	44
I.5.3. Reduction of blinking .....	46
I.5.3.1. Addition of molecules .....	46
I.5.3.2. Compositions gradient between the core and the shell.....	46
I.5.3.3. Thick-shell Quantum Dots .....	47
<b>I.6. Two-dimensional systems – Nanoplatelets.....</b>	<b>49</b>
I.6.1. Nanoplatelets : atomically flat nanocrystals.....	49
I.6.2. Quantum wells & unique optical features .....	50
<b>I.7. Conclusion .....</b>	<b>51</b>
<b>Chapter II. Synthesis of CdSe/CdS Quantum Dots.....</b>	<b>53</b>
<b>II.1. Setup used for the synthesis.....</b>	<b>53</b>
<b>II.2. Characterization methods.....</b>	<b>54</b>

II.2.1.	Absorption .....	54
II.2.2.	Fluorescence emission.....	56
II.2.3.	Determination of the Quantum Yield .....	57
II.2.4.	Excitation (PLE).....	57
II.2.5.	Transmission Electron Microscopy.....	58
II.2.6.	Energy dispersive X-ray spectrometry (EDX) .....	59
II.2.7.	X-ray Diffraction (XRD).....	60
II.2.8.	Magneto-optical measurements .....	60
<b>II.3.</b>	<b>Synthesis of CdSe cores.....</b>	<b>61</b>
II.3.1.	Preparation of precursors .....	61
II.3.2.	Zinc-blende CdSe cores.....	62
II.3.2.1.	One-pot synthesis .....	62
II.3.2.2.	Injection synthesis.....	63
II.3.3.	Wurtzite CdSe cores.....	63
<b>II.4.</b>	<b>Synthesis of CdSe/CdS Quantum Dots - Dropwise addition .....</b>	<b>63</b>
II.4.1.	Growth of a thick CdS shell on CdSe one-pot zinc-blende cores (studied in III.2): .....	64
II.4.2.	Growth of a thick CdS shell on CdSe injection-synthesized zinc- blende cores: .....	64
II.4.3.	Growth of a thick CdS shell on CdSe wurtzite cores: .....	64
II.4.4.	Growth of a composition gradient and thick CdS shell on CdSe wurtzite cores: .....	65
<b>II.5.</b>	<b>Summary of the Quantum Dots synthesized for the study .....</b>	<b>65</b>
<b>II.6.</b>	<b>Conclusion .....</b>	<b>66</b>
<b>Chapter III.</b>	<b>CdSe/CdS Quantum Dots with 100% quantum yield in air, at room temperature.....</b>	<b>69</b>
<b>III.1.</b>	<b>Setup used for spectroscopic studies.....</b>	<b>69</b>
III.1.1.	Epifluorescence microscope.....	69
III.1.2.	Confocal microscope and acquisition setup .....	70
III.1.3.	Time-resolved acquisitions .....	71
III.1.3.1.	Photoluminescence trace .....	71

III.1.3.2. Photoluminescence decay .....	72
III.1.3.3. Photoluminescence intensity autocorrelation .....	73
III.1.3.4. Preparation of the sample for single particle studies .....	74
<b>III.2. Thick-shell CdSe/CdS Quantum Dots .....</b>	<b>75</b>
III.2.1. Zinc-blende CdSe core with a thick CdS shell .....	75
III.2.1.1. Optical and Structural characterization .....	76
III.2.1.2. Two emissive states at room temperature .....	77
III.2.1.3. One grey state under vacuum .....	79
III.2.1.4. 100% quantum yield at cryogenic temperature .....	80
III.2.1.5. Thermal activation of Auger processes .....	81
III.2.2. Other samples .....	82
III.2.3. Conclusion .....	83
<b>III.3. Bulky-gradient QDs – thick-shell and gradient composition .....</b>	<b>83</b>
III.3.1. Optical and Structural characterization .....	84
III.3.2. Correlative optical/electron microscopy .....	86
III.3.3. 100% quantum yield in air, at room temperature .....	88
III.3.3.1. Low excitation regime .....	89
III.3.3.2. 100% quantum yield .....	90
III.3.3.3. High excitation power .....	91
III.3.4. Evolution under vacuum .....	92
III.3.5. Quantum yield of the biexciton .....	93
III.3.6. White-light emitting Quantum Dots .....	95
III.3.7. Lifetime measurements .....	97
III.3.8. Evolution at cryogenic temperature .....	98
III.3.9. Magneto-optical measurements .....	100
III.3.10. Slow recombination dynamics .....	101
III.3.11. Amplified spontaneous emission .....	102
III.3.12. Conclusion .....	103
<b>III.4. Golden-QD – hybrid Quantum Dots/gold nanoshell nanoparticles</b>	
<b>104</b>	
III.4.1. Surface plasmons and Purcell effect .....	104
III.4.2. Description of Golden-QDs and synthesis .....	105

III.4.3.	Determination of the Purcell factor .....	106
III.4.4.	First observations with thin-shell CdSe/CdS QDs .....	107
III.4.5.	Golden-QDs with thick-shell CdSe/CdS QDs .....	110
III.4.6.	Effect on blinking behavior .....	112
III.4.7.	Increased photostability.....	113
III.4.7.1.	...with time .....	113
III.4.7.2.	...with power.....	114
III.4.8.	Correlative light-electron microscopy .....	116
III.4.9.	Conclusion.....	117
<b>III.5.</b>	<b>Conclusion .....</b>	<b>118</b>
<b>Chapter IV.</b>	<b>Spectroscopic studies of thick-shell CdSe/CdS nanoplatelets</b>	<b>121</b>
<b>IV.1.</b>	<b>Synthesis of nanoplatelets .....</b>	<b>121</b>
IV.1.1.	Synthesis of CdSe NPLs.....	121
IV.1.2.	Synthesis of CdSe/CdS core/shell NPLs.....	123
<b>IV.2.</b>	<b>Optical properties of CdSe nanoplatelets .....</b>	<b>124</b>
IV.2.1.	Photoluminescence.....	124
IV.2.2.	Time-resolved photoluminescence .....	125
IV.2.3.	Blinking behavior.....	125
<b>IV.3.</b>	<b>Optical properties of CdSe/CdZnS core/shell nanoplatelets synthesized at room temperature .....</b>	<b>126</b>
IV.3.1.	Photoluminescence.....	126
IV.3.2.	Time-resolved photoluminescence .....	128
IV.3.3.	Blinking behavior.....	129
<b>IV.4.</b>	<b>Optical properties of new generation of core/shell nanoplatelets 130</b>	
<b>IV.5.</b>	<b>Conclusion .....</b>	<b>135</b>
<b>Chapter V.</b>	<b>Quantum Dots as probes for biological imaging</b>	<b>137</b>
<b>V.1.</b>	<b>Fluorescent probes for biology .....</b>	<b>137</b>
<b>V.2.</b>	<b>Quantum Dots vs organic fluorophores .....</b>	<b>138</b>

---

V.2.1. Photobleaching .....	139
V.2.2. Excitation and emission ranges .....	139
V.2.3. Lifetime .....	143
V.2.4. Functionalization and surface chemistry .....	143
V.2.5. Multimodal imaging .....	145
V.2.6. Cytotoxicity of Quantum Dots.....	146
<b>V.3. Ligand exchange on the surface of Quantum Dots .....</b>	<b>146</b>
V.3.1. Necessity of a ligand exchange .....	146
V.3.2. Choice of proper ligand .....	147
<b>V.4. Targeting of Voltage Dependent Calcium Channels in <i>C.elegans</i></b>	<b>148</b>
V.4.1. <i>C.elegans</i> – anatomy and interest .....	148
V.4.1.1. A model organism.....	149
V.4.1.2. ... widely used in biology.....	150
V.4.2. Voltage Dependent Calcium Channels in <i>C.elegans</i> .....	151
V.4.2.1. Genetic modification of <i>C. elegans</i> .....	152
V.4.2.2. Quantum Dots as bimodal probes for targeting of VDCCs.....	152
V.4.2.3. Quantum Dots for biological applications .....	153
V.4.3. New polymeric ligand .....	153
V.4.4. Preparation of antiGFP-QDs .....	154
V.4.4.1. Ligand exchange on the QDs.....	154
V.4.4.2. Coupling of anti-GFP antibody to an amino group.....	156
V.4.4.3. Coupling of anti-GFP antibody to a carboxylic group.....	157
V.4.4.4. Coupling of anti-GFP antibody to a thiol group.....	158
V.4.4.5. <i>In vitro</i> evaluation of the coupling specificity of the antiGFP-QDs....	159
V.4.5. Microinjection of antiGFP-QD .....	160
V.4.6. High-pressure freezing.....	160
V.4.7. Macroscopic targeting in living worms.....	161
V.4.8. Nanometer resolution analysis .....	164
V.4.9. Conclusion .....	167
<b>V.5. DNA nanocage as a functional biocompatible scaffold .....</b>	<b>167</b>
V.5.1. DNA nanocage: a versatile scaffold .....	168

V.5.2. Encapsulation of Quantum Dots in a DNA nanocage .....	171
V.5.2.1. Preparation of Quantum Dots.....	171
V.5.2.2. Encapsulation of QDs in the nanocage .....	172
V.5.2.3. Verification of encapsulation .....	172
V.5.3. Monofunctionalization of DNA icosahedron .....	177
V.5.4. Probing the Shiga toxin endocytosis pathway .....	179
V.5.5. Conclusion .....	184
<b>Conclusion .....</b>	<b>187</b>
<b>References .....</b>	<b>191</b>



## List of Abbreviations

<b>ALBR</b>	Anionic Ligand-Binding Receptor
<b>ASE</b>	Amplified Spontaneous Emission
<b>BME</b>	$\beta$ -mercaptoethanol
<b>c-ALD</b>	Colloidal Atomic Layer Deposition
<b>CBO</b>	Conduction Band Offset
<b>CLEM</b>	Correlative Light and Electron Microscopy
<b>DCC</b>	Dicyclohexylcarbodiimide
<b>DCP</b>	Degree of Circular Polarisation
<b>DHLA</b>	Dihydrolipoic Acid
<b>DLS</b>	Dynamic Light Scattering
<b>DMF</b>	Dimethylformamide
<b>DMF</b>	Dimethylformamide
<b>DMSO</b>	Dimethyl Sulfoxide
<b>DNA</b>	Deoxyribonucleic Acid
<b>DTT</b>	Dithiothreitol
<b>EDX</b>	Energy Dispersive X-ray
<b>EtOH</b>	Ethanol
<b>FA</b>	Folic Acid
<b>FACS</b>	Fluorescence-Activated Cell Sorting
<b>FWHM</b>	Full Width at Half Maximum
<b>GABA</b>	$\gamma$ -Aminobutyric Acid
<b>GFP</b>	Green Fluorescent Protein
<b>GNP</b>	Gold Nanoparticle
<b>HPF</b>	High-Pressure Freezing
<b>HPLC</b>	High-Performance Liquid Chromatography
<b>IgG</b>	Immunoglobulin G
<b>LDOS</b>	Local Density Of States
<b>MPA</b>	3-mercaptopropionic Acid
<b>MRI</b>	Magnetic Resonance Imaging
<b>NA</b>	Numerical Aperture
<b>NC</b>	Nanocrystal
<b>NHS</b>	<i>N</i> -Hydroxysuccinimide
<b>NPL</b>	Nanoplatelet
<b>ODE</b>	1-octadecene
<b>PEG</b>	Poly(Ethylene Glycol)
<b>PL</b>	Photoluminescence
<b>PLE</b>	Photoluminescence Excitation
<b>PVIS</b>	poly(1-vinylimidazole-co-vinyltrimethoxysilane)

---

<b>PVP</b>	poly(vinylpyrrolidone)
<b>QD</b>	Quantum Dot
<b>QY</b>	Quantum Yield
<b>RPM</b>	Revolutions Per Minute
<b>SA</b>	Streptavidin
<b>SB</b>	Sulfobetaine
<b>scFv</b>	Single-Chain Fragment-Variable Antibody
<b>SEC</b>	Size Exclusion Chromatography
<b>SEM</b>	Scanning Electron Microscope
<b>SeODE</b>	Selenium-in-octadecene solution
<b>SILAR</b>	Successive Ion Layer Adsorption and Reaction
<b>SODE</b>	Sulfur-in-octadecene solution
<b>SP</b>	Surface Plasmons
<b>STxB</b>	Shiga Toxin B subunit
<b>sulfo-Ic-SPDP</b>	sulfosuccinimidyl 6-(3'-(2-pyridyldithio)propionamido)hexanoate
<b>sulfo-SMCC</b>	sulfosuccinimidyl 4-(N-maleimidomethyl)cyclohexane-1-carboxylate
<b><i>t</i>BuOK</b>	<i>tert</i> -butoxide
<b>TCSPC</b>	Time-Correlated Single Photon Counting
<b>TDPA</b>	Tetradecylphosphonic Acid
<b>TEM</b>	Transmission Electron Microscopy
<b>TEMPO</b>	(2,2,6,6-Tetramethylpiperidin-1-yl)oxyl
<b>TEOS</b>	Tetraethylorthosilicate
<b>TOP</b>	Trioctylphosphine
<b>TOPO</b>	Trioctylphosphine Oxide
<b>TTR</b>	Time-Tagged-Time-Resolved
<b>VDCC</b>	Voltage-Dependent Calcium Channels
<b>W</b>	Wurtzite
<b>XRD</b>	X-ray Diffraction
<b>ZB</b>	Zinc-Blende



## Introduction

Decreasing the size of a material to the nanometer scale may change drastically its properties. Indeed, while its size decreases, its surface-to-volume ratio increases, conferring new physical and chemical properties. The properties are then mostly dependent of the surface and the finite size of the nanoparticles.

Several examples can be listed:

- Bulk metal is a reflective material, but metal nanoparticles (gold, silver, platinum...) absorb light. This is due to the collective oscillations of electrons at the surface of the nanoparticle, called surface plasmon waves. These plasmons absorb light over a range of wavelength defined by the size and shape of the metal nanoparticle.<sup>1,2</sup> Lately, a new area of research is that of non-noble-metal plasmonic nanoparticles where free charge carriers arise from the presence of a dopant or a metal vacancy.<sup>3</sup>
- Magnetic properties can be changed for nanoparticles compared to bulk. Magnetization can increase or decrease, some nonmagnetic materials exhibit magnetism when decreased to the nanoparticle size and surface defects can increase the magnetic anisotropy.<sup>4</sup>
- Semiconductor materials experience quantum confinement effect at the nanometer scale. This induces discretization of energy levels, similarly to individual atoms. These nanoparticles, made of a few hundreds or thousands of atoms, behave therefore as artificial atoms and are called Quantum Dots (QDs).

These quantum confinement effects are crucial for the properties of QDs. Their optical properties are different from the bulk material, and show unique, very interesting properties for a wide range of applications. Indeed, one of their most striking characteristic is that their fluorescence wavelength depends on their size. For example, CdSe QDs, made of cadmium and selenium atoms, can emit from 450 to 700 nm when their size changes from 2 to 10 nm.

The development of colloidal synthesis of QDs opened the road to applications. Not only do the syntheses yield billions of QDs with similar properties, but they are also easier to manipulate compared to epitaxially grown QDs. The improvement of physical comprehension (started in the 1980s by A. Henglein, A. Ekimov, A. Efros and L. Brus<sup>5-7</sup>) and of synthesis

methods of QDs (the first controlled synthesis of colloidal QD with a controlled size dispersion was performed in 1993 by C. Murray, D. Norris and M. Bawendi<sup>8</sup>) allow now to reach better emission quantum yields (or emission efficiency, *i.e.* the emitted intensity compared to the excitation power), which opens the way to new applications that were until now limited by a poor quantum yield.

This limitation is due to QD blinking. Even when under continuous excitation, a single QD do not emit light continuously, but blinks, *i.e.* switches randomly between an emissive and a non-emissive state.<sup>9</sup> These non-radiative recombinations have been attributed to Auger recombinations where the exciton (*i.e.* the electron-hole pair formed in the QD after excitation) energy does not create a photon but is transferred to an excess charge present in the nanoparticle.<sup>10</sup> This random blinking reduces the global quantum yield of the QDs and limits their applications.

Several strategies have therefore been developed to decrease the blinking of QDs and improve their quantum yield. The growth of a thick shell has been proven to be efficient to decrease the blinking,<sup>11,12</sup> as well as changing the environment of QD emitters by adding some passivating molecules,<sup>13</sup> or by coupling the exciton to gold surface plasmons.<sup>14</sup> These strategies, however, were not fully optimized as the thick-shell QDs still showed some flickering at room temperature in air (they were not blinking and highly emissive only at 4K),<sup>15</sup> or required working in a specific environment, therefore strongly limiting their applications.

In 2014, a conference in Paris celebrated the 30 years of colloidal Quantum Dots and showed the progress made in the synthesis, the physical understanding and the applications of QDs. This year's Consumer Electronic Show (CES2015), the biggest trade show in electronics and technology, highlighted new TV screens based on QDs (from TCL, Sony, LG or Samsung; Amazon already produces the Kindle Fire with a QD-based technology), proving the growing interest of manufacturers for QDs. The properties of QDs, however, can still be improved.



*Left: Vials with CdSe QDs of different sizes illuminated by a blue laser showing the dependence in size of the emission wavelength. Right: TCL H9700 television screen displayed at the CES2015 in Las Vegas in January 2015.*

In this work, we focused on the life of QDs from their birth (synthesis) to their final applications (mostly in biology here), while trying all the way to understand by optical spectroscopy how their properties could be explained. The project of this work was to continue the development of CdSe/CdS QDs with high quantum yield that could be used for different applications, which means non-blinking and highly emissive at room temperature under atmospheric pressure. Another part of this work was to develop QDs for biological bimodal imaging (light / electron microscopy) and the improvement of their surface chemistry to target specific molecules or pathways in cells or worms.

After an introduction in Chapter I of the description of optical and electronic properties of the semiconducting nanocrystals, as well as their synthesis methods, Chapter II will be focused on the synthesis of spherical QDs and their characterization methods. Chapter III will discuss the optical properties of three different non-blinking QD-based structures, thick-shell CdSe/CdS QDs, thick-shell CdSe/CdS QDs with a composition gradient between the core and the shell, and gold-capped CdSe/CdS nanoparticles. The shape of the semiconducting nanoparticle plays a major role in the emission properties, as Chapter IV will highlight with the study of non-blinking CdSe/CdS two-dimensional nanoplatelets. Finally, Chapter V will present two applications for biological imaging of QDs: bimodal light and electron microscopy for the localization of nanometer-sized receptors in *C. elegans* worms, and encapsulation of QDs in monofunctionalized DNA nanocage for the study of the dynamics of the Shiga-toxin-mediated retrograde endocytosis pathway in cells.



30 years  
of colloidal  
quantum dots

*Logo of the 30 years of colloidal Quantum Dots conference in Paris in 2014.*



# Chapter I. Colloidal semiconductor nanocrystals – Physics and chemistry of Quantum Dots

## I.1. Introduction

Colloidal semiconductor nanocrystals (often simply called Quantum Dots, or QDs) have constituted a growing field of research over the last 30 years. Their multiple and various applications explain the interest of the scientific community towards these nanoparticles. Due to their unique optical and electronic properties, they can be utilized for biological imaging<sup>16</sup>, photovoltaic conversion<sup>17,18</sup> or in display devices such as LEDs<sup>19–22</sup>. They can also act as lasing media<sup>23,24</sup>, single photon emitters<sup>25</sup> and on a more fundamental point of view, be considered as artificial atoms<sup>26,27</sup>.

### I.1.1. Description

Colloidal semiconductor nanocrystals are nanometer-sized crystals made of a semiconductor material, either pure such as Si or Ge (elements of group IV) or composed of two materials (binary composition) from the groups II-VI (CdSe, CdS, ZnSe, CdTe, PbS...), III-V (InP, GaP, GaAs), I-VII (CuCl, CuBr, AgBr...) or three materials (ternary composition) from the groups I-III-VI (CuInSe<sub>2</sub>, CuInS<sub>2</sub>...).

Those nanocrystals (NCs) are dispersed in a solid (polymer or glass) or liquid matrix (solvent). They are surrounded by a capping layer of ligands, which are molecules or ions that play two major roles: they ensure the colloidal stability of the nanocrystals in the matrix and passivate them, *i.e.* block the charge carrier traps due to the presence of dangling bonds at the surface of the NCs. Given their particularly small size, the surface/volume ratio is large in those structures and the surface role is crucial regarding the control of their properties.

Typically, QDs stabilized with long hydrocarbon chains are dispersible in non-polar solvents such as hexane or toluene, up to a size of approximately 20 to 30 nm where attractive Van der Waals forces become non-negligible and cause the QDs to start forming aggregates.

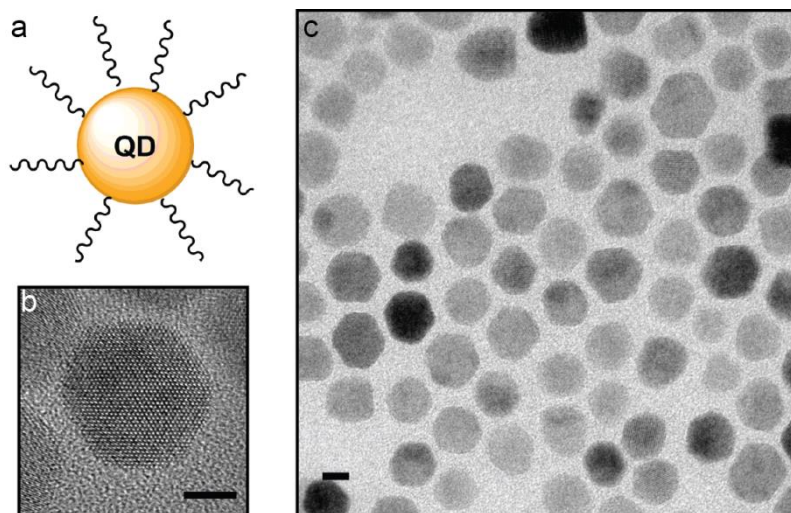


Figure I.1: a. Schematic representation of a Quantum Dot with its inorganic core surrounded by organic ligand molecules. b. and c. Transmission electron microscopy images of CdSe/CdS QDs. Scale bar is 5 nm.

### I.1.2. Crystallinity

The QDs studied in this work are II-VI based. They can exist in the form of two stable crystallographic structures: wurtzite (hexagonal) and zinc-blende (cubic). These structures are however very close energetically and QD syntheses can result in either one of these structures, or in polymorphic forms. This can influence the physical properties of the QDs. Indeed, the symmetry of the NC is different in the two structures, which modifies the degeneracy of the energy levels as well as the band gap separating them.<sup>28</sup>

### I.1.3. Historical background

The story of Quantum Dots started in the 1980s with A. Ekimov (Vavilov Institute), A. Efros (Ioffe Institute) and L. Brus (Bell Labs) who understood for the first time the size-dependence of the optical properties of semiconductor nanocrystals.

This, however, was not the first time scientists saw that optical properties depend on the size. In 1957, E.F. Gross and A.A. Kaplansky studied CuCl crystals in a crystalline NaCl matrix.<sup>29</sup> After doping NaCl with Cu atoms, they measured the absorbance and found it not

different than the one from NaCl. However, when they measured the absorbance one year later, two absorption bands appeared that had the same splitting as in bulk CuCl, but were blue-shifted by 100 meV. Two years later, the absorption spectra were the ones of bulk CuCl. Unfortunately, there was no understanding of this phenomenon at that time. In 1977, R. Katschmann, A. Rehfeld and R. Kranold observed what they called an *optical anomaly* when studying 1-to-5-nm-sized CdSe nanocrystals: they observed a band gap energy dependence  $E_g = 1/r^2$ . They attributed this dependence to a lattice contraction.<sup>30</sup>

The curiosity about the cause of the NCs size-dependent color drove A. Ekimov to work on the synthesis of NCs embedded in a glass matrix while L. Brus studied the aqueous synthesis of NCs. The idea that the optical properties depend on the size of the nanocrystals was skeptically accepted by the solid state community. In order to prove that statement, better controlled syntheses needed to be developed. In 1981, A. Ekimov and A. Onushchenko managed to control the size of CuCl NCs in a glass matrix by changing the temperature to limit the growth.<sup>31</sup> In 1984, they applied their method to prepare CdS NCs.<sup>32</sup> In 1982, A. Efros showed that the quantum confinement of the exciton explains the peculiar properties of nanometric semiconductor crystals. L. Brus in the USA, came to the same conclusion following the work of A. Henglein who reported in 1982 the first colloidal growth of CdS in aqueous solution.<sup>7,33,34</sup> By decreasing the concentration of precursors and the growth temperature, he observed a blue-shift of the absorbance (compared to bulk) that disappeared over time because the particles kept growing. Only by developing a synthesis technique based on reverse micelles did he manage to control the size of the NCs. They were however not stable in solution. A reflux in a mixture of 90% tributylphosphine: 10% tributylphosphine oxide helped cap the surface and redisperse the NCs. This phosphine : phosphine oxide mixture inspired the 1993 synthesis by C. Murray, D. Norris and M. Bawendi which was the first reliable technique to grow colloidal QDs with a small size dispersion.<sup>8</sup> The same year, A. Ekimov along with C. Flytzanis and A. Efros assigned the optical transitions in CdSe QDs to their corresponding energy levels.<sup>35</sup>

Other contributors to the field of colloidal QDs need to be pointed out: N. Borrelli who reproduced Ekimov's results and applied them to the synthesis of PbSe and PbS in glass,<sup>36</sup> F. De Rougemont with C. Flytzanis who showed that the Auger processes are very efficient in NCs,<sup>37</sup> P. Guyot-Sionnest who showed that capping CdSe QDs with a ZnS shell increases the quantum yield (QY) by a factor of ~10,<sup>38</sup> X. Peng and P. Alivisatos, as well as T. Hyeon and S. Ithurria with B. Dubertret who developed syntheses of shape-controlled NCs: nanorods, nanoribbons and nanoplatelets.<sup>39-41</sup>

## I.2. Electronic properties of Quantum Dots

Although composed of several thousands of atoms, QDs have discrete energy levels, which contribute to their “artificial atoms” properties. Studies of the electronic structure, mostly developed by Al. Efros, have permitted to understand the fine band structure in QDs.<sup>42,43</sup>

### I.2.1. Bulk material

As an example, CdSe is a direct band gap semiconductor with a band gap energy of 1.66 eV (resp. 1.74 eV) at room temperature for the zinc-blende (resp. wurtzite) crystalline structure.

For the bulk material (Figure I.2), the conduction band consists of the s orbital of cadmium ( $[Kr]4d^{10}5s^2$ ) while the valence band consists of the p orbital of selenium ( $[Ar]3d^{10}4s^24p^4$ ). At  $k=0$ , the conduction band is twice degenerate while the valence band is degenerate 6 times. The latter is partially lifted by the spin-orbit coupling (0.42 eV in CdSe) into two sub-bands,  $J_h=3/2$  and  $J_h=1/2$  where  $J_h = l_h + s_h$ , with  $l_h$  the hole orbital and  $s_h$  the hole spin contribution to the angular momentum. The hole spin  $s_h$  is  $\pm 1/2$  and its orbital moment  $l_h$  is 1 as the hole occupies the p orbital of the selenium. The angular momentum  $J_h$  is therefore 1/2 and 3/2 corresponding to the two sub-bands at  $k=0$ . The  $J_h=3/2$  is 4-times degenerate ( $m_{J_h}=+3/2; -3/2; +1/2; -1/2$ ) while the  $J_h=1/2$  is twice degenerate ( $m_{J_h}=+1/2; -1/2$ ). The  $J_h=1/2$  band is referred to as the split-off (so) band.

Away from  $k=0$ , the  $J_h=3/2$  band is further split into 2 sub-bands of different curvature,  $m_{J_h}=\pm 3/2$  and  $m_{J_h}=\pm 1/2$  by its projection on the crystalline axis. The one corresponding to the  $m_{J_h}=\pm 3/2$  projection has the lowest curvature and is referred to as the heavy hole (hh), while the  $m_{J_h}=\pm 1/2$  projection has the largest curvature and corresponds to the light hole (lh). In a wurtzite structure, due to the asymmetry of the crystal lattice,  $J_h=3/2$  is split at  $k=0$  due to the crystal field effect ( $\Delta_{cf} = 25$  meV).

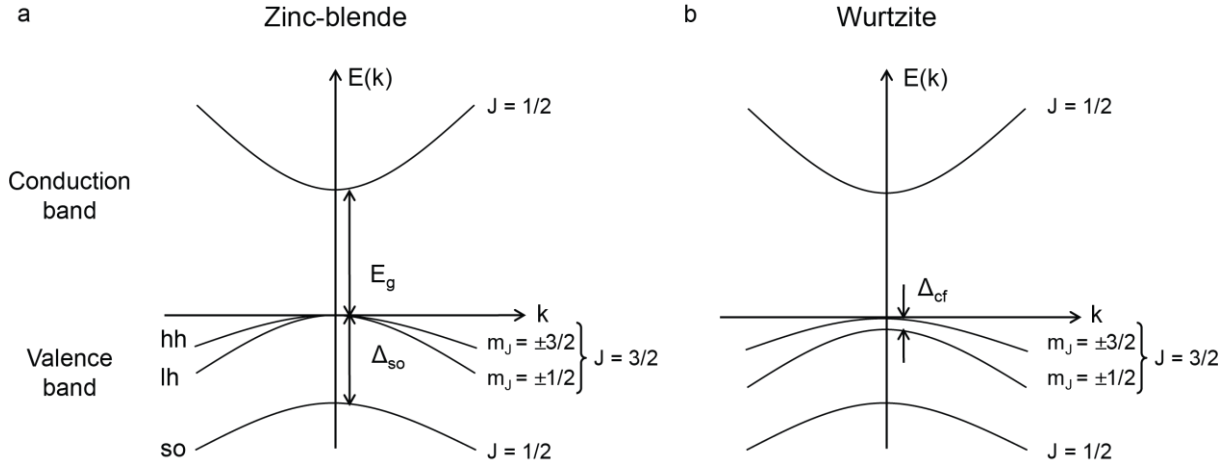


Figure 1.2: Band diagram of bulk CdSe in a. zinc-blende and b. wurtzite crystalline structures.

## 1.2.2. Quantum confinement theory

When the size of the semi-conductor crystal decreases, quantum confinement effects appear and need to be taken into account. The cohesion of the exciton created in the crystal after excitation is affected by the coulombian interaction between the two charges and by the confinement effects. Each of these effects behaves differently as the size decreases: the coulombian energy increases as  $1/a$  while the confinement effects increase as  $1/a^2$ , where  $a$  is the nanocrystal radius.

### 1.2.2.1. Different confinement regimes

More precisely, the quantum size effect occurs when the size of the nanocrystal is comparable to or smaller than the natural extension of the electron or hole. This length scale can be estimated through the Bohr radius of the particle defined as follows:

$$a_B = \varepsilon \frac{m_e}{m_{exc}^*} a_0$$

where  $\varepsilon$  is the dielectric constant of the material,  $m_{exc}^*$  is the mass of the exciton (defined by the reduced mass of the electron-hole pair  $m_{exc}^* = \frac{m_e m_h}{m_e + m_h}$ ),  $m_e$  is the mass of the electron and  $a_0$  is the Bohr radius of the hydrogen atom ( $a_0 = \frac{4\pi\varepsilon_0 \hbar^2}{m_e e^2} \sim 0.53 \text{ \AA}$ ). Once this size limit is defined, three different types of confinement can be defined:

- The weak confinement regime that appears when the radius of the nanocrystal is comparable to the Bohr radius of the exciton ( $a_e, a_h < a < a_B$ ). In this case, the charge carriers are not confined, only the exciton is, and the binding energy of the

exciton, *i.e.* the Coulomb interaction between the hole and the electron, is larger than the confinement energy of the charge carriers.

- The strong confinement regime which occurs when the size of the nanocrystal is smaller than the exciton Bohr radius ( $a < a_e, a_h, a_B$ ). The electron and the hole are both confined within the NC. The optical transitions happen between quantified energy levels of the hole and electron.
- Finally, the intermediate confinement regime ( $a_h < a < a_e, a_B$  or  $a_e < a < a_h, a_B$ ) where only one charge carrier is strongly confined while the other is not.

These confinement regimes depend not only on the size of the NC but also on the material. For CdSe, the Bohr radius is around 5.6 nm.

### 1.2.2.2. Particle-in-a-sphere model

Whatever the confinement regime, at least one charge carrier is always confined. Thus, the simple model of the particle in a sphere can be applied to describe quantitatively the size dependence of the optical properties of QDs.

This model considers a particle (electron, hole or exciton) of a mass  $m_0$  in an infinite spherical potential well of radius  $a$ :

$$V(r) = \begin{cases} 0 & r < a \\ \infty & r > a \end{cases}$$

The solutions of the Schrödinger equation with the Hamiltonian  $H = -\frac{\hbar^2}{2m_0}\nabla^2 + V(r)$  are the following wavefunctions:

$$\Phi_{n,l,m}(r, \theta, \phi) = C \frac{j_l(k_{n,l}r) Y_l^m(\theta, \phi)}{r}$$

where  $C$  is a normalization constant,  $Y_l^m(\theta, \phi)$  is a spherical harmonic,  $j_l(k_{n,l}r)$  is the  $l^{\text{th}}$  order spherical Bessel function, and  $k_{n,l} = \alpha_{n,l}/a$  where  $\alpha_{n,l}$  is the  $n^{\text{th}}$  zero of  $j_l$ . The energy of the particle is therefore given by:

$$E_{n,l} = \frac{\hbar^2 k_{n,l}^2}{2m_0} = \frac{\hbar^2 \alpha_{n,l}^2}{2m_0 a^2}$$

This model describes the conduction and valence bands as parabolic bands for which the eigenfunctions can be described by quantum numbers  $n$  (1, 2, 3...),  $l$  ( $s, p, d, \dots$ ) and  $m$ . The energies are identical to the kinetic energy of the free particle with the exception of the wavevector  $k_{n,l}$  which is quantized by the boundary conditions. The energy levels are proportional to  $1/a^2$  which shows their strong dependence to the size of the nanocrystal.

This model might seem simplistic as the calculations were performed for an empty sphere and not for a nanocrystal filled with semiconductor atoms. However, some

approximations allow considering the charge carriers as particles inside an empty sphere of potential.

First, the effective mass approximation states that the carriers behave as free particles with an effective mass  $m_{eff}^{c,v}$  ( $c$  and  $v$  stand for conduction and valence bands and correspond respectively to electron and hole). According to Bloch's theorem, bulk crystal wavefunctions can be written as:

$$\Psi_{nk}(\vec{r}) = u_{nk}(\vec{r}) \exp(i \cdot \vec{k} \cdot \vec{r})$$

where  $u_{nk}$  is a function with the same periodicity as the crystal lattice. For a crystalline material, the band diagram represents the eigenenergies  $E$  as a function of  $k$ . In the effective mass approximation, the bands are approximated to parabolic curves near  $k = 0$ :

$$E_k^c = \frac{\hbar^2 k^2}{2m_{eff}^c} + E_g$$

$$E_k^v = \frac{-\hbar^2 k^2}{2m_{eff}^v}$$

where  $E_g$  is the band gap. Physically, the effective mass takes into account the periodic potential felt by the charge carriers in the crystal lattice, and this approximation allows the electron and the hole to be treated as free particles and to ignore the atoms of the lattice.

However, the use of the effective mass approximation requires the criteria for the application of Bloch's theorem to be met. This in turn requires the crystallites to be treated as bulk, *i.e.* the NC size to be larger than the crystal lattice (this is the case in CdSe NC where the lattice parameter is around 0.6 nm). This second approximation is called the envelope function approximation. The wavefunction of a single charge carrier can then be written as a linear combination of Bloch functions:

$$\Psi(\vec{r}) = \sum_k C_{nk} u_{nk}(\vec{r}) \exp(i \cdot \vec{k} \cdot \vec{r})$$

where  $C_{nk}$  coefficients ensure that the sum satisfies the spherical boundary conditions of the NC. As the  $u_{nk}$  functions have a weak  $k$  dependence:

$$\Psi(\vec{r}) = u_{n0}(\vec{r}) \sum_k C_{nk} \exp(i \cdot \vec{k} \cdot \vec{r}) = u_{n0}(\vec{r}) f(\vec{r})$$

where  $f(\vec{r})$  is the single charge carrier envelope function.  $u_{n0}$  functions can be determined by tight-binding calculations. The NC problem is therefore reduced to determining the envelope functions for a single charge carrier wavefunction,  $f(\vec{r})$ . This is exactly the problem solved by the particle-in-a-sphere model described earlier.

1.2.2.3. Optimization of the model

The band structure of semi-conductors cannot however be fully approximated to parabolic bands: experimental data do not match the calculated transition energies.<sup>44</sup> Several other models, such as the  $k \cdot p$  model, the Luttinger Hamiltonian or the Kane model offer different levels of complexity to calculate more precisely the band structure of QDs (Figure I.3).<sup>43</sup> These models rely on more accurate calculations, degeneracy of the valence band or the coupling between the conduction and valence bands. Finally, for CdSe QDs for example, the size dependence of the energy levels can be calculated and plotted as seen on Figure I.4.

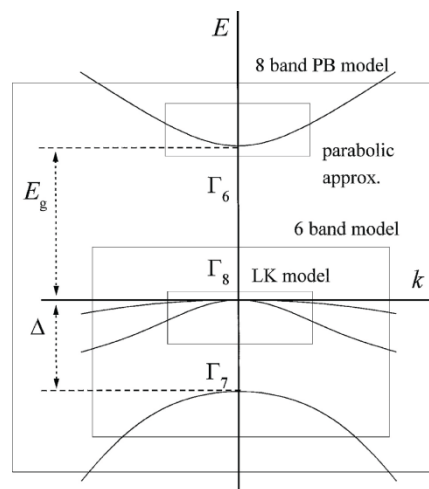


Figure I.3: Bulk band structure of typical direct band gap semiconductor with zinc-blende structure. The boxes show the region of applicability of different models.<sup>42</sup>

The transitions seen on the absorbance spectra can then be assigned to the corresponding energy levels. The fundamental transition, for example, is attributed to the  $1S_e$  -  $1S_{3/2}$  transition.

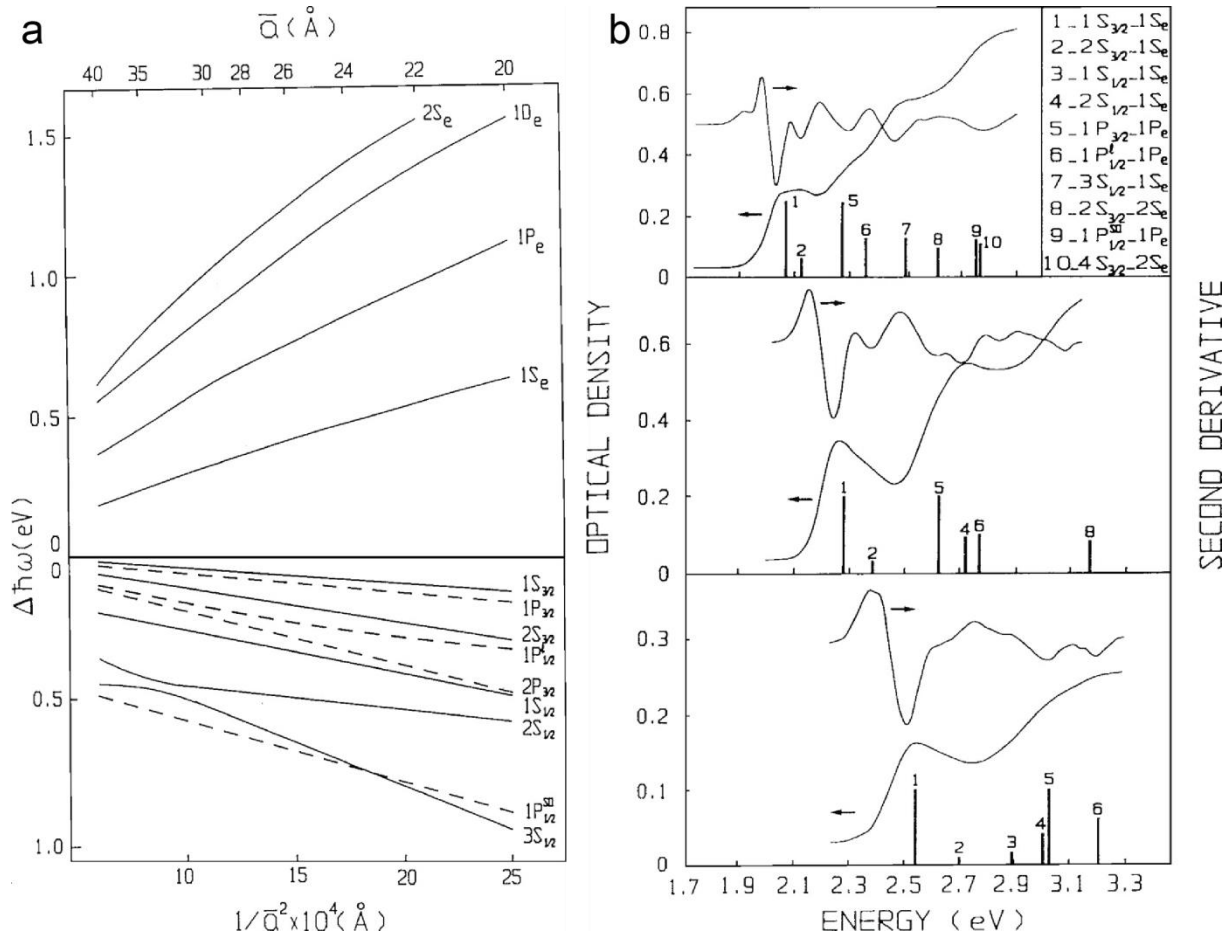


Figure 1.4: a. Theoretical size dependence of the electron and the hole energy levels in a CdSe QD. b. Absorption spectra and their second derivatives for CdSe QDs whose radii are respectively (from top to bottom) 3.8, 2.6 and 2.1 nm. The vertical bars indicate the position of the transition, and the height their relative strength. The inset shows the assignment of these transitions.<sup>42</sup>

### 1.2.3. First excited state : $1S_e - 1S_{3/2}$

The first, lowest-energy excited state plays an important role in the physical properties of the QDs. After excitation, the charge carriers relax rapidly<sup>45,46</sup> to the exciton lowest energy level  $1S_e 1S_{3/2}$  where photons are emitted from. The understanding of its fine structure allowed explaining the Stokes shift between the first absorption and emission peak<sup>47</sup> or the presence of a dark exciton that accounts for CdSe QDs long fluorescence lifetime at low temperature.<sup>47,48</sup>

#### 1.2.3.1. Degeneracy of first excited state

The electron ground state  $1S_e$  is twice degenerate. The hole ground state  $1S_{3/2}$  is 4-times degenerate. Thus, the excitonic first excited state is 8-times degenerate for spherical

zinc-blende NCs. This degeneracy can be lifted due to the non-sphericity of the QD or the non-symmetry of the wurtzite structure. The latter separates the  $1S_{3/2}$  state of the hole into two sub-bands, and the interaction between the spin of the electron and the spin of the hole lifts the degeneracy of the  $1S_e1S_{3/2}$  state (as well as the degeneracy of the corresponding transition). Finally, the fine structure of the  $1S_e1S_{3/2}$  exciton for spherical, wurtzite CdSe QDs can be described by five sublevels (Figure I.5).<sup>42</sup>

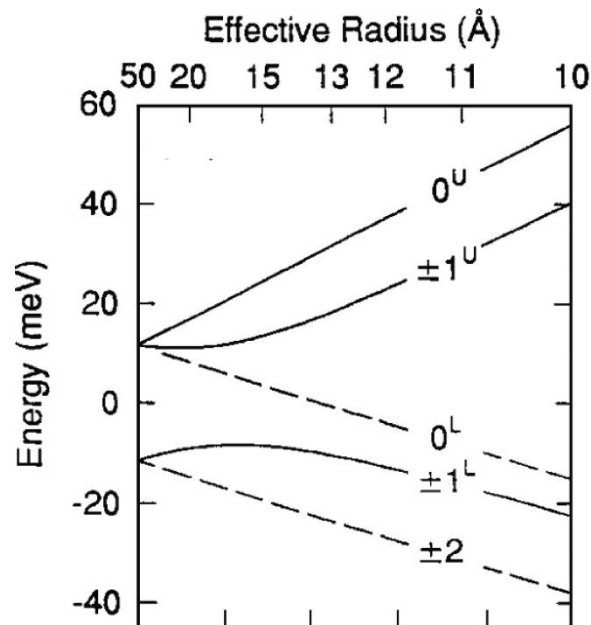


Figure I.5: Size dependence of exciton band edge fine structure in spherical wurtzite CdSe QDs. Solid lines indicate optically active levels, dashed lines indicate passive levels.<sup>42</sup>

### 1.2.3.2. Dark and bright excitons

In this description of the fine structure of the  $1S_e1S_{3/2}$  exciton in CdSe, the optically active states are the ones with the highest oscillator strength (proportional to the overlap of the wavefunctions of the electron and the hole). As seen in Figure I.5, the transition from the  $\pm 2$  and  $0^L$  states are forbidden. On the contrary, the  $0^U$ ,  $\pm 1^L$  and  $\pm 1^U$  states are optically active (the superscripts “L” – lower, and “U” – upper, are used to distinguish between states having the same projections of the total moment). The excitonic state leading to optically active transitions are called bright excitons while those resulting in optically inactive transitions are called dark excitons.

This fine structure explains the dark exciton observed at low temperature. At room temperature, the five sublevels are thermally populated, and the radiative recombination of the exciton comes from optically active levels. On the other hand, at cryogenic temperature,

only the lowest-energy optically-inactive excitonic state is populated, which explains the long recombination lifetimes observed as the transition is forbidden.<sup>47–49</sup>

### **I.3. Optical properties of Quantum Dots**

#### **I.3.1. On an ensemble of Quantum Dots**

##### **I.3.1.1. Absorption**

The absorption spectra show the excitonic structure of the QDs studied (Figure I.6). This informs on the discrete energy levels in the NCs as each different excitonic level appears as a peak on the absorption spectrum. The width of the peak is determined by the coupling of the energy levels with phonons, and in ensemble measurements, by the polydispersity in size, thus in energy, of the QDs. The properties described in I.2 can be observed on the absorption spectrum: the position of the main excitonic band (highest-wavelength band) provides information on the band gap energy, which decreases with increasing size of the QDs. The differences in energy between the various excitonic levels gets smaller and smaller as the size increases, which can be observed on the spectra with peaks getting closer and closer to each other.

The bands observed correspond to transitions between the discrete energy levels which are present in small semiconductor NCs due to the quantum confinement effect. The energy levels in the valence band are closer to each other than the energies in the conduction band. This brings the energy levels to a quasi-continuum as the energy increases<sup>50</sup>, moving away from the band edge, which can be seen on the spectra by continuously increasing absorbance at low wavelengths.

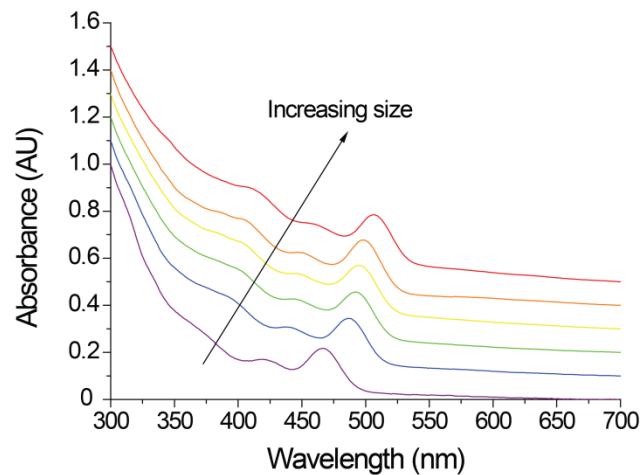


Figure I.6: Evolution of the absorbance spectrum with increasing size of CdSe QDs.

### I.3.1.2. Fluorescence Emission

Given the size-dependent electronic structure of the QDs, the fluorescence emission is easily tunable. For CdSe QDs, the emission colors can be chosen from blue (450 nm, for CdSe QDs ~2 nm in diameter) to red (700 nm for CdSe QDs ~6 nm in diameter), *i.e.* span the whole visible range (Figure I.7).

The position and the width of the emission band give information on the band-edge energies, the coupling to phonons and the polydispersity in size of the sample. The latter is usually low, below 5%, yielding emission spectra width below 30 nm at room temperature.

The emission is also characterized by a Stokes shift to the red, *i.e.* a shift between the wavelength position of the first absorption peak and the emission peak, of around 10 nm, or ~30 meV. This shift is due to the fact that the QDs are excited by the absorption of a photon that creates an exciton at high energies (levels  $0^U$  and  $\pm 1^U$ , see I.2.3), which then relaxes to lower energy levels ( $\pm 1^L$  or  $\pm 2$ ) from which it recombines to emit a photon.<sup>47</sup>

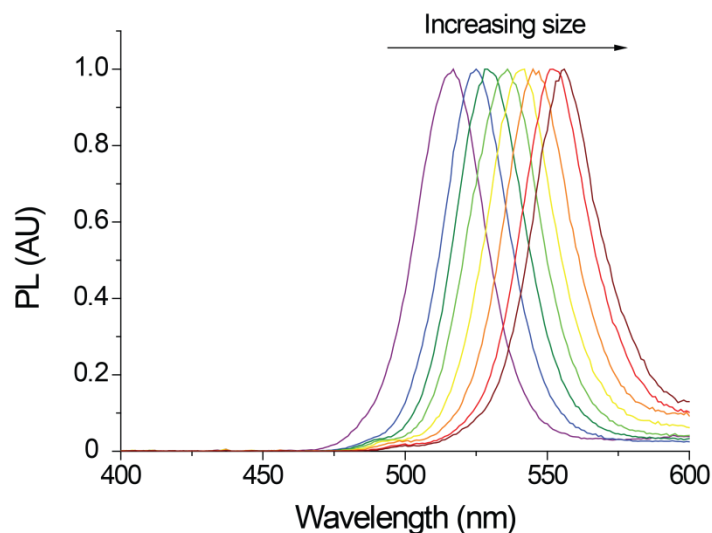


Figure I.7: Evolution of the photoluminescence spectrum with increasing size of CdSe QDs.

### I.3.2. On a single Quantum Dot

Studying individual QDs allows to get rid of any averaging of the properties over a sample that might contain different sizes, shapes or compositions of QDs. Thus, the inhomogeneous broadening is eliminated at the single particle level, and the measured physical properties provide more specific details on the studied NC. For example, the width of the emission band drops from  $\sim 30$  nm to  $\sim 12$  nm. This residual homogeneous broadening can be explained by the coupling of the exciton with phonons and spectral diffusion which corresponds to a modification of the emitted wavelength due to changes in the local electromagnetic environment.<sup>51,52</sup> The lifetime measurement is also easier to extract from the PL decay as it becomes multiexponential when acquired on an ensemble of QDs. On a single NC, the measured lifetimes do not correspond to mechanisms of exciton recombinations in different QDs, but to recombinations in the same QD, making it easier to understand the physical processes.

#### I.3.2.1. Creation of an exciton and thermal relaxation of charge carriers

After the excitation of a QDs with light (photoluminescence), current (electroluminescence<sup>53,54</sup>), temperature (thermoluminescence<sup>55</sup>) or electron beam (cathodoluminescence<sup>56,57</sup>), an electron-hole pair (or exciton) is formed in the QDs. If the excitation is high in energy, the created electron and hole have energies much higher than the band edge energies, and will relax by phonon emission towards the band edge. This relaxation happens at the picosecond time-scale<sup>46,58</sup>, *i.e.* faster than predicted ( $\sim 100$  ps).<sup>59</sup> As the difference between the discrete energy levels of the electrons is larger than the

phonon energies, a “phonon bottleneck” might be expected, preventing the charge carrier relaxation.

Indeed, the relaxation happens in a two-step process. First, the electron transfers its excess energy to the hole, which can then relax to the band edge through coupling with phonons.<sup>60,61</sup> The difference between the energy levels is higher for the electron in the conduction band than for holes in the valence band.<sup>50,62</sup> coupling to phonons is then possible for the hole to relax. All these processes result in fast relaxation of both charge carriers (Figure 1.8).

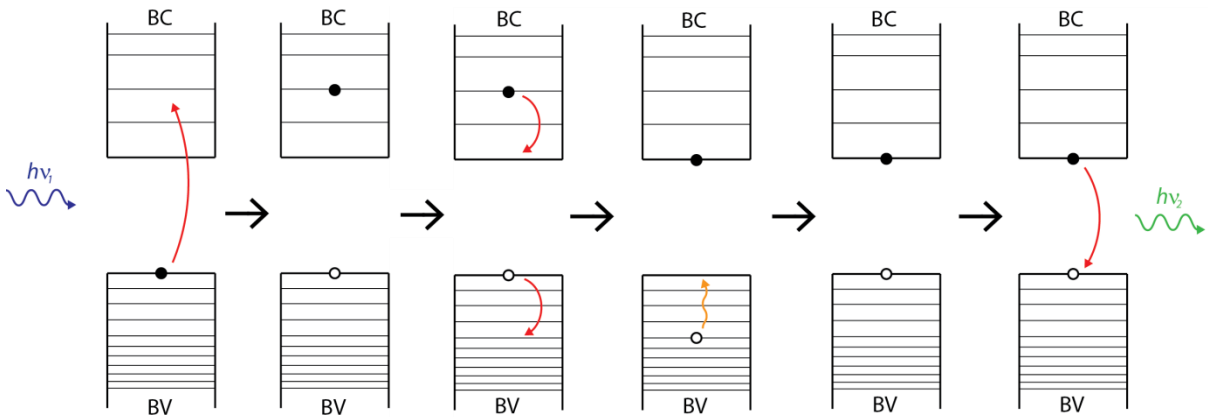


Figure 1.8: Scheme of formation, relaxation and radiative recombination of the exciton in a semiconductor NC.

### 1.3.2.2. Exciton recombination and lifetime

Once the charge carriers have relaxed to their respective band edge, the exciton has several ways of recombining.

It can recombine radiatively, meaning that a photon will be emitted (Figure 1.8). This recombination can happen from the band edge, and is then called band-edge emission, or from traps whose energy levels are located within the band gap (deep-trap emission), at lower energies.

It can also recombine non-radiatively: after the recombination, no photon is emitted. These non-radiative recombinations might involve traps where charge carriers can be blocked (defects, surface sites or dangling bonds) or a non-radiative energy transfer between charges called Auger process (see 1.3.2.3).

Each recombination happens with a characteristic time, called the lifetime. It is roughly the time needed for an exciton to recombine and leave the excited state. This recombination can be radiative with a rate  $k_R$ , or non-radiative with a rate  $k_{NR}$ . The population of the excited state  $N_e(t)$  varies as follows:

$$\frac{dN_e}{dt} = -kN_e(t) = -k_R N_e(t) - k_{NR} N_e(t)$$

The population of the excited state then follows an exponential decrease with a time constant  $\tau = 1/k = 1/(k_R + k_{NR})$  which is the lifetime:

$$N_e(t) = N_e(0)e^{-kt} = N_e(0)e^{-\frac{t}{\tau}}$$

This lifetime is measured by exciting the QDs and measuring the arrival time of the photons after the excitation pulse. These time-tagged photons allow to build the histogram of arrival times, *i.e.* the photoluminescence (PL) decay over time, whose exponential decrease is characterized by the lifetime. A monoexponential decrease means that there is only one exciton recombination pathway. Regarding multiexponential PL decay, several interpretations can be given: the polydispersity of the sample yields different monoexponential decays according to the different sizes of QDs, averaging the measured PL decay as multiexponential; or several recombination pathways occur. The study at the single particle level is therefore very useful to eliminate the average measurement and focus on the pathways present in one QD.

It is important to note that the measured lifetime gives information not only on the radiative rate, but also on the non-radiative rate of the exciton recombination:

$$k = k_R + k_{NR} \rightarrow \frac{1}{\tau} = \frac{1}{\tau_R} + \frac{1}{\tau_{NR}}$$

### 1.3.2.3. Auger recombination

After the relaxation of the charge carriers, the electron and the hole of the excitonic pair are located at the band edge. If a third charge carrier is present, the exciton can recombine transferring its energy to this excess charge carrier, without emitting a photon. This non-radiative energy transfer to an excess charge carrier is called Auger process (Figure I.9.b).

The excess charge carrier can come from another exciton present in the QD (multiexcitons are created at high energy excitation), or from the ionization process of a previously created exciton whose electron or hole was trapped or ejected from the NC (Figure I.9.a).

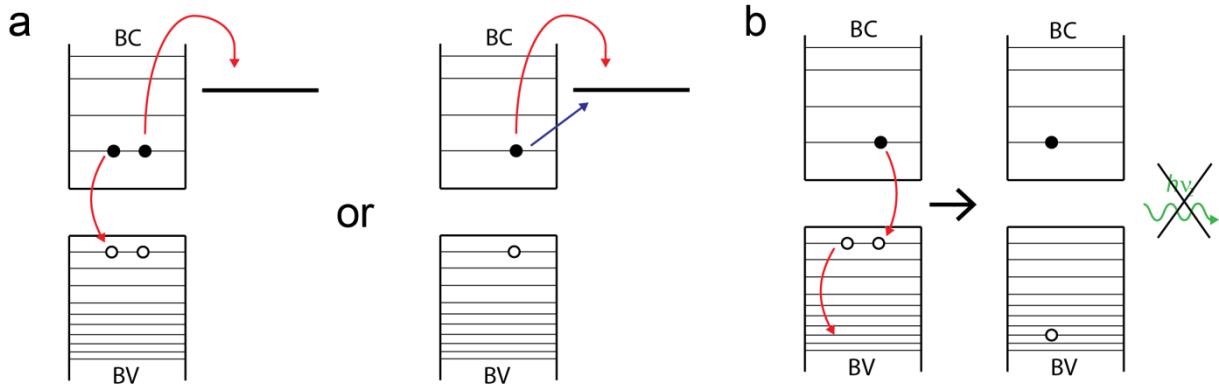


Figure 1.9: a. Scheme of charging of QDs through Auger auto-ionization (left) or thermoejection (right, red) or direct tunneling (right, blue). b. Scheme of non-radiative Auger recombination for a charged QD.

The Auger processes are fast: they happen at the sub-nanosecond time-scale.<sup>63</sup> Thus, non-radiative recombinations are favored over radiative ones that happen at the ns time scale. This has been the most commonly accepted explanation for the blinking behavior of the PL emission (see I.5).

The higher the excitation, the more multiexcitons are created in the QDs, favoring Auger recombinations, especially in small NCs as the Auger recombination lifetime scales with the volume of the NC.<sup>63,64</sup>

#### I.3.2.4. Quantum yield

In order to quantify the relative weights of radiative and non-radiative recombinations of the exciton, the Quantum yield (QY) is used. The QY measures the ratio between the emitted photons and the absorbed photons. The latter produce excitons that can recombine radiatively with a rate  $k_R$  or non-radiatively with a rate  $k_{NR}$ . Thus, the QY is:

$$QY = \frac{k_R}{k_R + k_{NR}}$$

When the QY and the total lifetime ( $1/\tau = k_R + k_{NR}$ ) are known,  $k_R$  and  $k_{NR}$  can be calculated to determine the characteristic lifetimes of the radiative and non-radiative processes.

## I.4. Synthesis of colloidal semiconductor nanocrystals

Different protocols have been developed over the past decades to ensure that the colloidal syntheses yield homogeneous QDs distributions together with excellent properties.

In order to avoid side phenomena such as secondary nucleation, the protocols are based on the principle of burst nucleation introduced by Victor K. LaMer in 1950.<sup>65</sup>

#### I.4.1. Nucleation-growth – LaMer theory

LaMer's theory is based on the principle that monodisperse samples can be obtained only if two important steps during the synthesis of NCs are efficiently separated: the nucleation and the growth. The nucleation needs to happen very quickly so that the nuclei formed in solution all have the same size, and the following growth process needs to be much slower to ensure the homogeneous growth of each nuclei. The nucleation is triggered when a concentration threshold is reached, either by playing on the reactivity of the precursors used or by injecting swiftly one of them at a given time.

This process can be described by LaMer's curve (Figure I.10):

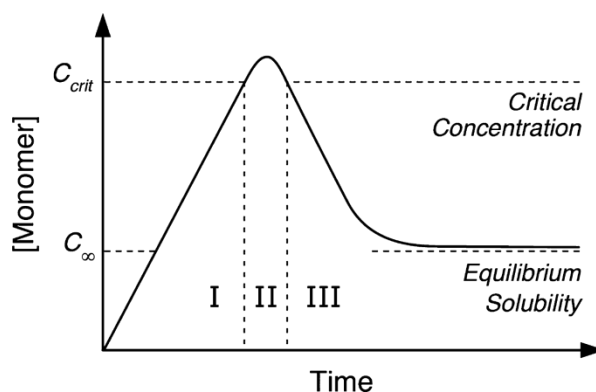


Figure I.10: Evolution of the monomer concentration with time according to LaMer's theory. Phase I corresponds to the supersaturation, phase II to the nucleation and phase III to the growth.<sup>66</sup>

When the precursors are mixed together, they form monomers whose concentration increases quickly with time. Once the nucleation threshold is reached (the energy barrier for nucleation is overpassed), the monomers react to form stable nuclei. This causes the concentration of monomers to drop quickly below the nucleation threshold: the nucleation stops, and the remaining monomers then react with the formed nuclei to grow them.

The chemical formation and growth of the NCs can be summarized as follows (Figure I.11):

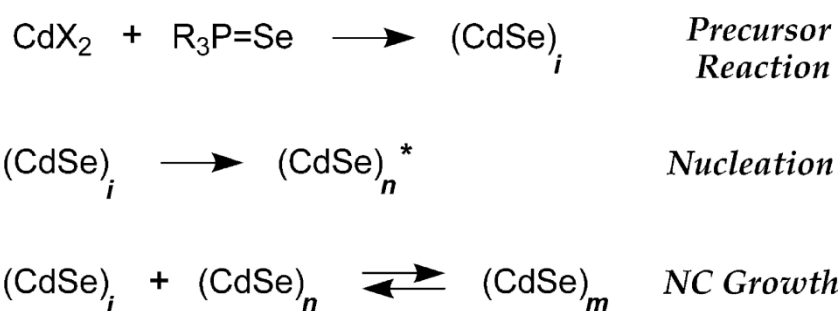


Figure I.11: Precursor conversion to monomers, nucleation and growth steps.  $(\text{CdSe})_i$  refers to a solute form of CdSe,  $(\text{CdSe})_n$  refers to NCs and  $(\text{CdSe})_n^*$  refers to nuclei.<sup>67</sup>

#### I.4.2. Ostwald ripening

After the nucleation and growth steps, if the solution is left at high temperature, the monomers that have reacted to form an NC can redissolve in solution and react with other NCs. This process is thermodynamically directed towards the dissolution of the smallest NCs in favor of the growth of the largest NCs. This is called Ostwald ripening.<sup>68</sup> Thus, the size dispersion of the sample increases if the synthesis is not stopped before the Ostwald ripening occurs.

#### I.4.3. Mechanistic approach

Studies have mostly focused on developing new syntheses to obtain high-quality, bright, monodisperse and shape-controlled QDs. The mechanism behind their formation still remains not fully understood, even though some works give insights into the molecular reactions that can take place during the nucleation and the growth of the NCs.



Figure I.12: Thermal decomposition of  $\text{CdMe}_2$  and its oxidation by  $\text{R}_3\text{PE}$  ( $\text{Me}=\text{CH}_3$ ,  $\text{E}=\text{S}$ ,  $\text{Se}$ ,  $\text{R}=\text{hydrocarbon chain or alkyl group}$ ).<sup>66</sup>

Until 2001, organometallic species were used as metal (in particular Cd) sources, and a chalcogen dissolved in a phosphine or in a phosphine oxide as the chalcogen source. The thermal decomposition of these precursors yields NCs (Figure I.12).

It has been shown that the phosphine oxide commonly used, trioctylphosphine oxide, or TOPO, contains sometimes up to 20% of impurities such as phosphonic acids.<sup>69</sup> The phosphonic functions can form *in situ* with  $\text{Cd}^{(II)}$  a phosphonate complex which becomes in turn the Cd source. This discovery allowed chemists to develop new, less dangerous

precursors of Cd, such as the above mentioned cadmium phosphonates but also cadmium carboxylates, from less dangerous Cd sources such as CdO (see Figure I.13).<sup>66,70</sup>

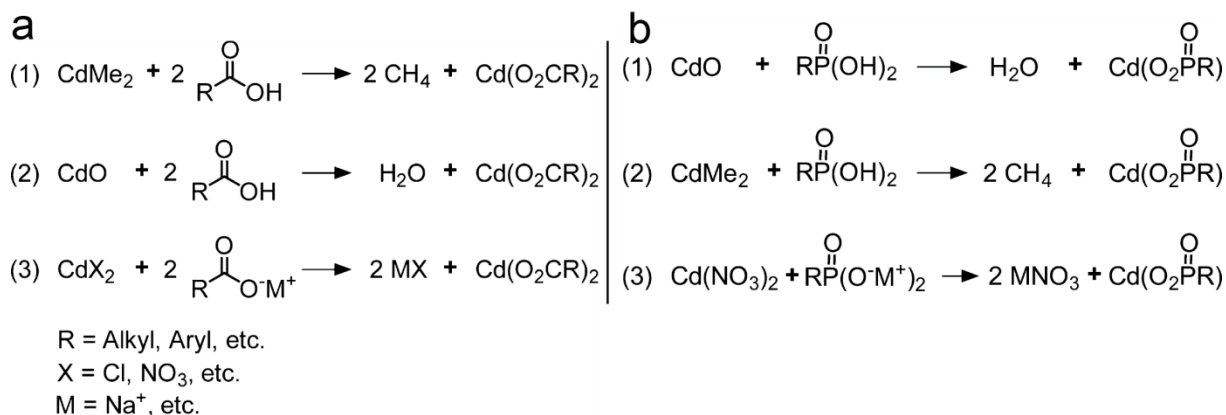


Figure I.13: Preparation of a. Cadmium carboxylates and b. Cadmium phosphonates from the reaction between various cadmium-based reagents and carboxylic or phosphonic acids derivatives.<sup>66</sup>

The reaction between the cadmium complex and the chalcogen complex can then be described as follows for the case of selenium (Figure I.14):<sup>71</sup>

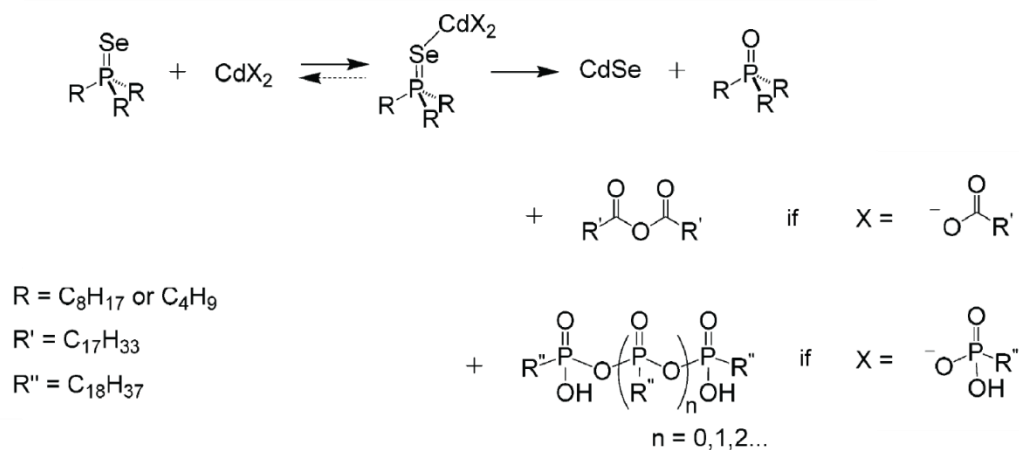


Figure I.14: Precursor conversion pathway leading to the formation of CdSe NCs.<sup>71</sup>

Other Se sources consist of elemental Se, either dissolved in 1-octadecene (ODE) or formed *in situ* by the reduction of SeO<sub>2</sub>.<sup>66,72</sup> It has been shown that heating Se in organic solvents such as ODE, TOPO, oleic acid or paraffin produces H<sub>2</sub>Se, which in turn reacts with the metal complex to form the NCs (see Figure I.15).<sup>73</sup>

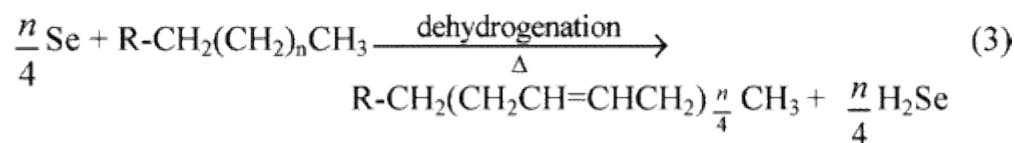
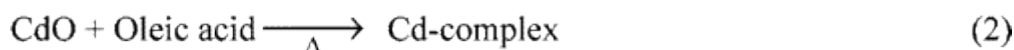


Figure I.15: Reactions occurring with Cd and Se sources to form the precursors leading to CdSe NCs.

(1) General reaction equation. (2) Formation of the Cd-precursor complex (see Figure I.13). (3)

Dissolution of Se powder in paraffin and dehydrogenation reaction generate Se precursor  $\text{H}_2\text{Se}$  in situ.

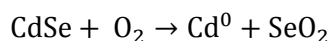
(4) Reaction between  $\text{H}_2\text{Se}$  and the Cd-complex to form CdSe NCs.<sup>73</sup>

#### I.4.4. Core/shell system

##### I.4.4.1. Advantages of a core/shell system

The syntheses of CdSe QDs produce nanoparticles with a wide range of possible emission wavelengths in the visible range. However, their emission intensity is quite low (QY < 10%), is polluted by deep-trap emission and decreases rapidly under continuous excitation (photobleaching).

In 1996, Philippe Guyot-Sionnest's group succeeded in depositing a ZnS shell over CdSe QDs, forming a CdSe/ZnS core/shell system.<sup>38</sup> This system showed a dramatic increase in the QY (up to 50%) and a better photostability. Indeed, the ZnS shell passivates the traps that are present at the surface of the CdSe core, limiting non-radiative recombinations, and protects the core from oxidation<sup>74,75</sup> and etching by oxygen that shifts the fluorescence to the blue (as the size of the semiconductor NC decreases):



The lower redox potential of selenides compared to sulfides ( $\text{S}^{2-}/\text{S}_2\text{O}_3$  : 0.006 V vs  $\text{Se}^{2-}/\text{SeO}_2$  : -0.276 V<sup>76</sup>) explains why the selenides are so prone to oxidation in the air and why the addition of a sulfur-based shell considerably reduces the oxidation phenomena (although they are not completely stopped<sup>77</sup>:  $\text{CdS} + 2 \text{O}_2 \rightarrow \text{Cd}^{2+} + \text{SO}_4^{2-}$ ).

The goal of the shell is therefore to prevent the charge carriers from reaching traps within the NC or at its surface, and thus to avoid non-radiative recombinations of the excitons. The ZnS shell succeeds in stopping the charges from reaching the surface because of its wide band-gap compared to CdSe: 3.61 eV for ZnS vs 1.74 eV for CdSe (type-I

alignment, see Figure I.16). The charges are confined in the CdSe core and cannot explore the ZnS shell, which makes the CdSe/ZnS structure a finite potential well. As the charges are confined within the NC, the emission of the QD is much less sensitive to modifications or environmental conditions (charging, ligand exchange...). However, in order to reduce even more the probability for the charges to reach the surface, a thick shell has to be deposited on the CdSe core. This turns out to be impossible with ZnS as the relative difference between the lattice parameters of ZnS ( $a_{ZnS} = 3.82 \text{ \AA}$ ) and CdSe ( $a_{CdSe} = 4.29 \text{ \AA}$ ) is too high (~10%) to grow more than two ZnS monolayers without forming crystallinity defects that significantly affect the QY.<sup>78</sup> This requires the development of different core/shell structures whose shell material has a wider band-gap than CdSe, but similar crystalline properties so that a thick crystalline shell can be grown to decrease the probability for the charge carriers to reach the surface of the NC.

#### I.4.4.2. Different types of core/shell structures

Different types of core/shell structures exist depending on the band alignment of the valence and conduction bands of the core and shell materials (see Figure I.16).<sup>79</sup>

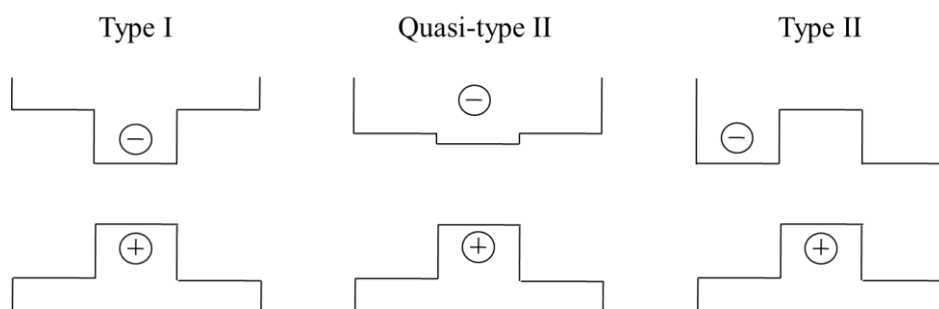


Figure I.16: Schematic representation of the energy levels of the conduction band edge and the valence band edge for core/shell structures.

In type I structures, such as CdSe/ZnS (see I.4.4.1), the band-gap of the shell material is larger than the band-gap of the core material. The shell valence band is lower and the shell conduction band is higher in energy, compared to the respective core bands: both the electron and the hole are confined in the core material and cannot reach the shell outer surface due to the energy barrier between the core and shell band energies.

In type II structures, such as CdSe/CdTe<sup>80</sup>, CdS/ZnSe<sup>81</sup> or CdSe/ZnTe<sup>82</sup>, the band alignment spatially separates the charges between the core and the shell. The band edge of either the conduction or the valence band of the core is located within the band gap of the shell. In these systems, the emission after exciton recombination happens with an important red-shift due to the indirect band gap recombination. The charge separation limits the overlap between the electron and hole wavefunctions, strongly decreasing the recombination lifetime.

This type of band alignment is interesting for applications where charge separation and recombinations with long characteristic lifetimes are needed, such as photovoltaics.<sup>83</sup>

Finally, quasi-type-I (or quasi-type-II) structures, like CdSe/CdS are structures where one of the bands (conduction or valence) of the shell is aligned with the band (resp. conduction or valence) of the core. For CdSe/CdS, the conduction bands of the core and the shell are aligned while the valence band of CdSe is higher in energy than the one of CdS. This leads to delocalization of the electron over the whole CdSe/CdS core/shell structure, while the hole stays confined in the core. The CdSe/CdS system provides the possibility to grow a large shell as the lattice parameter relative difference is only 4%. Such a thick shell decreases even more the probability for the electron to reach the surface, while the hole stays in the CdSe core.

#### 1.4.4.3. Band-gap engineering

Other structures, requiring more complex syntheses, can be obtained, such as multishell structures<sup>84</sup> (CdSe/CdS/ZnS), or alloyed<sup>85,86</sup> or graded compositions<sup>87–89</sup> (CdSe/CdZnS or CdSe/Cd<sub>1-x</sub>Zn<sub>x</sub>S). The idea is to grow a ZnS shell over a CdSe core, but with the help of CdS as a crystalline buffer between CdSe and ZnS to adjust the mechanical constraints due to the difference in the lattice parameter.

Core-shell systems also offer a wide range of band-gap engineering possibilities, such as tuning between type-I and type-II systems (taking advantage of the relative sizes of the core and the shell and the strains induced by the shell)<sup>90–93</sup>, simultaneous type-I and type-II behaviors<sup>94</sup> as well as doping procedures.<sup>95,96</sup>

#### 1.4.5. Synthesis methods

The first synthesis of colloidal CdSe QDs with a control of the size distribution was performed in 1993 by Murray, Norris and Bawendi.<sup>97</sup> It was based on the nucleation-growth principle and used organo-metallic and expensive precursors that are pyrophoric and unstable. New synthesis methods involving other types of precursors have therefore been developed to allow for easier synthesis of both QDs and core/shell structures.

##### 1.4.5.1. Synthesis of the cores – with precursor injection

The simplest way to grow nanocrystals according to LaMer's theory is to separate the phases of nucleation and growth. To accomplish this separation, hot-injection methods have been developed where one of the precursors (potentially with ligands) is heated to high

temperature ( $\sim 300^\circ\text{C}$ ), and the other precursor is swiftly injected in the reaction flask. The nucleation step is immediately reached: nuclei form with similar sizes and shapes. This causes the monomer concentration to decrease rapidly and the growth stage then occurs.<sup>98</sup>

#### I.4.5.2. Synthesis of the cores – one pot

Later, a synthesis that does not require any hot injection was developed. This protocol uses low-reactivity precursors that become reactive enough only at a given temperature. Once this temperature is reached, the precursors react to form nuclei, see their concentration decrease and the NCs undergo the growing step.<sup>99</sup> This does not affect the principle of the separation of nucleation and growth as the precursors react quickly once the proper temperature is reached.

Cadmium myristate ( $\text{Cd}(\text{C}_{13}\text{H}_{27}\text{COO})_2$ ) and elemental selenium were used as precursors to produce CdSe NCs via this type of synthesis. Cadmium myristate decompose at  $\sim 226^\circ\text{C}$  while Se has very low solubility in ODE below  $\sim 200^\circ\text{C}$ .<sup>100</sup> These factors limit the formation of monomers in solution below  $200^\circ\text{C}$ , and the nucleation occurs only above this temperature.<sup>99</sup> Elemental Se was later replaced by  $\text{SeO}_2$  to form similar quality NCs (in this case, ODE acted as a reducing agent to form  $\text{Se}^0$ , see Figure I.17).<sup>72</sup>

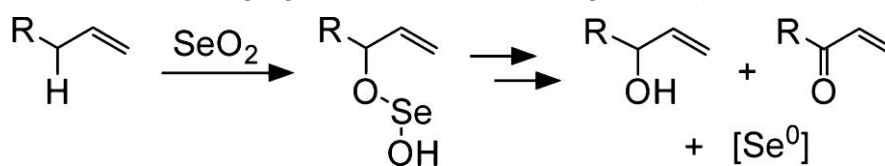


Figure I.17: Scheme of activation of  $\text{SeO}_2$  by unsaturated hydrocarbons.<sup>66</sup>

The reaction was followed *in situ* by small- and wide-angle X-ray scattering to show that the nuclei appear at  $218.7^\circ\text{C}$  after the monomer formation (see Figure I.18).<sup>101</sup>

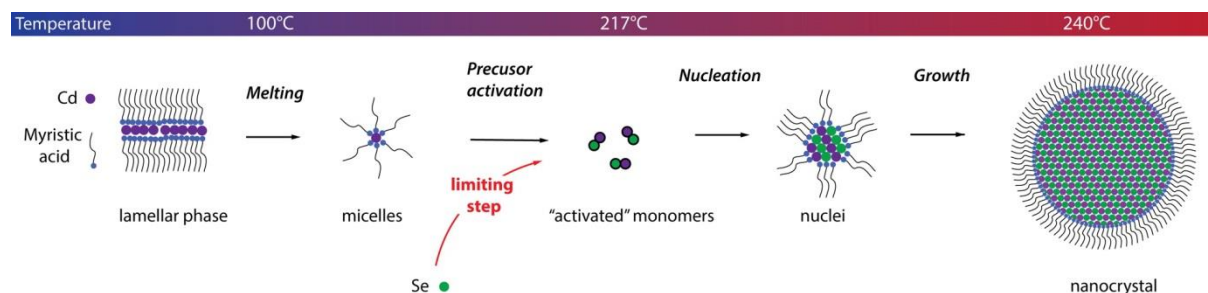


Figure I.18: Scheme of the formation of CdSe QDs from the Cd and Se precursors to the monomer formation, the nucleation phase and finally the formation of NCs.<sup>101</sup>

#### I.4.5.3. Synthesis of the shell – SILAR

After the synthesis of the core, several methods exist to synthesize a capping shell. In 2003, Peng's group showed that a CdS shell can be grown on CdSe cores using Successive Ion Layer Adsorption and Reaction (or SILAR) process.<sup>98</sup> This method consists in depositing one atomic monolayer after another. It requires the precise calculation of the amounts of both anionic and cationic precursors to be injected at each step. The amount of precursor solutions corresponding to one monolayer of the anionic species is injected slowly and the solution is left under stirring for the system to react. The corresponding amount of cationic precursor is then slowly added and left for reaction. This operation is repeated as many times as necessary to grow the expected shell thickness, taking into account the increase of the volume of the NCs in the calculations of the precursor solution volume to be injected. Although the SILAR method gives a good control over the monodispersity in sizes of the QDs and limits secondary nucleation, it is very time-consuming as the time between two injections ranges from 10 minutes to several hours, which extends the synthesis of thick shells to several days.<sup>11</sup>

#### I.4.5.4. Synthesis of the shell – dropwise addition

Thus, it appears that the SILAR method is not optimal for the growth of thick shells. Another method consists in injecting dropwise the precursor solutions in the flask containing the CdSe cores. This requires a good control of the temperature and of the speed of injection as well as of the reactivity of the shell precursors to avoid secondary nucleation of shell-material NCs. The amount of injected precursors can also be calculated to predict the final size of the QDs. Although much faster than the SILAR method, the dropwise addition usually results in less monodisperse samples.<sup>102</sup>

## I.5. Blinking of the Quantum Dots emission

### I.5.1. The blinking phenomenon

In the 1990s, the development of sensitive photodiodes made possible the observation of the fluorescence of single molecules or particles. Studies on single organic molecules showed that they blink, their emission switches over time between an *on* and an *off* state.<sup>103,104</sup> In the case of organic fluorophores, blinking is due to the transition of the excited molecule from a singlet emissive state to a triplet non-emissive state.<sup>105,106</sup> This phenomenon

follows a mono-exponential law for the distribution of *on* and *off* times, characteristic of a three-level system.

### I.5.2. Quantum Dots blinking

Once the syntheses yielded QDs with good and homogeneous optical properties (high quantum yield and low photobleaching), it was possible to study their behavior at the single-particle level. In 1996, Nirmal *et al.* observed for the first time that individual QDs also blink (see Figure I.19).<sup>9</sup>

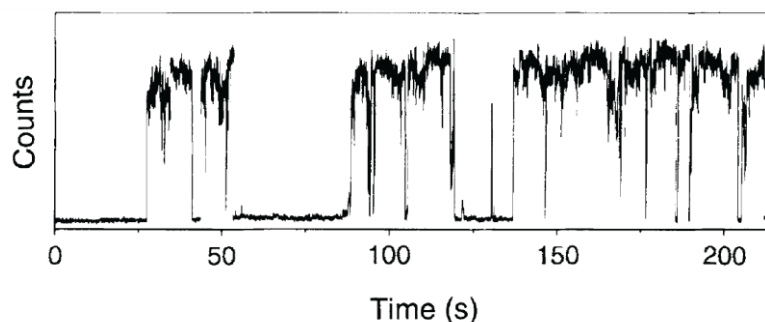


Figure I.19: Evolution of PL intensity with time for a single CdSe QD.<sup>9</sup>

#### I.5.2.1. Characterization of blinking

The blinking of QDs seems completely random, and the *on* (and *off*) duration distribution follows a power law (Lévy walk).<sup>107–110</sup> This low-exponent power-law behavior ( $P(\tau_{on/off}) \propto \tau^{-m_{on/off}}$  with  $m \sim 1.5$ , see Figure I.20)<sup>107</sup> implies that the mechanism of blinking of QDs is not the same as the mechanism for organic molecules. Besides, the QDs can switch on and off randomly and stay off for a time as long as the measurement duration, which limits QDs applications in single-particle tracking for example, and decreases their overall Quantum Yield.

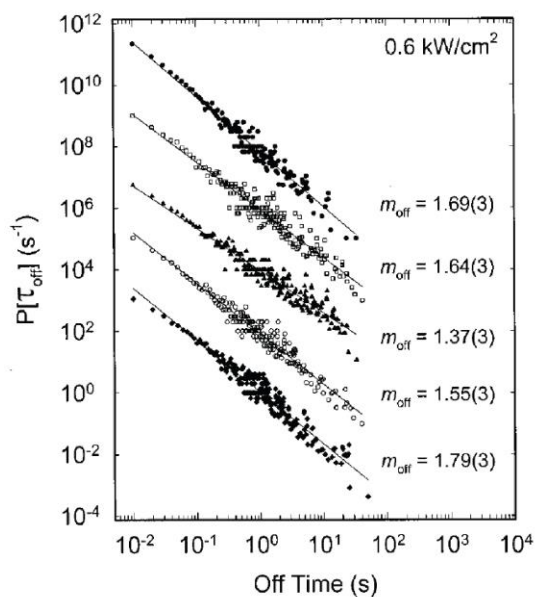


Figure I.20: Off-time probability density for 5 different CdSe/ZnS QDs and the slope  $m$  of the fitted curves.<sup>108</sup>

#### I.5.2.2. Causes of blinking

The *on* times were found to be dependent on the excitation power (their durations decrease with increasing excitation power) while the *off* time distribution remained constant. In the case of CdSe/ZnS QDs, charge carriers trapped at the surface of the ZnS shell were suggested to be an intermediate state, which seemed confirmed by the blue-shift of the emission wavelength. In addition, charged QDs were shown to have reduced fluorescence intensities due to Auger ionization, which scales consistently with the decrease of *on*-state durations with increasing excitation power.<sup>64</sup> Auger recombinations were then seen as a good way to explain the blinking behavior, and the corresponding model was developed by Efros and Rosen (Figure I.21).<sup>10</sup> This model was further supported by the measurement of a positive charge of the QDs after photoexcitation.<sup>111</sup> The *on* times were found to be truncated at shorter time scales when the excitation power was increased, suggesting again Auger processes.<sup>112,113</sup>

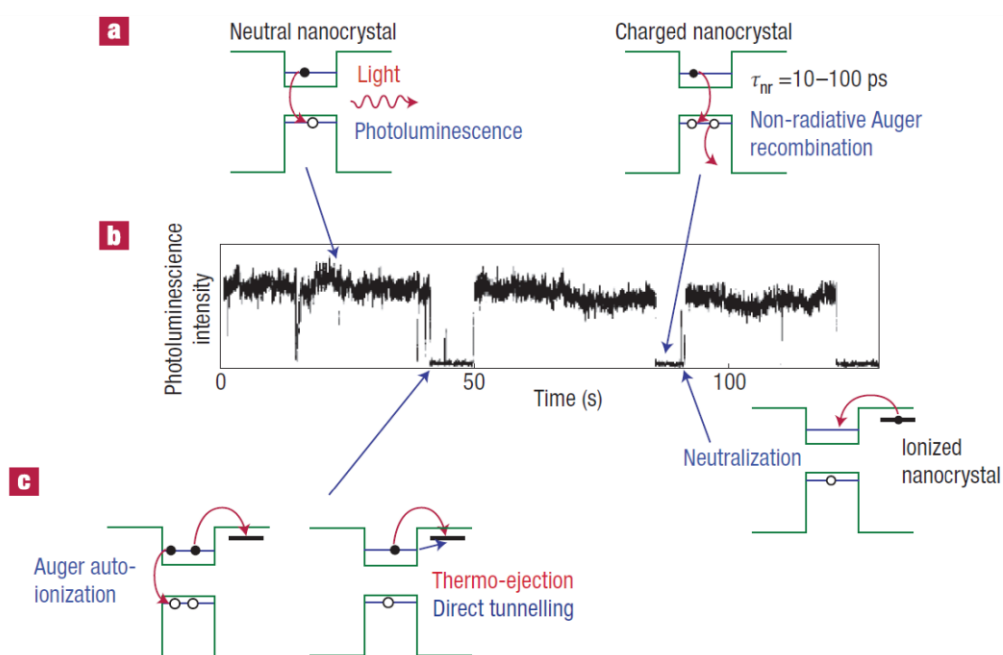


Figure I.21: Schematic diagram explaining the trace of a blinking QD (b). The neutral QD emits photons (a, left) while under its charged form, it undergoes faster, favored Auger recombination (a, right) due to the presence of an excess charge in the NC (c).<sup>114</sup>

However, time-resolved studies shed light on multiple emission states, with a large distribution of lifetimes, challenging the simple *on/off* Auger model which predicts two lifetimes, one for the neutral and one for the charged QD.<sup>115,116</sup> Besides, two types of blinking have been evidenced: A-type blinking where the reduction of the emission intensity is correlated to the reduction of lifetime, and B-type blinking where the lifetime stays constant independently of the fluctuations of the emission intensity. This was attributed to non-radiative recombinations of hot carriers.<sup>117</sup>

The blinking phenomenon of QDs therefore cannot be fully explained by the Auger processes. Long time scale trapping of charges might not be a requisite: spectral diffusion (change in the emission wavelength of the QD due to a charge rearrangement in the vicinity of the NC, or Stark effect<sup>51</sup>) might favor resonant transitions between the intraband transitions in the conduction band and available surface traps for the hole, which quenches the emission.<sup>118</sup> The carrier trapping model was also expanded to take into account multiple trapping centers which can explain the distribution of emission intensities.<sup>119</sup>

Finally, the blinking mechanism is still not fully understood, but several models seem to give a correct, however partial, explanation: Auger model where the *on* state corresponds to the neutral QD and the *off* state to the charged QD with non-radiative recombination of the trion (exciton + excess charge carrier); the charge trapping model, in which either band edge charge carriers relax and are then trapped (correlated with a decrease in the lifetime), or hot

carriers are trapped before relaxing to the band edge (with the same lifetime as the radiative state).<sup>120</sup>

### I.5.3. Reduction of blinking

Due to the limitations induced by the blinking behavior of the QDs (decreased QY or random turning *off* which makes single particle tracking difficult), research has focused on the synthesis of non-blinking QDs with high Quantum yield. Several methods have been developed over the last 15 years to decrease the blinking.

#### I.5.3.1. Addition of molecules

The first method developed aims at changing the environment of the QD. As blinking is related to charge trapping, a good way to suppress it consists in eliminating the traps at the surface of the QD. This has been shown on CdSe/ZnS QDs with the addition of  $\beta$ -mercaptoethanol (BME), a small molecule carrying an electron donor thiol moiety, that donates electrons to the surface electron traps. Once filled, these traps cannot accept other electrons anymore, in particular the electrons coming from the QD. This therefore stops the charging of the QD and eliminates blinking (Figure I.22).<sup>13</sup> However, this strategy requires working in an anti-oxidant environment which might be very restrictive for potential applications.

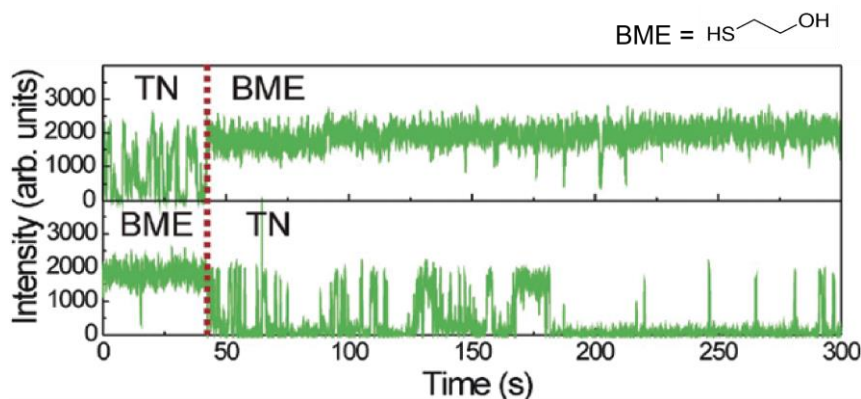


Figure I.22: Intensity trace of a single CdSe/ZnS QD in a buffer medium (called TN) or in presence of BME.<sup>13</sup>

#### I.5.3.2. Compositions gradient between the core and the shell

Strategies that modify the intrinsic composition of the QD are more suitable for a wide range of applications as they change the properties of the QD itself without any assistance from the environment. An example of such modification has been shown in 2009 and

consists of a composition gradient between the core (CdZnSe) and the shell (ZnSe) materials. These QDs show a stable emission intensity over time, with no observable blinking, but exhibit a peculiar emission spectrum (Figure I.23). At the single particle level, the emission spectrum presents three peaks separated by  $\sim 150$  meV. These emission peaks have been attributed to the trion recombination, where the radiative recombination of the exciton is accompanied by an energy transfer to the excess charge carrier present in the QD. The short lifetime of this recombination (4 ns) is similar to the Auger recombination lifetime: radiative and non-radiative recombinations compete, which yields an emission with 50% QY. The absence of blinking has been attributed to the smooth interface between the core and the shell which slows down Auger non-radiative recombinations.<sup>121</sup>

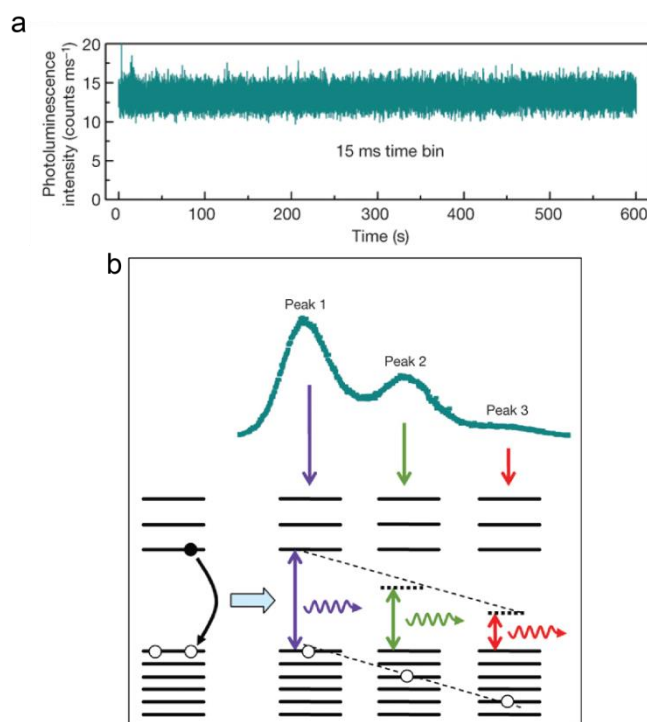


Figure I.23: Intensity trace of a single CdZnSe/ZnSe QD (a) and PL spectrum (b).<sup>122</sup>

These QDs however suffer from very bad resistance when exposed to air due to the photo-oxidation of ZnSe (I.4.4.1). The fluorescence is thus quickly quenched under illumination.

### I.5.3.3. Thick-shell Quantum Dots

Another strategy to eliminate the blinking was developed in 2008 on more air-stable CdSe/CdS QDs. Observed at the single-particle level, QDs with thicker shells showed less blinking than QDs with thinner shells (Figure I.24.a).<sup>11,12</sup>

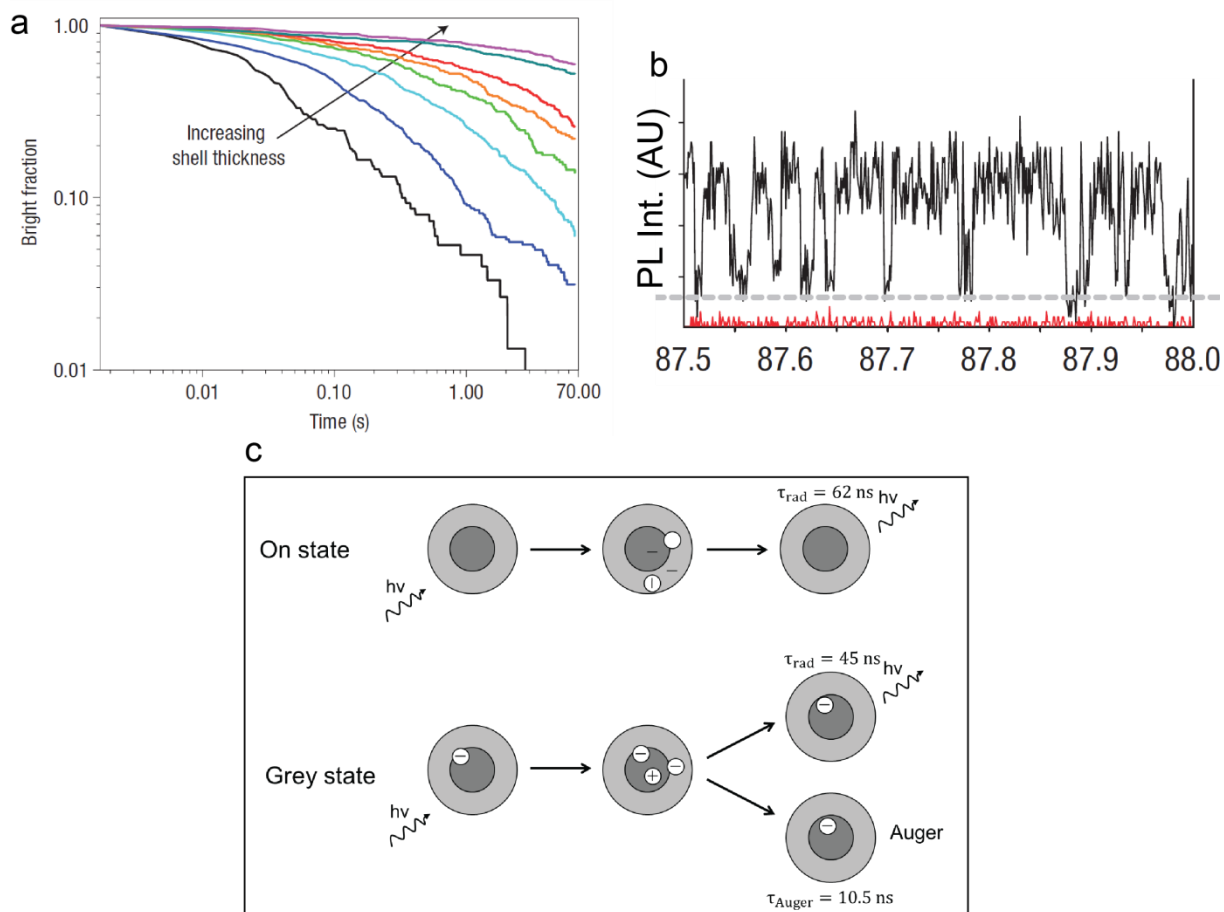


Figure 1.24: a. Bright fraction (i.e. fraction of QDs that never blinked) of thick-shell CdSe/CdS QDs over time. b. Typical PL trace of thick-shell CdSe/CdS QD showing to on and the grey state. c. The on state corresponds to radiative recombination, while the grey state corresponds to a competition between radiative and Auger non-radiative recombinations.<sup>12,123</sup>

When the fluorescence intensity over time of a single QD was measured, two states could be observed: an emissive, *on* state for which the QY is 100%<sup>124</sup>, and a lower-intensity emissive state, called *grey* state, for which the QY is 20%. This *grey* state, although lower in intensity, is not an *off* state, as the QD keeps emitting photons. The measured lifetime of the grey state is around 8 ns.

As previously seen, the *on* state corresponds to the neutral QD and the grey state to the charged QD (exciton and one excess charge carrier, or trion). Knowing the QY and the lifetime, the Auger recombination lifetime can be calculated: it is around 10 ns, which is 2 orders or magnitude lower than in usual CdSe/ZnS. Auger processes are thus strongly slowed down in these thick-shell structures, and are not predominant: the radiative and non-radiative recombinations compete, which yields a *grey*, not-completely-dark state (Figure 1.24.b).

Auger recombinations are slowed down in these thick-shell QDs most probably because the Auger recombination rate scales linearly with the NC volume<sup>63</sup>, or because the

quasi-type II structure separates efficiently the charge carriers in the QD, slowing down their (radiative and non-radiative) recombinations.

Some studies have showed later that the minimum volume for CdSe/CdS QD for blinking suppression is  $\sim 750 \text{ nm}^3$  ( $\sim 6 \text{ nm}$  in radius) and that the core size also influences the Auger recombination efficiency.<sup>125,126</sup>

## I.6. Two-dimensional systems – Nanoplatelets

As mentioned previously, the control of the shape of NC allowed the development of two-dimensional systems. In 2006, T. Hyeon's group showed 1D exciton confinement in CdSe wurtzite nanoribbons, and in 2008, S. Ithurria synthesized the first 2D colloidal zinc-blend CdSe nanoplatelets (NPL).<sup>40,41</sup>

### I.6.1. Nanoplatelets : atomically flat nanocrystals

NPLs are flat colloidal semiconductor nanocrystals with a thickness of around 2 nm and lateral dimensions around 10 nm or above. The exciton created in NPLs after photoexcitation is therefore confined in one dimension, giving NPLs the properties of quantum wells.

Their formation is controlled by the use of long- and short-chain ligands, such as oleates and acetates, that passivate respectively the large and the small cadmium-rich facets of the NPL during growth. The large facets are stabilized by the interaction between long-chain ligands, while the short-chain ligands are more labile, and allow the lateral growth of the NPLs, their thickness remaining unchanged. Their lateral dimensions can be extended to several hundreds of nanometers while the thickness is not affected by the extension protocol.<sup>127</sup>

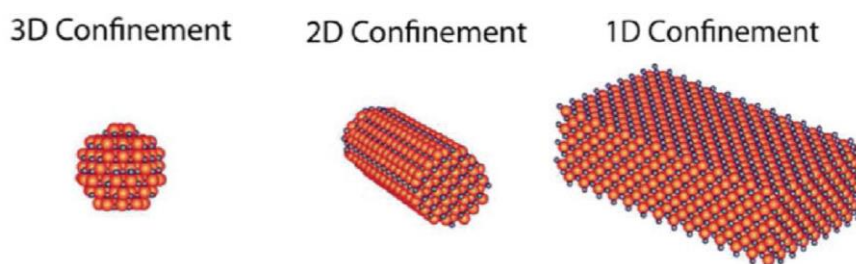


Figure I.25: Different shapes implying different exciton confinements.<sup>128</sup>

## I.6.2. Quantum wells &amp; unique optical features

The density of states for a 1D confinement differs from the density of states for a 3D confinement, which is the case of spherical QDs.

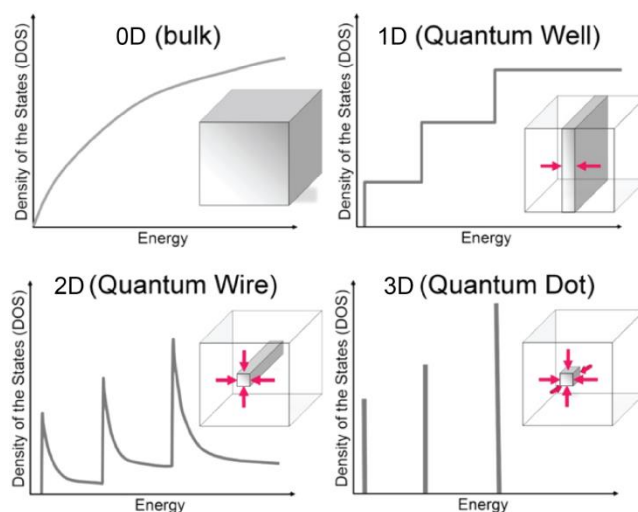


Figure I.26: Densities of states for different confinements.<sup>129</sup>

This electronic structure as well as the atomic control of their thickness yield interesting optical properties. First, the ensemble photoluminescence peak is much narrower than the peak for spherical QDs (FWHM~8 nm vs ~25 nm) (see Figure I.27.a). This is due to the fact that in a batch of spherical QDs, not all the QDs have exactly the same shape or size, which yields inhomogeneous broadening and gives the PL spectrum a Gaussian profile. However, for NPL, as their thickness is controlled to the atomic layer, and their optical properties are due only to their thickness along which the excitons are confined, the spectrum is much narrower, and is only limited by the homogeneous broadening which gives it a Lorentzian profile.

The optical transitions can be seen and assigned on the absorbance spectrum (Figure I.27.a). The Stokes shift is much smaller than for spherical QDs. Finally, the lateral extension does not change the thickness of the NPL, therefore the optical transition energy is unchanged, but an increase in the thickness of the NPL decreases the confinement leading to a red-shift of the transition.

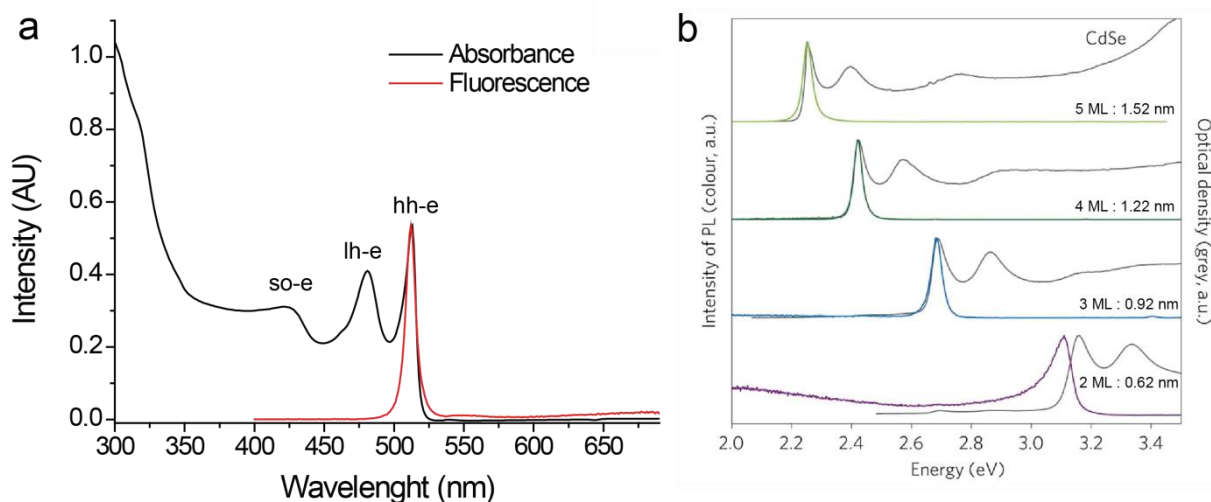


Figure I.27: a. PL and absorbance spectra of an ensemble of CdSe NPLs of 4 monolayers with the assigned optical transitions. b. PL and absorbance spectra of CdSe NPLs of different thicknesses, from 2 to 5 monolayers (ML).<sup>130,131</sup>

The thickness of the NPLs can be determined by TEM measurements or optical measurements: the position of the transition is related to the thickness of the NPL, itself related to the number of atomic monolayers (half a lattice parameter) of the NPL (see Figure I.27.b).

The very short recombination lifetime in NPLs ( $\sim 10$  ns) suggests that the binding energy of the exciton is higher in NPLs than in spherical QDs.<sup>130</sup>

The syntheses have later been extended to form CdS,<sup>130</sup> CdTe,<sup>132</sup> core/shell<sup>131,133</sup> or core/crown NPLs.<sup>80</sup>

## I.7. Conclusion

Colloidal semiconducting nanocrystals, or Quantum Dots, have unique optical properties such as bright, narrow and tunable emission, that are strongly affected by quantum confinement effect and band-gap engineering. Their chemical syntheses have been improved over the last thirty years to develop solutions of monodisperse QDs. New protocols allowing for a control of the shape of the NCs (spherical, rods or platelets) opened the road to even more tunability and new properties. Their applications are however still limited due to the blinking of their emission which comes from non-radiative Auger recombinations in charged nanocrystals. Although some strategies have been suggested to decrease their blinking, QDs with completely stable emission and high quantum yield have yet to be synthesized.



## Chapter II. Synthesis of CdSe/CdS Quantum Dots

Several synthesis protocols have been developed over the last twenty years to grow stable colloidal Quantum Dots with low size dispersion, narrow emission band and high quantum yield.

### II.1. Setup used for the synthesis

The synthesis of colloidal Quantum Dots is performed in a round-bottomed flask in organic solvents. Because of the low reactivity of the precursors, the reaction is carried out at high temperature ( $\sim 300^{\circ}\text{C}$ ); and the temperature needs to be controlled, in particular to separate efficiently the nucleation and the growth of the NCs (see I.4). To limit the oxidation of the QDs during the synthesis, the reaction is performed under inert atmosphere (argon gas) after evacuating oxygen and water from the medium and the solvent by degassing under vacuum. Different protocols are available for the synthesis of NCs. For the protocols requiring an injection of one or several precursors, a syringe can be used, whose injection rate can be controlled by a syringe pump if necessary. The setup is illustrated in Figure II.1.

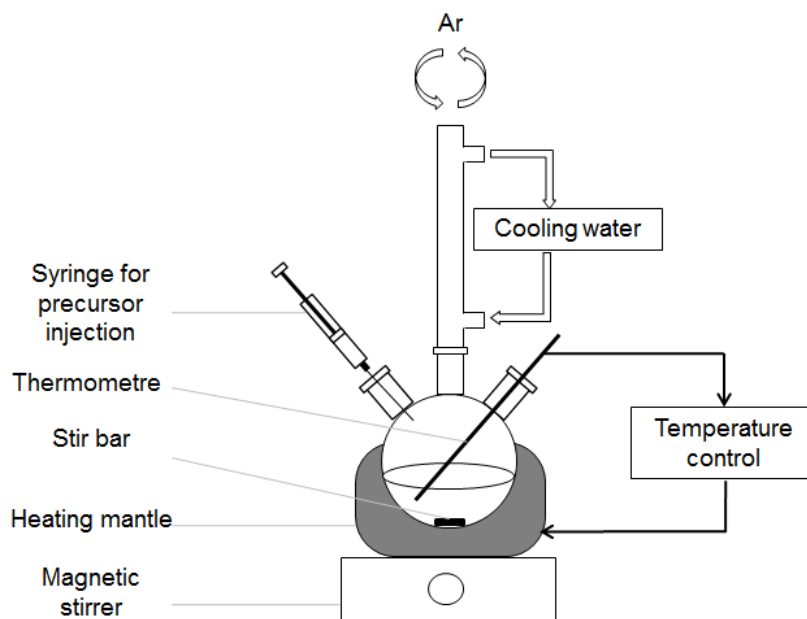


Figure II.1: Experimental setup for the synthesis of colloidal QDs.

## II.2. Characterization methods

### II.2.1. Absorption

Absorbance measurement is an easy way to obtain crucial information about a colloidal suspension of NCs (Figure II.2). It gives the excitonic structure of the Quantum Dots, allows a rough estimation of the emission wavelength, informs on the amount of secondary nucleation during the reaction thanks to a comparison with photoluminescence excitation spectrum (PLE, see II.2.3), but can also be used to extract information on the size and concentration of the QDs in the suspension.

The determination of the size and the concentration was developed by Leatherdale *et al.*<sup>134</sup> and Yu *et al.*<sup>135</sup>, and further confirmed by other works.<sup>136,137</sup> The analysis of transmission electron microscopy images (see II.2.5) and the correlation to the position of the first excitonic peak yields a formula that gives the size of the QD:

$$D = (1.6122 \times 10^{-9})\lambda^4 - (2.6575 \times 10^{-6})\lambda^3 + (1.6242 \times 10^{-3})\lambda^2 - 0.4277\lambda + 41.57$$

where  $D$  is the diameter of the QD and  $\lambda$  the wavelength at the first excitonic peak, both in nm. This equation is valid for CdSe QDs, but similar equations can be found for CdS and CdTe.<sup>135,138</sup>

A similar approach leads to the molar extinction coefficient dependence with size. However, when studied at the position of the first excitonic peak, quantum confinement

effects require taking into account the effective band-gap of the material. Leatherdale *et al.* worked at high excitation energies, far from the band edge, at 350 nm to ensure that the quantum confinement effects are negligible: the material behaves as if it was bulk and the linear absorption coefficient, which defines the extent of light absorption through the material, is independent of its size. The particle cross-section ( $\sigma$ ) or the molar extinction coefficient ( $\epsilon$ ) can further be calculated:

$$\epsilon (\text{CdSe at 350 nm}) = 1.438 \cdot 10^{26} \cdot r^3 \text{ M}^{-1} \cdot \text{cm}^{-1}$$

$$\sigma (\text{CdSe at 350 nm}) = 5.501 \cdot 10^5 \cdot r^3 \text{ cm}^2$$

where  $r$  is the particle radius in cm.

The concentration  $C$  (in  $\text{M}^{-1} = \text{mol} \cdot \text{l}^{-1}$ ) of CdSe QDs can therefore be estimated using Beer-Lambert's law:

$$A = \epsilon l C$$

where  $A$  is the absorbance and  $l$  the length of the optical path length in the absorbing medium (width of the measurement cuvette, in cm)

With the position of the first excitonic peak in the absorbance spectrum, and the absorbance at 350 nm, a simple absorbance spectrum gives the size and the concentration of the CdSe particles in colloidal suspension.

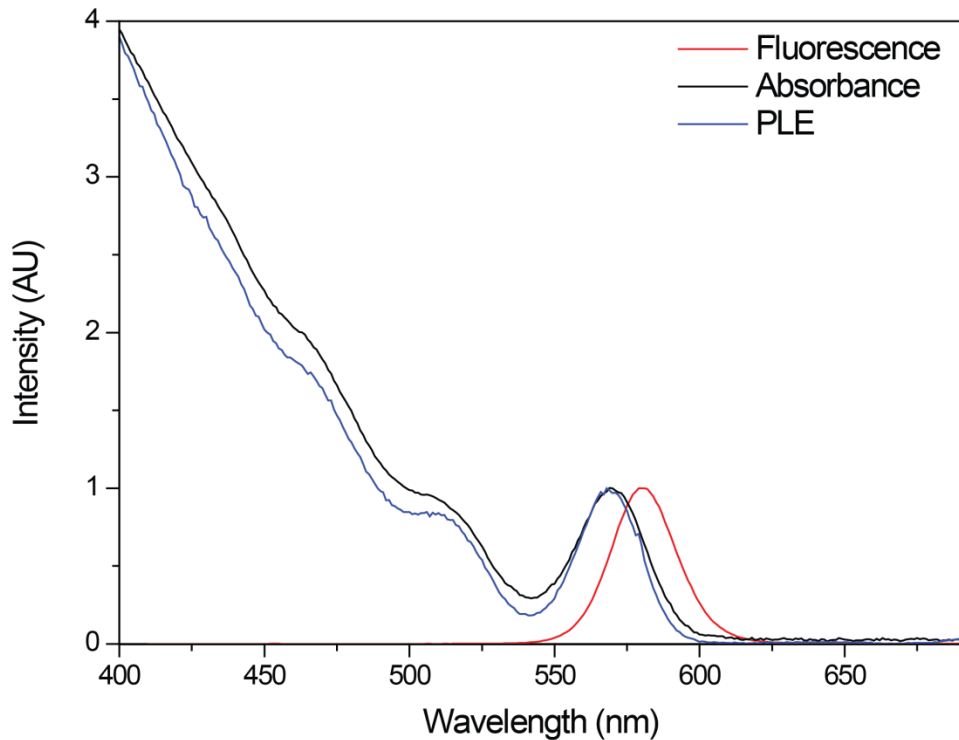


Figure II.2: Fluorescence, absorbance and photoluminescence excitation spectra of an ensemble of CdSe/CdS Quantum Dots in colloidal suspension.

## II.2.2. Fluorescence emission

Fluorescence measurement is also an easy-to-implement characterization to follow the evolution of nanocrystal growth during the synthesis. Several information can be extracted from a fluorescence spectrum, otherwise called photoluminescence (PL) spectrum (Figure II.2).

First, the relative intensity collected on a PL spectrum informs on the quantum yield of the QDs. Indeed, the comparison, at the same relative absorption, between the emission intensity of a sample of QDs and that of a reference sample of known QY allows to determine the QY of the QDs (see II.2.3).

As seen previously (see I.3.1.2), the QDs have a narrow emission band, typically around 20 to 30 nm of full-width at half maximum (FWHM). Thus, the broadness of the band can inform on the inhomogeneity of the NC growth. Indeed, the FWHM can be correlated with the size dispersion of the sample. The inhomogeneities can come from the presence of different sizes of QDs or from the heterogeneous growth of a shell of core QDs. The larger the size dispersion, the broader the band. This correlation is however limited as it assumes the NCs of different sizes have the same QY.

The appearance in the spectrum of another emission peak than the one originating from the band edge recombination informs on the existence of either secondary nucleation or emission from traps. Typically, secondary nucleation occurs when the synthesis parameters are not optimized and when the precursors that should deposit on existing particles and make them grow, nucleate in solution and form new, smaller seeds, emitting at a lower wavelength. Emission from traps can be seen mostly in the case of the smallest NPs for which the surface-to-volume ratio is the highest: not all the surface bonds are well passivated, forming traps for the charge carriers within the band gap, which yields emission at lower energy. Those peaks can be seen on the PL spectrum only if the secondary nuclei are fluorescent or the recombinations from traps is radiative.

The PL spectra are acquired on a F900 spectrometer from Edinburgh Instruments. It is equipped with several detectors: the R928P in the 200-870 nm region; an MCP-PMT in the same region, but with a response time ~12 times faster; the R2658P for the NIR (200-1010 nm); and a NIR-PMT up to 1700 nm. For CdSe/CdS QDs, the R928P provides the good spectral range, adequate sensitivity and a response time fast enough (600ps) for typical CdSe/CdS NCs lifetime measurements.

### II.2.3. Determination of the Quantum Yield

As presented previously (see I.3.2.4), the quantum yield can be defined at the single particle level, but it can also be measured on an ensemble of NCs. The idea here is to compare, for the same relative absorption, the number of photons emitted by the sample of interest (QD) and by a reference sample of already known QY. The reference needs to be carefully chosen: its emission wavelength needs to be close to the emission wavelength of the studied QDs, and it has to absorb at the same wavelength (which should not be a problem for QDs as they have a wide range of absorption wavelengths). For CdSe/CdS Quantum Dots, we usually use Rhodamine 6G, which emits around 550 nm and has a QY of 95% in ethanol.

To measure the quantum yield, a series of dilute solutions are prepared (absorbance at the excitation wavelength  $< 0.1$  to avoid reabsorption effects). Their absorbance and PL are measured, and the integrated PL are plotted vs the absorbance. This curve can be fitted by a straight line whose slope is then used to determine the QY:

$$QY_{sample} = QY_{ref} \cdot \frac{Slope_{sample}}{Slope_{ref}} \cdot \frac{n_{sample}^2}{n_{ref}^2}$$

where  $QY_{ref}$  is the QY of the reference used,  $Slope_{sample}$  and  $Slope_{ref}$  are the slopes of the integrated PL vs absorbance curves respectively for the sample and for the reference, and  $n_{sample}$  and  $n_{ref}$  are the refractive indices of the solvents used respectively for the sample and for the reference.<sup>139</sup>

The precision of this ensemble quantum yield measurements is relatively low and a 10% error is commonly accepted. It represents an average over the whole sample, including the low-QY, or non-emitting nanoparticles if present, and consequently leading to an underestimation of the QY of the brighter NCs.

### II.2.4. Excitation (PLE)

The excitation (or Photoluminescence Excitation, PLE) spectrum is based on the detection of the PL intensity at a given wavelength with a changing excitation wavelength (Figure II.2). Given the fact that the PL efficiency, or QY, for CdSe NCs is independent from the excitation wavelength,<sup>140</sup> this allows to probe the absorbance of one population of NCs, the one that emits at the selected wavelength. If no secondary nuclei are present, the absorption is not increased by NCs that absorb but do not emit, or emit at a different wavelength, and the PLE and absorbance spectra should be very similar. Besides, as only one population of QDs is probed, the excitonic peak on the PLE spectra is narrower than the

one on the absorbance spectra: the size dispersion is masked by the fact that only one wavelength is observed.

PLE is therefore a good tool to investigate the growth of QDs and to verify the absence of secondary nucleation (Figure II.3). But it is also useful to monitor the growth of a shell. For example, if CdS is grown on CdSe, due to its larger band-gap (around 515 nm), the intensity of the PLE spectrum below 515 nm will increase showing that the CdS shell absorbs and is involved in the emission at the probed wavelength.

Finally, the narrow peak observed on the PLE spectrum is due to the diffusion through the sample of the excitation beam when its wavelength is the same as the probed one, *i.e.* the wavelength at which the detector is set.

The PLE spectra are acquired on a F900 spectrometer from Edinburgh Instruments.

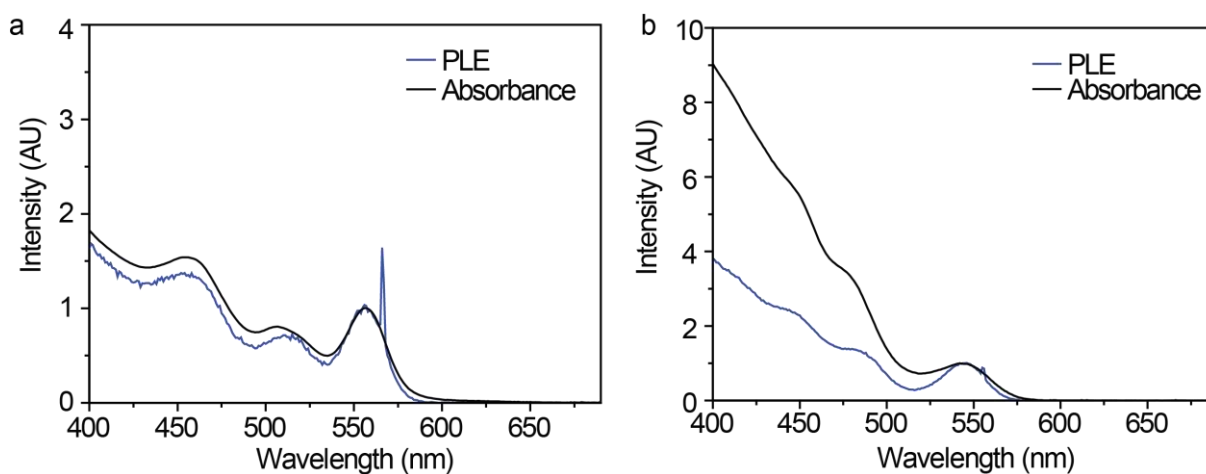


Figure II.3: Comparison between absorbance and PLE spectra in the case of a CdSe/CdS synthesis a. without secondary nucleation and b. with secondary nucleation of CdS nanocrystals.

### II.2.5. Transmission Electron Microscopy

The structural characterization of QDs can be performed by transmission electron microscopy (TEM, also Transmission Electron Microscope). This technique allows to directly visualize the nanoparticles and to get information on their size, size distribution, morphology, crystallinity, etc. (Figure II.4)

When accelerated under 200 kV, electrons can be transmitted through a thin sample. When they hit the detector, they produce an image whose contrast is correlated with the atomic mass (and therefore with the electron density) of the elements in the material and with its thickness. The resolution of a TEM is around 1 nm, or even a few tenths of nanometer: individual atoms and their organization in the crystal can be seen on high-resolution images (magnification of 500,000 to 1,000,000). Finally, TEM allows to carry out electronic diffraction which is particularly useful to determine the crystal structure of the QDs.

The sample is prepared as follows: several washing steps in ethanol are performed to get rid of the excess of organic ligands in solution (they do not stand a long exposure to the electron beam, and degrade rapidly decreasing the contrast of the image). The QDs are then redispersed in hexane at a concentration of around 5  $\mu\text{M}$  and a 10- $\mu\text{L}$  drop is deposited on a standard carbon grid. The grid is left to dry at atmospheric pressure and then put under vacuum overnight to remove as much ligands and solvent as possible.

The observations are performed on a Jeol 2010-F for the TEM or on a FEI Titan Themis for the Scanning Transmission Electron Microscopy (STEM) in collaboration with Gilles Patriarche from Laboratoire de Photonique et de Nanostructures, Marcoussis.

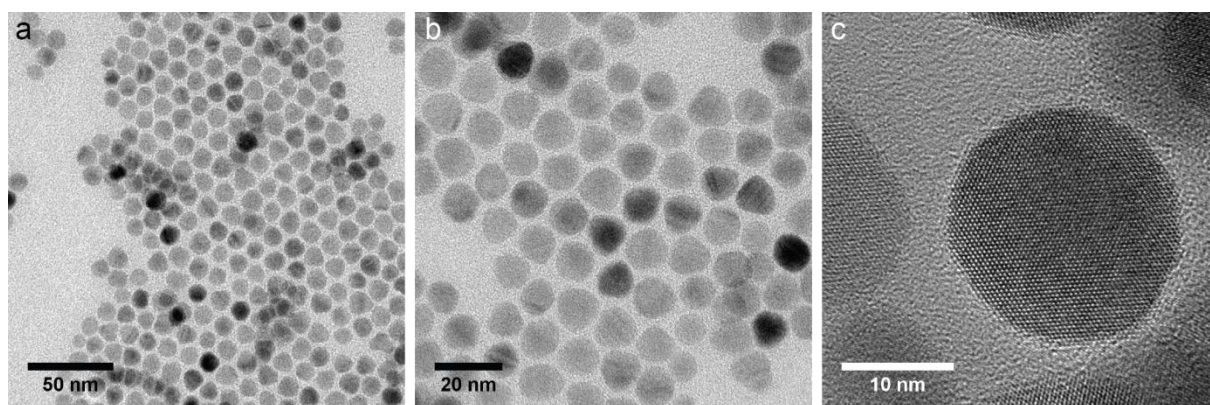


Figure II.4: TEM images of CdSe/CdS Quantum Dots at different magnifications: a.x60,000, b.x120,000, c.x500,000.

## II.2.6. Energy dispersive X-ray spectrometry (EDX)

Elemental composition of the sample can be performed thanks to energy dispersive X-ray spectroscopy, or EDX. When QDs are exposed to a high-energy electron beam (electrons are accelerated by a voltage between 5 and 20 kV), electrons from inner atomic energy levels can be ejected out of the electron cloud. For an atom to relax, an electron from a higher energy level goes down in energy to take the place of the ejected electron, giving its excess energy to the environment in the form of a photon in the X-ray range. This energy is characteristic of the atom; thus, by detecting the number and the energy of all these emitted X-ray photons, the elemental composition of the sample can be deduced.

The EDX experiments were performed in collaboration with Gilles Patriarche from Laboratoire de Photonique et de Nanostructures, LPN, Marcoussis, France, on a Titan Themis.

### II.2.7. X-ray Diffraction (XRD)

To determine the crystal structure of the synthesized NCs, X-Ray Diffraction (XRD) is a particularly useful technique. Most commonly produced by the  $K_{\alpha}$  emission of copper at a wavelength of 1.54 Å, the X-rays are diffracted in different directions by the electrons of the atoms that compose the crystal. In the powder XRD method, the incident beam hits an ensemble of randomly-oriented nanocrystals, and a detector collects the diffracted signal at a  $2\theta$  angle compared to the incident beam. The obtained diffractogram presents peaks at given angles that are characteristic of the crystal structure of the material. By comparing to the diffractograms present in the crystallographic databases, the crystal structure of the studied sample can be determined.

This however requires the crystals to be large enough. Indeed, the width of the peaks on the diffractogram can be related to the size of the crystals through the Scherrer formula:

$$FWHM(2\theta) = \frac{0.91\lambda}{R \cos(\theta)}$$

where  $FWHM$  is the full-width at half maximum of the peak,  $\lambda$  is the incident beam wavelength (which in our case corresponds to the  $K_{\alpha}$  emission line of copper,  $\lambda = 1.5418$  Å),  $R$  is the average size of the crystals and  $\theta$  is the diffraction angle. The smallest the particles, the largest the  $FWHM$ . Zinc-blende (ZB) and wurtzite (W) structures, the two possible structures for CdSe and CdS crystals, have characteristic peaks at  $2\theta$  angles close to each other, which makes it difficult to distinguish between small (< 3 nm) ZB or W nanocrystals as the peaks are broad for such small sizes.

A typical sample is prepared by drop-casting several drops of a concentrated dispersion of QDs on a silicon wafer. The diffractograms are acquired on a Philips X'Pert diffractometer.

### II.2.8. Magneto-optical measurements

As the exciton created in the QDs after excitation is composed of charge carriers, it can interact with the surrounding magnetic field. Indeed, when a magnetic field is applied, the interaction between the exciton and the field induces a modification of the energy levels available in the QD.

For wurtzite structures, the field component parallel to the  $c$ -axis induces a Zeeman splitting of the excitonic levels. The degeneracy is lifted, which in turn changes the optical properties of the QD. By changing the energy levels available, given the selection rules for optical transitions, the emitted photon can be polarized  $\sigma^+$  or  $\sigma^-$  perpendicularly to the  $c$ -axis.

The field component perpendicular to the  $c$ -axis induces a mixing of the excitonic bright and dark states, modifying the recombination lifetime.

The determination of the sign of the degree of circular polarization (DCP) enables to determine unambiguously the global sign of the charges present in the QDs. A neutral QD, with one electron and one hole, will show a non-polarized emission. On the other hand, a charged exciton (trion) will have a  $\sigma^+$  or  $\sigma^-$  polarized emission if it is charged respectively positively or negatively. The DCP is calculated as follows:

$$DCP = \frac{I(\sigma^+) - I(\sigma^-)}{I(\sigma^+) + I(\sigma^-)}$$

where  $I(\sigma^+)$  is the intensity of the  $\sigma^+$  polarized emission, and  $I(\sigma^-)$  is the intensity of the  $\sigma^-$  polarized emission. The measurement of the PL as a function of the polarization allows to determine the charge of QD, *i.e.* the sign of the excess charge present in the QD.

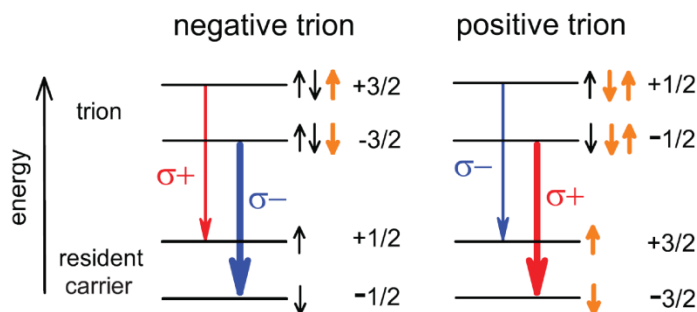


Figure II.5: Schematic representation of the spin level structure in an external magnetic field. Spins of the electrons (holes) are depicted by black (orange) arrows. The most intense transition is represented by a thicker arrow and corresponds to the  $\sigma^-$  transition in the negative trion and to the  $\sigma^+$  transition in the positive trion.<sup>141</sup>

### II.3. Synthesis of CdSe cores

Several types of QDs have been synthesized for the study of the blinking. Different CdSe cores (in size, in crystalline structure) have been used to check the influence of a thick CdS shell on their optical properties.

#### II.3.1. Preparation of precursors

- Cadmium myristate: prepared according to a procedure published previously.<sup>99</sup> 3.13 g of sodium myristate is dissolved in 250 mL of methanol under magnetic stirring for 1 h. In parallel, 1.23 g of cadmium nitrate tetrahydrate is dissolved in 40

mL of methanol. The two solutions are then mixed, forming a white precipitate that is then filtered and washed with methanol, and dried overnight under vacuum.

- Cadmium oleate solution ( $\text{Cd(oleate)}_2$ : 0.5 M in oleic acid): 1.28 g of cadmium oxide in 20 mL of oleic acid is heated at 160°C for 1 hour under argon until it turned colorless. The solution is then degassed under vacuum at 70°C for 30 min.
- Selenium solution (SeODE: 0.1 M in 1-octadecene (ODE)): 140 mL of ODE is degassed under vacuum at 100°C, then heated to 170°C under argon atmosphere. The temperature is then slowly increased to 205°C. In parallel, 1.185 g of Se powder is dispersed in 10 mL of ODE, and added dropwise to the hot ODE as the temperature is rising. After the injection, the solution is left for 30 min at 205°C for complete Se dissolution.
- Sulfur solution (SODE: 0.1 M in ODE): 320 mg of sulfur is heated in 100 mL of degassed ODE at 120°C until complete dissolution.
- Trioctylphosphine selenide solution (TOPSe: 1 M in trioctylphosphine (TOP)): 7.9 g of selenium powder is dissolved in 100 mL TOP under magnetic stirring.

#### II.3.2. Zinc-blende CdSe cores

##### II.3.2.1. One-pot synthesis

This protocol adapted from Yang *et al.*<sup>99</sup> is a one-pot synthesis of CdSe cores in zinc-blende (ZB) crystalline structure. A mixture of 16 mL of ODE, 0.3 mmol of cadmium myristate and 0.15 mmol of selenium powder was degassed under vacuum at room temperature for 30 min, heated under argon flow up to 240°C, and then kept at 240°C for 10 min. Afterwards, 200  $\mu\text{L}$  of oleic acid were added just before cooling down the mixture to room temperature. The nanocrystals were washed with ethanol and used for the CdS shell growth as described below. This protocol provides nanocrystals of 3 nm in diameter.

A small variation of the above protocol gave access to CdSe cores with a diameter of around 5 nm.<sup>142</sup> After the injection of 200  $\mu\text{L}$  of oleic acid, the temperature was raised to 260°C. At 260°C 2 mL of oleylamine were injected. After 20 min, the temperature was further raised to 280°C. At 280°C, the temperature was set to 305°C and, at the same time, a solution of 5 mL of 0.1 M SeODE and 1 mL of 0.5 M  $\text{Cd(oleate)}_2$  was injected dropwise at 36 mL/h. The injection was stopped when the nanocrystals wavelength reached about 630 nm, and the mixture was cooled down to room temperature. The nanocrystals were washed with ethanol and used for the CdS shell growth as described below.

### II.3.2.2. Injection synthesis

This protocol is adapted from Mohamed *et al.*<sup>143</sup> A mixture of 2 mL of 0.5 M Cd(oleate)<sub>2</sub> and 3 mL of ODE was degassed under vacuum at 70°C for 30 min and heated under argon flow up to 240°C. A mixture of 1.5 mL of 1 M TOPSe, 1.5 mL of oleylamine and 1 g of tetradecylphosphonic acid (TDPA) was heated until complete dissolution, then injected and the solution was annealed for 8 min at 190°C. The reaction mixture was cooled down to room temperature, washed with ethanol and dispersed in 10 mL of toluene. The solution was centrifuged in order to precipitate TDPA. The nanocrystals were washed again in ethanol, and dispersed in 10 mL of hexane. The nanocrystals obtained with this protocol had a diameter of around 3 nm.

### II.3.3. Wurtzite CdSe cores

This protocol is adapted from Li *et al.*<sup>98</sup> A mixture of 0.75 mL of 0.5 M Cd(oleate)<sub>2</sub>, 1.3 mL of TOPO and 5 mL of ODE was degassed under vacuum at 70°C for 30 min and heated under argon flow up to 300°C. A mixture of 4 mL of 1 M TOPSe and 3 mL of oleylamine was injected and the solution was annealed for 6 min at 280°C. The mixture was cooled down to room temperature and the nanocrystals were washed with ethanol and dispersed in 10 mL of hexane. The nanocrystals obtained with this protocol had a diameter of around 3 nm.

## II.4. **Synthesis of CdSe/CdS Quantum Dots - Dropwise addition**

In this work, we are interested in the synthesis and optical properties of thick-shell QDs. Thus, the continuous dropwise injection of precursors was chosen as a method to grow the shell. It provides a quick and easy way to grow a thick shell contrary to the SILAR method which is very time consuming and not adapted for long injection steps.

The idea of this protocol is to inject enough weakly reactive Cd and S precursors to grow a CdS shell on the CdSe cores in solution, without forming secondary nuclei of CdS. The amount of precursors needed is calculated on the basis that the CdSe cores are spherical, CdS grows with the wurtzite structure, and the reaction yield is 100%. This, of course, is an approximation: however, only a small difference was usually observed between the final theoretical size and the size of NCs observed under TEM (less than 15%).

In order to grow thick shells on different kinds of cores, the protocol was slightly modified and adapted to the type of the core and the final thickness of the shell.

II.4.1. Growth of a thick CdS shell on CdSe one-pot zinc-blende cores (studied in III.2):

These QDs are studied in III.2.

In a three-neck flask, a mixture of freshly-made 5-nm-CdSe cores (40 nmol), ODE (5 mL) and cadmium myristate (10 mg) is degassed for 30 min at 70 °C under vacuum. The flask is then filled with argon and heated up to 260 °C. At this temperature, oleylamine (2 mL) is injected and the reaction is further stirred for 20 min. 4.5 mL of a mixture of SODE (0.1 M, 16.5 mL) and cadmium oleate (0.5 M, 3.5 mL) is added dropwise (2.25 mL/h). After injection, the temperature is raised to 310 °C. Then, the remaining 15.5 mL of the precursors' mixture are added dropwise (7 mL/h). After injection, 22 mL of the reaction medium are withdrawn, and another 20 mL of a mixture of SODE (0.1 M, 16.5 mL) and cadmium oleate (0.5 M, 3.5 mL) are added dropwise (7 mL/h) to the QDs remaining in the flask. The solution is then cooled down to room temperature. The core/shell CdSe/CdS QDs are finally washed with ethanol and redispersed in hexane ( $C = 1.42 \mu\text{M}$ ). The CdSe/CdS QDs are characterized optically and by electron microscopy. Their final diameter is 30 nm (ZB-1, Figure II.6), corresponding to a CdS shell thickness of 12 nm.

II.4.2. Growth of a thick CdS shell on CdSe injection-synthesized zinc-blende cores:

These QDs are studied in III.2.2.

In a three-neck flask, a mixture of freshly-made CdSe cores (250 nmol), ODE (5 mL) and cadmium myristate (50 mg) is degassed for 30 min at 70 °C under vacuum. The flask is then filled with argon and the temperature is set to 300°C. At 280°C, oleylamine (1 mL) is injected. At 290°C, 20 mL of a mixture of SODE (0.1 M, 15 mL), cadmium oleate (0.5 M, 3 mL) and oleylamine (2mL) is added dropwise (first at 4 mL/h for 2 mL, then at 18mL/h). After injection, 20 mL of a mixture of SODE (0.1 M, 15 mL), cadmium oleate (0.5 M, 3 mL) and oleylamine (2 mL) are added dropwise (20 mL/h). The solution is then cooled down to room temperature. The core/shell CdSe/CdS QDs are washed with ethanol and redispersed in hexane. The same protocol is applied once more for the injection of 20 mL of precursors, the NCs are washed and redispersed in hexane. Their final diameter is 16 nm (ZB-2, Figure II.6), corresponding to a CdS shell thickness of 7 nm.

II.4.3. Growth of a thick CdS shell on CdSe wurtzite cores:

These QDs are studied in III.2.2.

In a three-neck flask, a mixture of freshly-made CdSe cores (160 nmol), ODE (5 mL) and cadmium myristate (50 mg) is degassed for 30 min at 70 °C under vacuum. The flask is then filled with argon and the temperature is set to 300°C. At 280°C, oleylamine (1 mL) is injected. At 290°C, 20 mL of a mixture of SODE (0.1 M, 15 mL), cadmium oleate (0.5 M, 3 mL) and oleylamine (2mL) is added dropwise (first at 4 mL/h for 2 mL, then at 18mL/h). After injection, 18mL of the reaction medium are withdrawn, and 20 mL of a mixture of SODE (0.1 M, 15 mL), cadmium oleate (0.5 M, 3 mL) and oleylamine (2 mL) are added dropwise (20 mL/h). 2 mL of 0.5M Cd(oleate)<sub>2</sub> are added and the solution is annealed for 10min. The solution is then cooled down and 2 mL of oleylamine and 2 mL of oleic acid are added at 140°C. The core/shell CdSe/CdS QDs are washed with ethanol and redispersed in hexane. Their final diameter is 18 nm (W, Figure II.6), corresponding to a CdS shell thickness of 8 nm.

#### II.4.4. Growth of a composition gradient and thick CdS shell on CdSe wurtzite cores:

These QDs are studied in III.3.

In a three-neck flask, a mixture of freshly-made CdSe cores (120 nmol), ODE (5 mL) and cadmium myristate (10 mg) is degassed for 30 min at 70 °C under vacuum. The flask is then filled with argon and heated up to 260 °C. At this temperature, oleylamine (2 mL) is injected and the reaction is further stirred for 20 min. 4.5 mL of a mixture of SODE (0.1 M, 16.5 mL) and cadmium oleate (0.5 M, 3.5 mL) are added dropwise (2.25 mL/h). After injection, the temperature is raised to 310 °C. Then, the remaining 15.5 mL of the precursors' mixture are added dropwise (5 mL/h). The reaction solution is then annealed for 4h30 at 310°C. The core/shell CdSe/CdS QDs are finally washed with ethanol and redispersed in hexane. Their final diameter is around 50 nm (b-QD, Figure II.6).

## II.5. Summary of the Quantum Dots synthesized for the study

The studied QDs were all synthesized in a similar manner for the shell, consisting in a dropwise injection of precursors. The cores, however, are all different and were synthesized according to different protocols. Sample ZB-1 is made of zinc-blende CdSe synthesized *one-pot*; sample ZB-2 is made of zinc-blende CdSe synthesized via an injection method; and

sample *W* is made of wurtzite CdSe cores. The gradient composition QD sample, b-QD, is made of a *W* core and a modified protocol has been applied for the shell growth.

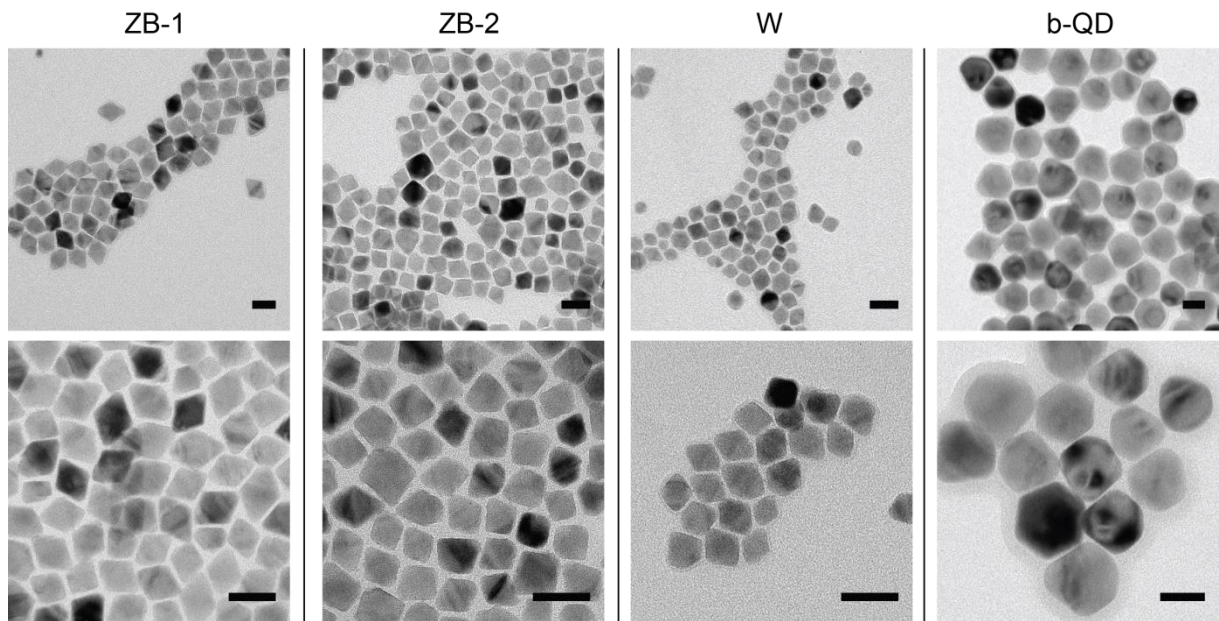


Figure II.6: TEM images of the CdSe/CdS QDs samples prepared for this study. Scale bar is 30 nm.

## II.6. Conclusion

Several types of thick-shell CdSe/CdS QDs have been synthesized, with different crystalline structures for the CdSe cores, and with an abrupt or smooth interface between the core and the shell. They have been further characterized via optical spectroscopy to determine their blinking behavior.





## **Chapter III. CdSe/CdS Quantum Dots with 100% quantum yield in air, at room temperature**

The potential applications of QDs for single-particle tracking or for display devices require the development of non-blinking NCs with a high emission quantum yield. To obtain such QDs, the development of new syntheses is required and their properties need to be thoroughly studied.

### **III.1. Setup used for spectroscopic studies**

The precise study of individual Quantum Dots gives information on the photophysical phenomena occurring after their photoexcitation: blinking, dynamics of recombination, photoresistance to higher excitation powers, behavior under vacuum and low temperature... These measurements require an optical setup able to acquire and analyze the signal coming from a single nanoparticle.

#### **III.1.1. Epifluorescence microscope**

The optical setup used is an inverted epifluorescence microscope, the Olympus IX71. It is equipped with a mercury short-arc lamp that covers a wide range of wavelengths with a high intensity in the UV-blue region (Figure III.1). The power received on the sample is then around  $20\text{W}/\text{cm}^2$ , and can be limited by the use of neutral density filters. A wide variety of filters can be used to select the excitation and collection wavelengths; for typical studies, we used a short-pass 550 nm filter for excitation and a long-pass 590 nm for collection. The sample is excited and observed through different objectives: x100 oil NA1.4 or x60 water NA0.7 for studies under vacuum or at cryogenic temperature. The image can be recorded with a high-sensitivity EM-CCD camera (Photometrics QuantEM:512SC) at a maximum rate of 30 Hz and then analyzed with a home-made MatLab software to identify the QDs and extract their trace, *i.e.* their PL intensity vs time. This allows making of statistics for the blinking behavior on a large number of individual QDs (up to ~100).

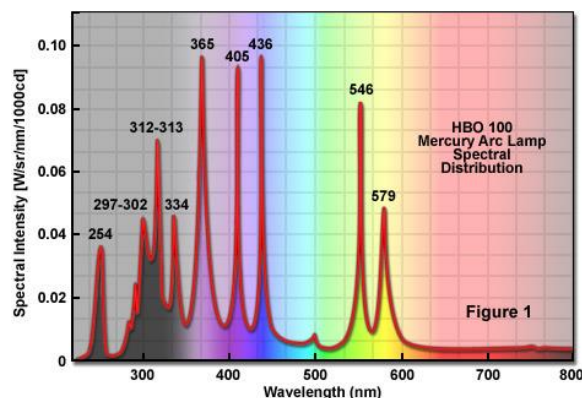


Figure III.1: Emission spectrum of mercury arc lamp. ([zeiss-campus.magnet.fsu.edu](http://zeiss-campus.magnet.fsu.edu))

### III.1.2. Confocal microscope and acquisition setup

The setup described previously is limited for a complete analysis of the fluorescence of a single nanocrystal: the spectrum and the PL decay cannot be collected. To improve contrast and resolution, the typical setup used for single-particle study is a confocal microscope. Confocal imaging consists in exciting and collecting signal from the same, small volume. A small confocal hole, or pinhole, cuts the light coming from out-of-focus planes, allowing only the signal from the confocal volume to be collected. This method improves the z resolution by limiting the depth of field to the micrometer scale. The confocal image is then formed by scanning the imaged volume in x and y directions. In the case of NCs, confocal microscopy allows to localize one particle on the glass slide, and to collect the emission signal coming from that particular NC.

The confocal microscope used for these studies is the Microtime 200 developed by PicoQuant (Figure III.2). The excitation source is a pulsed laser emitting at 405 nm (Picoquant, LDH-D-C-405). The repetition rate can be tuned from 80 MHz to 31.25 kHz. The objective is mounted on two piezoelectric stages, one for scanning in x and y directions, the other one for manually adjusting the z position to precisely focus the image. The maximum size of the area scanned is 80 x 80  $\mu\text{m}$ . The fluorescence signal is then collected through the confocal setup and can be directed to a spectrometer or two photodiodes. The spectrometer will record the signal at a given wavelength, whereas the two photodiodes will record the fluorescence signal and temporal information about every photon.

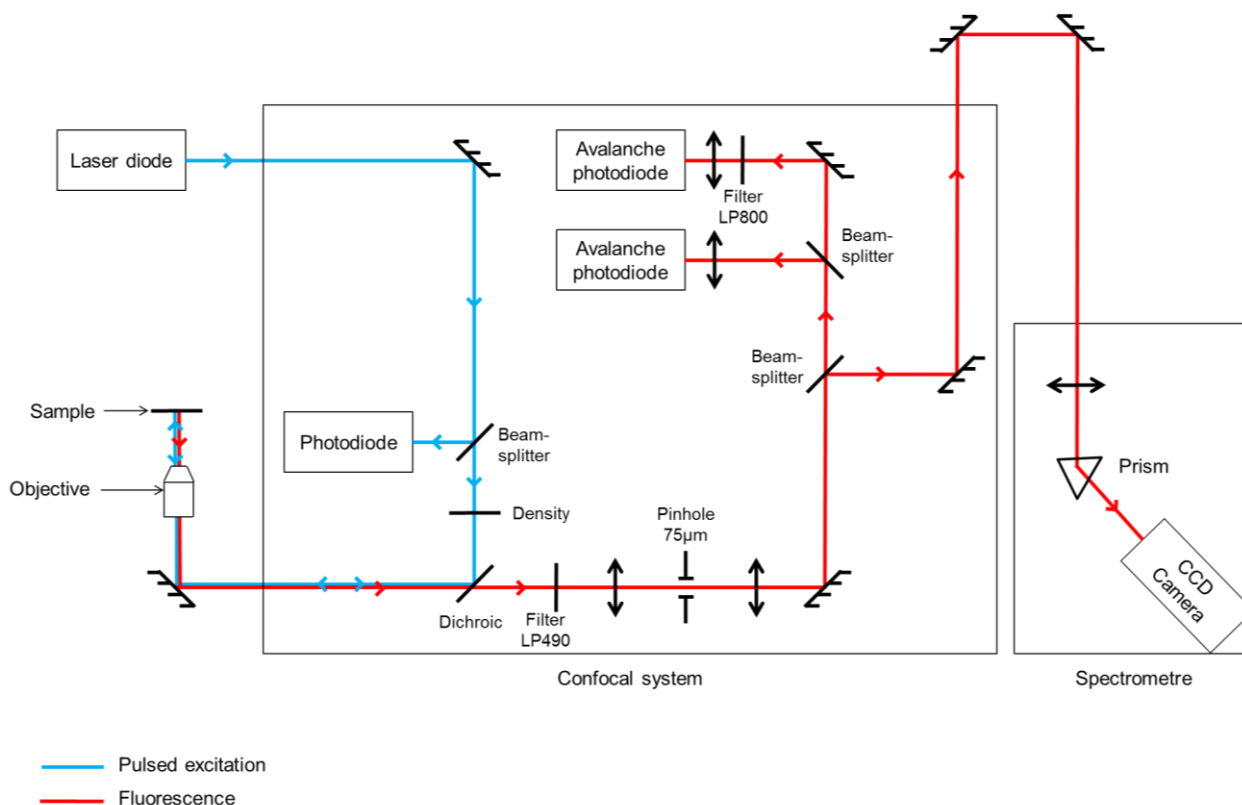


Figure III.2: Scheme of setup used for confocal imaging of individual nanocrystals.

### III.1.3. Time-resolved acquisitions

The photodiodes are connected to a counting board (Picoquant, Hydraharp 400) that records every photon in a Time-Tagged-Time-Resolved (TTTR) mode. Every photon is recorded with its absolute arrival time, its arrival time relatively to the latest laser pulse, and the photodiode on which it arrived.

Such a system enables measuring of several pieces of information on each nanocrystal: the emitted intensity and its evolution with time, the photoluminescence decay and the autocorrelation of its intensity.

#### III.1.3.1. Photoluminescence trace

The acquisition of the photons by the setup gives the temporal evolution of the fluorescence intensity emitted by the NC, *i.e.* its trace. It can be binned with different times, with the shortest one being the temporal resolution limit of the acquisition card. A QD trace informs on its blinking behavior (Figure III.3).

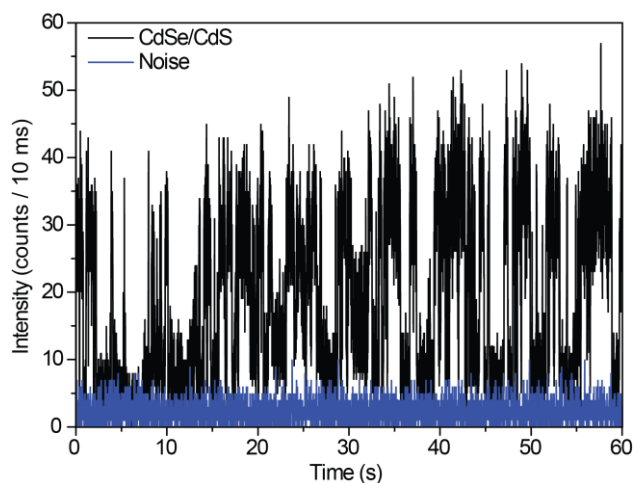


Figure III.3: Intensity trace of a single CdSe Quantum Dot and noise. Bin time: 10 ms.

### III.1.3.2. Photoluminescence decay

The TCSPC (Time-Correlated Single Photon Counting) mode of the acquisition board records the arrival time of the photons relatively to the latest laser impulsion, *i.e.* ideally the laser pulse that created the exciton whose recombination gave birth to the recorded photon. This enables the plotting of the histogram of delays between the excitation and the arrival of photons on the photodiodes. From this histogram can be extracted the lifetime that characterizes the recombination dynamics at the origin of the emitted photons (Figure III.4). Thus, the repetition rate must be slow enough to ensure that all the charges had time to recombine before the next laser impulsion. Typically, the repetition time was at least 3 times longer than the lifetime of the NCs.

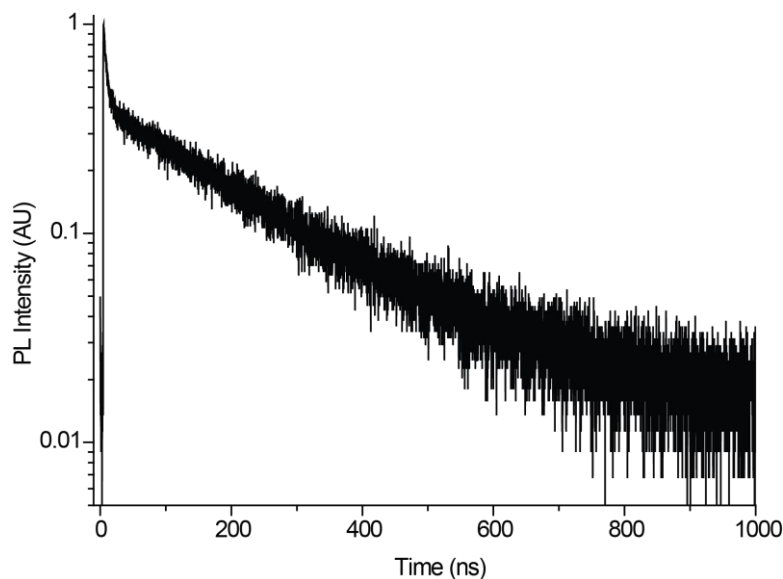


Figure III.4: Typical PL decay of a single CdSe/CdS Quantum Dot

## III.1.3.3. Photoluminescence intensity autocorrelation

The setup used for spectroscopic imaging is a Hanbury-Brown and Twiss setup. The signal is sent on a 50/50 beamsplitter then to the photodiodes. When a photon is detected by a photodiode, it triggers an internal clock that runs until a photon is detected on the second photodiode. The delays measured can be plotted on a histogram: if two photons are collected within the same period of the excitation laser, the central peak at  $\tau = 0$  will show more counts. If they are detected for two different pulses, they will contribute to the peak at the corresponding delay  $\tau$ . For the study of two photons, this is equivalent to measuring the second-order autocorrelation function:

$$g^{(2)}(\tau) = \frac{\langle I_1(t)I_2(t + \tau) \rangle}{\langle I_1(t) \rangle \langle I_2(t + \tau) \rangle}$$

where  $I_1(t)$  and  $I_2(t)$  are the signal intensities recorded by each photodiodes.<sup>144</sup> Thanks to the Hanbury-Brown and Twiss setup, it is possible to plot the histogram of coincidences of the photons detected by each photodiode. The photodiodes have a dead-time of 80 ns during which they cannot detect any photon; this time is relatively long and having two photodiodes improves the detection at short  $\tau$ .

As typical, small QDs have been shown to be single-photon emitters due to efficient Auger recombinations,<sup>25</sup> this method is used to check the unicity of the Quantum Dot studied. Indeed, at low excitation power, when no more than one exciton per dot is formed, only one photon should be collected after the laser pulse. In this case, the area of the  $g^{(2)}$  function at  $\tau = 0$  should be much lower than the area of the adjacent peaks, indicating an antibunched behavior of the emitted photons. On the contrary, when the observed emitter is not a single QD, it can emit several photons after one excitation pulse, which will increase the area of the peak at  $\tau = 0$ .

However, the fact that the peak at 0-time delay is as important as the peaks at  $t =$  the repetition period of the laser does not necessarily involve that the emitter is not unique. Nair *et al.*<sup>144</sup> have theorized the fact that at low excitation powers, the ratio between the area of the peak at 0-time delay and the peaks on the side can be approximated to the ratio between the quantum yield of the biexciton XX and the monoexciton X:

$$\frac{\text{Area } g_{center}^{(2)}}{\text{Area } g_{side}^{(2)}} = \frac{QY_{XX}}{QY_X}$$

Assuming that during the emission cascade, the XX emission does not modify the subsequent X emission (the X and XX fluorescence processes are independent of each other), and that the QY of QDs studied is close to unity, at low excitation power a residual signal at 0-time delay persists corresponding to the biexciton emission. The autocorrelation curve can also be corrected by the background effects coming from scattered excitation light

or from another NC. The background noise can be neglected (<1% of the central peak area) for a signal-to-noise ratio around 10, and the unicity of the QDs can be checked with correlative optical/electron microscopy (see III.3.2). This gives a convenient way of measuring the QY of the biexciton knowing the QY of the monoexciton at the single particle level.

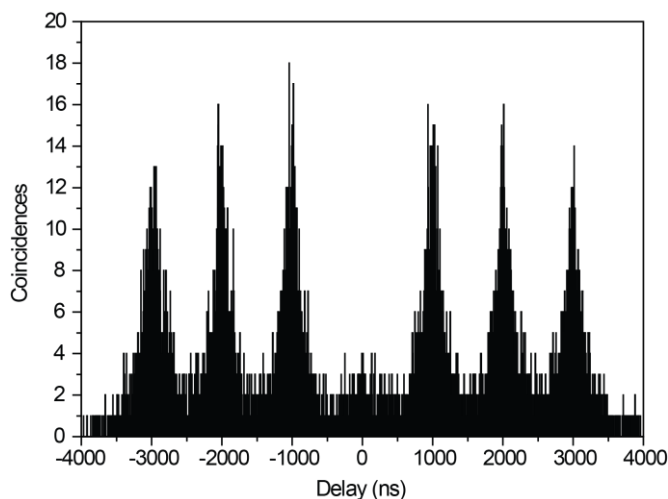


Figure III.5: Autocorrelation plot of a single CdSe/CdS Quantum Dot. The lower peak at 0-time delay indicates antibunching: the observed QD is a single-photon emitter.

#### III.1.3.4. Preparation of the sample for single particle studies

In order to study nanocrystals on a single-particle scale, they need to be deposited on a glass slide with enough space between themselves (at least twice the resolution of the optical setup) to make sure that the collected signal does not come from multiple dots. The solution of QDs in hexane after synthesis is diluted in a solution of hexane:octane (9:1) to a concentration of about 1 nmol. A small volume (10 $\mu$ L) is then drop-casted on a quartz slide (24 x 60 x 0.16 mm) and the solution is left to dry several minutes. The mixture of hexane and octane dries homogeneously avoiding the coffee-ring effect that concentrates the NCs on the border of the drop.

For samples of thick-shell QDs, some aggregation is observed: some spots are much brighter and bigger than others suggesting that several dots are stuck together and cannot be distinguished given the diffraction limit of the setup (~ 300 nm). Thus, we developed a washing procedure that was implemented before every dilution in hexane:octane mixture to efficiently separate the aggregated QDs. A few microliters (typically around 10  $\mu$ L) of the solution in hexane after synthesis is diluted in 1.5 mL of hexane mixed with 2  $\mu$ L of oleic acid and 2  $\mu$ L of oleylamine. The solution is then sonicated for ~30s, and left on a UV-table for 10 min. This allows the ligands to reorganize at the surface of the NCs, helping the colloidal dispersion and the separation of the aggregated QDs. The solution is then washed thrice

with EtOH to precipitate the QDs and eliminate the excess of ligands. The QDs are redispersed in hexane every time and sonicated for several seconds. Finally, the solution is diluted in the hexane:octane mixture and dropcasted for observation.

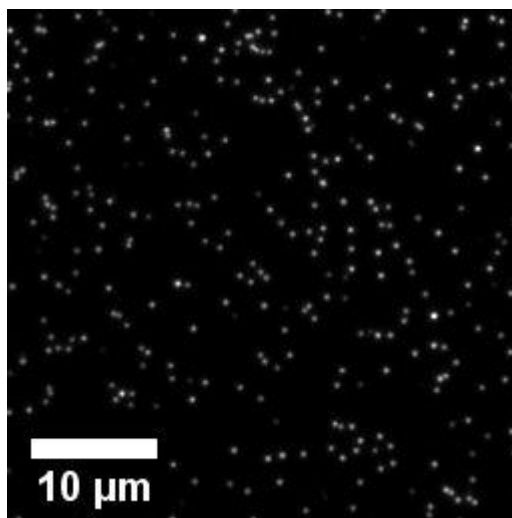


Figure III.6: Epifluorescence image of numerous CdSe/CdS Quantum Dots deposited on a glass slide.  
Magnification:  $\times 100$ .

With this method, only a few aggregates are seen and not considered for analysis. The average distance between each QD is several micrometers. This method might also improve the photophysical properties of the QDs as UV irradiation provides enough energy to reorganize not only the ligands but also chemical bonds at the surface for better passivation of potential traps.<sup>89</sup>

## III.2. Thick-shell CdSe/CdS Quantum Dots

The protocol described in II.3 and II.4 allows the synthesis of several thick-shell CdSe/CdS samples that have improved optical properties. We focus the next section on the study of QDs with a 5 nm diameter CdSe core and 6 nm thickness CdS shell (sample ZB-1). Their thorough spectroscopic studies have been performed by Clémentine Javaux.

### III.2.1. Zinc-blende CdSe core with a thick CdS shell

The CdSe core was synthesized with a protocol adapted from a one-pot synthesis, yielding CdSe NC with zinc-blende crystalline structure.<sup>99</sup> The CdS shell was grown on the cores using a continuous injection method.<sup>145</sup>

## III.2.1.1. Optical and Structural characterization

The final size of these QDs is around 30 nm. Their emission is centered around 656 nm with a FWHM of 33 nm. The absorbance and PLE spectra show that the absorbance of the CdS shell is prevalent, and mostly responsible for the emission (Figure III.7).

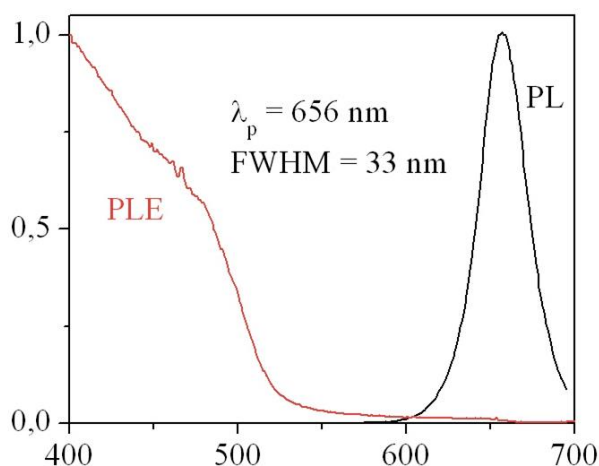


Figure III.7: Normalized PL and PLE spectra of thick-shell CdSe/CdS Quantum Dots.<sup>15</sup>

The crystalline structure is confirmed by XRD diagrams (Figure III.8). The CdSe cores grow in a zinc-blende structure while the CdS shells grow in a wurtzite structure.

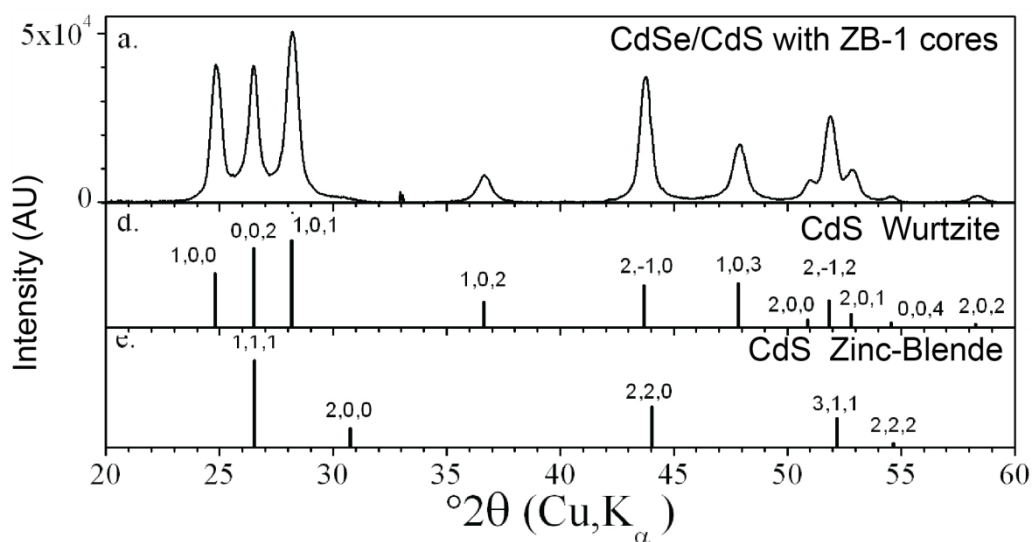


Figure III.8: XRD diagrams of thick-shell CdSe/CdS QDs.

The final size of these thick-shell CdSe/CdS QDs is around 30 nm (Figure III.9). The EDX profile confirms that the interface between the CdSe core and the CdS shell is abrupt (Figure III.10).

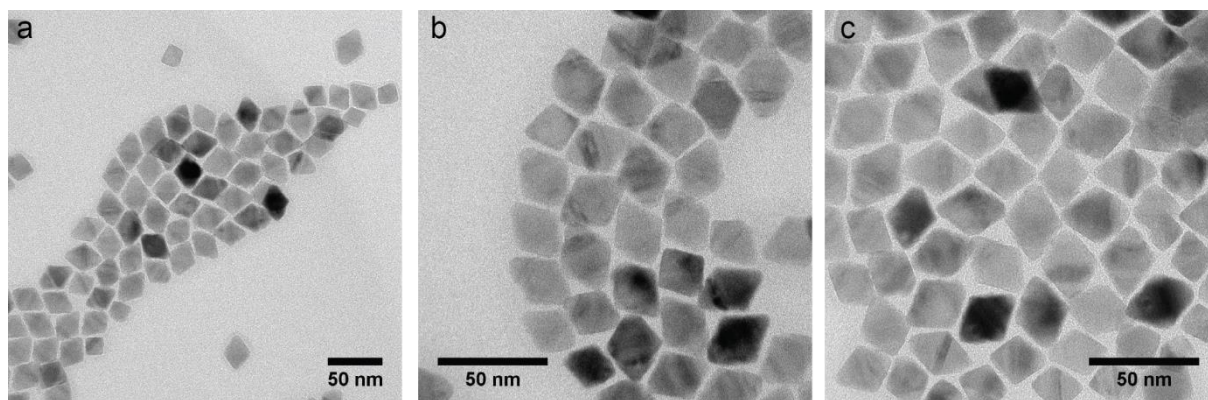


Figure III.9: TEM images of thick-shell CdSe/CdS QDs at a. and b. x60,000 and c. x120,000.

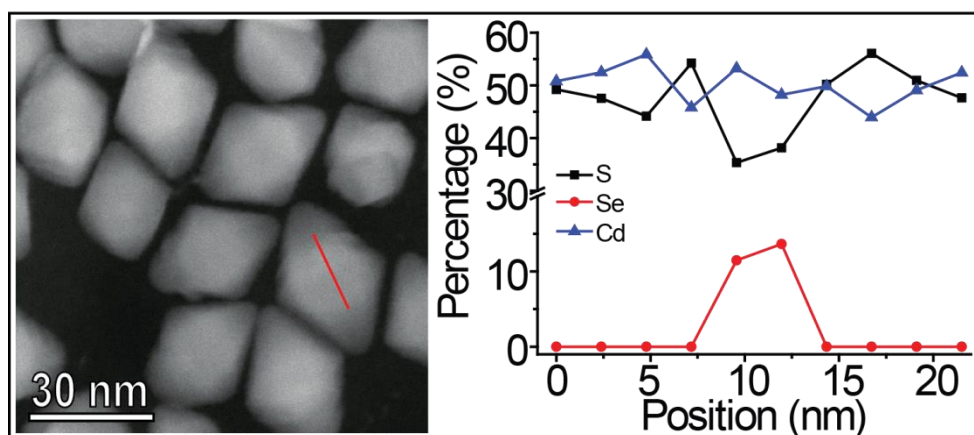


Figure III.10: Left: EDX profile for thick-shell CdSe/CdS QD along the red line on the TEM image on the right.

### III.2.1.2. Two emissive states at room temperature

When observed at the single particle level at room temperature, these QDs show some flickering, but no blinking (with a typical bin-time of 10 ms to ensure a good enough signal-to-noise ratio). They switch between an *on*, bright state, and a second emissive state of lower quantum yield, the *grey* state. The on state has been attributed to neutral QDs while the grey state corresponds to a charged QD where non-radiative, Auger recombinations can occur.<sup>15,123,146</sup> This state, however, is not dark (at the minimal binning of the setup) as Auger recombination are relatively long in thick-shell QDs, non-radiative processes are not as probable as is thin-shell QDs. Radiative and non-radiative processes can now compete emitting photons more often than if Auger was favored over radiative recombination, yielding the emission of the grey state (Figure III.11.a). Indeed, the radiative lifetime of the trion is calculated to be 29 ns while the lifetime of the Auger recombinations is 18 ns, much longer than in thin-shell CdSe/CdS QDs.<sup>147,148</sup>

This is confirmed by the PL decay measurements: the decay can be fitted by a biexponential curve, with two characteristic lifetimes. The longest one, at 60 ns, corresponds to the neutral QD (*i.e.* to the radiative recombination of the monoexciton X) while the short one, at 11 ns, confirms the presence of non-radiative recombinations in the charged QD (charged exciton or trion  $X^*$ ) (Figure III.12.a).

The QY of the *on* state is determined by the comparison with the *on* state of CdSe/ZnS QDs that has been shown to be at 100%. The *on* state for thick-shell CdSe/CdS QDs has, for the same excitation power, the same intensity as the *on* state for CdSe/ZnS QDs, thus its QY is close to unity.<sup>123,124</sup> By comparison of the emission intensity of the *on* state and the *grey* state, the QY of the latter has been measured to be 38%.

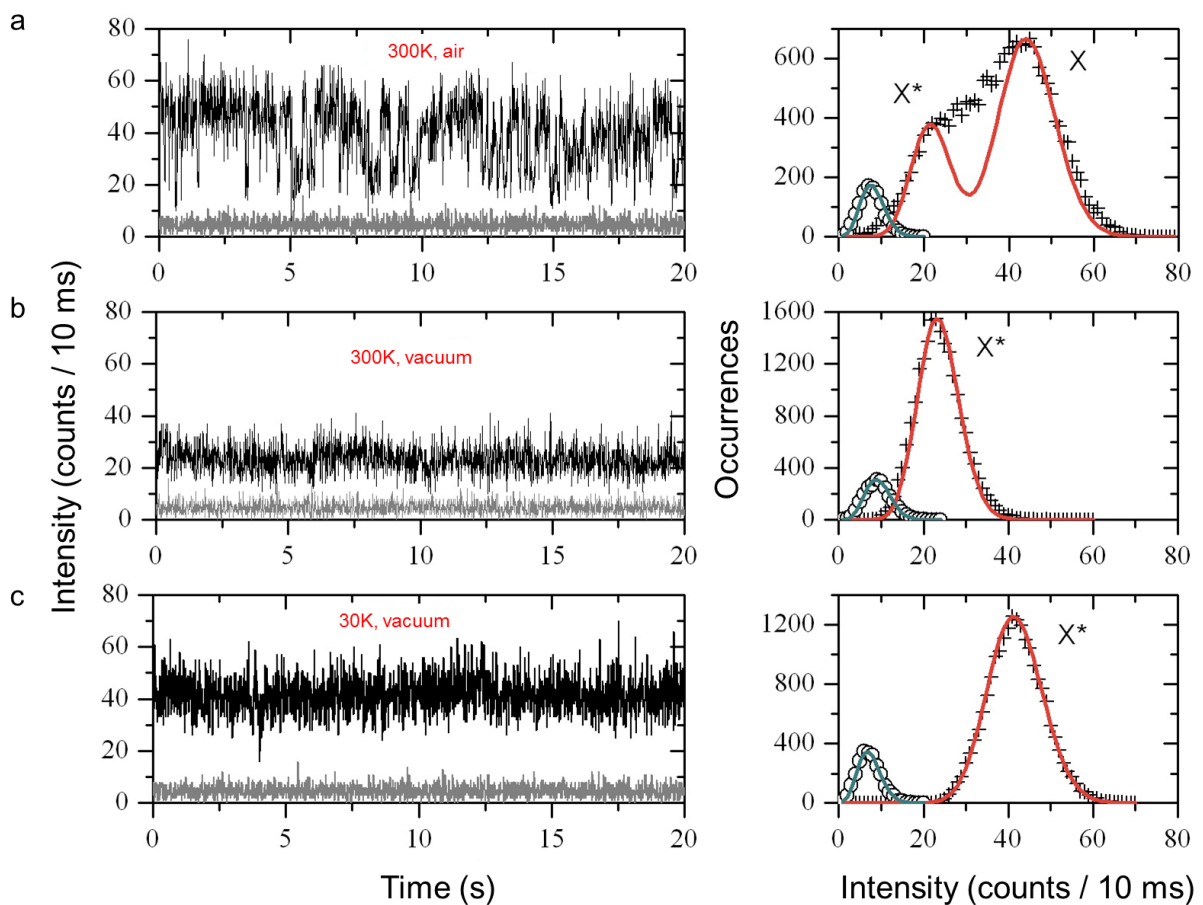


Figure III.11: Left: Intensity traces for a single CdSe/CdS thick-shell QD a. in air at 300K, b. under vacuum at 300K and c. under vacuum at 30K. The grey trace is the background noise. Bin time: 10 ms. Right: Intensity histograms of the QD trace (crosses) and noise (circles). The red curve is a Poisson fit of the intensities, proving the trace is shot-noise limited. X corresponds to the neutral exciton,  $X^*$  to the charged exciton.<sup>15</sup>

## III.2.1.3. One grey state under vacuum

When studied under vacuum ( $\sim 10^{-6}$  mbar), the PL trace changes. It is now stable, but at an intensity level comparable to the intensity of the PL of the grey state in air (Figure III.11.b). Indeed, under vacuum, the oxygen and water molecules that could react with the excess charge present in the QD, neutralizing it, are absent.<sup>149</sup> The QD is therefore bound to stay charged under vacuum, and the emission is the emission of the charged QD, *i.e.* the one of the trion  $X^*$ .

This is further confirmed by the PL decay. It can be fitted by a biexponential, with a long lifetime of 11 ns, corresponding exactly to the lifetime of the trion measured in air (the short lifetime is attributed to the charged biexciton  $XX^*$ ) (Figure III.12.b).

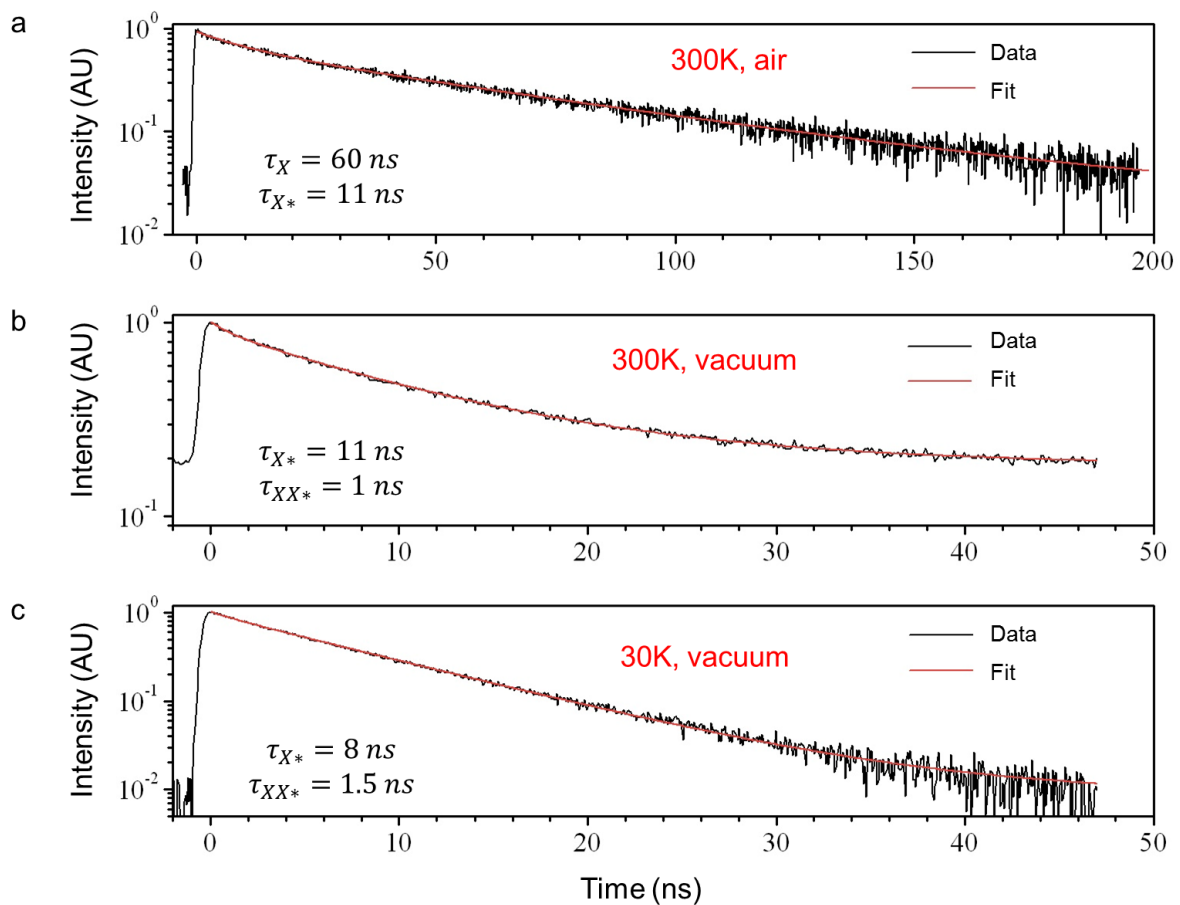


Figure III.12: PL decay curves of a single thick-shell CdSe/CdS QD a. in air at 300K, b. under vacuum at 300K and c. under vacuum at 30K. The red curve is a biexponential fit from which the values of the lifetime are extracted.<sup>15</sup>

## III.2.1.4. 100% quantum yield at cryogenic temperature

The decrease in the temperature to 30K increases the intensity of the PL to a level similar to that of the bright state in air (Figure III.11.c). The PL trace is stable and corresponds to a QY of 100%.

Interestingly, the PL decay shows an even shorter lifetime of 8 ns (Figure III.12.c). This is uncommon for low temperature measurements for CdSe and for CdSe/CdS where the lifetime at low temperature increases due to the presence of a low-energy dark state in the fine structure of the electronic levels for neutral QDs.<sup>48,150,151</sup> However, in this case, the short lifetime associated with an increase in the PL intensity shows the absence of this low-energy dark state, suggesting that the QDs are charged.<sup>152</sup> Besides, thanks to magneto-optical measurements, the trion has been shown to be negatively charged (Figure III.13) (see III.3.9 for more details).

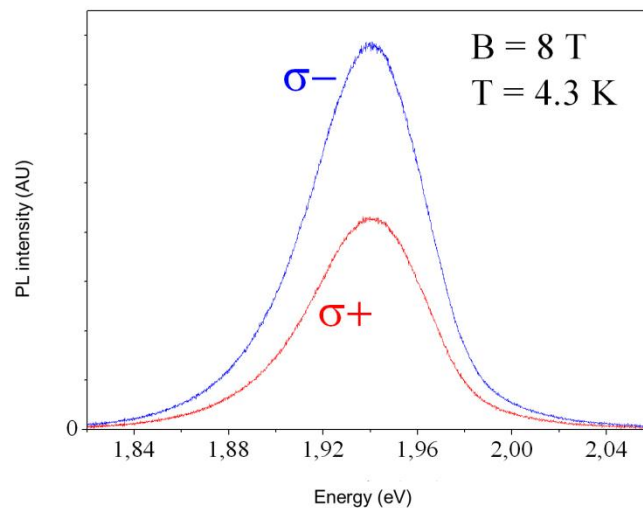


Figure III.13: Polarization-resolved PL spectra of an ensemble of thick-shell CdSe/CdS QDs under magnetic field.<sup>15</sup>

To conclude, at cryogenic temperature, the QDs are negatively charged but have a QY of 100%: thus, the Auger processes are completely suppressed at 30K, but present at room temperature where they decrease the QY.

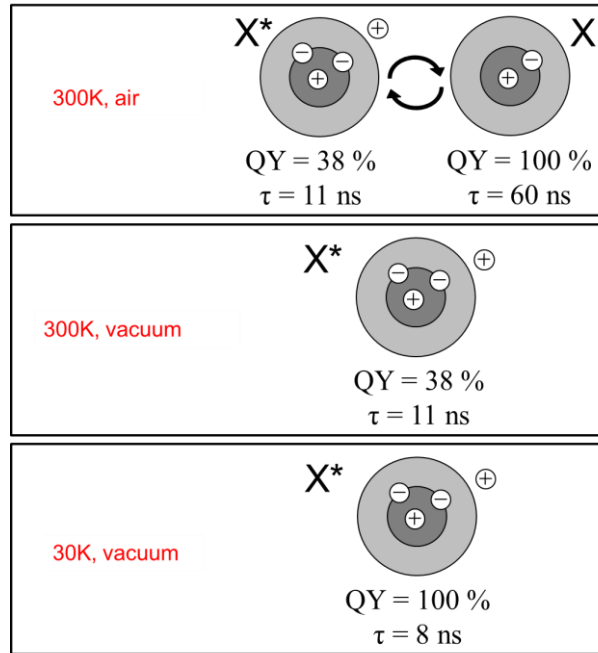


Figure III.14: Scheme of charge state of thick-shell CdSe/CdS QDs.<sup>123</sup>

### III.2.1.5. Thermal activation of Auger processes

How can we explain the seemingly contradictory facts that the lifetime decreases and the PL increases with decreasing temperature?

The evolution of lifetime can be correlated to the evolution of the electron and hole wavefunctions overlap with temperature. At room temperature, the conduction band offset (CBO) between the CdSe core and the CdS shell, although still subject to discussions,<sup>153–156</sup> is close to zero. The electrons in the conduction band are therefore theoretically allowed to explore the whole CdS shell. However, the hole is strongly confined in the CdSe core, creating an attractive Coulomb potential that localizes the electrons closer to the core.

At room temperature, the thermal energy is efficient to unbind the trion: the excess electron is no longer localized in the core and can visit the surface of the CdS shell. Moreover, due to crystalline defects that may be present at the interface between the core and the shell, Auger recombinations can occur in the NC volume.<sup>121</sup> At cryogenic temperature, on the other hand, not only the Coulomb interaction takes places, decreasing the mobility of charges, but the CBO is increased, and reaches  $-120$  meV,<sup>15</sup> confining the trion even more in the core region. The spatial extension of the electron wavelength is strongly decreased and gets smaller than the spatial size of the QD: the electrons cannot reach the outer surface anymore.

Thus, at cryogenic temperature, the charges are spatially localized in the same region, increasing their wavefunction overlap and decreasing the lifetime of the exciton

recombination. This explains the decrease of the measured lifetime when the temperature decreases. If we add that Auger recombination is favored at abrupt interfaces,<sup>121</sup> the fact that charges are no longer able to reach the surface at cryogenic temperature explains that non-radiative recombinations are non-existent, increasing the PL to 100% QY.

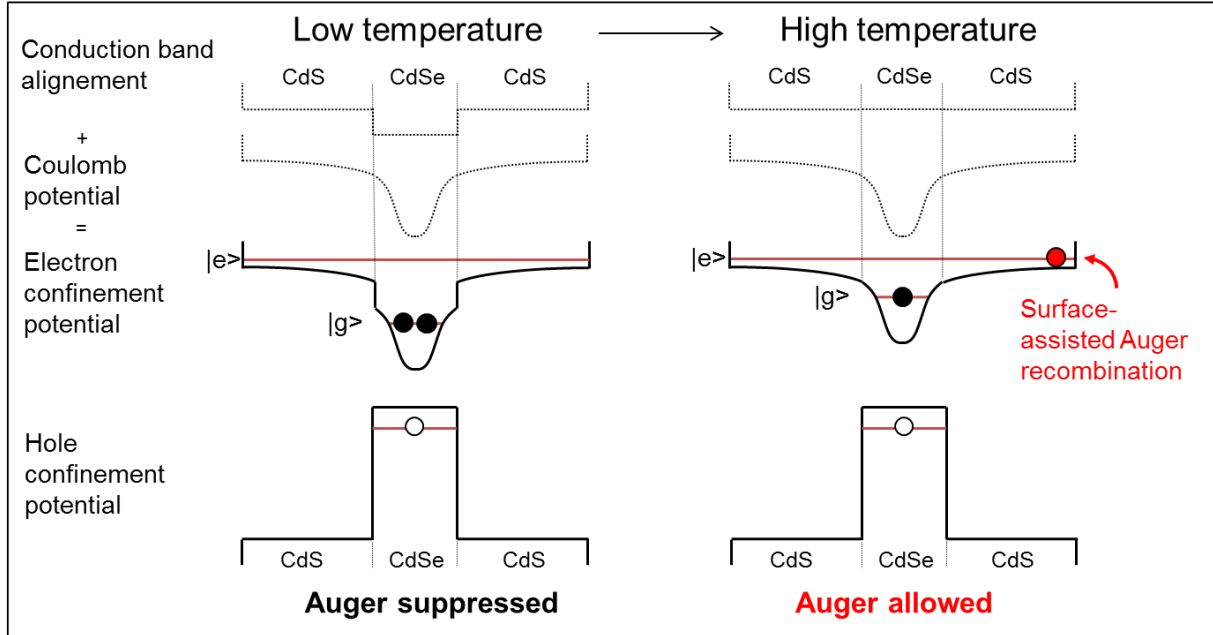


Figure III.15: Scheme of band alignment and mechanism of thermal activation of Auger recombination for the negative trion in thick-shell CdSe/CdS QDs.<sup>15</sup>

### III.2.2. Other samples

As described previously, the protocol developed for the growth of thick CdS shells on CdSe cores was also used on different sizes and crystal structures of cores. Similar results were found for thinner CdS shells (10 nm in diameter) with even less flickering at room temperature. Although the detailed analysis was not performed on the following NCs, the blinking characteristics were checked. For NCs with different zinc-blend cores with different ligands as well as for wurtzite cores, the blinking statistics were as good as for the previous NCs studied, showing not only that the protocol developed for this synthesis is robust and adaptable to different sizes and crystalline structures, but also that the increase of the size of the core is a universal method to decrease Auger recombinations (Figure III.16).

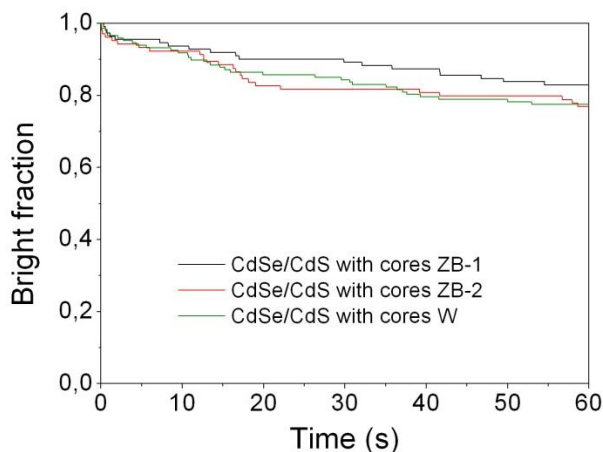


Figure III.16: Blinking statistics for CdSe/CdS core/shell structures with shell thickness of 10 nm grown on different cores of different crystalline structure. The statistics is realized on around a hundred nanocrystals for each sample.

### III.2.3. Conclusion

Thick-shell CdSe/CdS QDs show no blinking. Only flickering can be seen on the photoluminescence trace. This flickering is due to the switching of the QDs between a neutral, *on*, and a charged, *grey*, state. In the neutral state, the exciton recombines radiatively while in the charged state, the radiative and Auger, non-radiative recombinations compete. At cryogenic temperature, due to a limited access to the surface, Auger processes are eliminated, yielding emission with 100% QY. Auger recombinations are thermally activated. Blinking suppression has been seen for different types of CdSe QDs all capped with a thick CdS shell.

## III.3. Bulky-gradient QDs – thick-shell and gradient composition

The previous samples show that it is possible to synthesize non-blinking QDs at room temperature, however, they still show some flickering. The Auger processes, although lengthened to compete with the radiative recombination lifetimes, is still present and decreases the overall quantum yield of the nanoparticles. Indeed, only at cryogenic temperature does the QY reach 100%.

Thus, for any application that requires a high quantum yield, such as lightning or lasing, or completely stable fluorescence emission for single-particle tracking for biological imaging,

these QDs are not good enough. Besides, as QDs make their way to commercial applications, the need to lower the energy consumption of QD-based devices requires a high output yield.

As discussed in section I.5.3, several strategies have been implemented to improve the overall quantum yield of QDs, but none of them has been completely efficient in eliminating Auger recombinations. We have therefore tried to combine two strategies that shown interesting results: thick shells and a composition gradient between the core and the shell.

### III.3.1. Optical and Structural characterization

The synthesis of these thick-shell CdSe/CdS QDs with a gradient of composition between the core and the shell (referred to as bulky-shell QDs, or b-QDs) has been performed as described in the section II.4. Briefly, precursors of cadmium and sulfur were added dropwise at high temperature on CdSe wurtzite cores, and the reaction solution was then annealed for 4h30 at 310°C.

The ensemble measurements show a photoluminescence spectra at 685 nm, with a full width at half maximum (FWHM) of 55 nm (Figure III.17). This value is quite large compared to previously studied samples (II.5) or to what can be found in the literature.<sup>11,15</sup> This suggests that the synthesis might yield QDs with some composition variations.

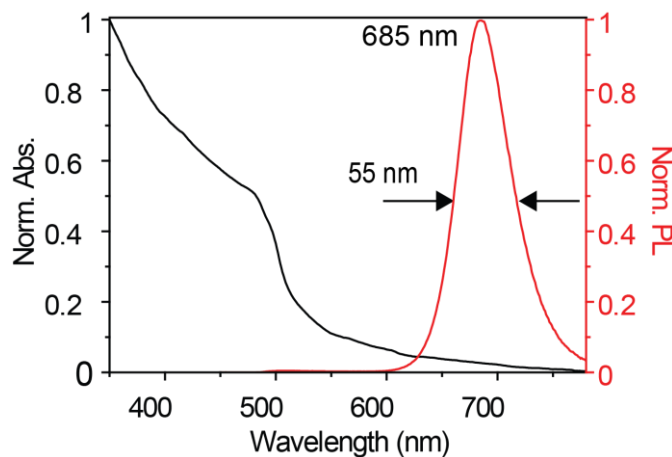


Figure III.17: PL and absorbance spectra of bulky-shell gradient QDs.

Interestingly, the final size of these QDs exceeds what theoretical calculations have predicted. Indeed, starting with 3 nm-diameter CdSe cores, and given the amount of shell precursors added, the theoretical final size of those QDs should be around 11 nm. However, as can be seen on the TEM images, the final diameter of those structures is around 40 nm (Figure III.18), yielding core/shell QD much larger than what has been reported so far.<sup>11,15</sup> This might be explained by some dissolution of the cores during the shell-growth process. The CdSe cores dissolve, releasing in the reaction solution some Cd and Se precursors that

will react with the injected Cd and S precursors to form a gradient of composition from a CdSe only core to a CdS only shell, with an intermediate region of CdSe<sub>1-x</sub>S<sub>x</sub>. In order to confirm this hypothesis, we studied the elemental analysis of the QDs with EDX experiments.

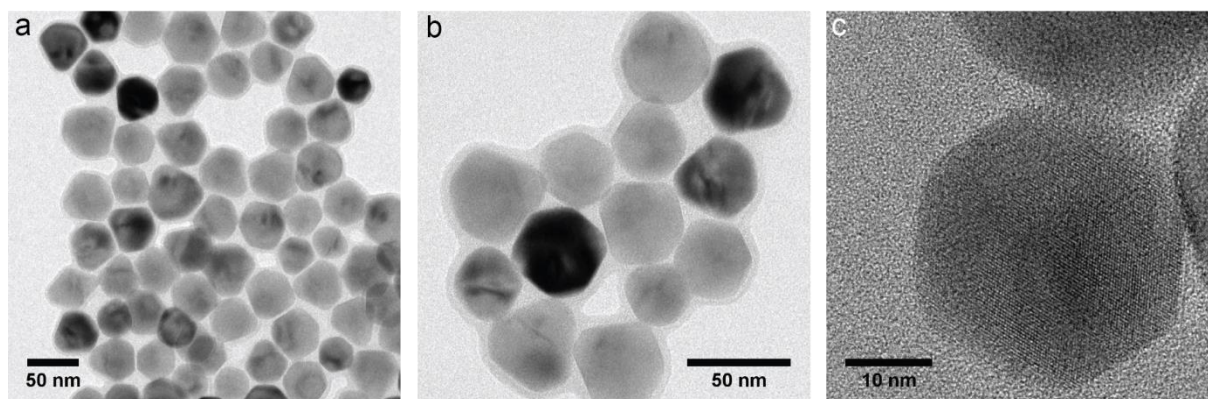


Figure III.18: TEM images of b-QDs at a. x30,000, b. x60,000 and c. x250,000.

The EDX experiments confirmed that the Se, initially only contained in the CdSe core of 3 nm in diameter, is actually present over a large region in the nanocrystals, spreading over 15 nm from the center. The Se composition also decreases smoothly on both sides of the core, confirming that the interface between the core and the shell is not abrupt, but smooth thanks to the gradient of composition (Figure III.19 and Figure III.20).

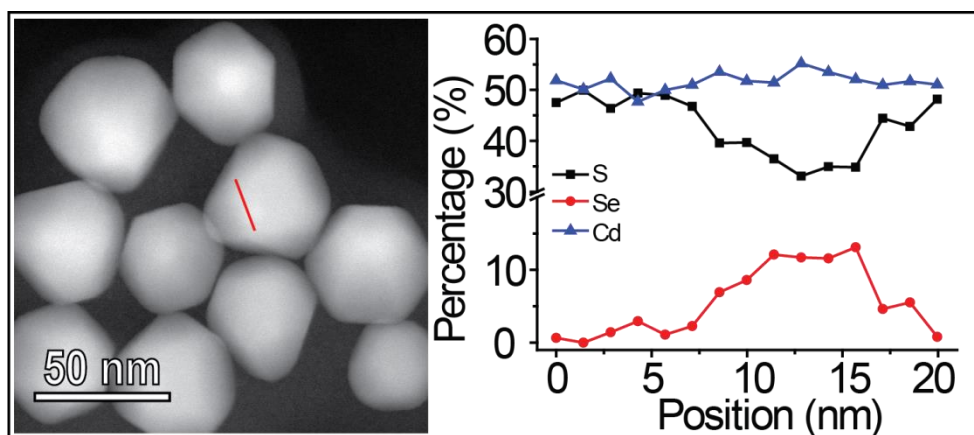


Figure III.19: Left: EDX profile for b-QD along the red line on the TEM image on the right.

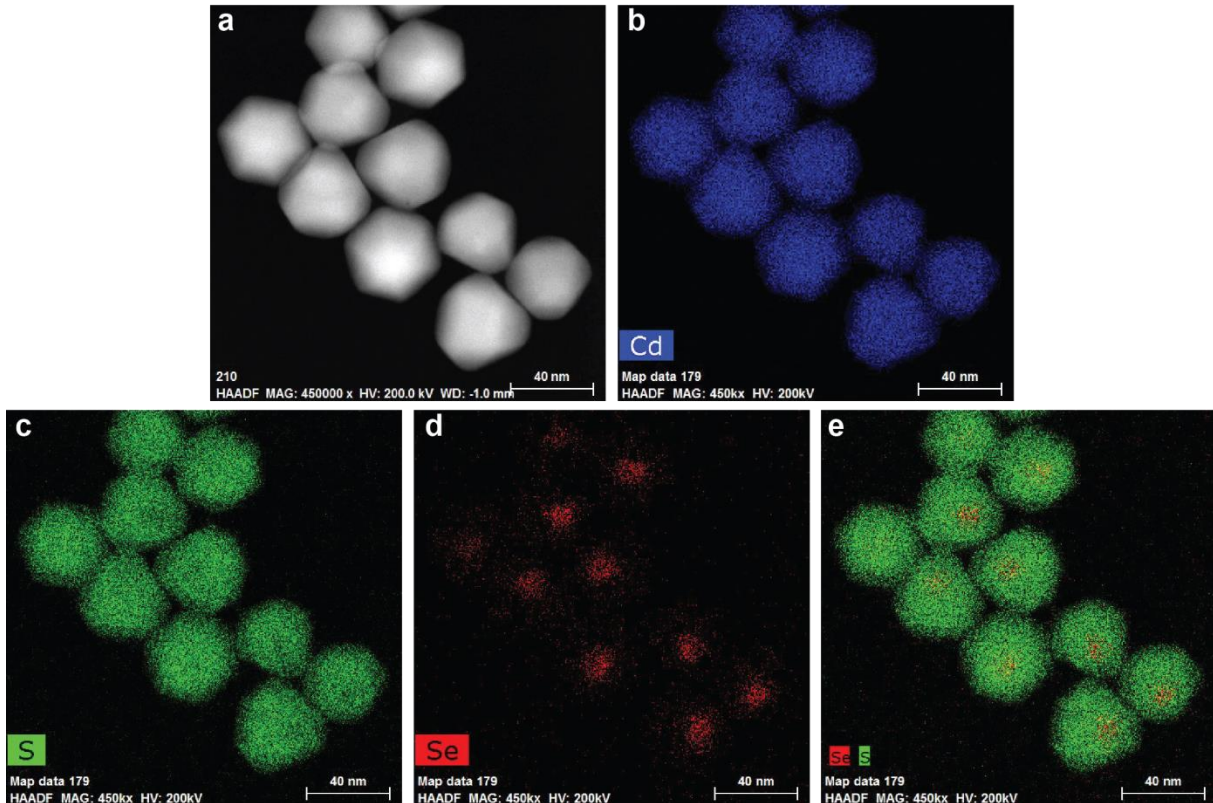


Figure III.20: EDX maps for b-QDs. a. HAADF image at  $\times 450,000$ . Localization of b. cadmium, c. sulfur, d. selenium and e. selenium and sulfur (overlap).

Given these structural characteristics that combine two efficient strategies to reduce the blinking and increase the quantum yield, we expect very good optical properties at a single-particle level from those QDs.

### III.3.2. Correlative optical/electron microscopy

When observed with the naked eye under a microscope, these QDs look very bright and do not blink at all. Preliminary studies with a TCSCP (time correlated single photon counting) system show very stable fluorescence over time, no blinking and no flickering, over very long periods of time (the acquisition is actually limited not by the photobleaching or degrading of the QDs, but by the mechanical stability of the optical setup). However, there were big differences from dot to dot in the measured intensity level (up to a factor of 3). This might be due to inhomogeneities in the emission between dots, or from the fact that we are looking at aggregates of several dots whose intensity will depend on the number of dots in the aggregate.

In order to ensure that we study individual quantum dots and not aggregates, we performed autocorrelation measurements as described in section III.1.3.3. On all the dots we measured, the  $g^{(2)}$  analysis never showed antibunching, suggesting the observed QDs are

not individual particles. We wanted to confirm that with TEM measurements, and we prepared a grid with a dilution slightly higher than the one used for optical studies. On this grid, we saw some aggregates, and some individual quantum dots. Therefore, even though the autocorrelation measurements suggested the analyzed QDs were not individual, the TEM observation confirmed that at least some of the QDs we observed under the microscope were individual.

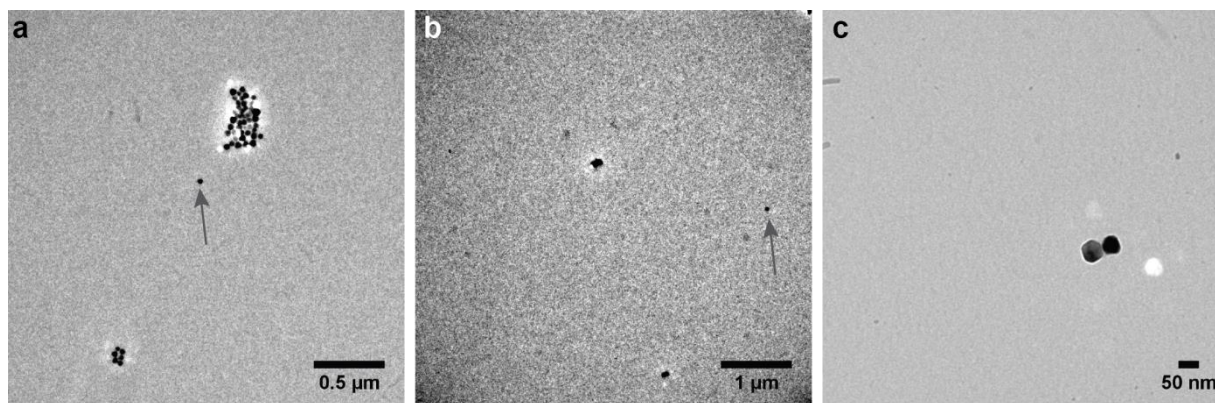


Figure III.21: TEM images of b-QDs diluted on carbon grid at a. x2,000, b. x4,000 and c. x12,000. The arrows points at individual b-QDs. Some aggregates of several tens of QDs can be seen (like in a.), but easily eliminated for the optical study as they are brighter than the average. Dimers (like in c.) can however be easily mistaken for single QDs.

To increase the number of individual QDs, *i.e.* to decrease the number of aggregates and to ensure that we do analyze single particle, we developed the washing and capping procedure described in section III.1.3.4. After this procedure, TEM observations confirmed that most of the QDs deposited on the grid were individual QDs (Figure III.22).

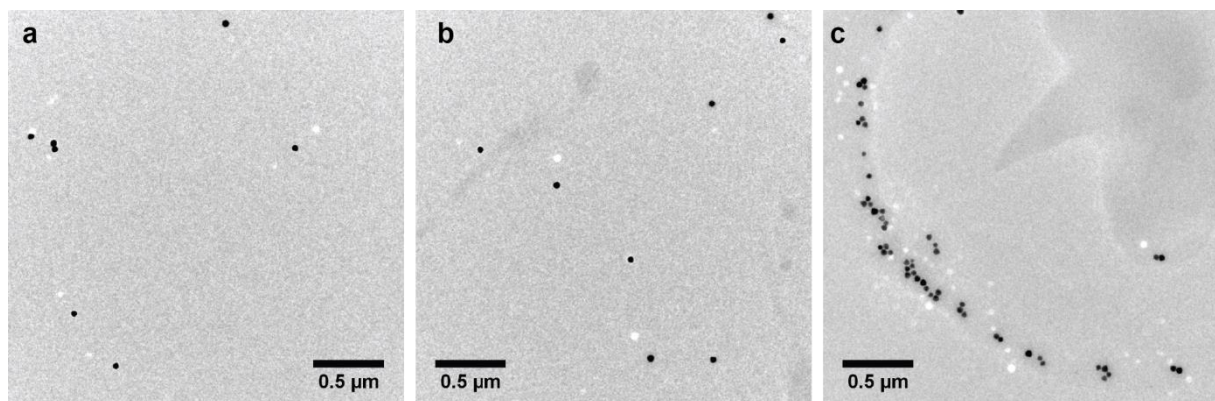


Figure III.22: TEM images of b-QDs on a carbon grid after washing and capping procedure (at x4,000). Most of the QDs are now individual QDs. The aggregation in c. is due to defects in the carbon grid.

To check the optical properties of individual QDs, we performed a correlative optical/electron microscopy study. We used for this purpose a silicon nitride  $\text{Si}_3\text{N}_4$  grid with 9 windows of  $100\mu\text{m} \times 100\mu\text{m}$ . A diluted solution of QDs after washing and capping procedure

was dropcasted on this grid. Around 30 QDs were then observed under a microscope, their trace, lifetime and autocorrelation function were measured. Once the optical analysis was done, we checked with TEM that the observed particles were indeed unique. The aggregates were not taken into account in the following studies (Figure III.23).

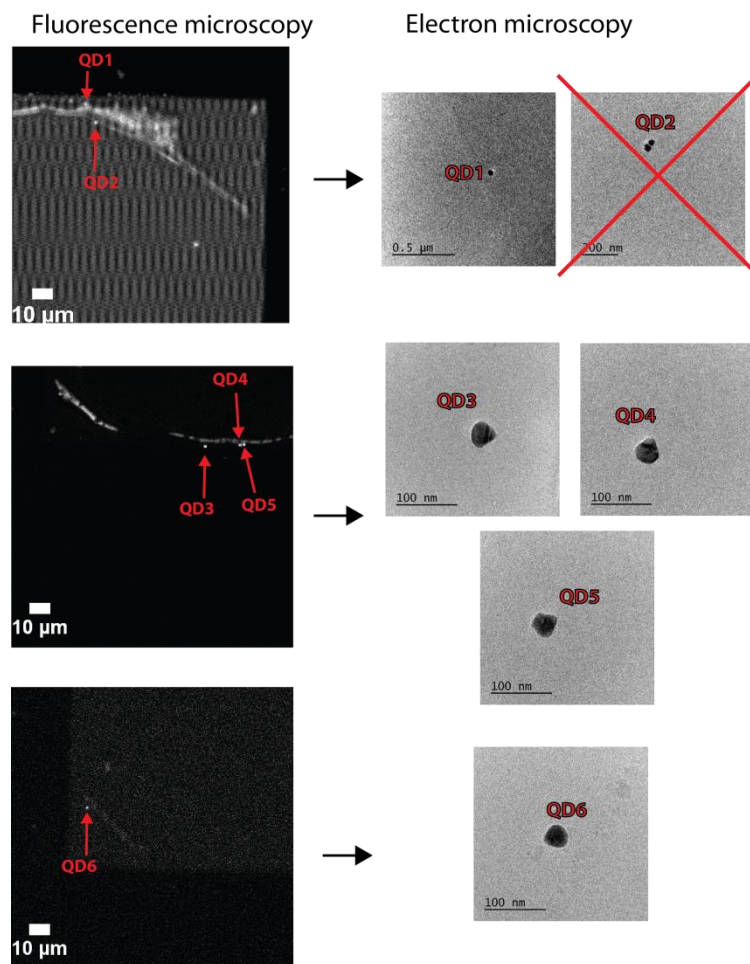


Figure III.23: Optical and electron correlative imaging of b-QDs. The optical properties were measured and the unicity of the QD was then checked under TEM. Data from individual QDs were kept, data from aggregates were discarded.

This allowed us to check that the b-QDs, at a single particle level, have similar emission intensities (<20% difference probably due to the dispersion in composition) and similar lifetimes.

### III.3.3. 100% quantum yield in air, at room temperature

Once we ensured that we observe individual b-QDs, we recorded their emission traces and lifetimes with our optical setup. The aim of these measurements was to see the behavior of the b-QDs in different conditions: low and high excitation power, in air or under vacuum, at room temperature or at low temperature, and to measure their quantum yield. As a reference

for comparison of their properties, we took the best sample of thick-shell CdSe/CdS quantum dot described in III.2.

### III.3.3.1. Low excitation regime

To study the blinking statistics of the b-QDs, we first excited them at low power. This is indeed necessary to avoid the creation of multiexcitons. The number of excitons formed in the QD was calculated following the works of Bawendi's and Klimov's groups.<sup>157,158</sup> Knowing the cross-section of the QDs  $\sigma$ , the power of the excitation source  $P$ , its frequency  $f$  and the cross-section of the excitation beam  $A$ , we can calculate the average number of excitons formed per QD per pulse:

$$\langle N \rangle = \frac{P/f}{hc/\lambda} \cdot \frac{\sigma}{A}$$

where  $h$ ,  $c$  and  $\lambda$  are respectively Planck's constant, the speed of light and the excitation wavelength. The cross-section of the QDs is based on the studies performed by Leatherdale *et al.*<sup>134</sup> where the absorption cross-section of CdSe at 350 nm is measured. Its value was corrected with a factor of 1.45 to take into account the difference of absorption at 350 nm and the excitation wavelength of our setup (405 nm) and the fact that at the excitation wavelength of our setup (405 nm), the absorption is mainly due to the thick CdS shell of the b-QDs. The absorption cross-section is therefore:

$$\sigma^{405nm} = 3.7 \cdot 10^5 \cdot a^3 \text{ cm}^2$$

where  $a$  is the nanoparticle radius (in cm).

In the low excitation power regime, we excited the dot so weakly and scarcely ( $\langle N \rangle = 0.05$ , which means that for every pulse, we create 0.05 exciton per QD) that the majority of excitation pulses did not create any exciton in the QD and only a few pulses formed one exciton; the probability of forming two excitons is very low. This allows the excited charges to recombine and to return to their fundamental state before the next excitation pulse. For a better comparison with other measurements, and to free ourselves from the repetition rate dependence of  $\langle N \rangle$ , we decided to work not with a number of excitons per pulse, but with a number of excitons per microsecond. For  $\langle N \rangle = 0.05/\mu\text{s}$ , it means that in the QD, 0.05 excitons are created per microsecond.

This allows to study the behavior of the b-QDs when one electron-hole pair is created. The recording of the PL trace over time shows a completely stable intensity, without blinking or flickering (Figure III.24 left). As seen previously, the blinking (switching the emission on and off) or the flickering (oscillation between two emissive states) is due to Auger recombinations that decrease the number of radiative recombinations, decreasing the

number of collected photons by the photodiodes in the case of ionized QDs. In the b-QDs, the absence of any change in the emission trace is a strong suggestion that non-radiative recombinations are completely eliminated. This is further confirmed by the fact that the intensity distribution can be fitted by a Poissonian curve: the collected signal is only shot-noise limited, confirming there is only one emissive state without any flickering (Figure III.24 right).

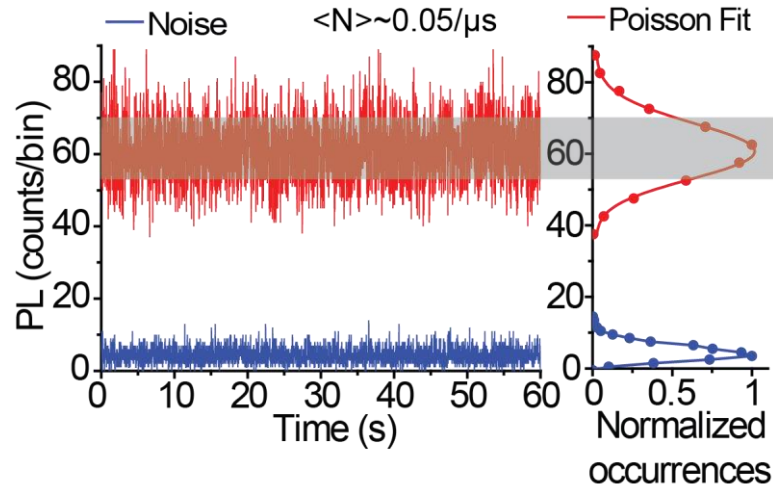


Figure III.24: Left: intensity trace of a single b-QD in air, at room temperature. Right: fit of the distribution of intensities. Excitation wavelength: 405 nm. Repetition rate: 1 MHz. Bin time is 20 ms.

### III.3.3.2. 100% quantum yield

In the low excitation regime, where only one exciton is created, it is possible to compare the emission intensities of the b-QDs and a reference QD in the same conditions. The reference QDs used are the thick-shell CdSe/CdS described previously (see III.2). This study was performed at a single-particle level and a statistics was performed on ~30 b-QDs and thick-shell CdSe/CdS.

Previous studies<sup>15,124,159</sup> have shown that in low excitation regime, the highest intensity state in the PL trace of the thick-shell QDs, corresponding to neutral QDs, is a state with 100% quantum yield. By exciting b-QDs and thick-shell QDs in the same conditions and at low excitation power ( $\langle N \rangle = 0.05/\mu\text{s}$ ), and by comparing the measured signal of the b-QDs to the high-intensity state of thick-shell QDs, we observe that both sets of QDs show the same emission intensity (Figure III.25). This proves that the single emissive state of b-QDs is a state with 100% quantum yield, in air and at room temperature.

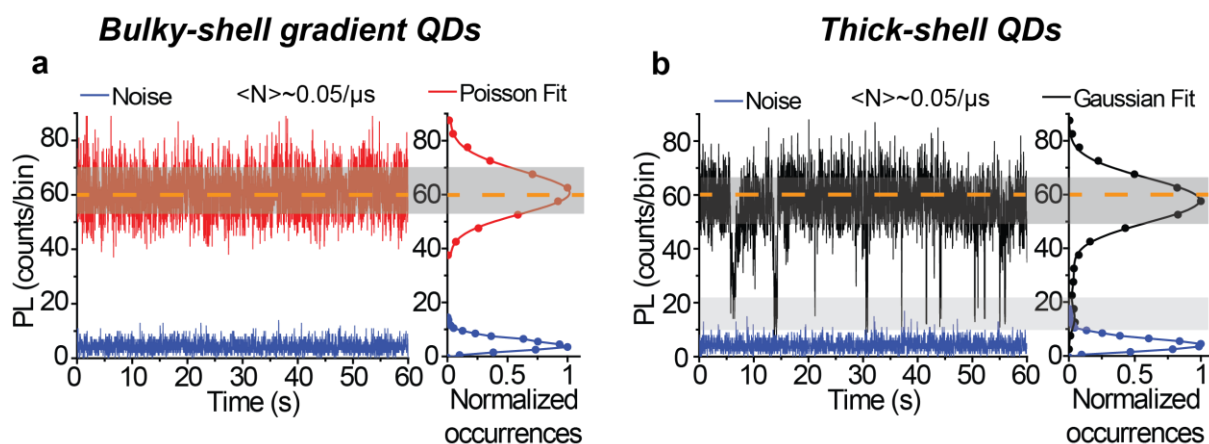


Figure III.25: Compared intensity traces at the same relative excitation power for a. b-QDs and b. thick-shell CdSe/CdS QDs. The high-intensity state of the thick-shell QD has been shown to be at 100% QY, therefore the only emissive state of the b-QD is also at 100% QY. Excitation wavelength: 405 nm. Repetition rate: 1 MHz. Bin time is 20 ms.

### III.3.3.3. High excitation power

When excited at higher power, more excitons will be created in the QDs. Thus, the presence of multiple charge carriers as well as the higher probability of ionization, will increase the probability of Auger recombinations.<sup>160</sup> With more non-radiative recombinations, flickering or blinking should occur. However, even when excited 4 times higher, at  $\langle N \rangle = 0.2/\mu\text{s}$  (corresponding to a 12-fold increase in the probability of absorbing two photons and thus creating two excitons), the PL trace of the b-QD remains completely stable, and the intensity distribution is still shot-noise limited. When for the previous generation of thick-shell QDs more flickering appeared at higher excitation power because of more efficient Auger processes for multiexcitons, for b-QDs, Auger recombinations seem to be overcome even when multiple charges are created in the QDs (Figure III.26). This is a first proof that the charge state of the QD does not infer on the emission intensity of the QD: whether one or multiple excitons are formed in the QD (some charge carriers may be trapped, charging the QD), Auger processes are not competing with radiative recombinations that are more efficient. The charge state of the QD can be controlled by the control of the environment: in air or under vacuum.

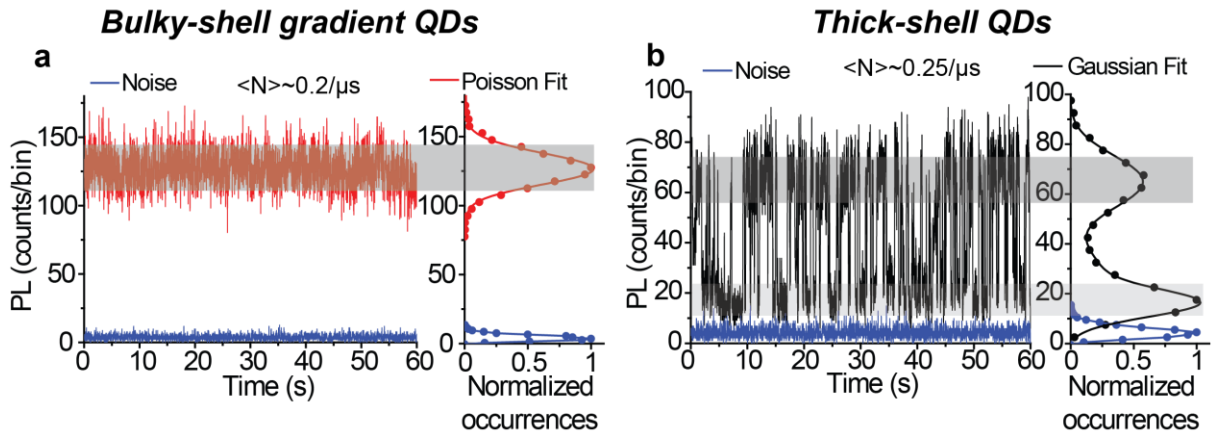


Figure III.26: Compared intensity traces at higher excitation power for a. b-QDs and b. thick-shell CdSe/CdS QDs. In b., Auger recombinations become more probable as the QD gets charged, while in b-QD non-radiative recombinations do not compete with more efficient radiative recombinations. Note: the traces have been recorded on different QDs than in Figure III.25. Excitation wavelength: 405 nm.

Repetition rate: 1 MHz. Bin time is 20 ms.

#### III.3.4. Evolution under vacuum

The Auger recombinations happen when an excess charge is present in the QD. This excess charge can react with molecules present in the environment, neutralizing the QD. Such reactions are, in air, the reduction of  $\text{O}_2$  molecules to  $\text{O}_2^-$  with the help of water<sup>149</sup> or the better passivation of surface traps with small molecules such as  $\text{O}_2$  or  $\text{H}_2\text{O}$ .<sup>146</sup> It has been previously shown<sup>15,146,149</sup> that under vacuum, the absence of water or dioxygen molecules prevents the QDs from neutralizing, favoring Auger recombinations.

When studied under vacuum, b-QDs show a very stable trace. Interestingly, the intensity level does not change when the measurements are performed in air or under vacuum (Figure III.27). This proves that even when forced to stay charged, b-QDs exhibit only one state with no blinking, whose intensity is the same as in air. Therefore, the emission of b-QDs is completely independent from the charge state of the QDs: the Auger processes are eliminated.

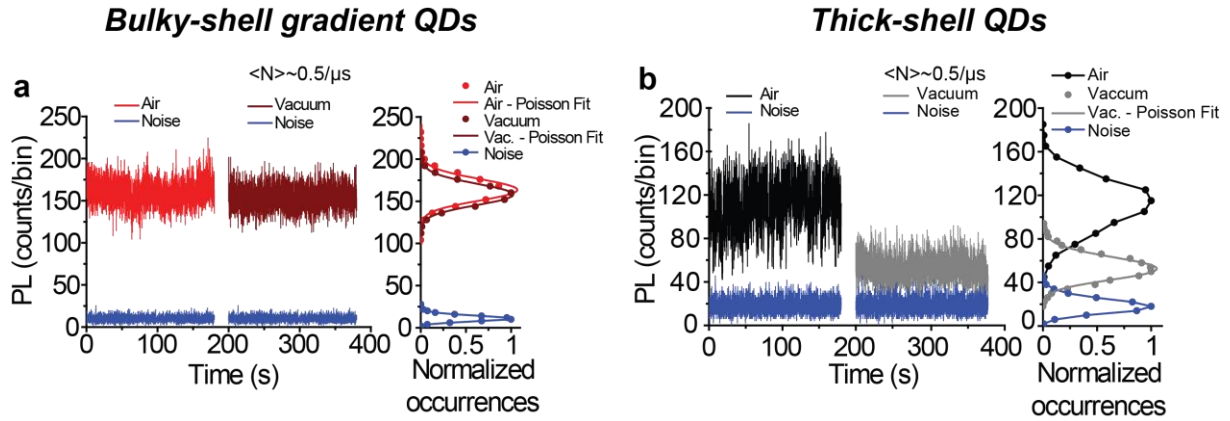


Figure III.27: Compared intensity traces in air and in vacuum for a. b-QDs and b. thick-shell QDs.

Thick-shell QDs stay charged under vacuum and emit in their gray state while the b-QDs show no difference between air and vacuum. Excitation wavelength: 405 nm. Repetition rate: 1 MHz. Bin time is 50 ms.

We have thus shown that in air and at room temperature, non-radiative recombinations are far less efficient than radiative ones. The QY of the b-QDs is 100%, and their trace show no blinking neither flickering and do not change in intensity when studied under vacuum where Auger processes are favored. However, these studies were performed at low excitation powers, and the results obtained so far are relevant for the monoexciton, but not necessarily for higher order multiexcitons.

### III.3.5. Quantum yield of the biexciton

Our optical setup is built with two photodiodes which allows determining the relative quantum yield of the biexciton and the monoexciton (see section III.1.3.3). We performed the analysis on b-QDs at very low excitation ( $\langle N \rangle = 0.025/\mu\text{s}$ ) to ensure that no multiexcitons higher than the biexciton are created. The signal-to-noise ratio,  $\sim 10$ , was high enough to neglect the background noise in the autocorrelation curve (see III.1.3.3) and the observed QDs were verified to be individual with correlative light/electron microscopy (see III.3.2): the signal at 0-time delay in the autocorrelation curve is only due to QDs emission.

For single nanoparticles, the ratio between the area of the peak at 0-time delay and the adjacent peaks gives the ratio between the QY of the biexciton and the QY of the monoexciton:  $QY_{XX}/QY_X$  (see III.1.3.3). For b-QDs, the areas of the peaks are almost identical, showing that the mono- and biexciton have the same quantum yield. As proved before, the  $QY_X$  of the monoexciton is at 100%, giving a quantum yield for the biexciton at 100% (Figure III.28).

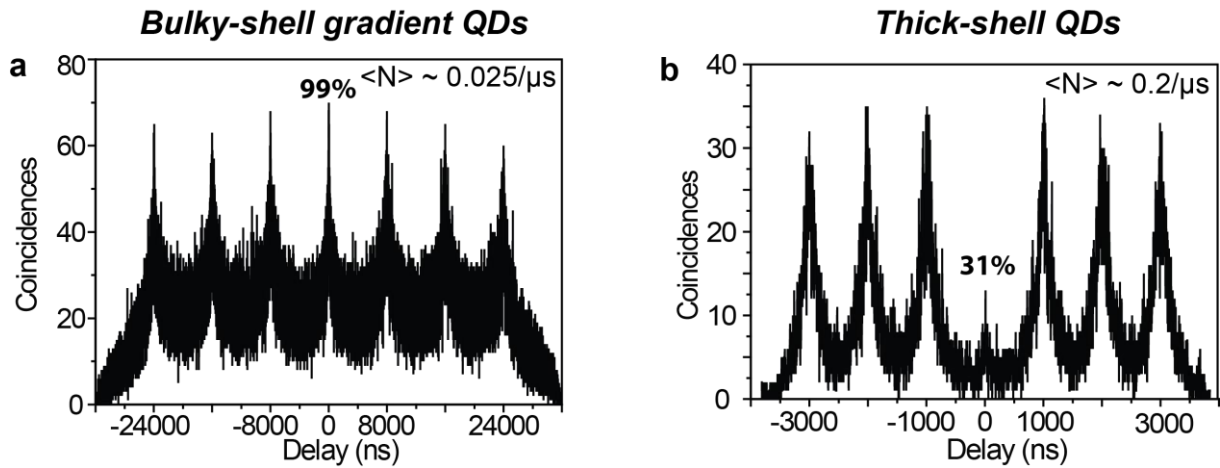


Figure III.28: Autocorrelation function of the PL intensity for a. b-QDs and b. thick-shell CdSe/CdS QDs. (a. Excitation wavelength: 405 nm. Repetition rate: 125 kHz. Bin time is 2 ns. b. Excitation wavelength: 405 nm. Repetition rate: 1 MHz. Bin time is 3 ns.) The thick-shell CdSe/CdS QDs show antibunching, confirming their single-photon emitter behavior and the low QY of the biexciton. b-QDs show 99% bunching on individual NCs, proving their high biexciton QY.

Similar studies have been performed by Klimov's group on CdSe/CdS quantum dots. However, the experiments were performed at 4K,<sup>161</sup> where Auger processes are much less efficient than at room temperature<sup>15</sup>. Another study<sup>158</sup> shows good biexciton quantum yields (up to 90% in the best cases), but the dispersion from dot to dot yields an average  $QY_{XX}$  of around 40% (Figure III.29), whereas the b-QDs show close-to-unity biexciton QY for all the studied dots.

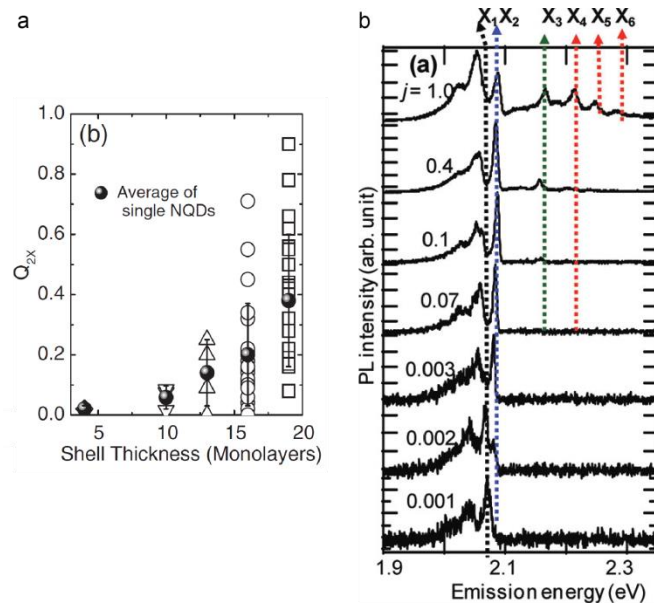


Figure III.29: Klimov's group showed (a.) high biexciton QY for only a few thick-shell CdSe/CdS QD with an average of ~40% and (b.) efficient multiexcitonic emission at 4K where Auger recombinations less favorable.<sup>158,161</sup>

## III.3.6. White-light emitting Quantum Dots

In b-QDs, the quantum yield of both the mono- and the biexciton is 100%. This suggests that even for higher order multiexcitons, the QY might be quite good. To study the multiexcitonic emissions, we performed a simple measurement: a single b-QD's emission spectra were collected at increasing excitation powers. The resulting spectra are shown in Figure III.30.

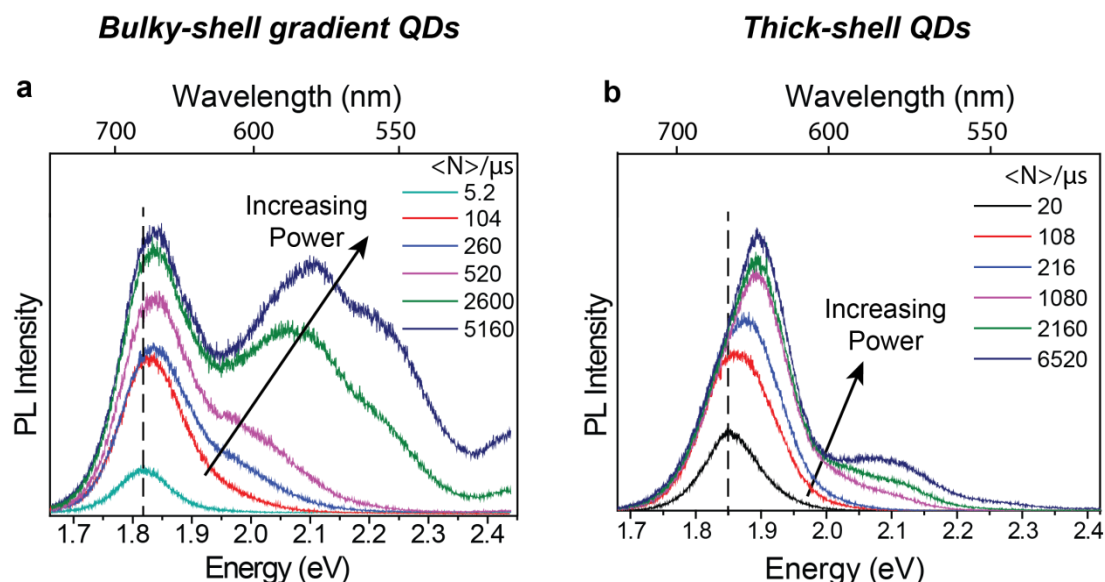


Figure III.30: Compared emission spectra at increasing excitation powers for a. b-QDs and b. thick-shell CdSe/CdS QDs. Multiexcitonic peaks are clearly visible on the spectra of b-QDs at lower fluence than for thick-shell QDs where Auger recombinations prevent multiexcitonic emission. Excitation wavelength: 405 nm. Repetition rate: 40 MHz.

When excited stronger, emission peaks at higher energies appear. These peaks are due to the recombinations of higher-order multiexcitons:<sup>42</sup> as lower energy states are filled with charge carriers, the excitons of orders higher than 2 must fill more energetic states, yielding recombinations at higher energies. The fact that these transitions are so clearly visible, and occur at relatively low excitation powers show that even for higher-order multiexcitons, the radiative QY is quite high. Compared to the reference thick-shell QDs, the QY of the multiexciton seems much higher for b-QDs where intense peaks appear at lower excitation powers. Similar results from Klimov's group<sup>158</sup> show emission peaks at higher energy, but they are much lower in intensity and occur at higher fluence.

Finally, a single b-QD, when excited at high fluence, show high energy transitions originating from multiexcitonic recombinations. The intensity of those transitions reaches the intensity of the monoexcitonic peak, and even exceeds it at high fluences, yielding single nanoparticle that emit white light (Figure III.31).

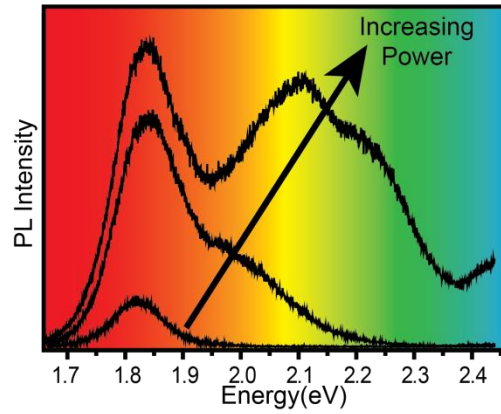


Figure III.31: White-light emitting single b-QD.

In order to confirm that the Auger processes do not play a major role in the multiexcitonic recombinations, we performed a study of the PL intensity with increasing excitation fluence. This study shows that for excitations as high as  $\langle N \rangle = 1/\mu\text{s}$ , the increase of the intensity is linear with  $\langle N \rangle$ , and follows a slope that is consistent with no Auger recombinations.<sup>158,161</sup> At higher fluences, the increase of the intensity with  $\langle N \rangle$  is sublinear, suggesting that non all the excitation photons trigger the emission of a photon from the QD: non-radiative recombinations start to appear. However, even when excited very strong, at  $\langle N \rangle = 20000/\mu\text{s}$ , the intensity does not show any saturation yet and continues to increase when the power is increased. This shows that even when Auger recombinations appear, they never become predominant and the radiative recombinations in the QD are still more efficient than non-radiative ones. This proves that the QY of multiexcitons, although not at 100%, remains very high.

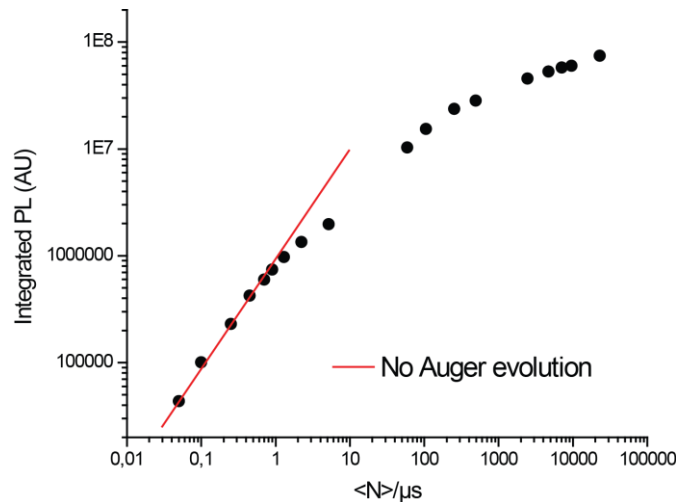


Figure III.32: Emission intensity vs excitation fluence for a single b-QD at room temperature. The red line depicts the evolution of the PL intensity without non-radiative recombinations. Even at higher excitation, the PL intensity does not saturate, suggesting radiative recombinations are still favored over Auger recombinations.

### III.3.7. Lifetime measurements

For the mono- and the biexciton, b-QDs show no Auger recombinations. Non-radiative transitions are also very weak for higher order multiexcitons. This should be reflected on the photoluminescence decay. The PL decay, even at low excitation powers, is multiexponential. We would expect, for high-QY QDs a monoexponential decay as there are no non-radiative recombinations that would be responsible for a short lifetime decay on the PL decay curve. However, there are multiple lifetimes that are visible on the curves, and they seem too long to be due to radiative recombinations competing with Auger processes.<sup>148,162</sup> Indeed, at room temperature, 3 lifetimes can be extracted from the PL decay curve: a long lifetime, at approximately 4 $\mu$ s, much longer than what has been reported in the literature so far,<sup>163</sup> an intermediate one at 800 ns and a short one at 150 ns (Figure III.33). Although we are not able to accurately assign these lifetimes to the excitons within the QD, we can emit some hypothesis as for their origins.

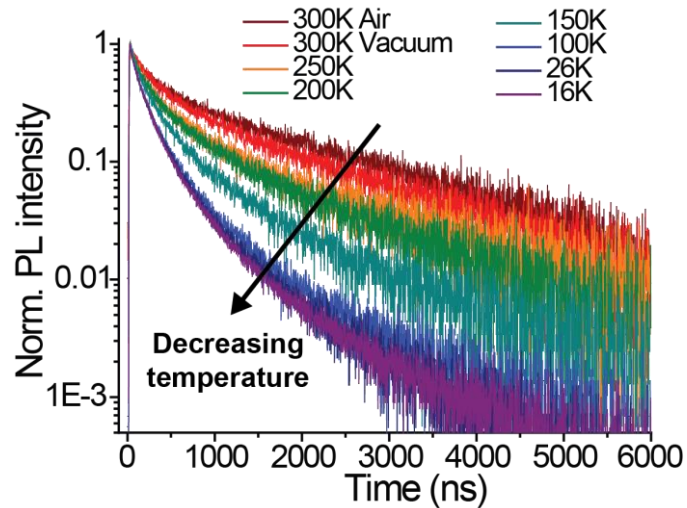


Figure III.33: PL decay at different temperature for an ensemble of b-QDs. A triexponential fit gives three lifetimes: 150 ns, 800 ns and 4  $\mu$ s. Excitation wavelength: 377 nm. Repetition rate: 100 kHz.

The longest lifetime is most probably due to emission from the traps. After the formation of the exciton, some charge carriers can be trapped, stopping the recombination of the electron-hole pair. These traps can be traps at the surface of the QDs or within its crystal structure. For the charges to recombine, untrapping must occur: this may take some time, yielding long lifetimes in the PL decay.

The intermediate and short lifetimes probably come from the monoexciton. Due to the trapping events discussed above, it is highly probable that the monoexciton switches between neutral exciton and charged exciton (trion). These two different states of the monoexciton will recombine with different dynamics, thus with different lifetimes.

Finally, these experiments were performed at low fluence to minimize the contributions of the multiexcitons. However, even at this low fluence, we cannot completely exclude the formation of biexcitons or even higher order excitons, which will recombine with different short lifetimes (the expected ratio between the lifetime of the mono- and the lifetime of the biexciton is 4 and 2 between the lifetimes of the monoexciton and the one of the trion, while the ratio of lifetimes 800/150 is around 5. The ratio between the trion and the charged biexciton lifetimes was measured to be around 7. Thus, the short lifetime might be an average over the fast recombination lifetimes: trion, biexciton or higher multiexcitons.).<sup>147</sup>

When the QDs were forced to stay charged, *i.e.* under vacuum, the PL decay did not show different dynamics than in air. This again is proof that the charge state of the QD does not play a role in the emission, and that Auger processes are eliminated.

### III.3.8. Evolution at cryogenic temperature

According to previous studies,<sup>15</sup> at cryogenic temperature, the band alignment changes: the difference in energy between the conduction bands of the CdSe and the CdS increases. The confinement potential of the electron in the CdSe increases as the conduction band of the CdSe gets lower than the one of CdS at low temperature. This plays a role of the dynamics of the exciton recombinations. As the confinement is increased, the wavefunction overlap between the electron and the hole increases, allowing for faster exciton recombination. This can be seen on b-QDs where the lifetimes at 16K drop to 1.5  $\mu$ s, 350 ns and 100 ns (Figure III.33).

This increased confinement also plays a role on the accessibility of surface traps. As the charges are more confined, surface-assisted Auger recombinations are less probable, and the QY of the structure should increase (as seen in III.2.1.4 and III.2.1.5).

When we performed this experiment on b-QDs at low fluence with a continuous wave excitation, no increase in the PL intensity was seen. Therefore, this means that the emission at room temperature was already independent from the presence of traps, and that Auger processes were indeed eliminated (Figure III.34).

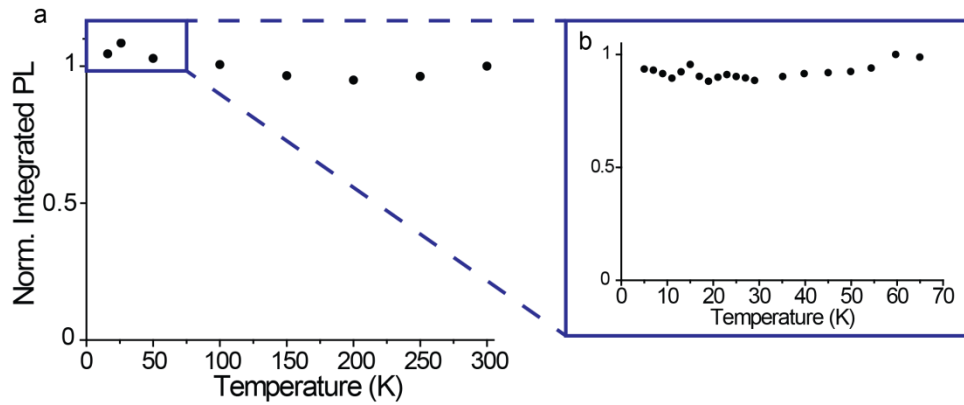


Figure III.34: Evolution of the integrated PL intensity with decreasing temperature a. from 300K to 16K and b. from 70K to 4K.

To see how they behave at low temperature, we performed experiments between 4.2K and 70K on an ensemble of b-QDs. As seen previously, the PL intensity does not increase when the temperature decreases: this has confirmed that Auger recombinations are eliminated at RT for the monoexciton. However, even when excited much stronger (with a pulsed laser), we see no change in the PL when the temperature decreases (Figure III.35). Although it is difficult to estimate the number of multiexcitons created in the QDs in the film, the calculation of  $\langle N \rangle$  described in III.3.3.1 shows that with the same excitation power (5.7 $\mu$ W at 5MHz) on a single dot, more than 6000 excitons/ $\mu$ s would be created, confirming the high excitation regime and the fact that multiexcitons are formed in the QDs. This suggests that even the multiexcitons have a very high QY, as their PL does not increase when the temperature decreases.

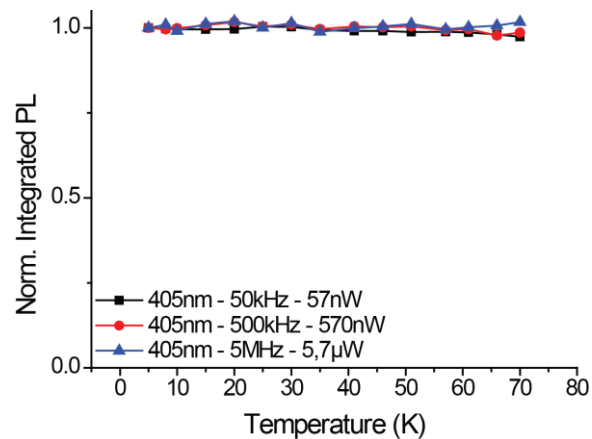


Figure III.35: Evolution of the integrated PL intensity with decreasing temperature from 70K to 4K and with increasing excitation power.

To ensure that the multiexcitons exhibit a high quantum yield, we measured the PL intensity at different excitation powers. For two different excitations, continuous wave laser at 405 and 532 nm, we see that the PL intensity varies linearly with the fluence, proving that no

saturation occurs and that the multiexcitons do have a high QY. The fact that the excitation at low energy (532 nm), *i.e.* mainly in the CdSe core, shows a similar behavior to the excitation in the CdS shell (405 nm) suggests that the surface does not play in the role in the Auger recombinations for these systems. This confirms that at low temperature, the surface-assisted Auger processes are completely eliminated. As the PL does not decrease when the temperature increases, it corroborates the fact that there are almost no Auger recombinations even at higher temperature.

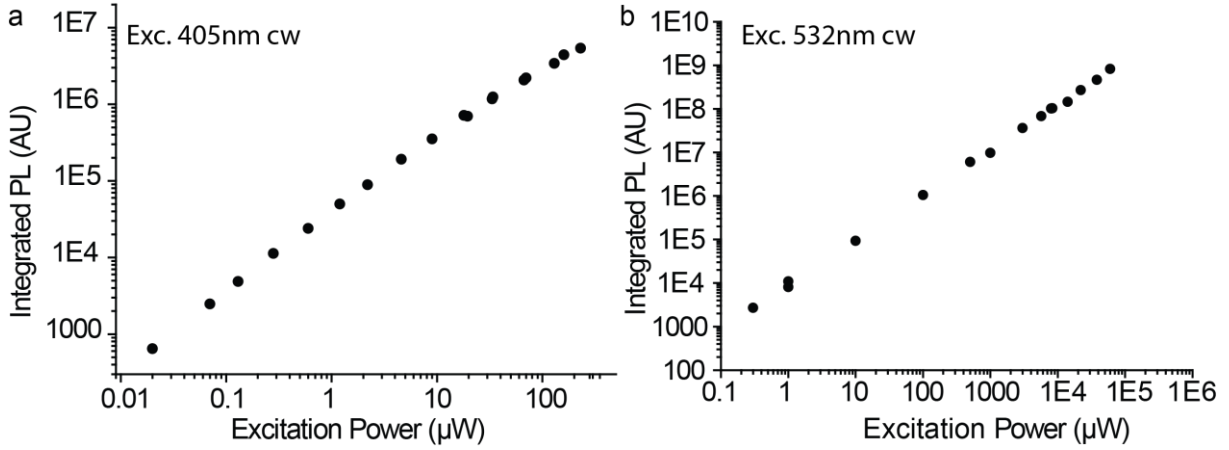


Figure III.36: Evolution of the emission intensity with increasing excitation power for an ensemble of b-QDs at 4K at a. 405nm cw excitation and b. 532 nm cw excitation.

This conclusion is of course limited to low temperatures (between 4.2 and 70K), and it might be explained therefore by the stronger confinement of charges within the core, but similar results have been shown at room temperature (see III.3.6).

### III.3.9. Magneto-optical measurements

In order to confirm that these QDs are charged, preliminary magneto-optical measurements were performed in collaboration with Manfred Bayer's group at TU Dortmund. The PL at different polarizations were collected under different magnetic fields at low temperature. The polarization degree is related to the nature of the charge carrier in the nanostructures (see II.2.8)<sup>164</sup>:

$$P = \frac{I(\sigma^+) - I(\sigma^-)}{I(\sigma^+) + I(\sigma^-)}$$

where  $I(\sigma^\pm)$  is the PL intensity at polarization + or -.

The spectra confirm that the b-QDs are negatively charged (Figure III.37), which however does not affect the monoexciton and biexciton QY which are at 100%.

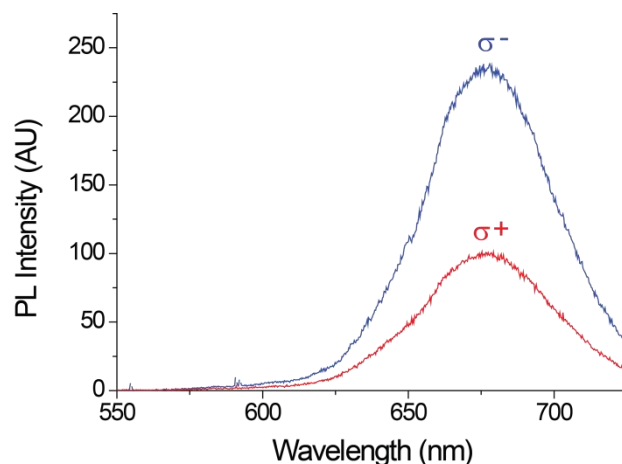


Figure III.37: Polarization-resolved PL spectra of b-QDs at 4K under 15T.

### III.3.10. Slow recombination dynamics

As seen previously, the recombination dynamics seen in the measured lifetime are particularly slow. This suggests the presence of traps which block the charge carriers, slowing the recombination of the exciton. The presence of traps is also suggested by the wavelength dependence of the PL decay. The blue region of the spectra shows faster recombination while the red region shows much slower recombination: this suggests the presence of intraband levels with slower, trap-like dynamics (Figure III.38).

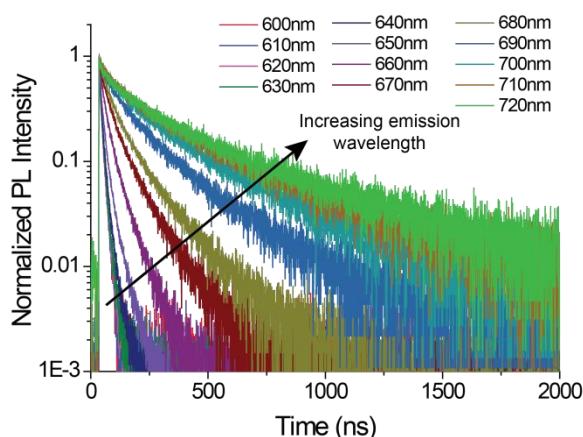


Figure III.38: Emission wavelength dependence of PL decay of b-QDs at 4K. Excitation wavelength: 405 nm. Repetition rate: 300 kHz.

The ensemble measurements of the PL intensity show interesting results on the position of the emission peak and its FWHM. When the excitation power is increased, the emission peak blue-shifts, which is expected and can be attributed to multiexcitonic emission. However, counter-intuitively, the FWHM decreases significantly when the

excitation power is increased. If the blue-shift was due to multiexcitonic emission, the FWHM should increase as the contribution of the multiexcitons adds up to the contribution of the monoexciton. This suggests that at higher excitation powers, before having multiexcitonic emission, the emission from the traps is overcome: the QDs are excited again before the trapped charges had time to recombine.

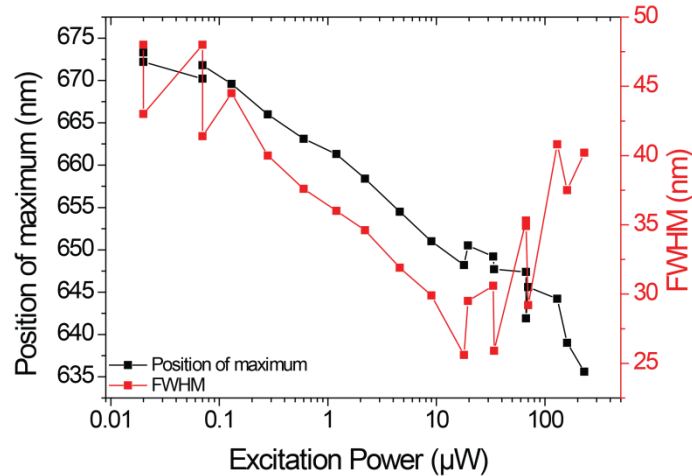


Figure III.39: Evolution of the maximum and the FWHM of b-QDs with increasing excitation power at 405 nm cw, at 4K.

This might explain the relatively low quantum yield seen in solution as the QDs are excited very rarely (continuous-wave excitation excites the QDs weakly and rarely as they are subject to Brownian motion) and most of the emission comes from trapped charges. On a film or on a single particle, however, the QDs are excited more strongly, the traps are filled, and the next excitation happens before the traps had time to release the charges. This second recombination (of the exciton while the traps are filled) is, according to our understanding, the recombination at 100% QY.

### III.3.11. Amplified spontaneous emission

Several reports have shown the possibility to achieve amplified spontaneous emission (ASE) on semiconductor nanocrystals.<sup>157,165–167</sup>

Preliminary tests have shown that when excited at very high fluence, the b-QDs PL peak show no ASE, however, a narrow peak appears around 510 nm, which corresponds to the ASE emission from the CdS shell. Indeed, the volume ratio between the shell and the core is, in those giant shell QDs, in favor of the shell. The electron and hole wavefunction overlap decreases, the recombination is slowed down, and high-energy excitons are formed

in the shell before they can relax in the core, yielding a narrow emission peak after the ASE threshold is reached.

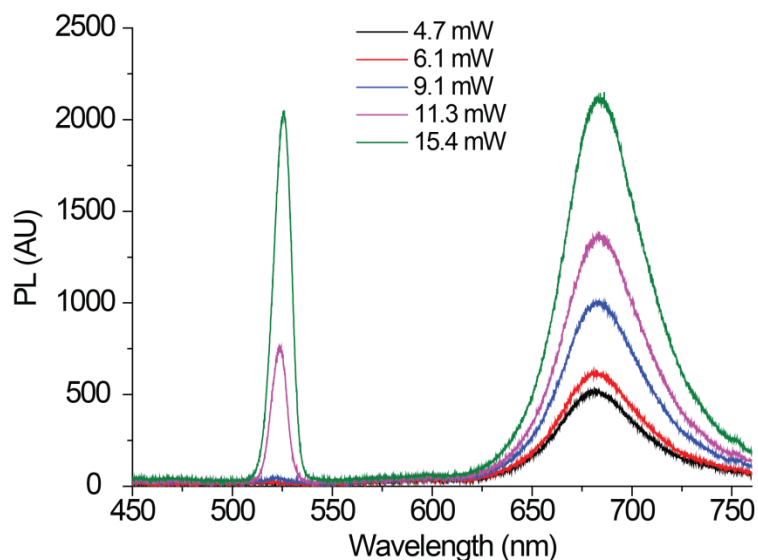


Figure III.40: PL spectra of b-QDs at very high excitation powers.

The absence of red ASE might be due to a low packing-density of the film of QDs. The CdSe cores, responsible for the red emission, might be too far away from each other to induce red band-edge ASE, whereas the CdS shell, which occupies most of the NC volume, are much more densely packed.<sup>168</sup>

### III.3.12. Conclusion

Bulky-shell gradient CdSe/CdS QDs have been synthesized: they consist of a thick CdS shell grown on a CdSe core in such a way to form a composition gradient between the core and the shell. This gradient limits the Auger recombination sites, and with the help of the thick shell, yields QDs with completely stable emission at room temperature. The blinking is efficiently suppressed, and the quantum yield is shown to be at 100% for both the mono- and the biexciton at room temperature and in air. b-QDs are shown to be negatively charged; the charge however does not favor non-radiative recombinations in b-QDs. Finally, not only the mono- and the biexciton, but also the multiexcitons see their QY increase, yielding at high excitation powers white-light emitting QDs.

## III.4. Golden-QD – hybrid Quantum Dots/gold nanoshell nanoparticles

Playing on the intrinsic structure of the QD is not the only way to modify its optical properties. We have already seen that the environment of the QD plays an important role in the blinking behavior (passivation or reduction by water or oxygen). The lifetime of the spontaneous emission of the QD is also not an intrinsic property, but strongly depends of the local density of states (LDOS).<sup>169</sup> The synthesis of golden-QDs has been performed by Botao Ji.

### III.4.1. Surface plasmons and Purcell effect

In 1946, Purcell described a relation between the LDOS and the ratio  $Q/V$  (called the Purcell factor  $F_p$ ) where  $Q$  is the quality factor and  $V$  the modal volume of a cavity.<sup>170</sup>  $F_p$  essentially represents the ratio of LDOS in a resonator to that in free space. By increasing the LDOS, it is possible to change the light-matter interactions, and accelerate the spontaneous emission rate.<sup>171</sup> This can be performed either by increasing the quality factor  $Q$  or by concentrating the mode in a small volume and decreasing  $V$ .

Both the strategies have already been used to couple the emission of a QDs to the mode of a cavity (few examples in Figure III.41). Dielectric cavities have already been used to show an efficient coupling between the QDs and Bragg reflectors, yielding a Purcell factor of approximately 2.5.<sup>172</sup> These structures show a high quality factor ( $Q > 1000$ ) but their modal volume is low ( $(\lambda/2)^3$ ) and they are not really adapted to the coupling to broadband emission of colloidal QDs.<sup>14,171</sup> On the other hand, plasmonic structures, thanks to surface plasmons (SP, collective oscillations of free electrons at the surface of the metal) and despite their relatively low  $Q$  factor (10 to 100 due to absorption and radiation losses), are able to concentrate the field on subwavelength modes.  $V$  is therefore strongly reduced, not to mention their broadband response; such structures can even outperform high- $Q$  dielectric cavities.<sup>171</sup> Gold antennas around QDs have been reported with a Purcell factor up to 100.<sup>14,173</sup>

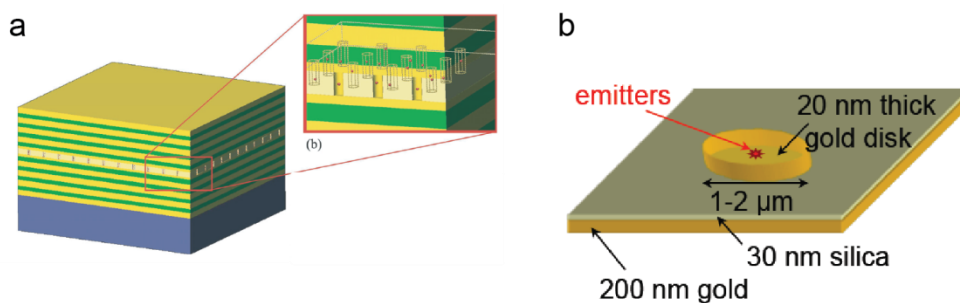


Figure III.41: a. Dielectric cavity and b. plasmonic coupling between gold and QDs for Purcell effect.<sup>14,172</sup>

### III.4.2. Description of Golden-QDs and synthesis

Coupling of SP modes to dipole emitters like QDs has already been shown, but in a rigid cavity, on a substrate, and not in colloidal solution. We wanted to fabricate a local cavity that would efficiently couple the exciton to an external electromagnetic field in a structure that retains its colloidal stability and is as small as possible. For that, because of its ease of synthesis and its ability to concentrate the modes at a subwavelength scale, we decided to use a gold nanoshell to form a local plasmonic cavity around the QD. A similar structure has already been synthesized, but did not show any Purcell effect.<sup>174</sup>

The synthesis of this gold-capped QD, called golden-QD, consists of several steps (Figure III.42).

CdSe/CdS QDs are coated with a silica spacer. Indeed, the distance between the QD and the gold needs to be precisely tuned in order to achieve high Purcell factors and to avoid quenching of the emission by the metal. This step is performed via a reverse micro-emulsion method (water in cyclohexane): the surfactants used are Triton X-100 and hexanol, and the silica precursor is TEOS (Tetraethylorthosilicate). The silica shell is grown by steps of hydrolysis and condensation of TEOS, and can be grown from 10 to 60 nm in thickness. Several washing steps with water and ethanol then follow to eliminate the excess surfactants. The QD/SiO<sub>2</sub> nanoparticles formed are then capped with a polymer, the poly(1-vinylimidazole-co-vinyltrimethoxysilane) or PVIS, which presents a silicate group to bind to the surface of the silica, and an imidazole moiety that has strong affinity for gold seeds. Indeed, the next step is to adsorb on the silica shell gold seeds previously formed by the reduction of HAuCl<sub>4</sub>. This yields QD/SiO<sub>2</sub>/Au<sub>seeds</sub>. The Au seeds are then grown by the addition of gold precursors and a reducing agent to form a continuous gold layer, and the speed of growth is controlled by another polymer, poly(vinylpyrrolidone) or PVP. This polymer complexes the Au<sup>(III)</sup> ions and adsorbs on the gold seeds, reducing the growth of the gold shell and limiting gold particle secondary nucleation in the solution, away from the

surface of QD/SiO<sub>2</sub>/Au<sub>seeds</sub>. It also acts as a stabilizing ligand as it can adsorb to gold, increasing the colloidal stability of the nanoparticles. This yields QD/SiO<sub>2</sub>/Au or golden-QDs with tunable gold shell thickness from 10 (the minimal thickness for the gold seeds to coalesce during the growth and to form a homogeneous film) to 30 nm. The final size of the golden-QDs is around 100 nm.

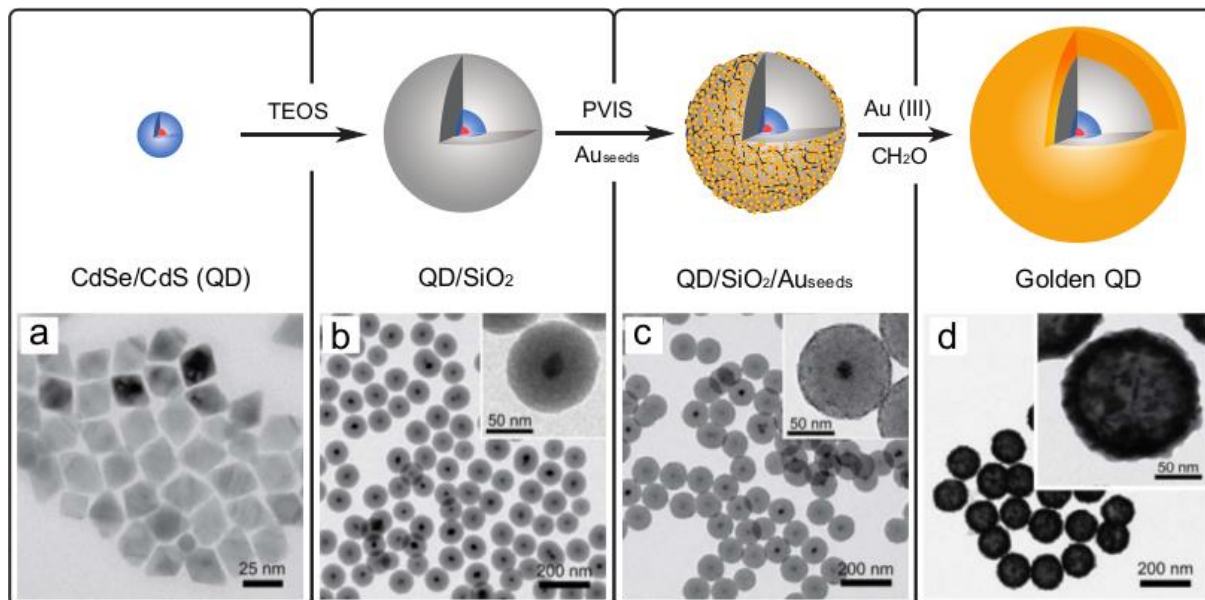


Figure III.42: Synthesis strategy of golden-QDs and corresponding TEM images.<sup>145</sup>

Several parameters can be tuned in order to increase the coupling between the dipole emission and the gold shell. First, the distance between the QD and the gold shell, *i.e.* the silica spacer, influences the proportion of spontaneous emission into the plasmonic modes and quenching (which decays as  $1/d^3$  where  $d$  is the distance between the dipole and the metal).<sup>14</sup> Thus, the typical silica thickness obtained in these studies (~35nm) ensures that non-radiative transfer between the emitter and the metal is negligible compared to the spontaneous emission. Second, the thickness of the gold layer (or more accurately the internal/external radii ratio) plays a role in the spectral position and broadness of the plasmon resonance.<sup>175</sup> The latter is to be compared to the position of the emission of the QD (third parameter): efficient coupling between the emitter and the SP occur when both the spectral positions overlap. The QDs used here emit between 630 nm and 670 nm while the SP resonance shows a large extinction spectra from 600 to 900 nm.

#### III.4.3. Determination of the Purcell factor

The structure of the aforementioned golden-QDs meets the criteria for an efficient exciton-plasmon coupling. Thus, a Purcell effect should be seen in this nanoparticle, modifying the spontaneous emission rate of the QD within the gold nanoshell:

$$\tau_{Golden-QD} = \frac{\tau_{QD}}{F_p}$$

where  $\tau_{Golden-QD}$  is the lifetime of the QD in the gold structure,  $\tau_{QD}$  is the lifetime of the bare QD and  $F_p$  is the Purcell factor.

#### III.4.4. First observations with thin-shell CdSe/CdS QDs

CdSe/CdS with 2 nm CdS shell thickness exhibit typical blinking of the PL emission, oscillating between two states. The higher the excitation power, the stronger the blinking due to the formation of multiple excitons within the nanocrystals, favoring Auger recombination. When covered with the gold nanolayer, the PL intensity becomes much more stable. This effect can be attributed to the efficient coupling between the gold nanoshell plasmons and the QDs excitons, decreasing the characteristic lifetime of the radiative recombination, thus decreasing the probability of Auger processes. However, the coupling is not efficient enough to compensate for all the non-radiative recombinations, as can be seen on the non-poissonian distribution of intensities in the PL trace. This proves a small residual flickering subsists in this golden-capped QD structure.

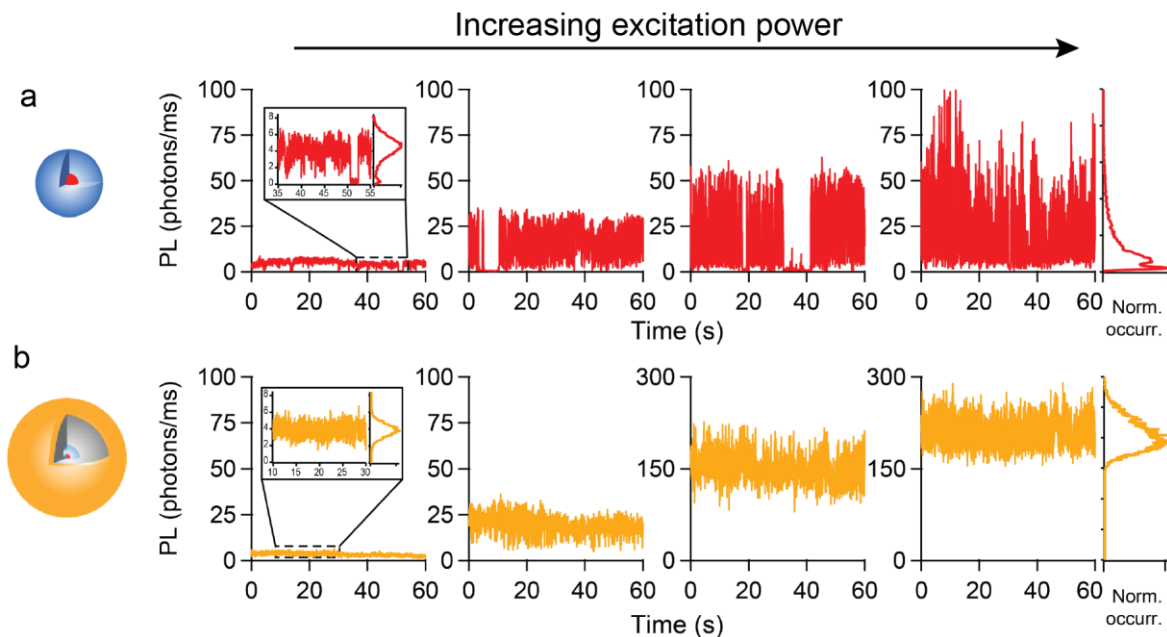


Figure III.43: Intensity trace of a. a bare thin-shell CdSe/CdS QDs and b. a golden-QD synthesized with thin-shell QDs. The blinking seems to be strongly reduced when the QD is capped with the gold nanoshell, but the distribution of intensities does not follow Poissonian statistics confirming some non-radiative recombinations still exist in this structure.

In order to quantify the coupling and to determine the Purcell factor, the evolution of the PL decay at different stages of the synthesis has been analyzed. Indeed, the Purcell effect,

responsible for the acceleration of radiative spontaneous recombinations, induces a decrease in the measured lifetime.

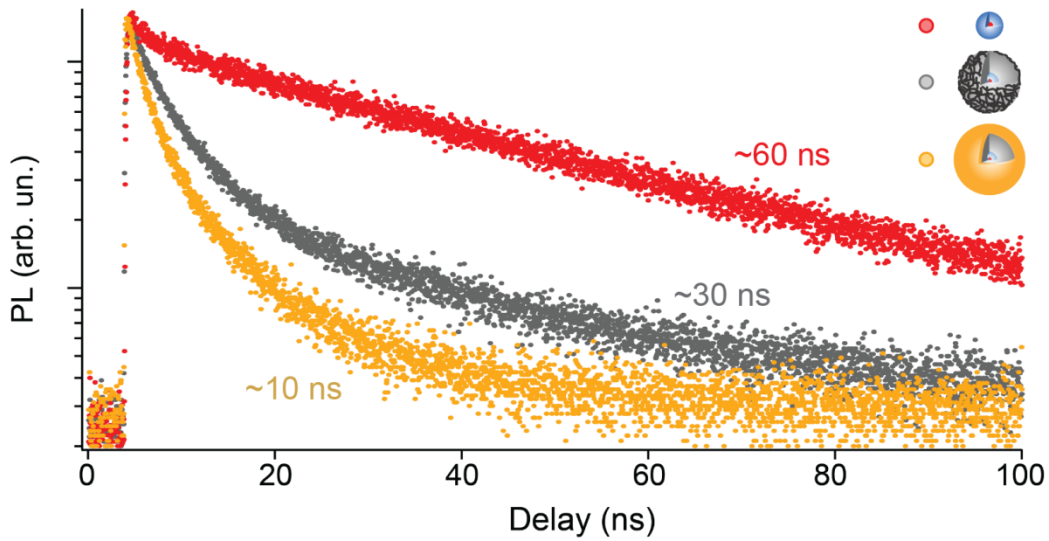


Figure III.44: PL decay of an individual thin-shell QD, capped with silica and gold.

After coating the QDs with the silica spacer, a decrease of the lifetime can be seen (Figure III.44). However, it cannot be due to Purcell effect as no gold has been deposited on the surface of the silica. Besides, this shortening is concomitant with a decrease of the PL, implying that new non-radiative recombination channels have been opened during the growth of the silica. Some chemical quenching during the growth or washing steps might explain this degradation of the QD.

Nevertheless, after growing the gold nanolayer, a new decrease of the lifetime can be observed, from  $\sim 32$  ns to  $\sim 10$  ns (for the longest lifetime corresponding to the neutral state, and from  $\sim 6$  ns to  $\sim 3$  ns for the charged state) (Figure III.44). Besides, the NCs were incubated for a time longer than the necessary reaction time with efficient PL quenchers like  $\text{Au}^{\text{III}}$  ions that can diffuse through the silica shell to the QD. This showed no decrease in the PL intensity (Figure III.45), suggesting that this lifetime shortening is at least partially due to Purcell effect, with a Purcell factor of  $\sim 3$ .

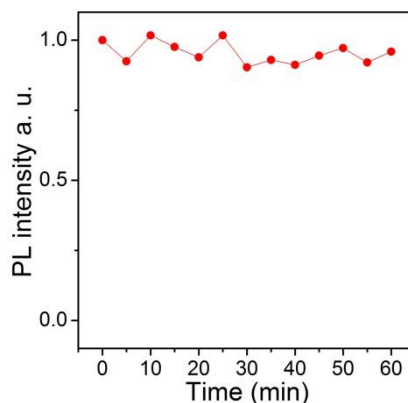


Figure III.45: PL evolution with time of QD/SiO<sub>2</sub>/Au seeds hybrids incubated with the gold(III) salt solution in the conditions used for the synthesis.

These first observations show that the colloidal structure of golden-QDs show an efficient coupling between the gold plasmons and the QD excitons.

In order to improve the efficiency of the coupling, the parameters described previously can be changed, and thicker-shell QDs can for example be used for more thorough studies.

Indeed, a higher emission wavelength (~670 nm) can better overlap with the gold plasmons. Besides, simulations performed by Benjamin Habert<sup>176</sup> from Institut d'Optique Graduate School show that, according to the emission wavelength of the QD and the size of the gold shell, higher Purcell factors can be reached for higher-wavelength emitting QDs (Figure III.46). Thick-shell QDs are also interesting for this kind of studies as they already present diminished Auger recombinations whose overcoming might be easier to achieve.

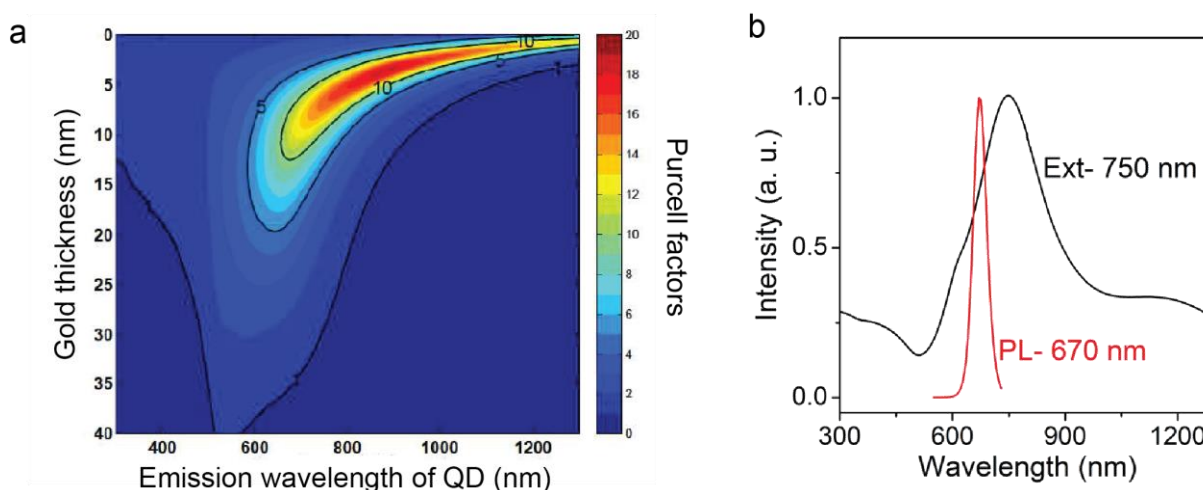


Figure III.46: a. Simulated Purcell factors for different gold thicknesses and QD emission wavelength. b. PL spectrum of thick-shell QDs and extinction spectrum of the gold nanoshell of 20 nm in thickness on an 85 nm QD-silica nanoparticle.

## III.4.5. Golden-QDs with thick-shell CdSe/CdS QDs

As presented previously, the thick-shell CdSe/CdS QDs present two lifetimes: a long one corresponding to the neutral monoexciton, and a short one corresponding to the charged exciton, or trion. This study will be focused on the long lifetime, although a similar analysis can be performed on the short lifetime.

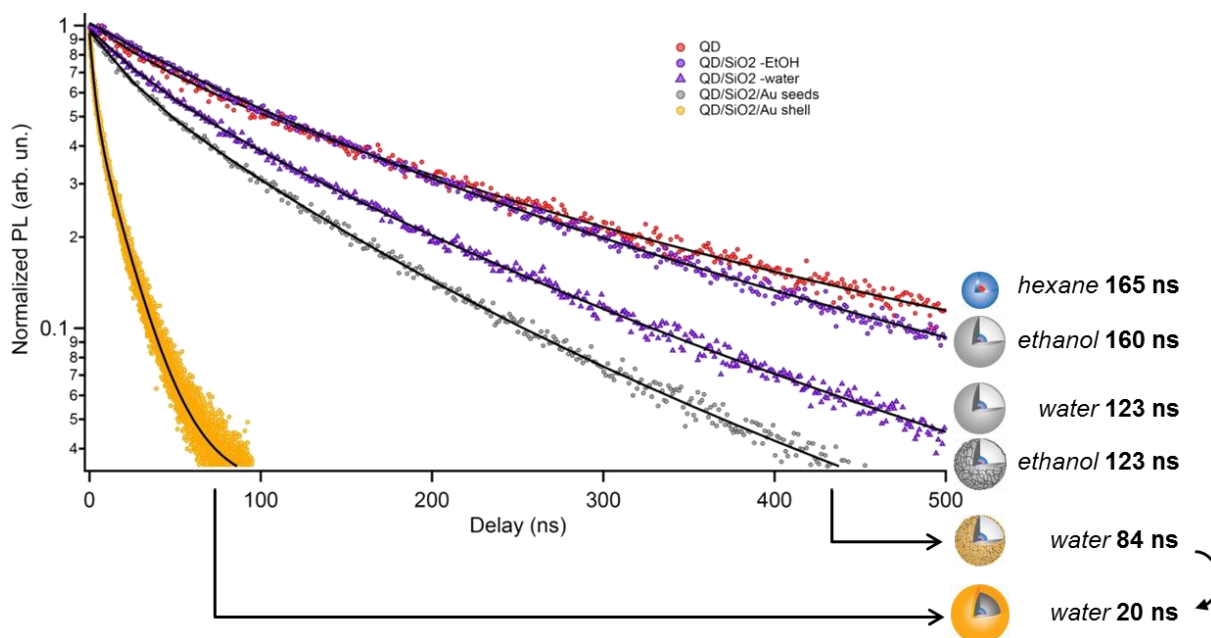


Figure III.47: PL decay evolution during the synthesis of golden-QDs.<sup>145</sup>

Bare QDs have a neutral exciton lifetime of 165 ns when measured in ensemble, in solution in hexane (Figure III.47). After the growth of the silica shell and changing the solvent to ethanol, the lifetime remains unchanged, at 160 ns. The following washing procedure, in water, causes a decrease in the lifetime to 123 ns. This is due to the opening of non-radiative channels for the recombination of the exciton, shortening the lifetime. Indeed, water molecules can diffuse through the porous silica shell and degrade the QD surface. This value however remains stable with time and subsequent washing steps. When gold seeds are adsorbed on the surface of the silica shell, the lifetime decreases to 84 ns. This is due to the temporary opening of non-radiative channels as small gold seeds are very good absorbers but poor scatterers. However, during the nanoshell growth, the gold seeds coalesce to give a uniform gold nanoshell, changing this effect for the coupling between the QD and the SP. This decreases dramatically the lifetime of the nanoparticle to 20 ns.

This decrease might be in fact due to the degradation of the QD and the opening of more non-radiative channels. However, several evidences confirm that this decrease is due to a Purcell effect and not to the degradation of the QDs.

If it was due to some chemical changes on the surface of the QDs or quenching, it would probably be due to the diffusion of gold ions through the porous silica. However, the fluorescence intensity of QD/SiO<sub>2</sub>/Au<sub>seeds</sub> mixed with Au growth solution decreases only slightly with time on a time scale larger than the one of the experiment (Figure III.48).

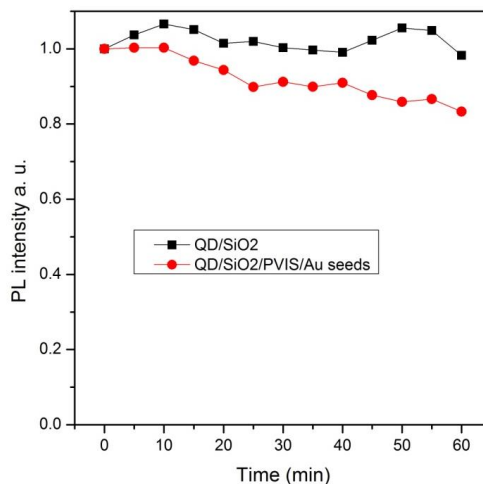


Figure III.48: PL evolution with time of QD/SiO<sub>2</sub> and QD/SiO<sub>2</sub>/Au seeds hybrids incubated with the gold(III) salt solution in the conditions used for the synthesis.<sup>145</sup>

Thus, because no PL quenching can be observed, it means that no non-radiative channels have been opened, and we can attribute this decrease in the lifetime to the Purcell effect.

When the surrounding media of the golden-QD is modified, the lifetime changes accordingly to what the simulation predicts. This is again conclusive proof that the lifetime change is not due to chemical degradation but to a coupling of the emitter to the electromagnetic field in its surrounding (Figure III.49). Thus, from the moment when gold seeds are adsorbed to the golden-QDs, there is a decrease of the lifetime from 120 to 20 ns due to an acceleration of the spontaneous emission (Purcell effect), with a Purcell factor of 6.

Finally, a last evidence is that this lifetime is confirmed by a numerical simulation that takes into account only the Purcell effect, and no chemical quenching. The simulation gives a lifetime for the golden-QDs of 20.7 ns, corresponding perfectly to the experimental measures.

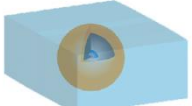
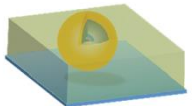
Nanoparticle		Experimental conditions	$\tau$ (ns)
	Golden QD in air ( $n = 1.00$ )	As-synthesized, on glass slide, in air (dried)	$13.3 \pm 0.2$
		Numerical simulation	12.4
	Golden QD in water ( $n = 1.33$ )	As-synthesized, in water/droplet	$20.0 \pm 0.2$
		Numerical simulation	20.7
	Golden QD in oil ( $n = 1.52$ )	As-synthesized, on glass slide, covered with oil	$28.7 \pm 0.2$
		Numerical simulation	27.9

Figure III.49: Table summarizing the predicted and measured lifetimes of golden-QDs in media of different refractive indexes.<sup>145</sup>

#### III.4.6. Effect on blinking behavior

The strong acceleration of radiative recombinations has an important effect on the emissive properties of thick-shell QDs. Those QDs emit in two different states: *on* for the neutral QD, *grey* for the charged one where Auger and radiative recombination compete. When coupled to the gold nanoshell, the emission trace is completely stable: there is no visible blinking (switching between *on*, bright state and *off*, dark state) or flickering (switching between *on* and *grey* state), and the distribution of intensities is poissonian, confirming there is no blinking even at very short time scales (the time resolution of the setup is  $\sim 1$ ms). This is due to the fact that the radiative recombinations are sped up and can now overcome Auger recombinations: because they are faster, they are more probable than non-radiative processes, leading to a structure that emits all the photons in the bright state.

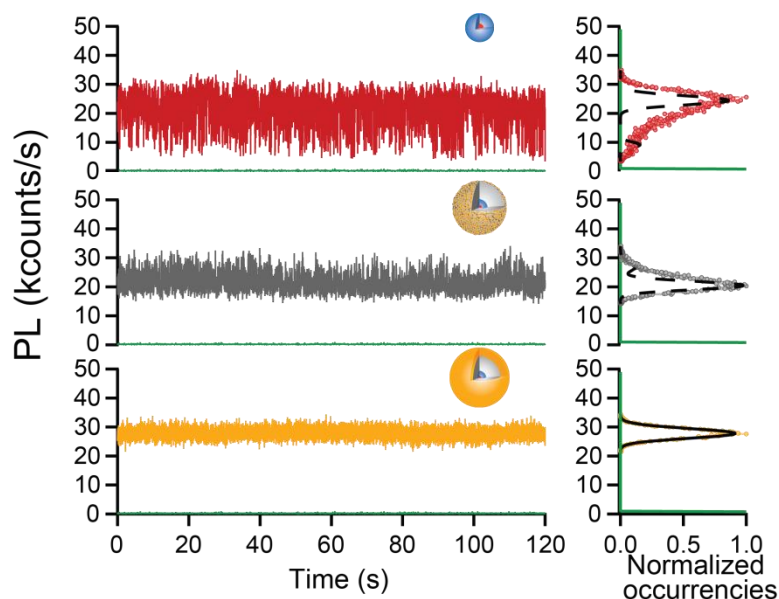


Figure III.50: Left: PL traces of bare QD (red), QD/SiO<sub>2</sub> (grey) and golden-QD. Right: distribution of intensities and comparison to Poisson statistics (black curve).<sup>145</sup>

Therefore, it is interesting to notice that the PL intensity of the bright state of the bare QD and the golden-QD are the same, suggesting no opening of non-radiative channels. The simulation, however, shows that the spherical symmetry of the silica and the gold nanoshell in this golden-QD acts as a lense and focuses the light within the structure, thus increasing the excitation power by a factor of  $\sim 3$ . This increase in excitation is compensated by the emission quantum yield of the plasmonic structure which is around 30%.<sup>176</sup>

#### III.4.7. Increased photostability...

Not only will the gold shell physically improve the optical properties of the QD, it will also act as a protective barrier against degradation.

##### III.4.7.1. ...with time

When observed under UV light, bare QDs tend to bleach. This is due to photooxidation where the combined action of light and oxygen contribute to the formation of an oxide layer around the QD, favoring the formation of surface defects.<sup>74,75,77,177</sup> In the case of golden-QDs, the gold shell acts as a protective barrier against the diffusion of oxygen to the QD. Therefore, even under long illumination, golden-QDs do not bleach.

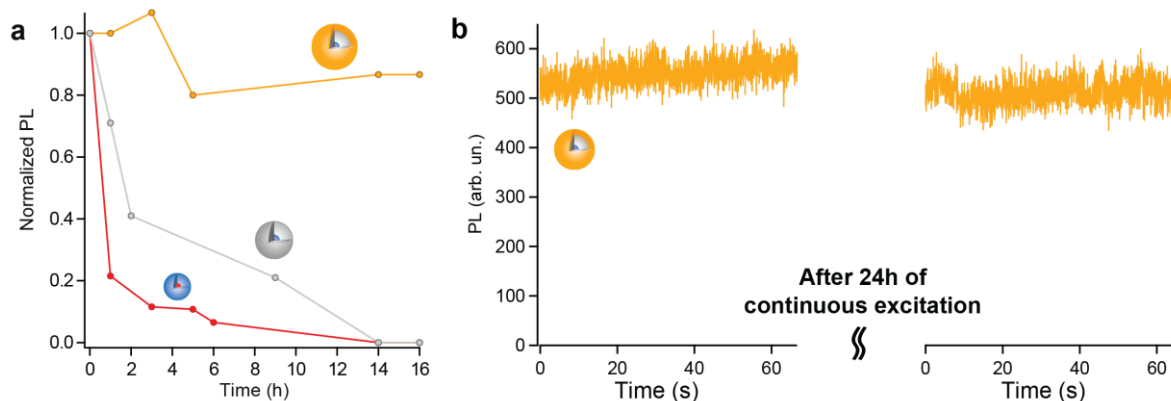


Figure III.51: Evolution of PL intensity with time under continuous excitation. a. average of PL intensity measured on  $\sim 30$  individual QDs, QD/SiO<sub>2</sub> or golden-QDs. b. PL intensity of a single golden-QD.<sup>145</sup>

Around 30 single QDs, QD/SiO<sub>2</sub> and golden-QDs were observed for 16 hours under continuous high power excitation ( $\sim 40$  mW) (Figure III.51). The bare QDs as well as the QD/SiO<sub>2</sub> see their fluorescence decrease within 1 or 2 hours after the beginning of the excitation. On the contrary, golden-QDs remain bright for at least the time of the experiment, *i.e.* 16 hours (except a small decrease at 6 hours attributed to the bleaching of the golden-QDs with an incomplete gold shell). When a single golden-QD was illuminated in the same conditions but for longer time ( $\sim 24$ h), its photoluminescence intensity did not drop and it still shows no blinking, confirming that the gold protects the surface of the QD from oxidation.

#### III.4.7.2. ...with power

The photostability with power at the single particle level was also studied and bare QDs and golden-QDs were compared (Figure III.52). At low excitation powers, in the linear regime, where  $\langle N \rangle < 1$ , both bare QDs and golden-QDs have very similar behavior. However, when the excitation power is increased, bare QDs rapidly saturate and reach a plateau. This is due to the fact that when the excitation is higher, more excitons are created in the QDs. The probability of Auger recombinations is increased, and the PL intensity saturates when Auger recombinations are more favorable than radiative recombinations. If the excitation power increases even further, the PL intensity drops to noise level: the QD is irreversibly degraded and is not luminescent any more.

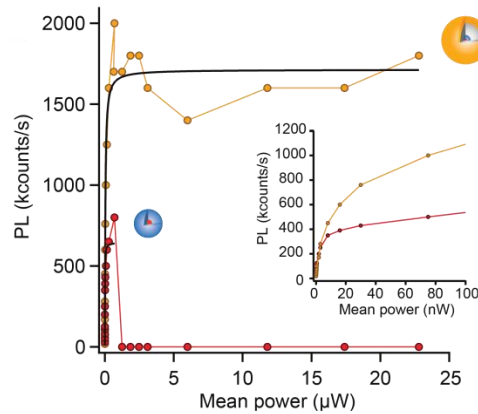


Figure III.52: Evolution of PL intensity with increasing excitation power for individual bare QD and golden-QD. Inset: zoom on low excitation powers.<sup>145</sup>

On the other hand, for golden-QDs, when the excitation power is increased just above the linear regime, the golden-QDs saturate at much higher excitation powers than the bare QDs. Indeed, the Purcell effect speeds up the radiative recombinations of the mono- as well as the multiexcitons. The latter, created at higher excitation power, are therefore still more favorable than Auger non-radiative processes, up to a certain point when Auger processes are faster and the emission saturates. This should be seen on the autocorrelation function where the peak at 0-time delay should be more intense for golden-QDs than for bare QDs (Figure III.53). Indeed, because multiexcitonic recombination is favored, the  $g^{(2)}$  function shows bunching. As this method is commonly used to check if the observed nanocrystal is unique (or acts as a single photon emitter), another strategy has to be developed to ensure that the studied nanoparticle is unique (see III.4.8).

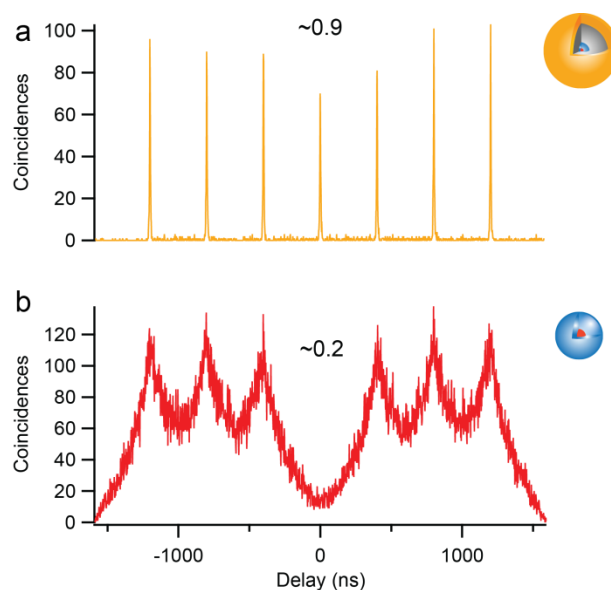


Figure III.53: PL autocorrelation functions for a. golden-QD and b. bare QD. The value above the 0-time delay peak corresponds to the ratio of the area of this peak to the area of the adjacent peaks, and measures the ratio between the biexciton quantum yield and the exciton quantum yield.<sup>145</sup>

Interestingly, even for higher excitation powers, the golden-QDs remain bright, and they do not degrade, emphasizing the protective role of the gold barrier. Golden-QD can withstand powers 10 times higher than bare QDs.

#### III.4.8. Correlative light-electron microscopy

As mentioned before, the usual method to ensure that the studied NC is unique is to measure the  $g^{(2)}$  function. If there is no peak at 0-time delay (antibunching), it means that the particle is a single photon emitter, and is unique. However, the presence of a central peak (bunching) does not necessarily mean that the particle is in a cluster (dimer or more emitters localized at the same position). Indeed, a single particle can have efficient multiexcitonic recombinations, yielding coincidences in the measured counts, forming a central peak in the  $g^{(2)}$ . Therefore, the autocorrelation function does not allow distinguishing between a cluster of single photon emitters or a single particle with multiexcitonic emission.

Golden-QDs are big enough (around 100 nm in diameter) to be seen with scanning electron microscopy (SEM). Therefore, we developed a correlative imaging technique between optical and electron microscope. The golden-QDs were deposited on a glass slide where gold markers were placed by lithography. The optical properties were measured on the confocal setup, the unicity was then checked under SEM. The data corresponding to clusters were discarded, while the data corresponding to unique golden-QD were further analyzed.

The resistance of the golden-QDs after energetic electron beam (a few keV) was checked by observing again the properties under the confocal microscope. The PL intensity as well as the lifetime were not altered proving the resistance of golden-QDs to high power electron beam, opening new perspectives for potential applications.

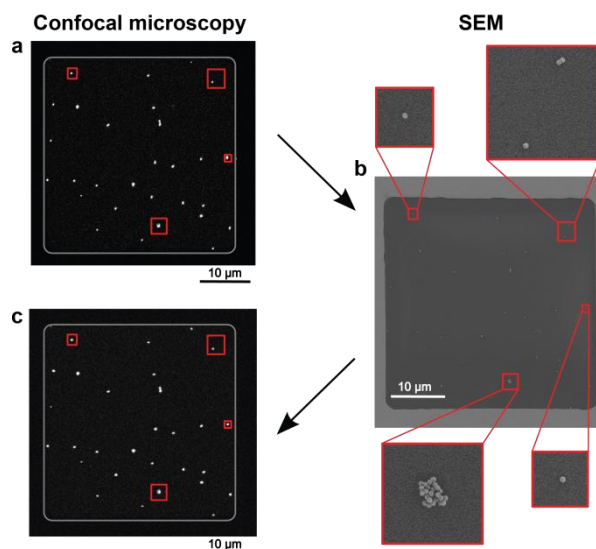


Figure III.54: Scheme of optical and electron correlative imaging of golden-QDs. The optical properties of golden-QDs are measured on a fluorescence confocal microscope (a) and their unicity is checked under SEM (b). The golden-QDs resist e-beam illumination and can be observed again in fluorescence microscopy (c) without modification of their properties.<sup>145</sup>

### III.4.9. Conclusion

With the golden-QDs, it is possible to take full advantage of the coupling between the gold plasmons and the QD excitons, while keeping a nanometer-scale size in a colloidal solution. The processing ease of these structures adds itself up to the improvement of the optical properties. Indeed, when plated with a gold layer, the QDs become non-blinking, their radiative recombination is sped up, and their resistance to degradation with time or with high-energy beams is strongly improved. After the growth of a thick shell that slows down the Auger processes, the golden-QDs open a new way of overcoming non-radiative recombinations by accelerating the radiative recombinations. The model developed with the Institut d'Optique enables to quantitatively predict the efficiency of the Purcell effect depending on the size of the silica spacer or the gold thickness (Figure III.55).

The Purcell factor of 6 reached in this study can be improved as the simulations show a factor of even 100 can be reached (Figure III.55.a). However, this requires very thin gold shells that are currently very difficult to synthesize. Besides, the final PL intensity of the golden-QDs is given by the radiative yield of the plasmonic structure. In the case studied above, this yield was around 30%. Unfortunately, the structural parameters for which to a

Purcell factor reaches a maximum correspond to a very low radiative yield (Figure III.55.b). Thus, increasing the Purcell factor does not necessarily imply a higher radiative efficiency. The parameters chosen for this study seem to be a good compromise between an efficient electromagnetic coupling and a relatively high radiative yield of the final golden-QD structure.

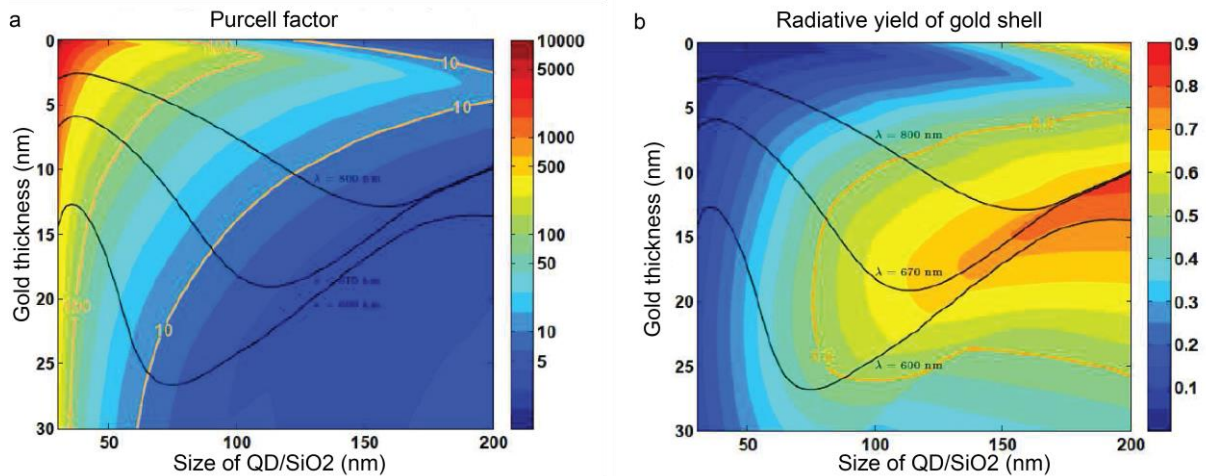


Figure III.55: a. Calculated Purcell factor as a function of size of QD/SiO<sub>2</sub> and gold thickness. b. Calculated radiative yield as a function of size of QD/SiO<sub>2</sub> and gold thickness.<sup>176</sup>

These structures can find applications in local, fluorescent probes resistant to e-beam lithography as well as biology where they can act as fluorescent labels, local thermometers and bimodal targets for imaging and photothermal heating for cell ablation, for example in cancer treatment.<sup>178</sup>

### III.5. Conclusion

Different kinds of nanostructures with QDs have been developed to decrease the blinking of their emission. Although thick-shell CdSe/CdS QDs have their blinking stopped, their emission still flickers between an *on* and an *off* state, and only at cryogenic temperature is the emission completely stable with 100% QY. These drastic conditions limit their use for potential applications, such as display devices or single-particle tracking in biological imaging. Therefore, a new type of CdSe/CdS QDs has been synthesized, with both a thick shell and a composition gradient between the core and the shell (b-QDs). This gradient eliminates Auger recombination sites to yield QDs with completely stable emission at room temperature, and in air. Besides, the QY for the b-QDs is close to unity for both the mono- and the biexciton, and relatively high for multiexcitonic recombinations. A recent work by D. Vanmaekelbergh's group might explain the long lifetimes: this delayed emission might be due to an intermediate trapped state which can block the recombination for several

microseconds. Finally, a hybrid nanostructure consisting in a CdSe/CdS QD surrounded by a gold nanoshell has been developed (golden-QDs). This structure takes advantage of the coupling between the exciton and the gold surface plasmons to speed up the radiative processes (Purcell effect) while conserving the colloidal stability and the nanometric size of the resonator. A Purcell factor of ~3 to 6 has been measured. The golden-QDs efficiently compete out the Auger recombinations yielding structures that do not blink, that have high multiexcitonic efficiencies, whose emission is not affected by long and high excitations and that resist electron beam exposure. However, the gold nanoshell reabsorbs some of the QD emission decreasing the overall quantum yield to ~30%. These hybrid structures are interesting for biological probing, bimodal imaging, local temperature probe or for photothermal heating.<sup>178</sup>



## Chapter IV. Spectroscopic studies of thick-shell CdSe/CdS nanoplatelets

In 2008, S. Ithurria developed a protocol to synthesize two-dimensional structures called nanoplatelets (NPLs, see I.6). The first NPLs synthesized were CdSe<sup>41</sup>, followed by CdTe and CdS.<sup>130</sup> New heterostructures were then developed: core/shell NPLs<sup>131,133</sup> or core/crown NPLs.<sup>80</sup> The first spectroscopic studies of CdSe NPLs, core/shell (described in IV.2 and IV.3) and core/crown NPLs have been performed by Mickaël Tessier.

The syntheses of NPLs allow for a perfect control of their thickness. Due to confinement effects, the optical properties are defined by the thickness, giving the NPLs unique properties such as very narrow emission.

### IV.1. Synthesis of nanoplatelets

#### IV.1.1. Synthesis of CdSe NPLs

The protocol for the synthesis of CdSe NPLs is derived from the protocol one-pot synthesis of CdSe QDs.<sup>99</sup> A mixture of 16 mL of ODE, 0.3 mmol of cadmium myristate and 0.15 mmol of selenium powder was degassed under vacuum at room temperature for 30 min and heated under argon flow up to 240°C. During the heating, around 203°C, when the solution becomes orange, an excess (typically 50 mg) of cadmium acetate dihydrate is added. The solution is then annealed for 12 minutes, cooled down. This synthesis forms QDs as well as NPL of different thicknesses that need to be separated thanks to size-selective precipitation in EtOH.

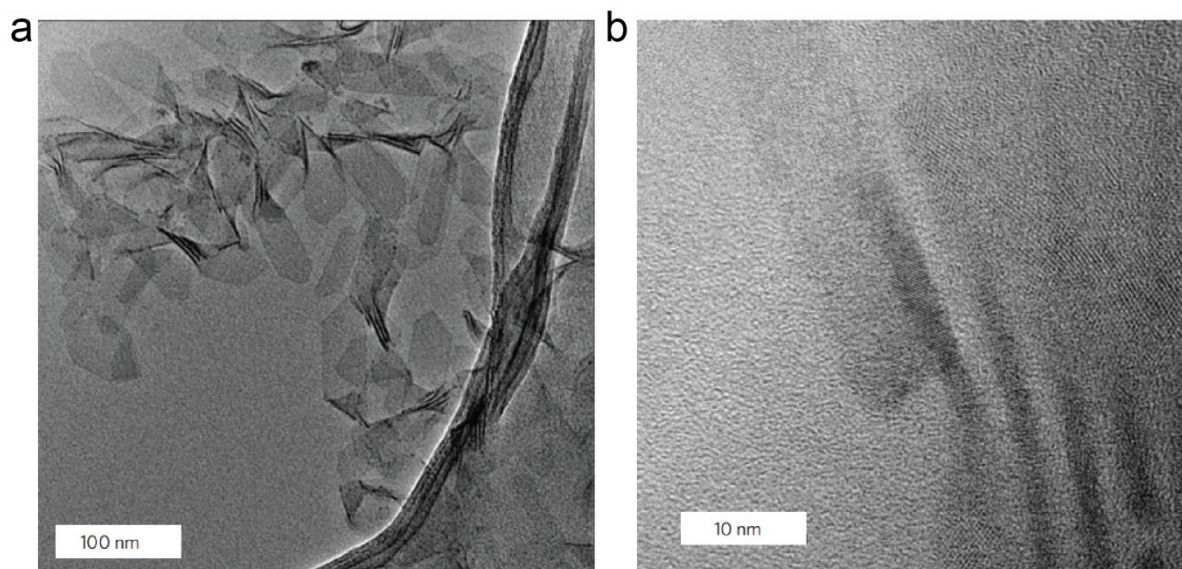


Figure IV.1: TEM images of a. 5-monolayer-thick CdSe NPLs and b. 6-monolayer-thick CdSe NPLs standing of their edge.<sup>130</sup>

The short chain acetate ligands are necessary for the formation of NPLs. There are two main hypotheses as to the formation mechanism: either small NPLs-like particles (NPLs seeds) are formed and they attach together to form larger NPLs (see Figure IV.2, pathway 1 and 3), or these seeds grow through precursor reaction to form NPLs (see Figure IV.2, pathway 2). This second pathway seems consistent with the experimental results.<sup>179</sup> Indeed, the fact that the continuous injection of precursors allows the lateral extension of NPLs<sup>127</sup> without any secondary nucleation suggests that the formation follows the continuous growth of NPLs seeds rather than the formation of new NPLs seeds (which would be visible with TEM as smaller NPLs).

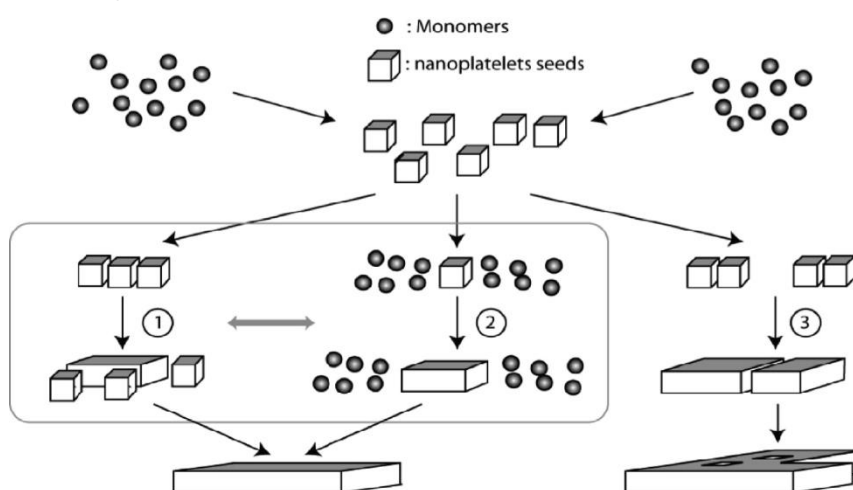


Figure IV.2: Different pathways for the formation of nanoplatelets.<sup>179</sup>

## IV.1.2. Synthesis of CdSe/CdS core/shell NPLs

Several strategies have been developed to synthesize core/shell NPLs at room temperature.

The continuous growth method consists in mixing the precursors together and let them react to form a shell on top of the CdSe NPLs. Typically, a solution of  $2 \cdot 10^{-2} \text{ mol} \cdot \text{L}^{-1}$  CdSe NPLs is diluted in 4 mL chloroform. 1.33 mmol of thioacetamide are added, the solution is sonicated, and 350  $\mu\text{L}$  of cadmium nitrate and 150  $\mu\text{L}$  of zinc nitrate dissolved at 0.2 M in ethanol are added. The reaction is left under magnetic stirring for 24h. A similar protocol can be used to grow CdS-only shell but the growth is inhomogeneous. The addition of 30% Zn smoothens the shell to form almost uniform CdSe/CdZnS core/shell NPLs.<sup>131</sup>

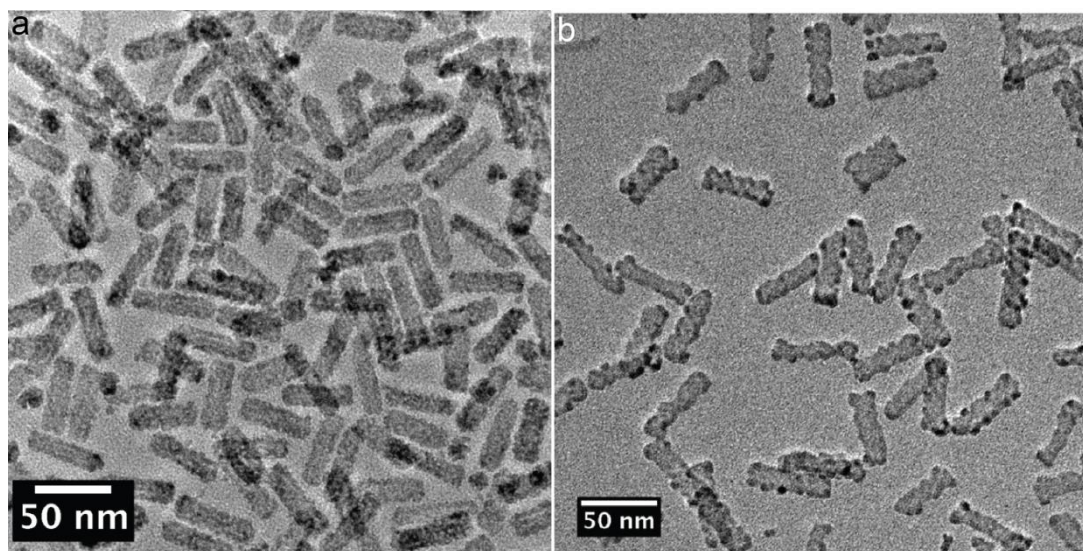


Figure IV.3: TEM image of a. CdSe/CdZnS NPL and b. CdSe/CdS NPL grown by the continuous growth method.<sup>131</sup>

The layer-by-layer method consists in growing the shell by depositing one layer after another, similarly to the SILAR method (described in I.4.5.3), but at room temperature (called colloidal atomic layer deposition, c-ALD). Typically, a solution of  $2 \cdot 10^{-2} \text{ mol} \cdot \text{L}^{-1}$  CdSe NPLs in hexane is mixed with 500  $\mu\text{L}$  N-methylformamide to form a biphasic solution. An excess ( $\sim 10 \mu\text{L}$ ) of 40% aqueous solution of sodium sulfide  $\text{Na}_2\text{S}$  is added to deposit the first layer of sulfur. The NPLs are transferred into the polar formamide phase which is washed with hexane. The NPLs are precipitated with acetonitrile, redispersed in N-methylformamide. 30  $\mu\text{L}$  of 0.1M cadmium acetate solution in N-methylformamide is added for the Cd to react with the S and form the first CdS layer. The solution is washed with toluene, and the NPLs are redispersed in N-methylformamide. These steps are repeated as many times as necessary to grow a CdS shell of wanted thickness.<sup>131,133</sup>

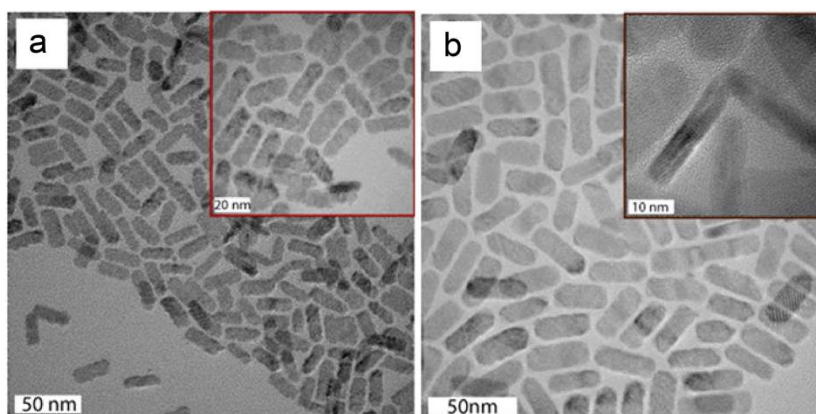


Figure IV.4: TEM images of a. CdSe/CdS (4 monolayers of CdS) NPLs and b. CdSe/CdS (7 monolayers of CdS) NPLs grown by c-ALD.<sup>133</sup>

## IV.2. Optical properties of CdSe nanoplatelets

### IV.2.1. Photoluminescence

One of the most interesting optical properties of NPLs compared to spherical QDs is their narrow emission spectrum. For CdSe QDs, the typical FWHM is around 25 nm for the PL spectrum, while it is below 10 nm for CdSe NPLs. When studied at the single-particle level, the width of the spectrum is similar than for the ensemble measurement, which proves the homogeneity of the NPLs in ensemble: their properties are defined by their thickness which is perfectly controlled for all the NPLs, yielding PL spectra without any inhomogeneous broadening (Figure IV.5.a).<sup>180</sup>

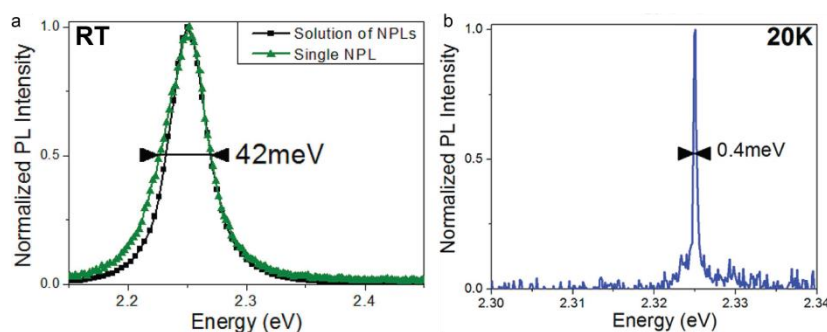


Figure IV.5: a. Comparison of PL spectra at room temperature of an ensemble and of a single CdSe NPL. b. PL spectrum of a single CdSe NPL at 20K.<sup>180</sup>

When studied at cryogenic temperature, the width of the PL spectrum of a single NPL decreases even more to reach  $\sim 0.1$  nm (0.4 meV at 2.32 eV) (Figure IV.5.b). This narrowing is due to the decreased interaction between the exciton and the phonons at 20K.<sup>180</sup> For an ensemble of NPLs studied at cryogenic temperature, the spectrum is broader, around 15 meV. This might be due to spectral shifting and Stark effect: the surface sites are not all passivated by ligands, and form traps for charge carriers. This trapped charges will change the electromagnetic field in the surrounding of the NPL, changing the energy level positions.<sup>51</sup> On an ensemble of NPLs, this will cause the broadening of the emission peak as not all the NPLs emit at the same energy.

#### IV.2.2. Time-resolved photoluminescence

Another interesting property of NPLs compared to QDs is their rapid decay time. Indeed, when studied at room temperature, CdSe NPLs show a PL decay lifetime of  $\sim 15$ -20 ns, slightly shorter than that of CdSe QDs, but when the temperature is decreased to 20K, CdSe QDs enter their dark-exciton state and show lifetimes up to  $1\mu\text{s}$ .<sup>181</sup> NPLs, on the other hand, show a PL decay lifetime that decreases at cryogenic temperature to approximately 200 ps (Figure IV.6).<sup>180</sup> This is concomitant with an increase of the PL intensity compared to studies in air, attributed to the thermal activation of non-radiative processes.<sup>182</sup> Both these observations suggest that when the temperature is decreased, the radiative lifetime shortens. This is probably due to giant-oscillator strength that is favored when the binding energy of the exciton is high, which is the case for NPLs compared to QDs.<sup>130</sup>

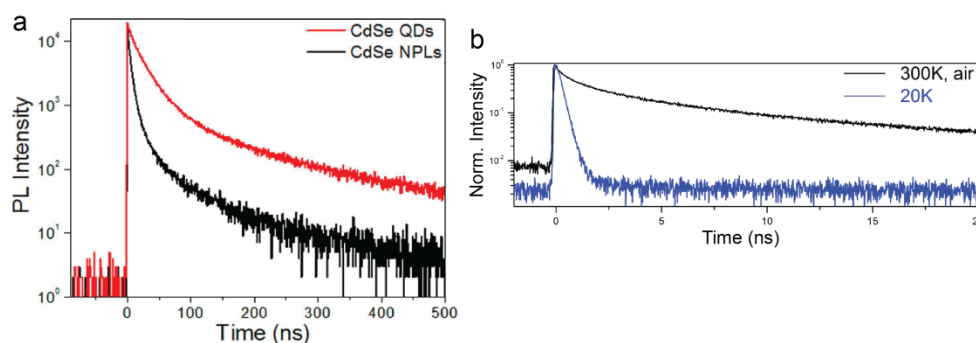


Figure IV.6: a. Comparison between PL decay of an ensemble of CdSe QDs and NPLs. b. PL decay of the same single CdSe NPL at room temperature and at 20K.<sup>180</sup>

#### IV.2.3. Blinking behavior

As the radiative lifetime gets shorter at cryogenic temperature, this should play a major role on the blinking behavior of these CdSe NPLs.

Indeed, at room temperature, when single NPLs are studied, their PL traces show intense blinking behavior similar to the one found in bare CdSe QDs (see I.5.2). However, when the temperature is decreased, the lifetime of NPLs shortens along with the increase of their PL intensity, which suggests a strong reduction of non-radiative recombinations at lower temperature. This should be seen on the PL trace by a reduction of blinking. Indeed, at 20K, the trace is stable (Figure IV.7).

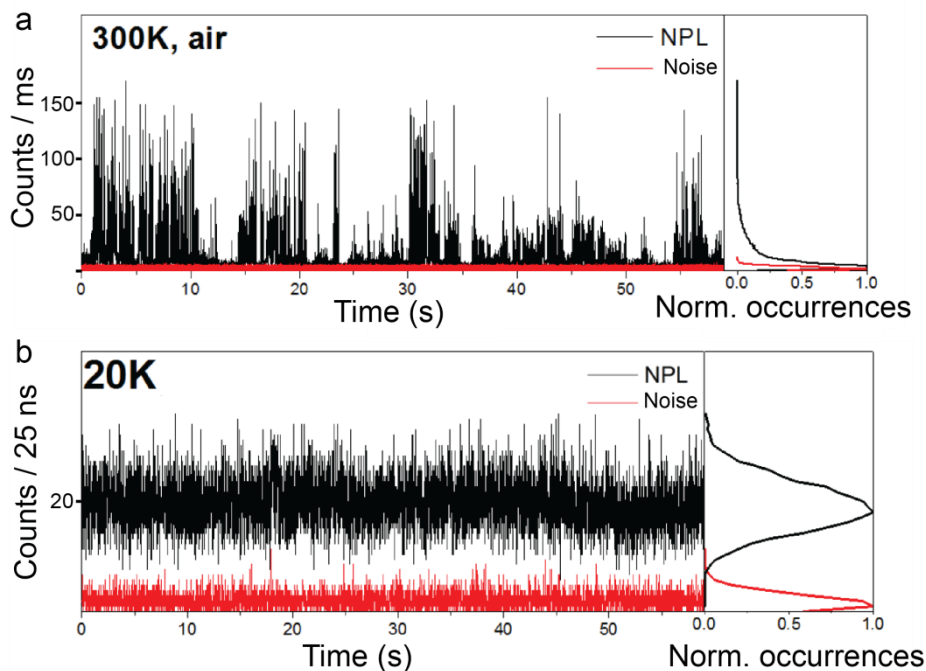


Figure IV.7: PL trace for a single QD at a. room temperature and b. 20K.<sup>180</sup>

### IV.3. Optical properties of CdSe/CdZnS core/shell nanoplatelets synthesized at room temperature

As for the QDs, growing a shell of CdSe NPLs improves their optical properties, starting with their QY which increases from 30% for CdSe NPLs to 60% for CdSe/CdZnS NPLs.

#### IV.3.1. Photoluminescence

After the deposition of a CdZnS shell on a CdSe NPL, the emission peak is shifted towards the red (Figure IV.8). This is due to the fact that the confinement of the exciton is decreased as the electrons are delocalized in the CdZnS shell, similarly to what happens in

CdSe/CdZnS QDs. However, the shift is larger for NPLs than for QDs, probably because the initial system is much more confined (only 4 or 5 monolayers of CdSe) than CdSe QDs.

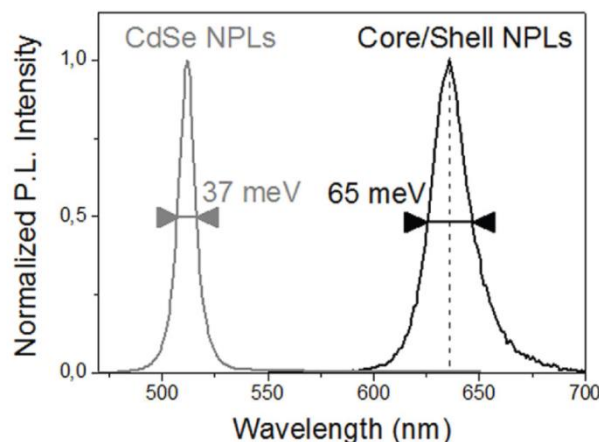


Figure IV.8: PL spectra of ensembles of CdSe and CdSe/CdZnS NPLs.<sup>183</sup>

Another observation is that the PL spectrum broadens after the addition of the shell (Figure IV.8). It remains, however, narrower than the PL spectrum of core/shell QDs (20 vs 30 nm). This has also been observed on QDs, and might be explained by the more efficient coupling to the phonons in CdZnS (where electrons are delocalized) than in CdSe. Indeed, the FWHM of the CdS emission peak is larger, confirming the more efficient coupling between the exciton and the phonons. The CdSe/CdZnS NPLs have a FWHM between the one of CdSe and that of CdS (Figure IV.9).

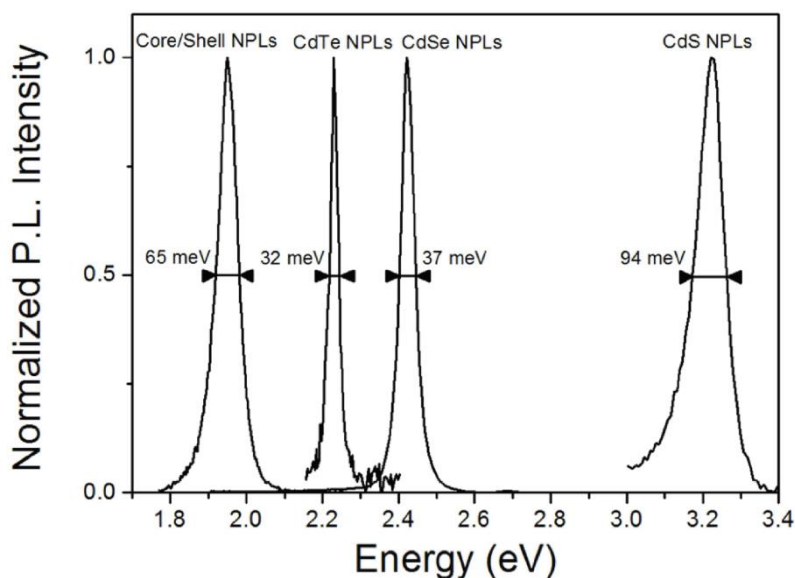


Figure IV.9: PL spectra of different NPLs at room temperature.<sup>183</sup>

Compared to single-particle measurements, the PL spectra of an ensemble of CdSe/CdZnS NPLs is not broader, showing that the shell growth protocol yields homogeneous core/shell NPLs.

The PL spectrum of CdSe/CdZnS NPLs shows some asymmetry at low energies at room temperature, but it becomes especially visible at low temperatures (Figure IV.10). This asymmetry is due to the filling and emission of traps at lower energies than the band edge. At room temperature, the emission comes from the band edge and gives a symmetric peak, but at low temperature, the thermal energy is not sufficient to free the charges that are trapped, and a strong emission at lower energies appears. This emission happens at longer lifetimes than the emission at the peak maximum, confirming it originates from traps, most probably interfacial traps between the core and the shell.<sup>183</sup>

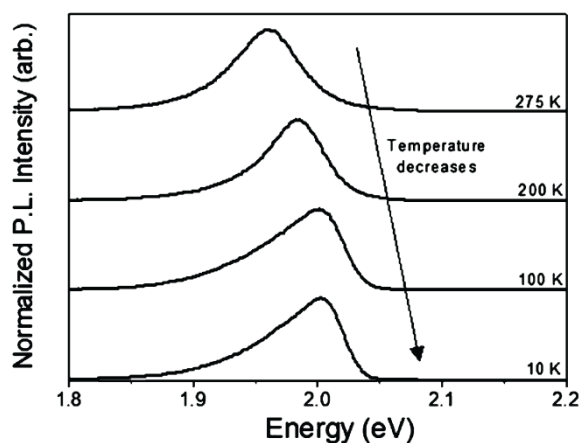


Figure IV.10: Evolution with temperature of PL spectra of an ensemble of CdS/CdZnS NPLs.<sup>183</sup>

#### IV.3.2. Time-resolved photoluminescence

As it might be expected, and similarly to CdSe/CdZnS QDs, the lifetime is higher in CdSe/CdZnS NPLs (~50 ns) compared to CdSe NPLs (~15 ns).<sup>183</sup> This is due to the delocalization of electrons in the shell which decreases the overlap of electron and hole wavefunctions, increasing their recombination time. This is further confirmed at cryogenic temperature where CdSe/CdZnS NPLs have a lifetime of around 10 ns compared to 300 ps for bare CdSe.

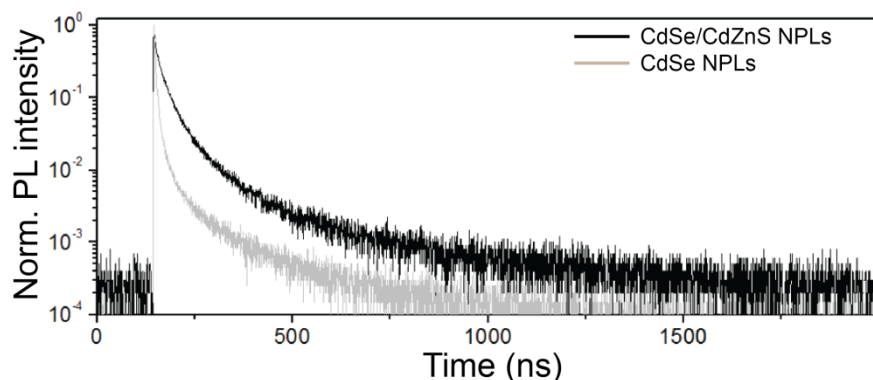


Figure IV.11: PL decay of CdSe and CdSe/CdZnS NPLs at room temperature.<sup>183</sup>

### IV.3.3. Blinking behavior

The deposition of a shell on CdSe QDs decreases their blinking due to a worse access to the surface where Auger recombinations are favored. A similar effect can be seen of CdSe NPLs where the addition of a CdZnS shell decreased the blinking (Figure IV.12.a). The effect is not as obvious with a CdS shell for which the PL trace still flickers a lot. This difference might be due to a worse deposition of the shell, or, for the charges, an easier access to the surface.

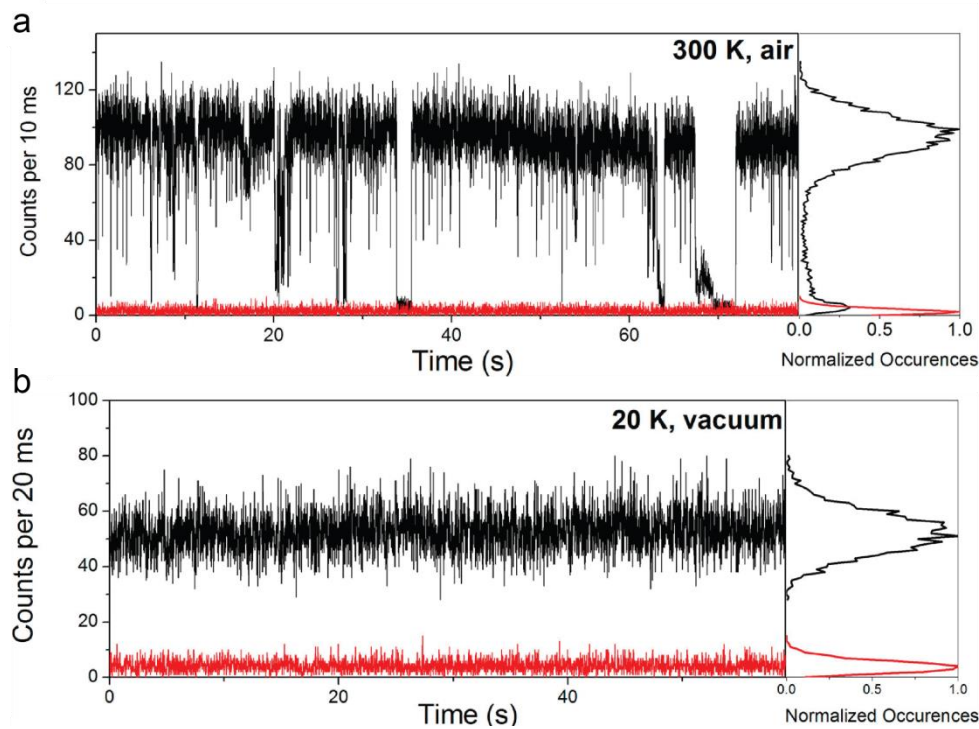


Figure IV.12: PL traces of individual CdSe/CdZnS NPLs at a. room temperature and b. 20 K.<sup>183</sup>

However, when the CdSe/CdZnS NPLs are studied at 20K, their PL trace is stable and does not fluctuate with time: the shell increases the radiative lifetime and suppresses the blinking of NPLs (Figure IV.12.b).

#### IV.4. Optical properties of new generation of core/shell nanoplatelets

Earlier this year was developed in the lab a new synthesis of core/shell NPLs. This synthesis is robust, easy to implement and versatile as it can be used to grow CdS, ZnS or CdZnS shells on CdSe NPLs.

This new synthesis method allows the growth of a thick shell of CdS on CdSe NPLs. This has been proven efficient in the case of spherical QDs to suppress the blinking behavior.

As seen on the TEM and EDX mapping pictures in Figure IV.13, the growth of the CdS shell is homogeneous on the CdSe shell. Several shell thicknesses can be grown, from 1 to 8 nm, yielding different optical properties.

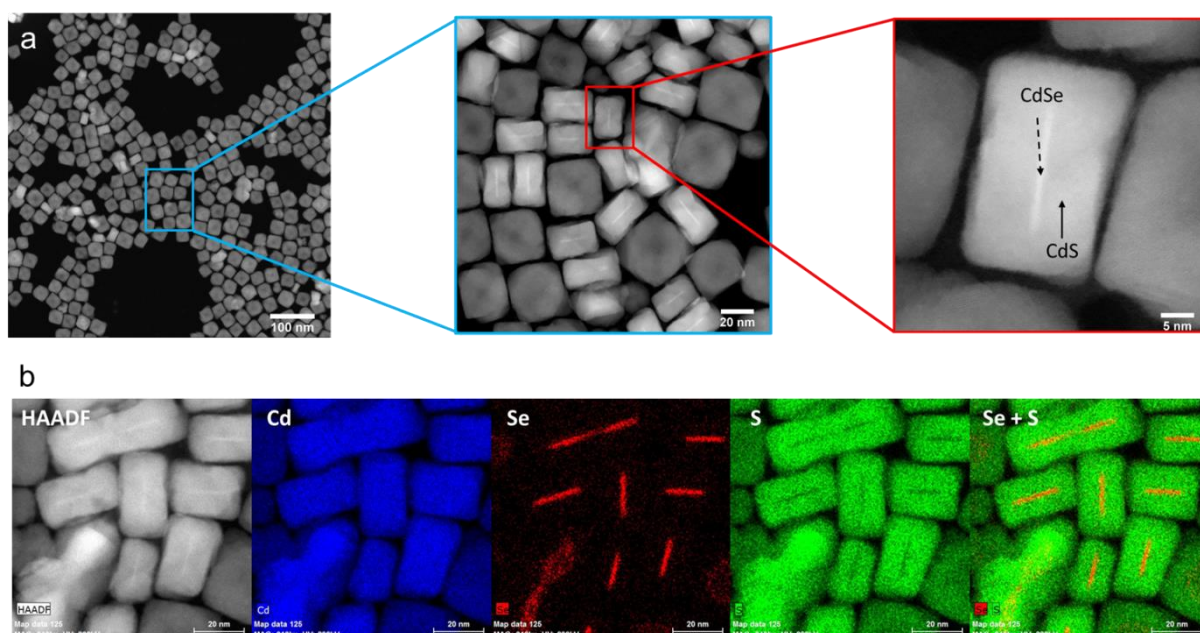


Figure IV.13: a. HAADF TEM images of thick-shell CdSe/CdS NPLs synthesized with the new protocol. b. EDX mapping of a thick-shell CdSe/CdS NPL showing the localization of Cd, Se and S.

When the PL traces of NPLs with different shell thicknesses are observed, the blinking decreases when the shell thickness increases (Figure IV.14). This is due, similarly to

spherical QDs, to a delocalization of charges that increases the Auger recombination lifetime which starts competing with the radiative recombination lifetime, yielding non-blinking NPLs. Interestingly, when the PL decay is measured for the non-blinking thick-shell CdSe/CdS NPLs, it can be fitted by a monoexponential curve (Figure IV.15.b) which suggests that only one radiative recombination process happens. Indeed, in spherical QDs with thick CdS shell, two lifetimes could be extracted corresponding to the recombination of neutral and charged exciton. Here, as only one lifetime is characteristic of the recombination phenomenon, the exciton is either charged or neutral, but does not switch between the two charge states.

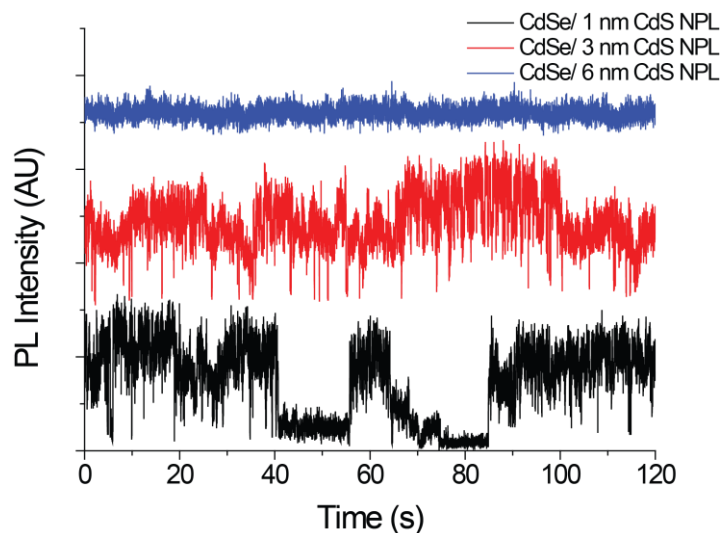


Figure IV.14: Traces of CdSe/CdS NPLs with different shell thicknesses. AY-offset has been applied.

In order to determine the charge state of the exciton, PL intensity and decay measurements were performed under vacuum. In these conditions, the NPLs should remain charged, and the exciton is a trion carrying, in the case of CdSe/CdS, a negative charge. Under vacuum, the PL intensity drops, but remains non-blinking, and the lifetime decreases from  $\sim 10$  ns to  $\sim 2.5$  ns. This suggests that the NPLs are charged and that the recombinations come from a trion, *i.e.* a charged exciton: it would explain the decreased lifetime as well as the decreased PL intensity as non-radiative recombinations compete with radiative recombinations. This in turn suggests that in air, the NPLs were neutral, and that the  $\sim 10$  ns lifetime corresponds to the neutral exciton.

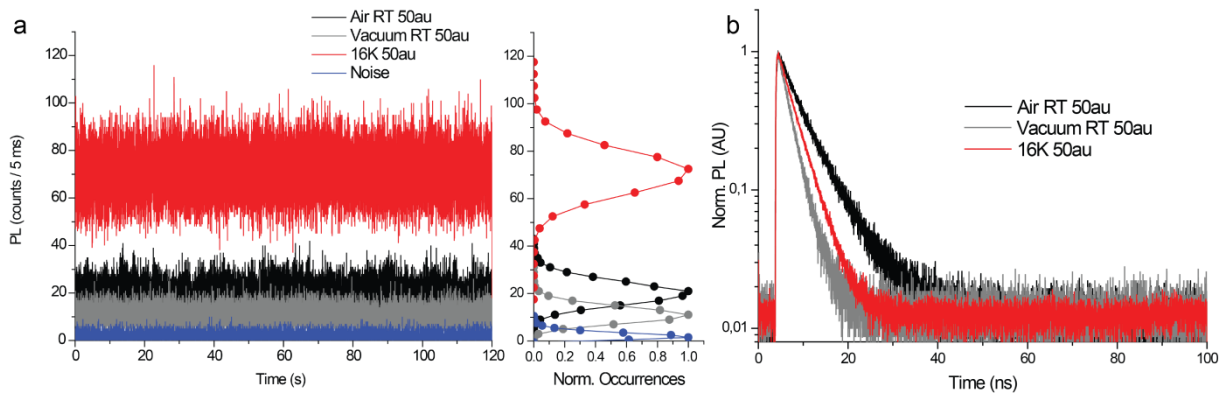


Figure IV.15: a. PL traces of a single thick-shell CdSe/CdS NPL in air, under vacuum and at 15 K, at the same excitation power. b. PL decay measurement of a single thick-shell CdSe/CdS NPL in air, under vacuum and at 15 K, at the same excitation power.

It has been shown that for spherical CdSe/CdS QDs, the QY of the neutral state is at 100%.<sup>15</sup> Thus, we might wonder if this is also the case for NPLs. Studies at cryogenic temperature show that the PL intensity of the NPLs increases, which is expected due to the fact that the excitons are now confined in the core and cannot reach the surface anymore where Auger recombinations are favored. However, the PL intensity reaches higher values than in air for the same excitation power. Thus, the QY in air could not have been 100%.

Which mechanism could therefore explain that in air, the QY is not at 100% for neutral NPLs but no blinking is observed? This might be due to the fact in NPLs, the excitons do not behave the same way as in QDs. Indeed, due to the confinement in one dimension, the binding energy is much stronger, and the NPLs can be fully considered as colloidal quantum wells. It is thus possible to form several excitons inside the NPLs in the same state (ground state in this case) as they evolve independently from each other. Thus, even when an NPL is neutral, it can contain several excitons that favor Auger recombinations. The PL intensity under vacuum is decreased as Auger recombination with an excess charge happens at the same time as this inter-exciton Auger process. Finally, at low temperature, the radiative recombination of the exciton is favored as the charges cannot reach the surface traps, and as the movement of the whole crystalline structure is slowed down, the inter-exciton Auger process is also limited, increasing the PL intensity.

Another explanation could be B-type blinking (see I.5.2.2).<sup>117</sup> Indeed, if the hot carriers are trapped before they relax to the band-edge, no photon is emitted. This however does not affect the emission dynamics of radiative recombinations. Thus, if there is a competition between radiative recombinations and the trapping of excitons in the NPLs before they relax to their ground state (which happens at very short time scales), only one lifetime can be measured corresponding to the radiative recombination, while the PL intensity is averaged

over several ms and shows no blinking. The traps seem to be localized at the surface of the NPLs as the emission intensity is higher when they are excited in the core (at 550 nm) than in the shell (405 nm; preliminary results). Besides, the measured lifetime is longer when the NPLs are excited in the core than in the shell, indicating probably some non-radiative pathways involving the surface of the NPLs that decrease the QY (Figure IV.16).

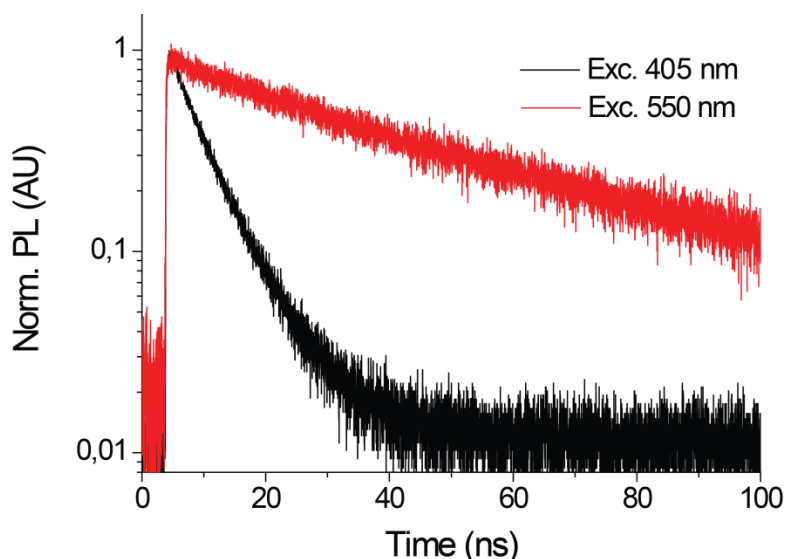


Figure IV.16: PL decay measurements for thick-shell CdSe/CdS NPLs at different excitation wavelengths.

An excitation in the CdSe at 550 nm gives longer recombination dynamics (~30-50 ns) than an excitation in the CdS at 405 nm (~10-15 ns). While exciting in the core, the recombination dynamics corresponds to the recombination of a 'free' exciton as charges do not reach the surface where Auger processes are favored. When exciting in the shell, the surface is accessible, and Auger processes favored, introducing some non-radiative recombinations pathways which decrease the measured lifetime.

Although more studies need to be performed, the low-temperature measurements show that the peak becomes asymmetric at low temperature, with a tail in the red wavelengths (Figure IV.17). This might be explained by a similar explanation than for the core/shell NPLs synthesized at room temperature: this low-energy emission might come from traps that get filled when the temperature decreases.

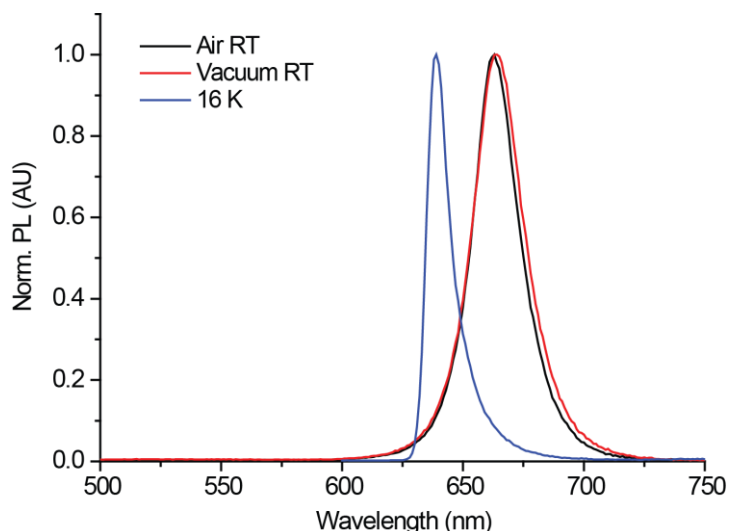


Figure IV.17: Ensemble PL spectra of CdSe/CdS NPLs in air, under vacuum and at cryogenic temperature.

Finally, at 16K, these NPLs show no blinking even at high excitation powers, proving that Auger recombinations in those structures is less probable. However, when the excitation power increases, the PL intensity increases at first, but then saturates, which might be due to multiexcitons recombining non-radiatively, or a saturation of the photodiodes used for the detection of emitted photons (they have a blind time of 80 ns, which means that once they receive a photon, they cannot detect a second one before 80 ns).

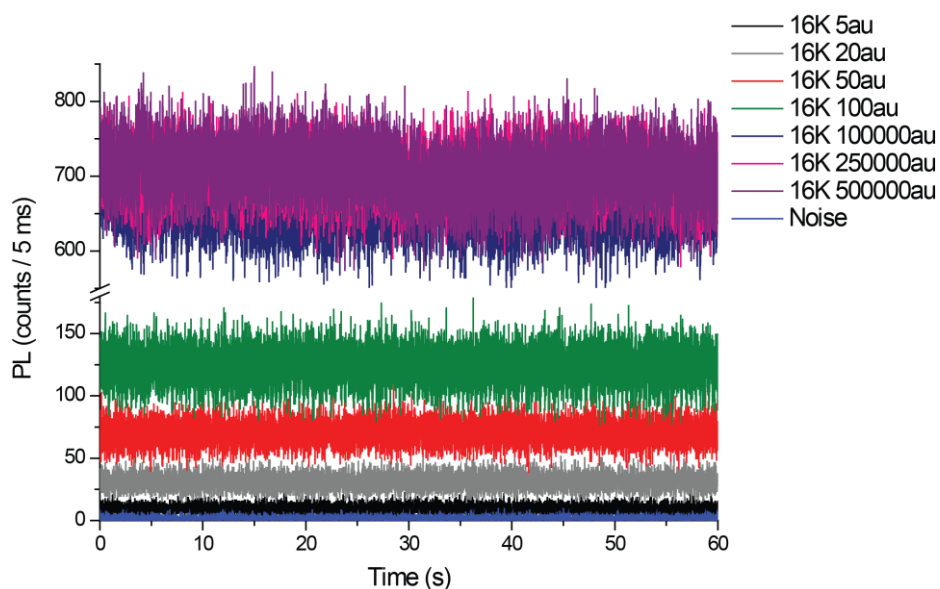


Figure IV.18: PL traces of a single thick-shell CdSe/CdS NPL at increasing excitation power at 16K.

## IV.5. Conclusion

The development of two-dimensional semiconducting nanocrystals (nanoplatelets) gave rise to emitters with interesting optical properties: narrower emission band compared to spherical QDs, shorter lifetime, stronger oscillator strength... However, the syntheses of core/shell NPLs were limited to room temperature where the CdSe cores did not undergo degradation. The development of a new synthesis allows the fine control of the shell growth, limits the crystalline defects and yields NPLs with stable emission trace at room temperature and in air. Additional experiments need to be performed to better understand the role of traps in these systems: transient absorption might give information on the dynamics of charge relaxation, studies under magnetic field might inform on the nature of the charges present in the NPLs, recombination-dynamics dependence on the excitation or emission wavelength need to be more thoroughly studied to learn about the localization of traps... However, these preliminary results show that these new NPLs are very promising in multiple domains such as displays or for optoelectronic applications.



## Chapter V. Quantum Dots as probes for biological imaging

The study of model biological systems, such as HeLa cells, *C. elegans* worms, mice, pigs or macaques brings crucial information on very different and essential physiological activities of organisms: metabolism, the way an organism functions, how each mechanism is triggered or what causes a disease to spread. These model systems are tools to study and collect information and knowledge before extending them to humans.

### V.1. Fluorescent probes for biology

Imaging of biological samples has been revolutionized by the discovery, in the 1960s, and the ability to clone the green fluorescent protein (GFP) in the 1990s.<sup>184</sup> The sequence coding for GFP can be inserted selectively in the DNA sequence, making it possible to mark only the endogenous proteins of interest. The maximum of the emission of GFP is around 500 nm, and its quantum yield reaches around 75%. Other fluorescent proteins have been synthesized later to cover a wider range of emission wavelengths.<sup>185</sup> Most of the probes used currently are organic fluorescent proteins or fluorescent molecules (Figure V.1) which can either be expressed endogenously or can enter the organism by several methods: *in vivo* injection, *in cellulo* micro-injection, electroporation, endocytosis...

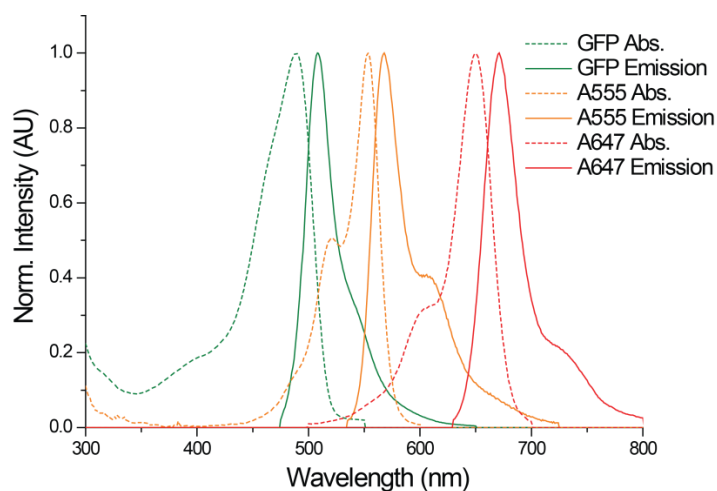


Figure V.1: Examples of absorbance (Abs.) and emission spectra of different fluorophores: GFP, Alexa 555 and Alexa 647.

Fluorescent organic molecules are particularly easy to use due to the fact that they are only a few nm in size, they can be easily manipulated, coupled to other molecules, and, in the case of proteins, they are made of organic molecules present in the organism (amino acids) and therefore by definition biocompatible. Lately, with the development of Quantum Dots, inorganic probes have emerged as a complementary tool for biological imaging. They solve several of the problems encountered with organic dyes such as poor photostability or the overlap between their excitation and their emission spectra.

## V.2. Quantum Dots vs organic fluorophores

In order to be used for fluorescence biological imaging, a labeling probe has to fulfill several criteria:

- it needs to be biocompatible (which includes being soluble in the appropriate buffer) and non-toxic, and in a general manner, it should exhibit a limited interplay with the organism by limiting non-specific interactions,
- both its excitation and emission wavelengths should be adapted to the biological sample so that the signal-to-autofluorescence ratio is good enough for unambiguous detection. Obviously, brighter probes have higher ratio.
- it needs to bear functional groups for targeting of specific molecules in the organism
- its size has to be suitable to access the region of interest, to be able to reach the target, and not to disturb the metabolism.

Both the organic dyes and the Quantum Dots, though to different extents, fulfill these criteria and can be used for biological imaging. Quantum Dots however show interesting optical properties that allow to overcome most of the issues met with organic dyes.

### V.2.1. Photobleaching

The mechanism of photobleaching in organic fluorophore is still under investigation:<sup>186</sup> after several seconds of excitation, the fluorescence of organic dyes drops to finally completely bleach.

In QDs, the oxidation of the surface species (selenium for example<sup>74,75,89,187</sup>) leads to the formation of defects (dangling bonds at the surface) that decrease the quantum yield. This surface oxidation is favored by UV illumination, but can be strongly reduced by the growth of a shell on the core (e.g. CdSe/ZnS) that passivates the dangling bonds and decreases the number of defects at the core surface. These well passivated QDs are thermally and photochemically stable, and this over a period of time long enough to perform biological imaging (Figure V.2).<sup>188,189</sup>

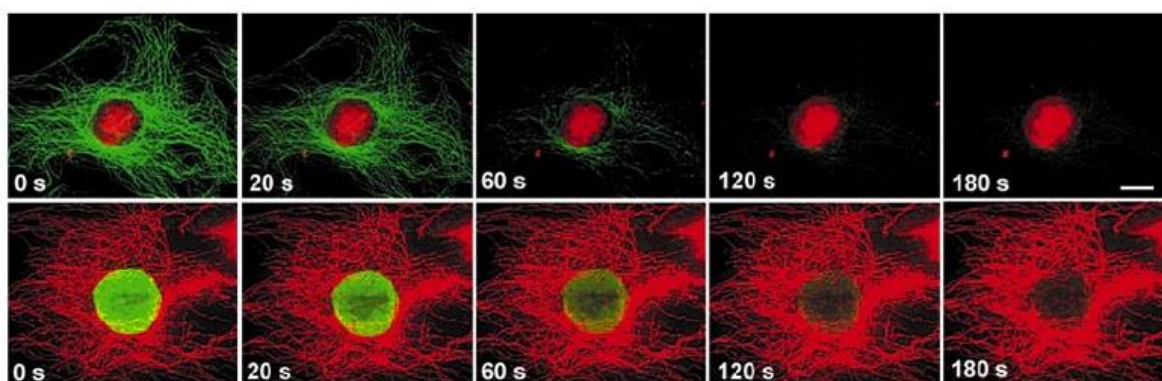


*Figure V.2: Compared photobleaching of Alexa488 (in green) and QDs (in red). Top row: QDs label nuclear antigens and Alexa488 label microtubules. Bottom row: QDs label microtubules and Alexa488 label nuclear antigens. QDs are much more resistant than Alexa488 to continuous exposure to 100-W-mercury-lamp excitation light.<sup>190</sup>*

### V.2.2. Excitation and emission ranges

The existing organic fluorescent dyes emit over a wide range of emission wavelengths. QDs cover an even larger range (especially in the infrared region) and present additional advantageous features: for example, a wide range of wavelengths can be covered by only one type of material, solely by varying on its size (Figure V.3).

Compared to organic dyes, QDs also have larger molar absorption coefficients for similar emission quantum yields in the visible range. The difference is more obvious in the

near-infrared (NIR) range, the QY of organic dyes is very low in this wavelength domain (12% for Alexa750<sup>189</sup>), when certain QDs can reach 40% (CuInSe<sub>2</sub>/ZnS)<sup>191</sup> to 70% for PbS or PbSe QDs,<sup>189</sup> making them excellent candidates for medical imaging in the so-called NIR therapeutic window (Figure V.4).<sup>189</sup>

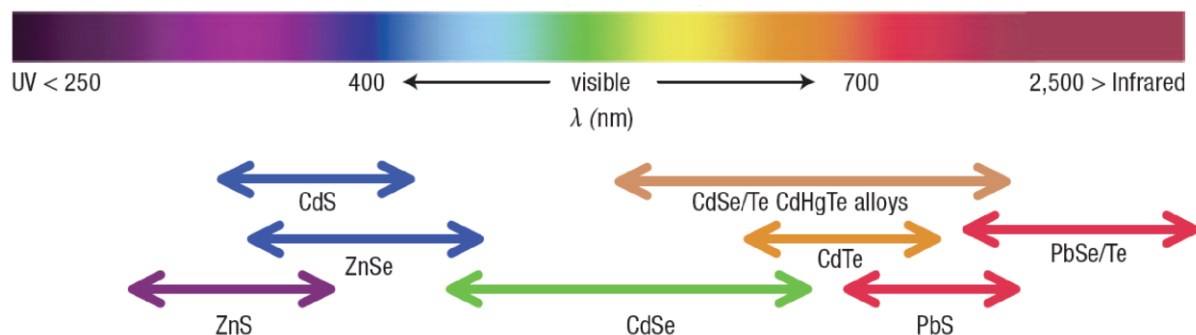


Figure V.3: Representative emission wavelength domains of QD cores of different materials, according to their size and chemical composition.<sup>192</sup>

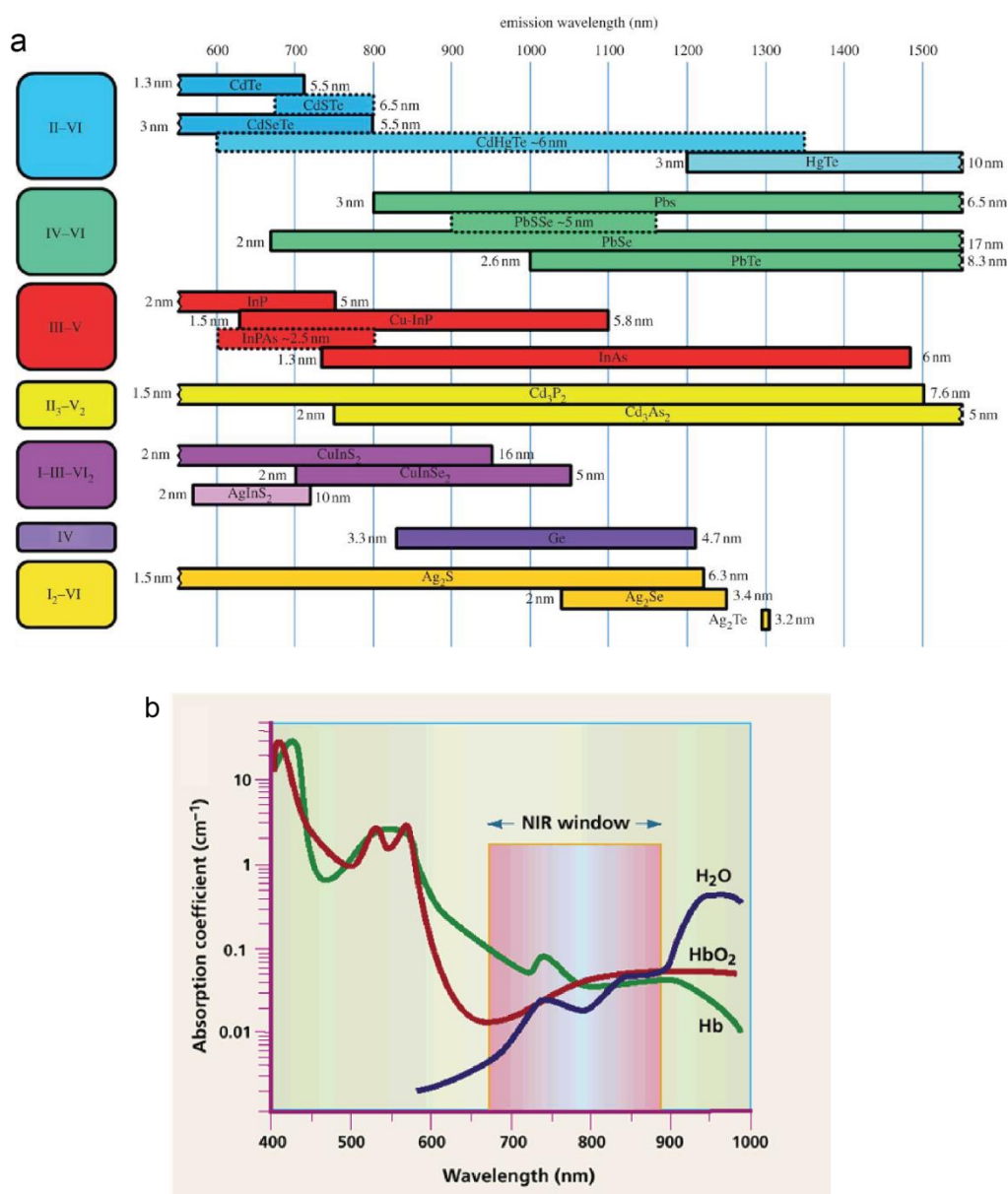
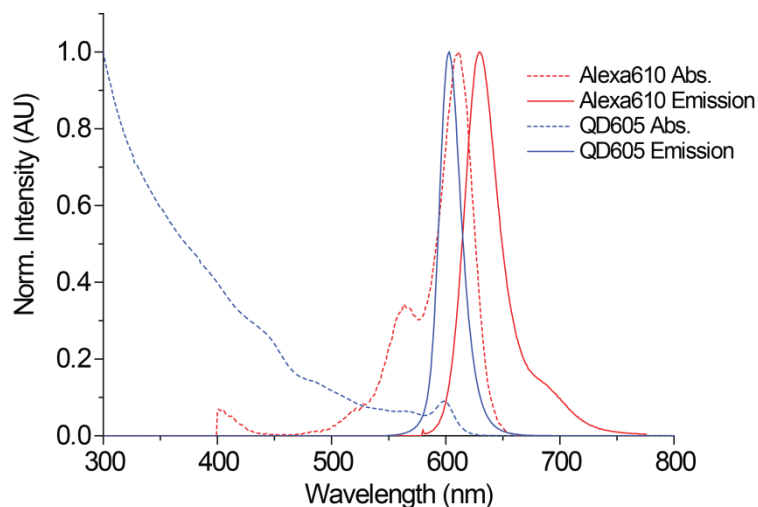


Figure V.4: a. Emission wavelength domains of NIR-emitting QDs, according to their size and chemical composition. b. Absorption spectra of water, oxyhemoglobin and deoxyhemoglobin. The NIR therapeutic window is the wavelength domain where the combined absorption of these three molecules is the lowest.<sup>193,194</sup>

One of the recurrent problems with organic dyes is their low Stokes shift, which implies a large overlap between the absorption and the emission bands. This makes it difficult to efficiently separate, in the collected signal, the emission from the excitation lights, thus reducing the collection of relevant emitted signal.

Due to their semi-conductor nature, QDs have an absorption that gradually increases when the excitation energy increases, *i.e.* the wavelength of the excitation photons decreases. Besides, their emission band is narrow, making it straightforward to separate the

excitation from the emission: an excitation in the blue yields an emission at much longer wavelengths for usual QDs (Figure V.5).



*Figure V.5: Compared absorptions, emissions and Stokes shifts of Alexa610 and 605-nm-emitting QDs. The overlap between the absorption and emission of Alexa610 makes it difficult to efficiently separate the excitation from the emission. The QDs can be excited at 350 nm which avoids any overlap with the emission at 605 nm.*

Interestingly, all QDs have the same absorption pattern. In addition, their emission spectra (FWHM  $\sim 30$  nm), narrower than the ones of organic dyes (FWHM  $\sim 40$  to  $80$  nm), makes multicolor imaging possible: different QDs can all be excited with the same wavelength, and the different emission wavelengths can be easily separated and filtered as the narrow and tunable emission prevents any overlap (Figure V.6).

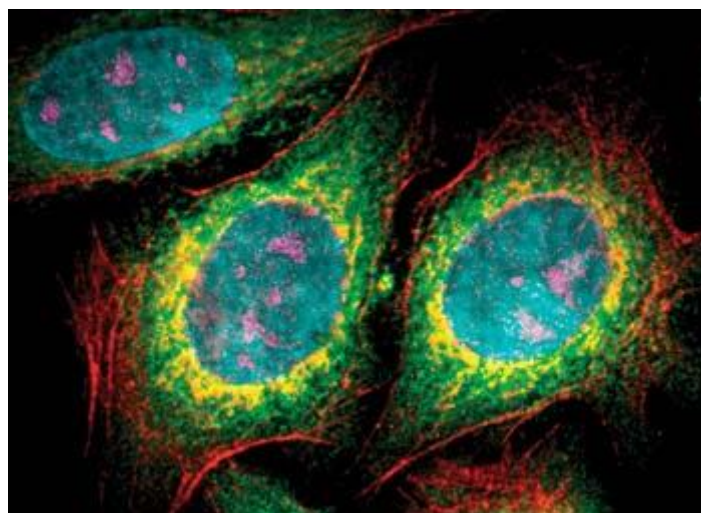


*Figure V.6: Five-color imaging of human epithelial cells thanks to five different kinds of Quantum Dots.*

*Cyan: 655-nm-emitting QDs labeling the nucleus; magenta: 605-nm-emitting QDs labeling KI-67 protein; orange: 525-nm-emitting QDs labeling mitochondria; green: 565-nm-emitting QDs labelling microtubules; and red: 705-nm-emitting QDs labeling actin filaments.<sup>192</sup>*

### V.2.3. Lifetime

The lifetime of organic dyes is short, around 5 ns in the visible range and 1 ns in the NIR domain, similar to the one of the tissue autofluorescence and of the scattered excitation light. For this reason, it is impossible to temporally distinguish between the signal and the noise.

On the other hand, QDs enable time-gated measurement where the collection of the emission signal starts only after the autofluorescence signal has decayed. Indeed, QDs' lifetime can be several orders of magnitude longer, from tens to hundreds of nanoseconds.<sup>195</sup> Time-gated measurements increase the signal-to-noise ratio and enhance the sensitivity (Figure V.7).

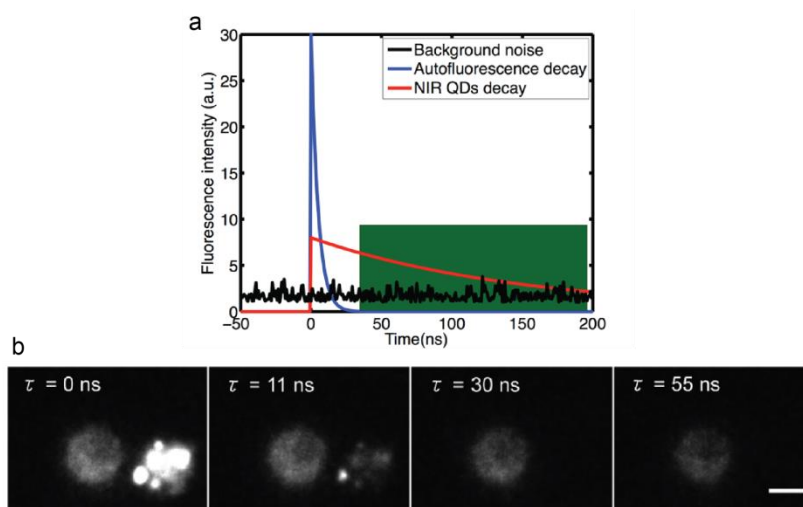


Figure V.7: a. Scheme of time-gated detection. The photoluminescence decay of the tissue autofluorescence is much faster ( $\sim 5$  ns) than the PL decay of QDs ( $\sim 100$  ns). By shifting temporally the detection window, the signal coming from autofluorescence can be ignored; the signal coming from the QDs only can be acquired. b. Images of a QD-loaded cell (left) and beads containing fluorescent organic dyes (right) after time-gated detection. As the window shifts, the fluorescence of the organic dyes is not collected anymore while the signal from the QDs is still acquired.<sup>195</sup> Scale bar is  $10 \mu\text{m}$ .

### V.2.4. Functionalization and surface chemistry

While organic dyes often present chemical groups that allow coupling to other molecules, the functionalization of QDs is more challenging.

Most of the QDs are synthesized in non-polar solvents and are capped with hydrophobic ligands, such as trioctylphosphine, myristic acid or oleylamine. The use of these nanocrystals for biological applications in aqueous media requires therefore the change of the polarity of the surface ligands. Three main strategies have been developed, each with their advantages and drawbacks.

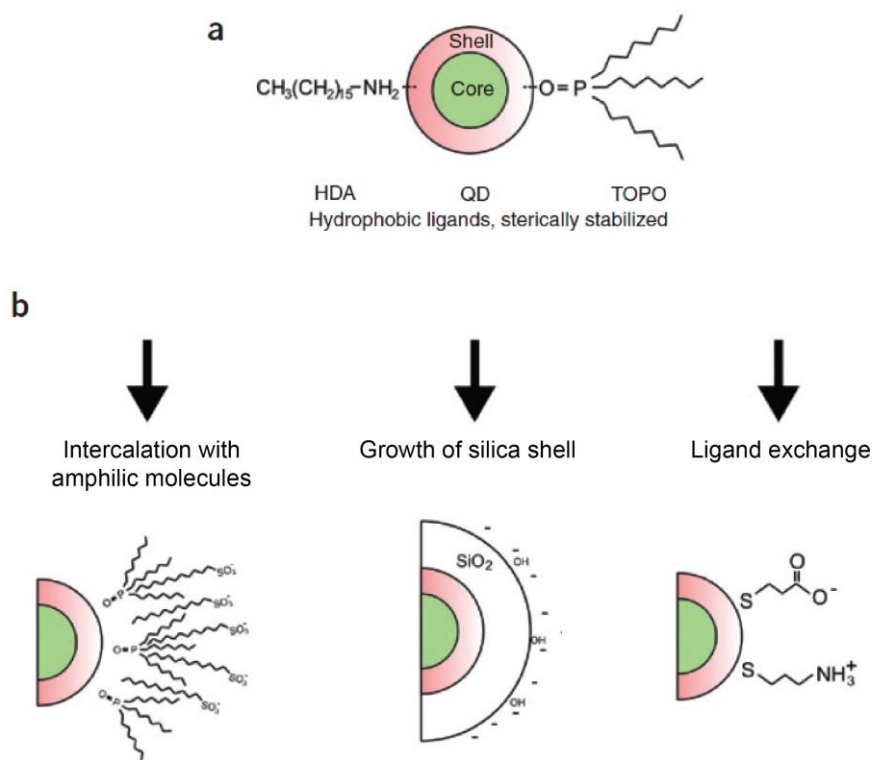


Figure V.8: Overview of the strategies allowing to prepare QDs dispersible in aqueous media. a. Hydrophobic-ligand capped QDs. (HDA: hexadecylamine, TOPO: trioctylphosphineoxide). b. Micelle-encapsulation, silica-shell growth and ligand exchange strategies to generate water-dispersible QDs.<sup>189</sup>

A first strategy preserves the native hydrophobic ligands around the inorganic core and uses a polymeric amphiphilic molecule or phospholipids to form water-dispersible micelle-like structures: the hydrophobic part interdigitates with the native QD ligands, while the hydrophilic parts ensures dispersibility in water (Figure V.8.b left).<sup>196</sup> This method is efficient for keeping a good QY as water molecules cannot reach the surface and no native ligands are ripped off the surface. However, the main drawback is that it increases the hydrodynamic size of the nanoparticles to ~30 nm which can be large enough to alter metabolic functions in cells or in living organisms. Additionally, the hydrophobic interactions between the amphiphile and the native ligands are weak, questioning the colloidal stability of such encapsulated QDs over time and at high dilutions.

In a second strategy, a hydrophilic silica shell is grown around the QD (Figure V.8.b center).<sup>16,197</sup> However this method increased the final size and alters chemically the surface of the QDs, decreasing its QY.<sup>198,199</sup>

Finally, a third strategy consists in exchanging the ligands at the surface of the QD (Figure V.8.b right). The native ligands are ripped off and replaced by hydrophilic ligands. This process is mainly driven by mass action. Small molecules can be used, such as 3-

mercaptopropionic acid that presents a thiol surface-anchoring group but bidentate (dithiol) molecules improve the QDs colloidal stability.<sup>192</sup> Zwitterionic molecules present the advantage of improving the stability in different pH or salinity conditions while keeping a small probe size.<sup>200</sup> The stability of the nanoparticles can be increased by using a polymer bearing several dithiol anchoring groups and zwitterionic hydrophilic moieties.<sup>201</sup> This strategy allows maintaining small-sized nanoparticles, but usually alters the QY as the surface of the QDs is directly modified, generating defects and traps.

All these methods, if developed for that purpose, allow functionalization of QDs. The amphiphilic polymer, the surface of the silica shell or the replacing ligands can be modified to exhibit one or several reactive groups for further functionalization, such as carboxylic acids, amines or thiols. Biomolecules (proteins, enzymes, streptavidin or biotin, antibodies...) can therefore be attached at the surface of the QDs: this yields targetable fluorescent probes. A large number of groups at the surface of QDs results in polyfunctionalization of the probe.<sup>16,202</sup>

### V.2.5. Multimodal imaging

Due to their composition (usually made of electron dense atoms such as Cd or Pb), their size (~5 nm) and their structure, QDs can be used for bimodal imaging. Optical fluorescence imaging gives information at the micrometer scale, while imaging with transmission electron microscopy (TEM) provides information at the nanometer scale. QDs can therefore be used as probes at both scales, providing different labeling information via various imaging techniques.

The core/shell structure can also be taken advantage of. The core can be responsible for fluorescence while the shell can provide other imaging possibilities. As an example, with a shell doped with  $Mn^{2+}$  paramagnetic ions, these probes can be used for fluorescence as well as magnetic resonance imaging (MRI) (Figure V.9).<sup>203</sup>



Figure V.9: a. NIR-emitting QDs doped with  $Mn^{2+}$  paramagnetic ions for magnetic resonance imaging (MRI). b. Left: MRI image of a lymph nodes in a mouse. Right: same region observed with fluorescence imaging.<sup>203</sup>

### V.2.6. Cytotoxicity of Quantum Dots

The cytotoxicity of any probe used for biological imaging needs to be checked. Although for *in vitro* or *in cellulo* studies, cytotoxicity is not an issue, it is important to examine the furtivity of the probe for *in vivo* use.

Most of the organic dyes do not show any acute cytotoxicity as these organic compounds are not toxic (with the exception of DNA intercalators). On the other hand, QDs are composed of elements whose toxicity has been demonstrated, such as cadmium. Ligands as well as nanoparticle aggregation can also be responsible for toxicity. Although the leakage of  $\text{Cd}^{2+}$  ions is believed to be critical as far as the toxicity of Quantum Dots is concerned, reports are equivocal as some show toxicity of the QDs and some show none, even in primates.<sup>189,204–208</sup> Some strategies like covering the QDs with cadmium-free shells (ZnS or  $\text{SiO}_2$ ) seem to prevent any cadmium leakage, therefore decreasing QD cytotoxicity.

Of course, cadmium-free QDs are currently under investigation, such as InP or InGaP, but their synthesis is much more difficult and their brightness and stability remains up to now below those of cadmium-based QDs.<sup>209,210</sup>

Finally, nanotoxicity can also be an issue: not only the elemental composition but the size of the probe might cause metabolism alteration. This aspect has not been thoroughly studied but preliminary results show it seems negligible.<sup>211</sup>

## V.3. Ligand exchange on the surface of Quantum Dots

### V.3.1. Necessity of a ligand exchange

As presented previously, most of the QDs are synthesized in organic, non-polar solvents, and are capped with hydrophobic ligands. Some aqueous syntheses have been reported, with water-soluble ligands capping the nanoparticles, but the obtained QDs showed worse properties than organic-solvent based QDs (lower quantum yield or larger FWHM of the emission bands).<sup>212–214</sup>

Several strategies are available for QD dispersion in water (see V.2.4). As reaching long-term colloidal stability, minimizing non-specific interactions with the biological environment, preserving a small size and maintaining good optical properties are crucial, a proper strategy needs to be chosen to perform the ligand exchange and to meet the requirements listed above.

### V.3.2. Choice of proper ligand

The surface chemistry of the QDs requires two moieties: one that is responsible for the ligand anchoring onto the surface of the QDs, and another that ensures the dispersion of QDs in water. Moreover, a small size needs to be maintained to help QDs diffusion *in vivo* and improve accessibility to narrow spaces, such as synapses for example. The colloidal stability implies that the ligands prevent the QDs from aggregating. This aggregation is mostly due to desorption of the ligands attached to the surface of the QDs: indeed, the ligands are in equilibrium between their adsorbed form and their free form in solution. If the affinity of the ligands for the QD surface is low (the anchoring group is not strongly attached to the surface of the QD like in the case of monodentate ligands) desorption is favored, triggering irreversible aggregation, or non-specific adsorption, as both the ligands and the surface of the QDs can interact with intracellular proteins and never meet again.

The interaction of the QDs with cellular components leads to QD non-specific adsorption, which can also be due to electrostatic forces between the charges present in the hydrophilic part of the ligands and the biomolecules or the plasma membrane of cells. This non-specific adsorption needs therefore to be minimized by improving the colloidal stability of QDs by increasing the affinity of the ligands for the surface of the QD and by decreasing their possible interactions with the biological medium.

A common anchoring group used for the attachment to the surface of QDs is the thiol group, present in cysteine<sup>215</sup> or in 3-mercaptopropionic acid (MPA, Figure V.10.a). Due to their relatively low affinity for the QD surface, these ligands have been replaced by dithiol-bearing molecules, such as dihydrolipoic acid (DHLA, Figure V.10.b).<sup>216</sup> They have in common the presence of a negatively charged carboxylate group at their other end, which ensures colloidal stability by electrostatic repulsion. However, the repulsion and the stability are lost in acidic media due to the protonation (and neutralization) of these groups, and in saline solutions where the charges are screened.

Poly(ethylene glycol)-based (PEG-based) ligands were then coupled to thiol anchoring groups to limit non-specific interactions (Figure V.10.c). This furative group however increases significantly the size of the nanoparticle, loses its antibiofouling properties at 37°C<sup>217</sup> and can bind to several types of proteins such as IgG antibodies.<sup>218</sup>

Zwitterionic groups present the advantage of a high furitivity over a wide range of pH (4 to 13, corresponding to the range of pH encountered in biological media) while keeping a small size. In a sulfobetaine group (SB) for example, the quaternary ammonium is stable whatever the pH and the sulfonate group stays in its basic negatively-charged form above pH~2.

To combine the properties of zwitterions and dithiol anchoring groups, a ligand called DHLA-SB was developed (Figure V.10.d). It maintains the small size of the QDs, remains stable for days in saline solutions at different pH, and show little non-specific adsorption on cells.<sup>200,219</sup>

In order to increase the affinity of the ligands towards the surface of the QDs and to improve the colloidal stability up to several months, polymer-based ligands have been further developed. As the ligands switch between the adsorbed and desorbed form, the polymer ensures that they always stay in close vicinity of the surface to reattach again. This robust, stable ligand coating strongly limits non-specific interaction between the surface and molecules present in the biological media.<sup>201,220</sup>

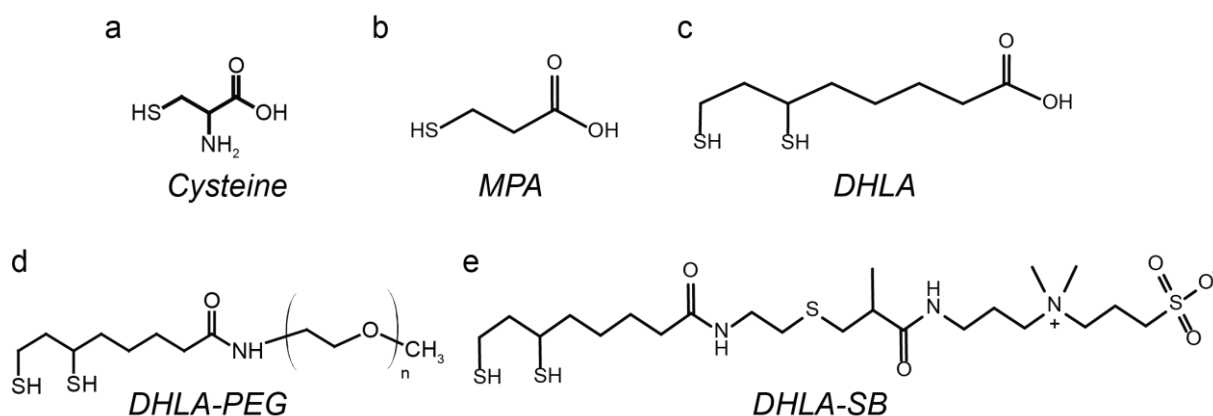


Figure V.10: Different hydrophilic ligands for ligand exchange on the QDs. a. Cysteine. b. 3-mercaptopropionic acid, MPA. c. Dihydrolipoic acid, DHLA. d. DHLA coupled to polyethylene glycol, DHLA-PEG, with n typically around 20 to 50. e. DHLA coupled to sulfobetaine, DHLA-SB.

## V.4. Targeting of Voltage Dependent Calcium Channels in *C.elegans*

### V.4.1. *C.elegans* – anatomy and interest

*Caenorhabditis elegans* (*C. elegans*) is a small non-parasitic nematode species widely found in soil or rotten fruit. First collected at the beginning of the 1900s, *C.elegans* rapidly became a model organism for biological studies (Figure V.11).



Figure V.11: Differential interference contrast image of a hermaphrodite *C. elegans* with eggs. Scale bar is 100  $\mu\text{m}$ . (Worm Atlas, Hermaphrodite introduction, <http://www.wormatlas.org/hermaphrodite/introduction/Introframeset.html>).

#### V.4.1.1. A model organism...

Many characteristics make the *C. elegans* a model organism. It is small but large enough to be manipulated easily: its length is around 1 mm for a thickness of around 100  $\mu\text{m}$ . It is easy to maintain and to grow as it can be kept on agar plates, fed with *Escherichia coli* and stored frozen at  $-80^{\circ}\text{C}$  for years without any alteration. Its lifespan is short, around 3 weeks, and its reproduction cycle is only between 2 to 3 days which makes it very quick to produce new generations of *C. elegans*. Their breeding is also particularly easy as 99% of the individuals are hermaphrodites (the rest consists of males). The self-fertilization of a hermaphrodite can produce up to 300 progenies with identical genomes.

*C. elegans* whole genome sequence was completed in 2002: it contains 100 million base pairs that encode for 20,000 proteins. The full knowledge of its genome allows genetic manipulations that can consist of gene knock-out (deletion of a gene sequence) or knock-in (addition of a sequence that encodes for example for a protein that was not originally expressed).

Despite its simplicity (hermaphrodite have only 959 cells), *C. elegans* is a multicellular organism with numerous complex behaviors such as locomotion, sensory perception (temperature sensing, touch, smell, taste), defecation, egg laying, mating, social behavior, learning and memory.<sup>221,222</sup>

Its development from embryo to adult is divided into four larval stages, where the worm finishes its growth without yet laying eggs. During these stages, the worm is particularly interesting for biological imaging as it is fully transparent in the visible region: observation of targeted proteins of interest can be performed easily.

*C. elegans* body consists of two concentric tubes separated by a pseudocoelom filled with fluid that helps regulating the hydrostatic pressure to maintain the tissues (cuticle, hypodermis, neurons, excretory system and muscle cells for the outer part, alimentary

system and reproduction system for the inner part; Figure V.12.a). This fluid-filled cavity is also involved in intercellular transport, such as antibody delivery. Importantly, it contains three pairs of coelomocytes, which are scavenger cells that act as a cleaning filter of the organism by collecting foreign material.<sup>223</sup> One pair is located near the head, another one in the center and the last one close to the tail (Figure V.12.b).

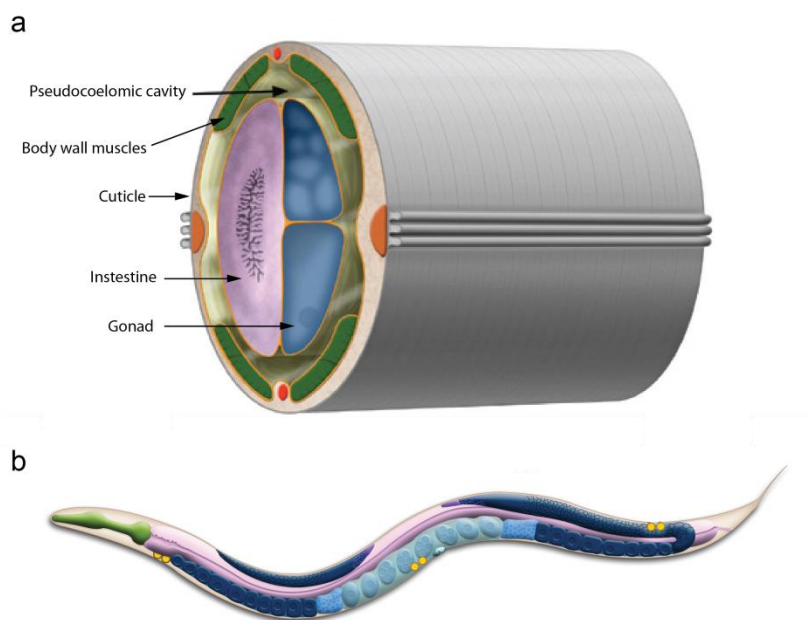


Figure V.12: a. Cross section of *C. elegans* body. b. Schematic drawing of anatomical structures. In yellow are indicated the six coelomocytes (three pairs). (Worm Atlas, Hermaphrodite introduction, <http://www.wormatlas.org/hermaphrodite/introduction/Introframeset.html>).

#### V.4.1.2. ... widely used in biology

Its short lifespan, its size, its ease of storage and maintenance, its transparency and the facility to genetically modify it make *C. elegans* a worm used in almost all areas of biology.<sup>224</sup> Many works have focused on the aging of the worm: a change in its environment or some genetic mutation might lead to an extended lifespan. Its relative closeness to the human genome (38% of worm genes are homologous to human genes) raises the scientists' interest in *C. elegans* as a model organism for the early studies of human diseases. The wide variety of physiological and behavioral phenotypes enables the observation of a molecular perturbation (drugs, gene modification...) at the whole worm level. For example, the insertion of genes promoting aggregation of peptides has been used to study human neurodegenerative diseases such as Alzheimer's or Huntington's diseases. Parkinson's disease as well as cancer or diabetes have also been induced in *C. elegans*.<sup>224,225</sup> Thus, *C. elegans* appears to be today an excellent choice for any early biological studies. It is the

simplest (biologically as well as practically speaking) fully characterized multicellular organism available to understand how complex life forms operate.

#### V.4.2. Voltage Dependent Calcium Channels in *C.elegans*

The study of the nervous system of *C. elegans* is therefore an important step for the early comprehension of the way it functions in more complex organisms. *C. elegans* nervous system is composed, in hermaphrodites, of 302 neurons. They are connected through synapses whose activity is controlled by the propagation of an electric signal. In electrical synapses, the nervous signal is transported through the synapse thanks to ions that travel across junction channels. In chemical synapses, the machinery is more complicated. The carriers of the information are neurotransmitters, such as acetylcholine,  $\gamma$ -aminobutyric acid (GABA) or glutamate. Those are molecules contained in vesicles located in a region of the presynaptic neuron known as the dense projection. They can be released in the synaptic cleft, *i.e.* the 20-to-100-nm-wide junction space between the two neurons. Their release is controlled by an influx of  $\text{Ca}^{2+}$  ions in the presynaptic neuron through channels that are electrically controlled: the voltage-dependent calcium channels (VDCCs). VDCCs generate domains with high  $\text{Ca}^{2+}$  concentrations that activate the exocytosis of neurotransmitters into the synaptic cleft. Hence, the synaptic activity and efficiency is highly dependent on the number and the distribution of VDCCs. These parameters remain partly enigmatic due to their low number and their localization in narrow spaces.

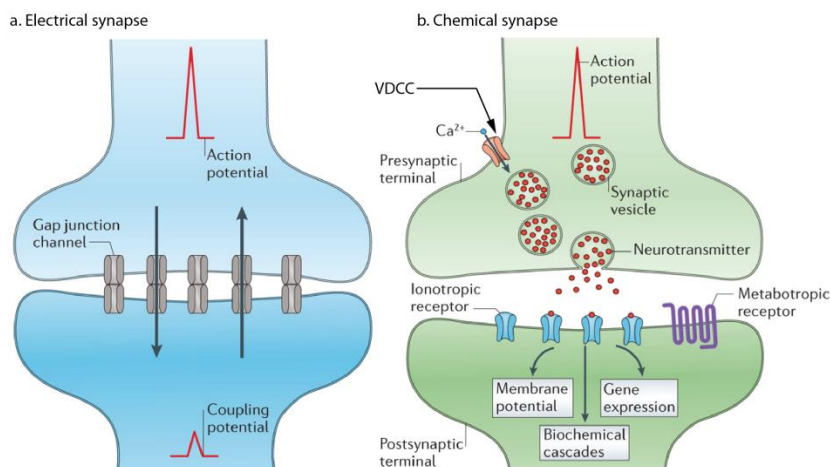


Figure V.13: Overview of the two different kinds of synapses. a. Electrical synapse. b. Chemical synapse. VDCCs are responsible for the influx of  $\text{Ca}^{2+}$  ions that triggers the release of neurotransmitters in the synaptic cleft.<sup>226</sup>

#### V.4.2.1. Genetic modification of *C. elegans*

A common way to study protein localization in an organism is to target it with a fluorescent antibody and detect the fluorescence signal. However, in the case of VDCCs in *C. elegans*, several challenges make it difficult to implement such a method: VDCCs are not numerous enough to display a strong signal, and antibodies usually employed show low affinity for VDCCs and have a limited access to the narrow synaptic regions where VDCCs are present.

Therefore another strategy had to be developed. To circumvent the low affinity of antibodies for VDCCs, genetic modification was performed on the worms to make them express Green Fluorescent Protein (GFP) in close vicinity of VDCC. Thus, VDCCs can be easily visualized, and the mobility as well as the function of VDCCs are maintained (Figure V.14). However, the study of their localization is limited to relatively low resolution optical imaging where information about their distribution and number is searched for at the nanometer scale.

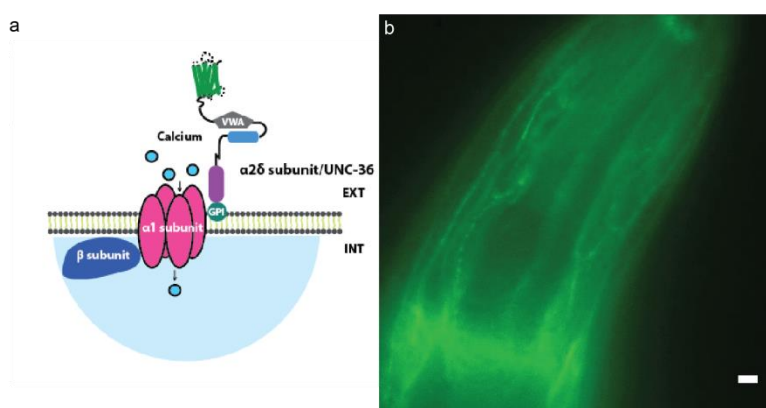


Figure V.14: a. Scheme of GFP coupled to VDCC. b. Fluorescence image of the head of a genetically-modified *C. elegans* to express GFP at VDCCs' locations. Scale bar is 10  $\mu\text{m}$ .

#### V.4.2.2. Quantum Dots as bimodal probes for targeting of VDCCs

TEM techniques reach nanometer scale resolution. Contrast in TEM depends on the electron density of the observed material. Organic compounds such as polymers or proteins exhibit low contrast and their contrast often needs to be enhanced with electron-dense atoms such as uranium or lead (in the form of uranyl acetate or lead citrate respectively).

Quantum dots are interesting probes for biological imaging. They are fluorescent particles presenting high absorption cross-section, good photostability, tunable and narrow emission wavelength, wide absorption domain and a size small enough to enter organisms,

cells or even subcellular compartments. Besides, as they are cadmium-based, they can be easily observed under an electron beam and provide good contrast in TEM imaging.

These two characteristics make QDs excellent candidates for bimodal biological imaging: they provide information not only at the mesoscopic scale thanks to their fluorescent properties, but also at the nanometric scale due to their electron density.

#### V.4.2.3. Quantum Dots for biological applications

Quantum dots have already been used in biology for biosensing,<sup>227–229</sup> single particle tracking,<sup>230</sup> fluorescence-activated cell sorting (FACS)<sup>16</sup> and are more and more considered for *in vivo* tumor detection.<sup>231–233</sup> However, the use of cadmium-based QDs raises the question of the cytotoxicity of these nanoparticles.<sup>204–207</sup> Many studies have shown the possibility of using cadmium-free QDs which brings the advantage of being non-toxic and having an emission in the near-infrared region, in the so-called therapeutic window between 700 nm and 900 nm where major tissue chromophores (water, lipids, oxyhemoglobin and deoxyhemoglobin) show low absorption.<sup>203,234–237</sup> Nevertheless, Cd-based QDs exhibit better QYs and narrower emission bands which are two important parameters for biological imaging.

Many studies have also been performed on the functionalization of the surface of the QDs to improve their dispersion and stability in aqueous media, their targeting abilities and detection efficiencies.<sup>192,196</sup>

Strategies to make water-compatible QDs and to functionalize their surface of the QDs have been described in V.2.4 and in V.3.

#### V.4.3. New polymeric ligand

In the group, E. Giovanelli developed a polymeric ligand that improves the colloidal stability of the QDs in aqueous media.<sup>201</sup> It is based on i) a dithiol anchoring group that binds to the cations at the surface of the QD and ii) zwitterionic groups for dispersion in water. The optimum molar ratio between the anchoring groups and the hydrophilic groups was found to be 20:80 for a polymer length of around 20 monomers per chain to ensure a good solubility of the polymer in water and a stable aqueous colloidal dispersion of QDs. This polymer has been proved to maintain QDs stable in water over a wide range of pH (3 to 13) and at high ionic strengths (up to saturated NaCl aqueous solution), which is necessary for a broad spectrum of biological applications as the acidity and the salt content may vary within the same cell.<sup>238,239</sup> Besides, the chemical synthesis can be modified for this polymer to present  $-NH_2$  groups that can be used for functionalization of the surface of the QDs; an organic

molecule (fluorescein...) or a protein (antibody, streptavidin...) can be coupled to this group yielding QDs exhibiting a biological entity that can interact with the organism (Figure V.15).

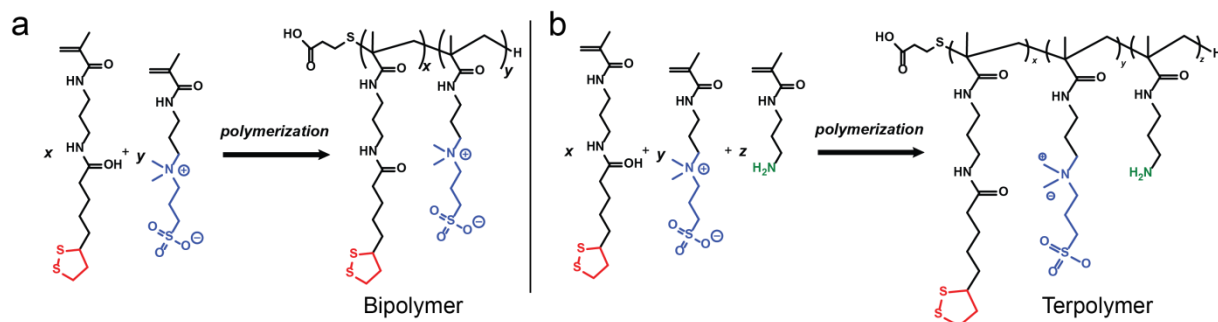


Figure V.15: a. Structure of bipolymer with an anchoring group (red) to attach to the QD surface and a zwitterionic group (blue) for dispersion in water. The disulfide bridge is reduced to form thiols that bind to the surface of the QD. b. Structure of terpolymer with a supplementary amine group (green) for further functionalization.

In order to study the distribution of VDCCs in *C. elegans*, we decided to use Quantum Dots as bimodal probes for imaging. It was therefore necessary to ensure their stability in biological conditions and to functionalize them with molecules that could bind to VDCCs. The polymer developed in the group was found to be an excellent candidate to fulfill all these criteria. Indeed, polymer-coated QDs can be functionalized with anti-GFP antibodies that will bind to the VDCCs in the mutant worms that were genetically engineered to express GFP at the VDCCs (see V.4.2.1). This strategy should circumvent the low affinity of the antibodies for the VDCCs by providing high-affinity anti-GFP antibody-coated QDs, thus allowing a better visualization of the distribution of VDCCs in *C. elegans*.

#### V.4.4. Preparation of antiGFP-QDs

The Quantum Dots used for this study are CdSe/CdS QDs of 8.5 nm in diameter. Their maximum emission wavelength is located at 610 nm, far enough from the emission wavelength of GFP (around 500 nm) to be able to distinguish between both emissions using proper filters.

##### V.4.4.1. Ligand exchange on the QDs

The first step for the preparation of antiGFP-QDs is the ligand exchange. After their synthesis, QDs are coated with long organic ligands: oleylamine, oleic acid and myristic acid. Those ligands prevent the QDs from dispersing in water. Thus, a ligand exchange is necessary to use those nanocrystals (NCs) for biological applications.

The first approach used was a classic biphasic exchange: a solution of the terpolymeric form in water was stirred with a solution of QDs in chloroform.<sup>200</sup> However, while this method gives good ligand-exchange yields with small ligands (DHLLA for example), the phase transfer did not occur with the polymer. This might be due to the low solubility of the polymer in chloroform; the partition coefficient between the two solvents is then low and the QDs are stuck at the interface between the two solvents.

This strategy was consequently changed to two monophasic-exchange steps (Figure V.16). In the first step, native ligands around the QD were exchanged to 3-mercaptopropionic acid (MPA), a small hydrophilic molecule. Typically, 4 nmol of QDs in hexane were precipitated with ethanol (EtOH), centrifuged and the supernatant was discarded. The precipitate was redispersed in 500  $\mu$ L of pure MPA and left overnight at 60°C. 3 mL of dimethylformamide (DMF) were then added followed by the addition of a few milligrams of potassium *tert*-butoxide (*t*BuOK) to deprotonate the carboxylic group. The solution was sonicated, stirred, and centrifuged: MPA-capped QDs precipitated while the excess MPA stayed in polar solution in the DMF. The precipitate was washed twice with EtOH, and finally redispersed in 1 mL of sodium tetraborate solution (10mM, pH=9). This allowed solubilization of the QDs in water.

This first step was followed by a ligand exchange from MPA to the polymer. 70 mg of the polymer were dissolved in 1.5 mL of water and placed in an ice bath. A few milligrams of NaBH<sub>4</sub> were added to reduce and open the disulfide bridge. The solution was stirred for 30 min after which the dispersion of MPA-coated QDs in the tetraborate buffer was added dropwise. The reaction mixture was left under stirring for 1 hour before leaving it overnight at 60°C. It was then centrifuged at 10,000 RPM to remove the largest aggregates, then purified and concentrated by ultrafiltration on a 50-kDa-cut-off membrane filter (to remove the excess free solubilized polymer) with three washing steps with an aqueous NaCl solution (20 mM). A final purification step was performed by ultracentrifugation in a density-gradient (10%-40% sucrose solution) at 50,000 RPM for 20 minutes. The colored band corresponding to the QDs was collected and the sucrose was removed by ultrafiltration (50-kDa-cut-off membrane) with three washing steps using a NaCl solution (20 mM in water). This yields water-soluble QDs, capped with the polymer. Depending on the polymer used for the ligand exchange, several groups could be available for grafting a protein on their surface (Figure V.16).

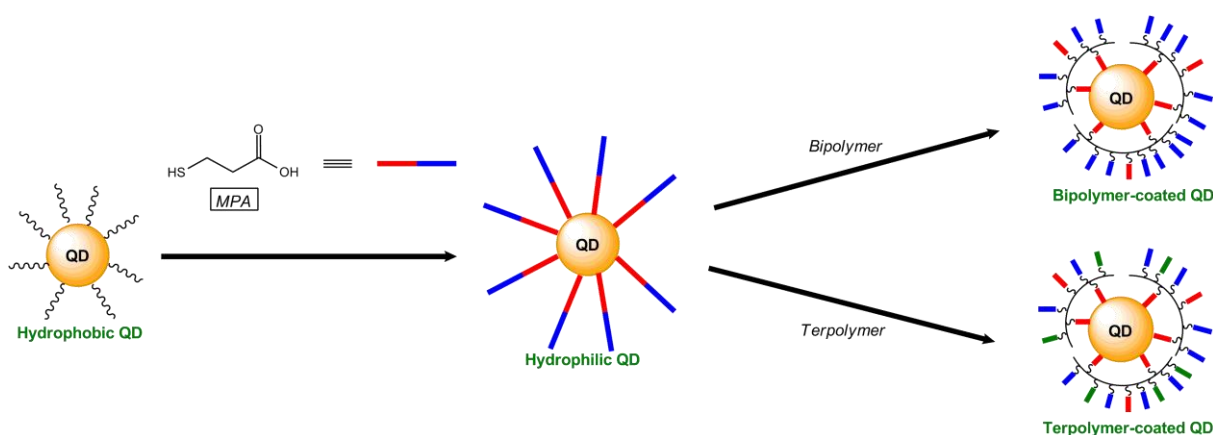


Figure V.16: General strategy for ligand exchange and for grafting of reactive groups at the surface of the QDs.

#### V.4.4.2. Coupling of anti-GFP antibody to an amino group

In a first approach, we tried to couple antibodies to QDs by attaching an amino group of the antibody to an amino group of the polymer coating the QDs. This requires the use of modified terpolymer that exhibits amino groups that serves as a reactive function. The coupling is performed through two heterobifunctional linkers, sulfo-*lc*-SPDP and sulfo-SMCC, whose aim is to transform the amine groups into more reactive moieties, respectively a thiolate and maleimide function, that can react chemoselectively together to form a covalent bond (Figure V.17).

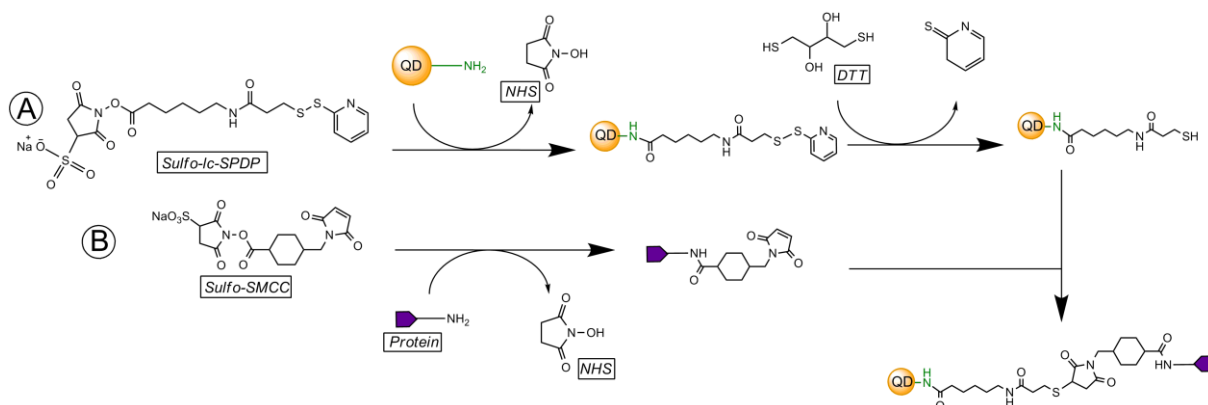


Figure V.17: Scheme of coupling of a protein to an amine-functionalized QD.

1.5 nmol of polymer-coated QDs are dispersed in 400  $\mu\text{L}$  of  $\text{NaHCO}_3$  solution (0.2 M in water). 45  $\mu\text{L}$  of sulfosuccinimidyl 6-(3'-(2-pyridyldithio)propionamido)hexanoate (sulfo-*lc*-SPDP) solution (10 mg/mL in dimethyl sulfoxide, DMSO) is added and the solution is stirred gently for 15 minutes. It is then concentrated and purified by ultrafiltration on a 50-kDa-cut-off membrane filter with  $\text{NaHCO}_3$  solution (0.2 M in water), and collected in 400  $\mu\text{L}$  of  $\text{NaHCO}_3$  solution (0.2 M in water). 15  $\mu\text{L}$  of Dithiothreitol (DTT) solution (23 mg/mL in DMSO) is then

added, stirred for 15 minutes, concentrated by ultracentrifugation and washed once with HEPES buffer. Finally, a size exclusion NAP-5 column from GE Healthcare was used to purify the dispersion of QDs before concentrating it by ultrafiltration and collecting in 150  $\mu$ L of HEPES buffer.

In parallel to that, 1.5 mg of streptavidin (SA; stored at 5 mg/mL in NaHCO<sub>3</sub> solution, 0.2 M in water) is added to 4  $\mu$ L of sulfosuccinimidyl 4-(N-maleimidomethyl)cyclohexane-1-carboxylate (sulfo-SMCC) solution (10 mg/mL in water), stirred gently for 10 minutes and washed by ultrafiltration (membrane cut-off: 10 kDa) with HEPES buffer (to remove the excess sulfo-SMCC).

The SA solution and QD dispersion are then mixed and stirred for 5 minutes and washed by ultrafiltration (membrane cut-off: 100 kDa) with HEPES buffer (to remove the excess SA whose size is around 56 kDa).

This protocol yields SA-functionalized QDs to which biotinylated anti-GFP antibodies can be attached. Indeed, the strong affinity between biotin and streptavidin enables the formation of a robust non-covalent bond between the two molecules. Assuming around 10 SA per QD,<sup>201</sup> the proper amount of antibody was washed through a NAP-5 column with an aqueous NaCl solution (20 mM), and added to the QDs dispersion and stirred for 30 minutes. A 20-fold excess of biotin was then added to saturate the free streptavidin sites and the reaction mixture was finally purified by ultrafiltration on 100-kDa-cut-off membrane filters.

After several experiments, the optimum concentration of antibody-capped QDs required for the injection in the worms was found to be around 2  $\mu$ M (measured by comparing the absorbance at 350 nm before and after the coupling); if not enough concentrated, the signal from the QDs is hardly detectable, and if too concentrated, the VDCCs are saturated with QDs and free QDs floating in the worm body mask the specific signal of the QDs attached to VDCCs.

#### V.4.4.3. Coupling of anti-GFP antibody to a carboxylic group

During the synthesis of the polymer, the terminating agent used is MPA. Therefore, one carboxylic group (-COOH) per chain is available and can be used for peptide coupling (Figure V.15). This carboxylic group can be activated by dicyclohexylcarbodiimide (DCC) and *N*-Hydroxysuccinimide (NHS) and then coupled to an amine group present in the SA (Figure V.18).

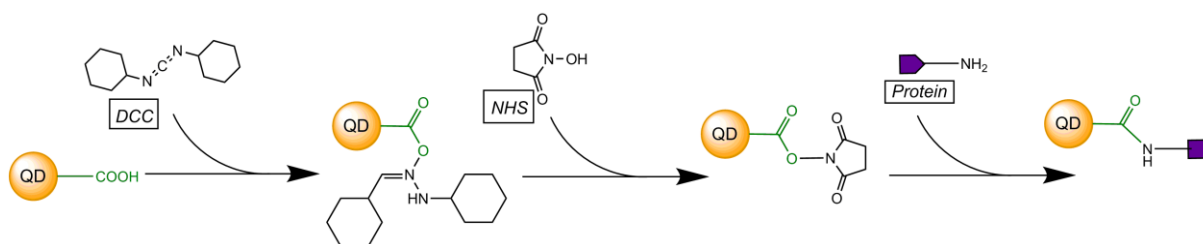


Figure V.18: Scheme of coupling of a protein to a carboxylic-acid-functionalized QD.

Typically, 2 nmol of bipolymer-coated QDs are lyophilized and then redispersed in 300  $\mu\text{L}$  of N-methylformamide at 0°C. 4 mg of DCC and 2.4 mg of NHS are then added, the dispersion is stirred for 4 hours and the QDs are precipitated and washed with 750  $\mu\text{L}$  of anhydrous acetonitrile. The solution of SA (prepared as described in V.4.4.2) is then added, stirred for 1h30, concentrated and washed thrice with HEPES buffer using ultrafiltration. The coupling of the biotinylated anti-GFP to the SA was carried out as described previously (V.4.4.2). The best results in terms of QDs stability in water were obtained with a polymer twice as long as the polymer developed by Giovanelli *et al.*

#### V.4.4.4. Coupling of anti-GFP antibody to a thiol group

Finally, a third strategy for coupling SA to the QDs consists in taking advantage of some of the thiol (-SH) anchoring groups that are not attached to the surface of the QD and thus available for activation. The SA was activated with sulfo-SMCC as described previously, and directly mixed with bipolymer-coated QDs (without the -NH<sub>2</sub> group and without activation of the -COOH group). As previously mentioned for the coupling to -COOH groups, a longer polymer was preferred for the coupling to -SH groups.

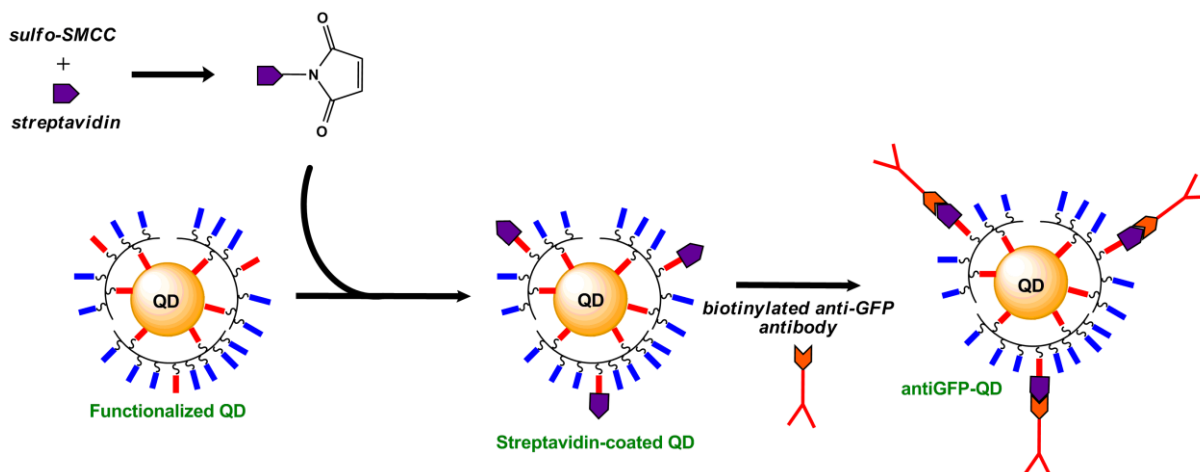


Figure V.19: Scheme of coupling of thiol groups of the QDs to anti-GFP antibodies. The streptavidin-biotin high affinity illustrated here is shared by all of the coupling strategies.

#### V.4.4.5. *In vitro* evaluation of the coupling specificity of the antiGFP-QDs

The affinity of the resulting antiGFP-QDs for GFP was tested *in vitro* on functionalized agarose beads. Those beads are Ni-NTA (nickel chelated by nitrilotriacetic acid) tagged: they have a high affinity for histidine (His) tags. His-tagged GFP was mixed with the beads to form beads that carry GFP on their surface. To these beads were added antiGFP-QDs. The QDs did successfully bind to the beads, proving the efficient coupling between the antiGFP-QDs and the GFP and the effective biofunctionalization of the QDs (Figure V.20). Only little non-specific adsorption was observed that might be due to the diffusion and trapping of QDs inside the porous agarose beads.

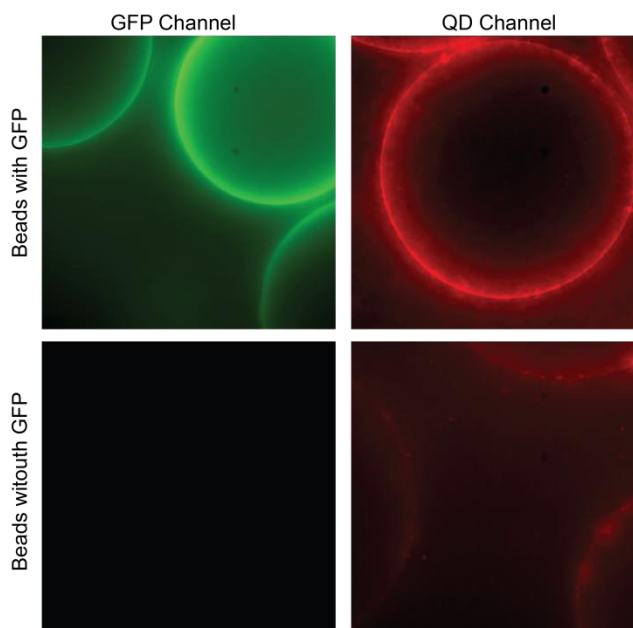


Figure V.20: *In vitro* test of the affinity of antiGFP-QDs for GFP using GFP-bearing agarose beads.

#### V.4.5. Microinjection of antiGFP-QD

The dispersion of polymer-coated antiGFP-QDs at 2  $\mu\text{M}$  was injected without dilution. Worms are put on 2% agarose (prepared in water) pads in mineral oil to help immobilization. With a microinjection setup, the solution of antiGFP-QDs is injected in the pseudocoelomic cavity, between the two pharyngeal bulbs where the cavity is the widest. After the injection, the worms were collected in a drop of buffer for *C. elegans* culture (M9 buffer),<sup>240</sup> deposited on fresh agar plates to remove the oil, and let recover for 30 minutes at 15°C before being transferred to 20°C. All worms survived the microinjection after 3 h to 12 h at 20°C and did not show any locomotion defects, thus excluding any obvious cytotoxicity of the Quantum Dots.

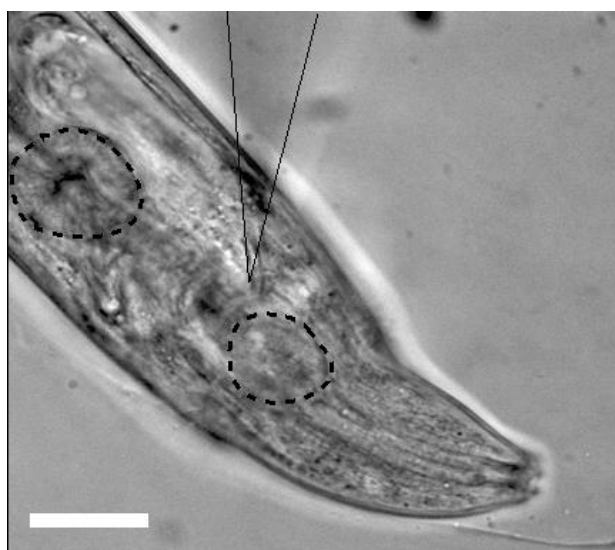


Figure V.21: Scheme of microinjection. Worms were immobilized on 2% agarose pad and immersed in mineral oil (Sigma H8898). The black dash lines represent the two pharynx bulbs between which the injection needle (black solid line) is inserted. Scale bar is 50  $\mu\text{m}$ .

#### V.4.6. High-pressure freezing

After the injection and the recovery, the worms were observed under light and fluorescence microscopy to check the labeling efficiency of the QDs (see V.4.7). When VDCCs were clearly labeled without too much non-specific binding, the worms were prepared for nanometric scale resolution observation, *i.e.* for TEM imaging.

Classic chemical fixation requires a fixative to penetrate the tissues and to immobilize them. However, the anatomy of *C. elegans* makes the penetration very slow due to its outer protective layer - the cuticle - that protects the inner body from the outside environment. During the diffusion of the fixative, the cellular structures that are not fixed yet are slowly

degraded and in the end, the fixed structures have a different morphology from the one they had in the living organism.

To circumvent the problem, our collaborators in Jean-Louis Bessereau's group used a cryo-technique to immobilize the worm and all its inner structures instantly. This technique called High-Pressure Freezing (HPF) solidifies the water contained in the body of the worm into vitreous ice, an amorphous state of water, which physically preserves tissues.<sup>241</sup> This ice is then substituted for different organic solvents, including a final step of embedding in a resin (araldite). Once the worm is fixed, it is mounted on a sectioning machine to cut 70-nm thick sections in the region of interest. Those sections are then collected on a grid for TEM observation (Figure V.22). From these sections, a 3D reconstruction algorithm can be used to get 3D distribution of the tagged VDCCs.<sup>242</sup>

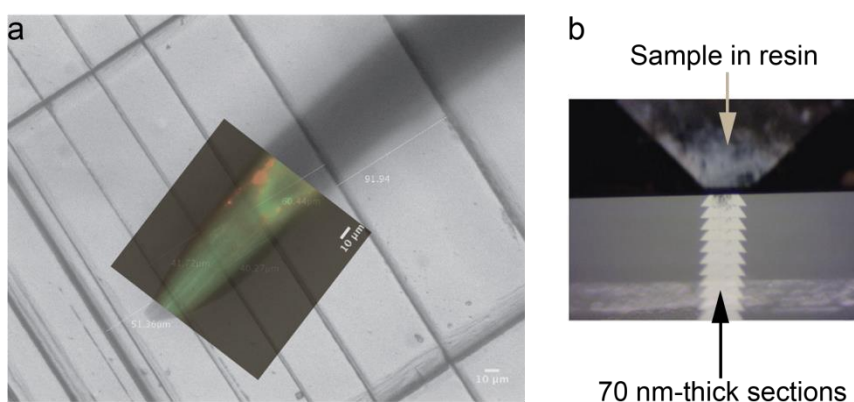


*Figure V.22: a. Superimposition of fluorescence image of antiGFP-QD-loaded worm and bright field image of the same worm after HPF and embedding in araldite. The black lines are the marks drawn for the selection of the region for sectioning. b. The sectioning is performed using a diamond knife, and the 70-nm thick sections are collected on a grid for TEM imaging.*

The optical microscopy and the electron microscopy provide macroscopic and nanoscopic information on the distribution of QDs, and thus of VDCCs in the worm body, enabling Correlative Light and Electron Microscopy (CLEM) to be performed on the injected worms. A region of interest, first localized by fluorescence microscopy, is then thoroughly observed under electron microscopy and reconstructed in 3D to study the distribution of VDCCs.

#### V.4.7. Macroscopic targeting in living worms

After injecting the bi- or terpolymer-coated QDs in the wild type worm, they were left several hours for recovery and then observed under fluorescence microscopy. The polymer-coated QDs without the antibody diffused freely in the pseudocoelomic cavity, showing little non-specific adsorption on the intestine or the pharynx. Most the QDs were however freely

floating in the cavity fluid, indicating good furtivity in the organism. Interestingly, the coelomocytes did not uptake many QDs from the body cavity. This might constitute a problem as unbound QDs are not efficiently removed from the body cavity and might introduce some background fluorescence noise that will make it harder to visualize to QDs specifically bound to VDCCs. Nevertheless, it might be a good indication that the QDs do not alter at all the metabolism of *C. elegans* as they are not detected by the scavenger cells of the body. A reason why the QDs may be undetected by the coelomocytes is because the latter engulf foreign protein through receptors at their surface that specifically bind to anionic molecules (anionic ligand-binding receptor, ALBR).<sup>239</sup> The hydration layer and the counter-ion layer around the QDs might mask the charges expressed at the surface of the QDs, preventing them from binding to the ALBRs on coelomocytes. Finally, the size of the QDs might play a role: even though the size of the invaginations in coelomocytes is close to 100 nm,<sup>223</sup> we do not know if the endocytosis efficiency is altered for nanoparticles of ~20 nm in hydrodynamic diameter.

In order to localize VDCCs in the *C. elegans* body, they were endogenously tagged with a GFP protein. This GFP is expressed on muscular and neuronal VDCCs. This fluorescent protein will not only enable visualization of the VDCCs, but also confirm the specific binding of antiGFP-QDs to the GFP, thus to the VDCCs by colocalization.

AntiGFP-QDs obtained by coupling between anti-GFP antibodies and the amine group of the terpolymer were first injected in mutant worms expressing GFP at VDCCs. These biofunctionalized nanoparticles showed aggregation when observed in fluorescence microscopy (Figure V.23).

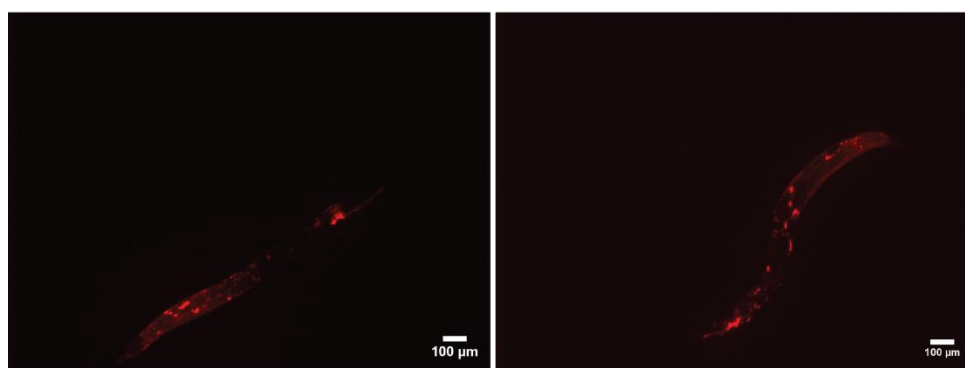


Figure V.23: Fluorescence images of QDs coupled to anti-GFP antibodies through an amine group show aggregation of the nanoparticles inside the worm.

However, the injection of antiGFP-QDs prepared through the coupling of the antibodies to the carboxylic acid or the thiol groups showed very good colocalization of GFP-tagged VDCCs and antiGFP-QDs (Figure V.24.a). The colocalization shows a punctuate pattern as

expected for neuromuscular junctions, and this along the entire body. The antiGFP-QDs specifically bind to VDCCs along the muscle cell membrane (Figure V.24.b). The control experiment in wild-type worms showed no specific binding of antiGFP-QDs (Figure V.24.c).

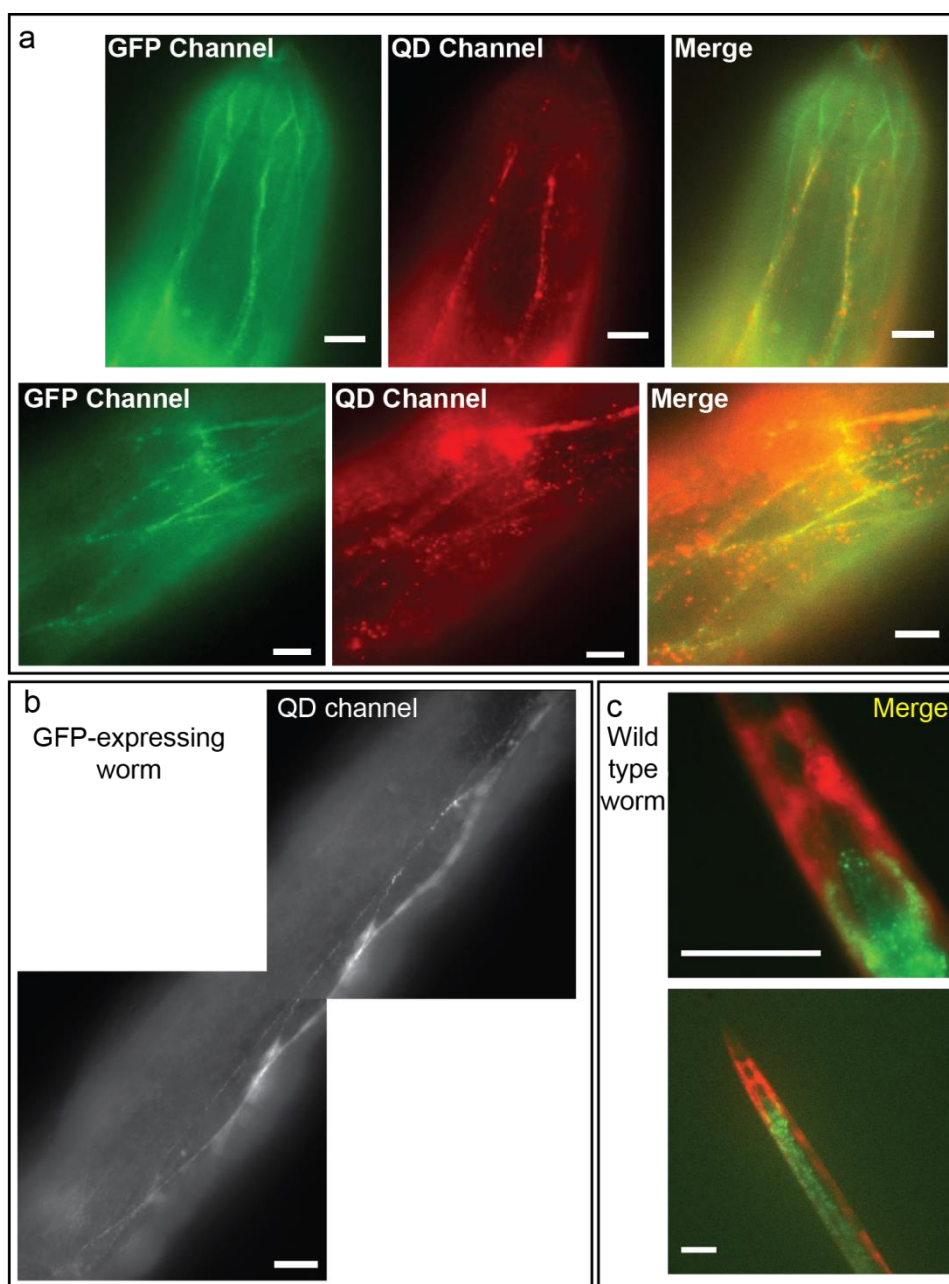
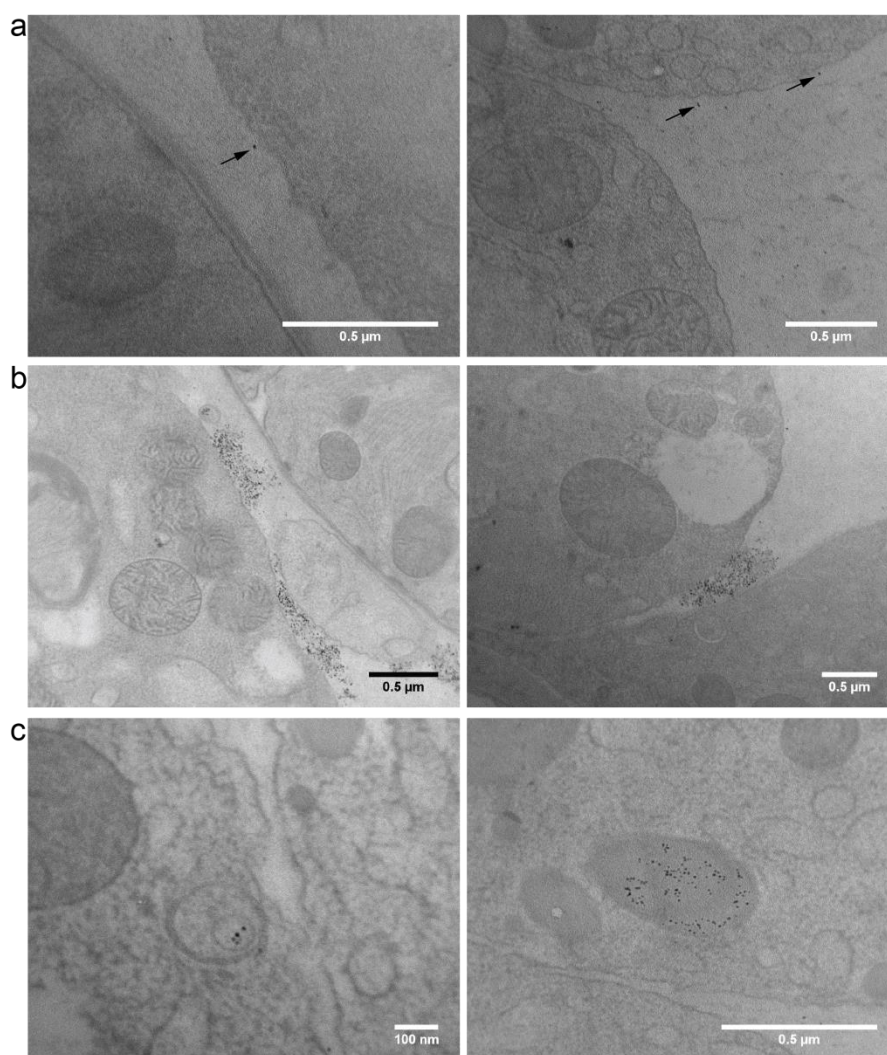


Figure V.24: a. Fluorescence images of GFP-expressing worms injected with antiGFP-QDs prepared through coupling to the thiol groups. Colocalization between the GFP signal and the QDs signal. Scale bar is 10  $\mu\text{m}$ . b. Image in the QD channel shows that the QDs bind to the surface of the muscle cells (diamond shape) where VDCCs are present. Scale bar is 10  $\mu\text{m}$ . c. Fluorescence images of wild-type worms injected with antiGFP-QDs coupled through the thiol group. No colocalization is observed between the signal in the QD channel and in the GFP channel (which corresponds to autofluorescence of the tissues). Scale bar is 100  $\mu\text{m}$ .

#### V.4.8. Nanometer resolution analysis

As expected after the optical imaging, for the QDs coupled to anti-GFP antibodies through amine groups, the TEM images after HPF and sectioning showed some isolated QDs (Figure V.25.a), but most of them were aggregated in narrow regions of the body cavity of the *C.elegans* (Figure V.25.b). This coupling strategy might favor the formation of QD-aggregates through the coupling of  $-NH_2$  groups that are present on different QDs. Surprisingly, a small fraction of QDs was found in vesicles inside the muscle cells (Figure V.25.c). It is not clear however how they entered the cells: it might be due to non-specific adsorption to the cell membrane followed by endocytosis; or QDs could bind specifically to the VDCC-GFP complex that undergoes endocytosis.



*Figure V.25: TEM images around muscle cells of sections of worm injected with QDs coupled to anti-GFP through amine groups. a. Some isolated QDs can be seen close to muscle cells. b. Most of the QDs however form large aggregates that get stuck in narrow regions of the body cavity of the worm. c. Surprisingly, some QDs get internalized in the muscle cells.*

On the other hand, the fluorescence images obtained after the injection of QDs coupled to anti-GFP through thiol groups show no obvious aggregation and show colocalization of the GFP and QD signals. This strategy is therefore promising for nanometer scale resolution analysis and was chosen for further studies.

Once the good localization of the antiGFP-QDs was confirmed with optical microscopy, the worms were high pressure frozen and after freeze-substitution, were cut into 70 nm-thick sections that were imaged under TEM. The QDs were mostly found on muscle boundaries and between muscle cells where VDCCs are present.

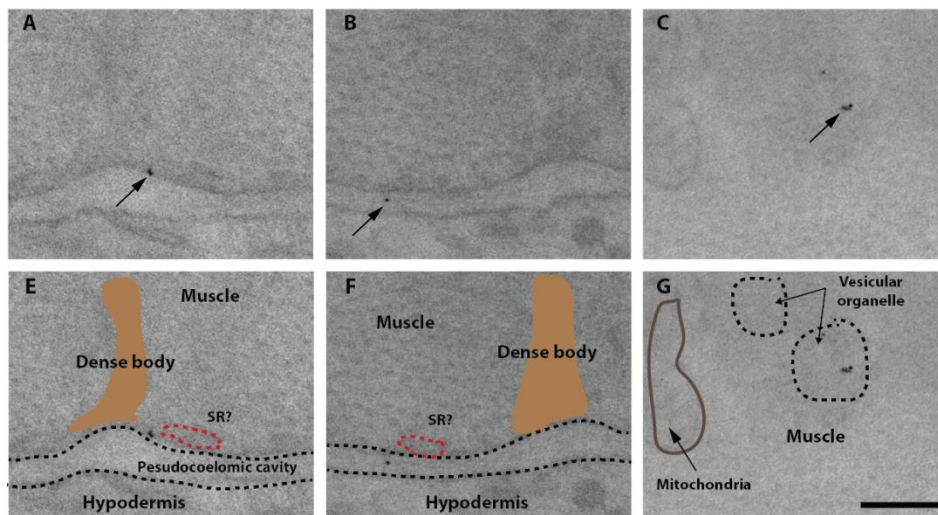


Figure V.26: TEM images of sections of worms injected with QDs coupled to anti-GFP antibody through thiol groups. Black arrows point to the QDs. E, F and G images are the same as A, B and C but annotated with some highlighted organelles. QDs are present at VDCCs at the muscular level.

Scale bar is 200 nm.

Nevertheless, the QDs found at the neuro-muscular junctions are associated to synapses and thus to VDCCs. By TEM imaging and reconstruction of several sections, a 3D view of the region of interest can be generated. In presynaptic neurons, the QDs were found to be in the dense projection - the active zone of the synapse. The number of QDs found in this area is around 5, which is consistent with the low number of VDCCs estimated in previous studies (Figure V.27).<sup>243,244</sup> The control experiment in wild-type worms did not show any signal colocalized with dense projections.

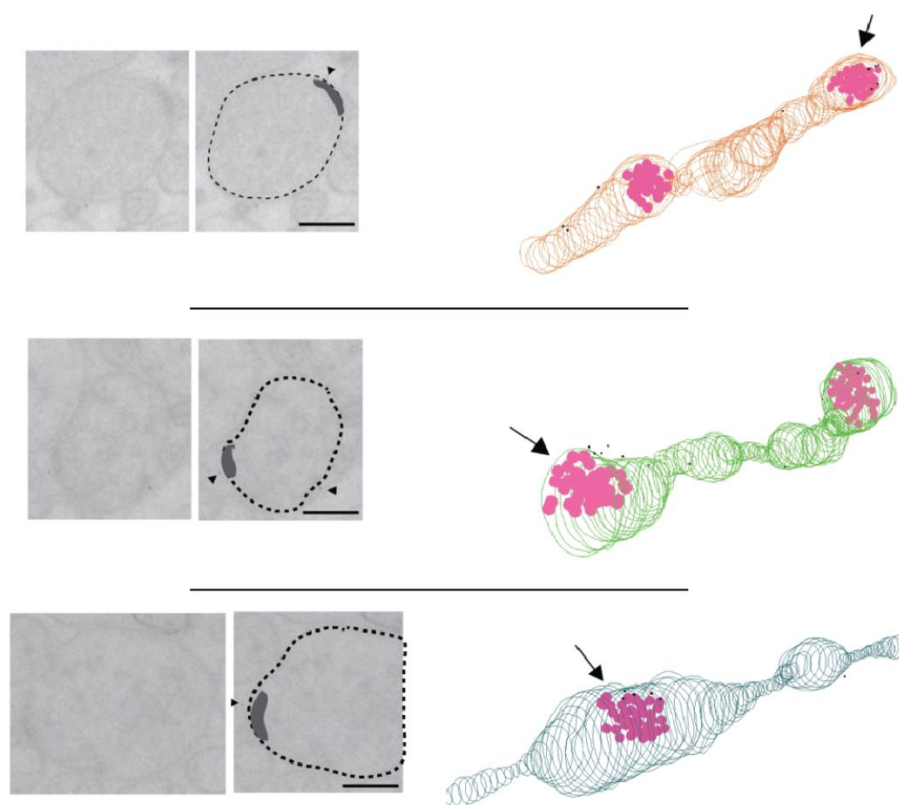


Figure V.27: Three 3D reconstructions of serial TEM of sections of antiGFP-QD-injected worms. Left: TEM images. Black arrowheads show QDs. Right: 3D reconstructions. Pink circles are synaptic vesicles, black dots are QDs and the synapses are localized with black arrows. Scale bars are 200 nm.

The labeling of VDCCs however remains not completely effective. Although VDCCs at the muscles are marked, it seems that VDCCs in neurons or in the nerve ring (the largest pool of neurons) are not labeled with QDs. This might be due to the size of the antiGFP-QDs that cannot reach narrow spaces. Indeed, IgG has a diameter of 15 nm to 20 nm which increases the size of antiGFP-QDs that might be too large for the space around the nerve ring (Dynamic Light Scattering, DLS, measurements show a hydrodynamic size of approximately 20 nm for the polymer-coated QDs). Thus, two strategies were developed to try and produce smaller QDs that can bind to GFP: in the first one, an -SH function of the polymer was attached directly to an anti-GFP antibody (without the intermediate biotin-streptavidin complex that increases the global size of the particle by  $\sim 12$  nm<sup>245</sup>). However, no specific binding could be seen in *C. elegans* using this type of QDs. This is probably due to the fact that the direct coupling of the antibody to the QDs can alter the antibody spatial organization or binding site.

The second strategy consisted in using a small single-chain fragment-variable anti-GFP antibody (scFv) developed with Clément Nizak (Laboratoire de Biochimie, ESPCI,

Paris). Those antibody fragments present several advantages: their structure is restricted to the smallest size necessary for efficient antigen detection and binding, and they are composed of only one domain which prevents from crosslinking side-reactions. To attach this anti-GFP scFv to the QDs, an aldehyde tag, that could be used for coupling, was introduced at the opposite end of the antibody in relation to its binding site. However, the level of the scFv expression by *E. coli* was very low and the amount of produced antibody fragments was not sufficient to consider coupling to QDs.

#### V.4.9. Conclusion

Quantum Dots can be used as multimodal imaging probes: their fluorescence properties make them good and robust probes for optical imaging, while their electron-dense composition makes them excellent probes for electron microscopy imaging. CdSe/CdS QDs were used to mark VDCCs in *C. elegans*. The labeling efficiency was verified by fluorescence microscopy. The localization and number of QD-tagged VDCCs were then studied with TEM. The ligand exchange strategy used, necessary to yield QDs dispersible in aqueous solutions, provided the QDs with good stability and low non-specific adsorption in the *C. elegans* body. The coupling strategy used to attach antibodies to the QDs showed efficient and specific labeling of VDCCs. With this strategy, it is however impossible to control the exact number of antibodies that are attached to the surface of the QD: different antibody coverage might induce different metabolic responses.

### V.5. **DNA nanocage as a functional biocompatible scaffold**

Surface functionalization of QDs by ligand exchange is an efficient way to transfer them into aqueous media and attach a protein to their surface. However, after mixing with the hydrophilic ligands, there is no way to exactly handle the number of ligands around the QDs, nor the number of functional groups introduced. Several studies have featured a monofunctionalization of QDs but they are mostly based on the isolation of one population of QDs from a mixture of multifunctionalized nanoparticles,<sup>246–250</sup> or on a statistical binding of one protein to one QD.<sup>251</sup> Therefore, the simple ligand exchange strategy does not allow to precisely control the monofunctionalization of the QDs.

It is thus worth developing another strategy for the functionalization of the QD surface. Encapsulating QDs in a host which can be easily coupled to a protein of interest switches the

problem of functionalization of the QDs to the problem of the functionalization of the host. Hence, an easy-to-build, easy-to-modify and monofunctionalizable host that could encapsulate cargos like QDs seems to be an interesting approach. Besides, in order to be used in biological systems, it needs to be biocompatible.

DNA presents several advantages for this kind of applications: owing to its nature, it is biocompatible, its synthesis is cheap, standardized and Watson and Crick base pairing enables tunable and highly selective binding between single-stranded DNA yielding uniform double helixes with chemical and mechanical robustness in a wide variety of environmental conditions.

### V.5.1. DNA nanocage: a versatile scaffold

Given the properties of DNA, DNA nanostructures have been developed showing the versatility of this molecule for building nanoscale structures (Figure V.28).<sup>252–254</sup> Structures that are of particular interest because they can be used as nanocontainers for targeted drug delivery are DNA polyhedra: they can encapsulate cargos (biomolecules, drugs, fluorescent or magnetic probes) within their cavity while the DNA scaffold ensures biocompatibility and allows surface modification for targeting.

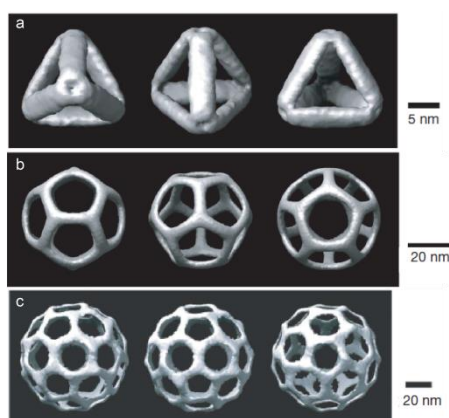


Figure V.28: Examples of 3D views of reconstruction after cryo-TEM of self-assemblies of DNA into polyhedral structures. a. Tetrahedron, b. Dodecahedron and c. Buckyball.<sup>254</sup>

We collaborated with Yamuna Krishnan's group in NCBS (National Center for Biological Sciences, India) who had developed a DNA icosahedron built by self-assembly of carefully chosen DNA strands.<sup>255</sup> The icosahedron was chosen as it constitutes the best compromise between a large encapsulation volume and a small pore size: this allows the incorporation of a relatively large cargo, while preventing it from leaking through the pores and from leaving the nanocage.

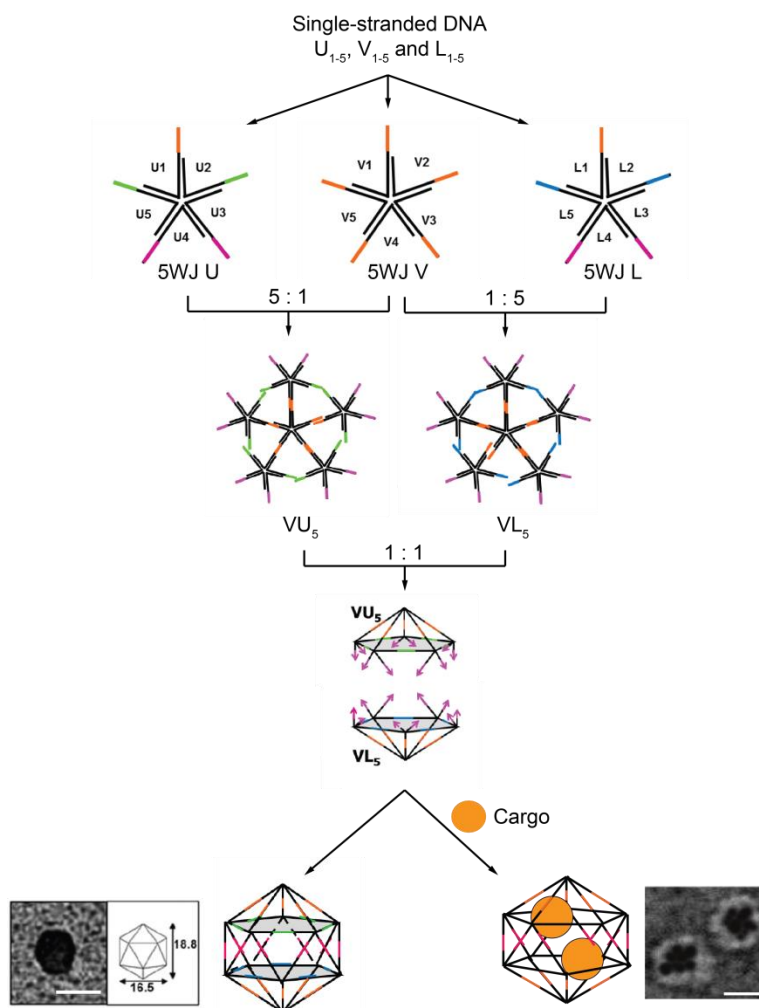


Figure V.29: Schematic of DNA icosahedron formation and of cargo encapsulation.<sup>255</sup> Scale bars are 20 nm.

The DNA icosahedron was built through self-assembly of single-stranded DNA (Figure V.29). Thanks to the highly specific hydrogen-bonding between complementary base pairs, three 5-way junctions (5WJ) were formed. There are called V (for vertex), U (for upper) and L (for lower). The annealing of a mixture of V and U in 1:5 ratio leads to a half-icosahedron, VU<sub>5</sub> that can in turn be annealed with the other half-icosahedron, VL<sub>5</sub>, produced in a similar fashion. This yields a full icosahedron with an encapsulation volume of  $\sim 1000 \text{ nm}^3$  and a pore size of  $\sim 2.8 \text{ nm}$ . Such an icosahedron is eventually around 20 nm high and 16 nm thick according to simulations that are confirmed by TEM (average size around 23 nm). A simple experiment of encapsulation of citrate-capped gold nanoparticles (GNPs) of different sizes in those icosahedra showed that the maximum size of an encapsulable nanoparticle is around 13 nm (10 nm for the inorganic core) and that the smallest encapsulable nanoparticle is around 2.5 to 3 nm, confirming the predicted pore size of 2.8 nm: smaller nanoparticles, even if encapsulated, leave the nanocage through those pores (Figure V.30).<sup>255</sup>

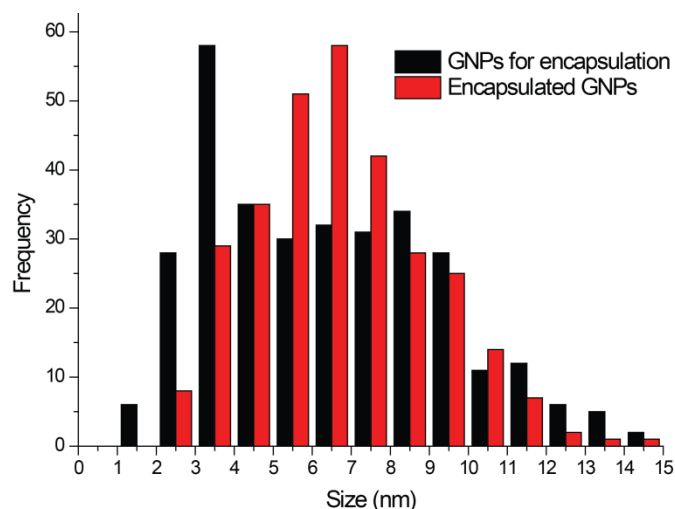


Figure V.30: Frequency count of GNPs before and after encapsulation determined by TEM observations. GNPs smaller than 2.5 nm do not get encapsulated as they are smaller than the pore size and can leak out of the icosahedron.

Modifications can be easily made in the DNA sequences that compose the icosahedron. A specific tag can thus be attached to the nanocage for functionalization of its surface. An important point is that the DNA can be modified anywhere along the base sequence as long as it does not alter the formation and stability of the scaffold. This allows binding a molecule to a base that is oriented towards the outside of the DNA cage to maximize both the exposure to the environment and the interaction between the molecule and its target (Figure V.31). Finally, as the icosahedron is built from oligonucleotides some of which are present in only one copy in the final icosahedron structure, monofunctionalization is possible: modifying only one DNA strand ( $V_1$  to  $V_4$ ) will only introduce a single modification in the whole final DNA structure. The functionalization can actually be very precisely tuned as the DNA sequences can be modified to express only a given number of coupling groups in the nanocage: functionalization with a specific number of groups can be achieved and their position on the nanocage can be accurately controlled.

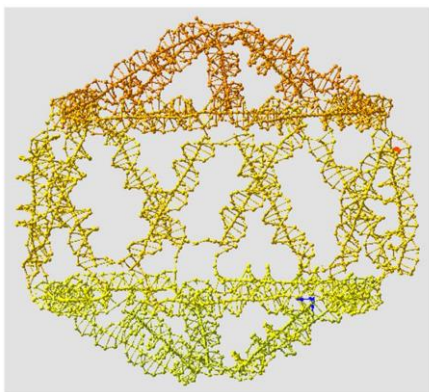


Figure V.31: Computed model of DNA icosahedron. The orientation of the functionalizing group towards the outside of the nanocage can be checked according to its position.

## V.5.2. Encapsulation of Quantum Dots in a DNA nanocage

The DNA icosahedron provides us with a biocompatible scaffold, easily functionalizable, that can encapsulate cargoes for targeted imaging. For this purpose, we used Quantum Dots as fluorescent probes.

### V.5.2.1. Preparation of Quantum Dots

In order to encapsulate QDs within the DNA nanocage, a step of ligands exchange is necessary to make the QDs dispersible in aqueous media where the DNA icosahedron is formed.

The first studies were performed on DHLA-capped QDs. DHLA is a short molecule that exhibits two thiol anchoring groups and a carboxylic group enabling dispersion in water. It is commonly used as hydrophilic ligand for Quantum Dots (Figure V.10).

In a typical ligand exchange procedure, 4 nmol of QDs in hexane are precipitated with ethanol (EtOH). The supernatant is discarded, and the precipitate is redispersed in 500  $\mu\text{L}$  of pure DHLA and left overnight at 60°C. 3 mL of dimethylformamide (DMF) are then added, followed by the addition of a few milligrams of potassium *tert*-butoxide (*t*BuOK) to deprotonate the carboxylic group. The solution is sonicated, stirred, and centrifuged: DHLA-capped QDs precipitate while the excess DHLA stays in polar solution in the DMF. The precipitate is washed twice with EtOH and finally redispersed in 1 mL of sodium tetraborate buffer solution (10 mM in water, pH=9).

The QDs used for this study are CdSe/CdS/ZnS QDs of 5 nm in diameter with an emission at 605 nm. The ligand layer around the QDs adds an additional volume to the nanoparticle and its size needs therefore to be checked by Dynamic Light Scattering (DLS) to ensure it is small enough to be encapsulated within the DNA host. Indeed, DLS

measurements take into account a hydration layer around the inorganic core of the QDs that includes the ligand layer, the counter-ions close to the carboxylic group and the water molecules responsible for the dispersion of the nanoparticles. The hydrodynamic diameter is around 9 nm in solution, *i.e.* below the maximal encapsulable size of 13 nm (Figure V.32).

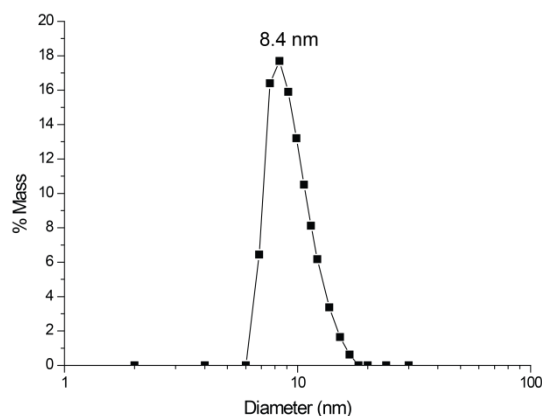


Figure V.32: Hydrodynamic diameter of the studied QDs, measured by DLS. The diameter of the QDs with their solvated ligand shell is around 9 nm.

#### V.5.2.2. Encapsulation of QDs in the nanocage

The encapsulation of QDs is performed as follows: a 4-fold excess (so that every DNA cage carries at least one QD) of QDs (4  $\mu\text{M}$  in sodium tetraborate buffer solution) is mixed with a solution of VU<sub>5</sub> and VL<sub>5</sub> half-icosahedra (1  $\mu\text{M}$  in 10 mM sodium phosphate buffer, pH 6, 100mM NaCl, 1mM MgCl<sub>2</sub>). The solution was annealed for 4h at 45°C and the temperature was then slowly decreased at a rate of 1°C per 20 minutes to room temperature. Several scenarios are then possible:

- The QDs get encapsulated. The DNA half-icosahedra possess some positive pockets (including Mg<sup>2+</sup> ions) that attract the negatively charged QDs.
- The QDs do not get encapsulated. The negative charges of DNA may repel the negatively charged QDs.
- The QDs can get stuck to the DNA icosahedra, from the outside, but do not get encapsulated inside.

Thus, a verification step is necessary to ensure that the QDs are encapsulated inside the DNA nanocage.

#### V.5.2.3. Verification of encapsulation

After the encapsulation step, a purification step is performed to separate the free QDs from the QDs in the cages or attached to them from the outside.

A first purification step was performed by gel electrophoresis, on a 0.8% agarose gel, run in a 1xTAE (Tris base / acetate / EDTA) buffer solution. The buffer increases the ionic concentration and the electrical conductivity, making the charged samples migrate faster. The icosahedra are composed of 1566 base pairs; their arrangement in an icosahedral shape makes reptating movement of the DNA in the gel matrix extremely difficult. Hence, the icosahedra do not migrate and remain stuck in the wells. Since free quantum dots have a smaller radius of gyration, they migrate into the gel, depending on their size. Thus, only icosahedra and quantum dots that are either encapsulated, or stuck to them, remain in the well.

This can be observed in Figure V.33.a where the migration of free QDs and a mixture of QDs and DNA icosahedra is shown. The gel shows two populations: the QDs that interact with the DNA nanocage that remain in the wells, and the free QDs that migrate out of the wells.

The second purification step is performed via size exclusion chromatography (SEC) on a BioSEP S3000 column (containing 5  $\mu\text{m}$  silica particles, with a pore size of 29 nm). During gel purification, aggregated quantum dots, along with encapsulated QDs in the DNA icosahedra (I-QDs), may be stuck in the wells and need to be separated using SEC. The chromatography profile is followed by absorbance at 254 nm (absorbance of DNA and QDs) and 350 nm (absorbance of QDs only), and by fluorescence (at 605 nm, QDs only). The QDs were found not to interact with the column and thus elute in the void volume (between 4 and 5 minutes of elution time for a flow rate of 0.5 mL/min). The QD-DNA complex, on the other hand, eluted at 8 min, which corresponds to the elution time of the DNA icosahedron (Figure V.33.b).

After this high-performance liquid chromatography (HPLC) purification, the hydrodynamic size was checked by DLS. Only one peak was observed, for 27 nm, corresponding to the hydrodynamic diameter of the DNA icosahedron. No peak at 8 nm was observed confirming that free QDs were correctly removed by gel electrophoresis and HPLC (Figure V.33.c). These results confirm that the addition of QDs does not affect the formation of the DNA cage. Furthermore, they prove that the QDs associate with the DNA in a way that the complex possesses the same size as the DNA capsule, suggesting the QDs are encapsulated within the cage and not attached to its surface.

Finally, direct visualization of the host-cargo complex can be performed through TEM imaging (Figure V.33.c). The QDs are electron-dense particles with high contrast in TEM, but DNA needs to be stained with 2% uranyl acetate in water: this staining is a negative staining, meaning that the stained DNA appears lighter than its surroundings.

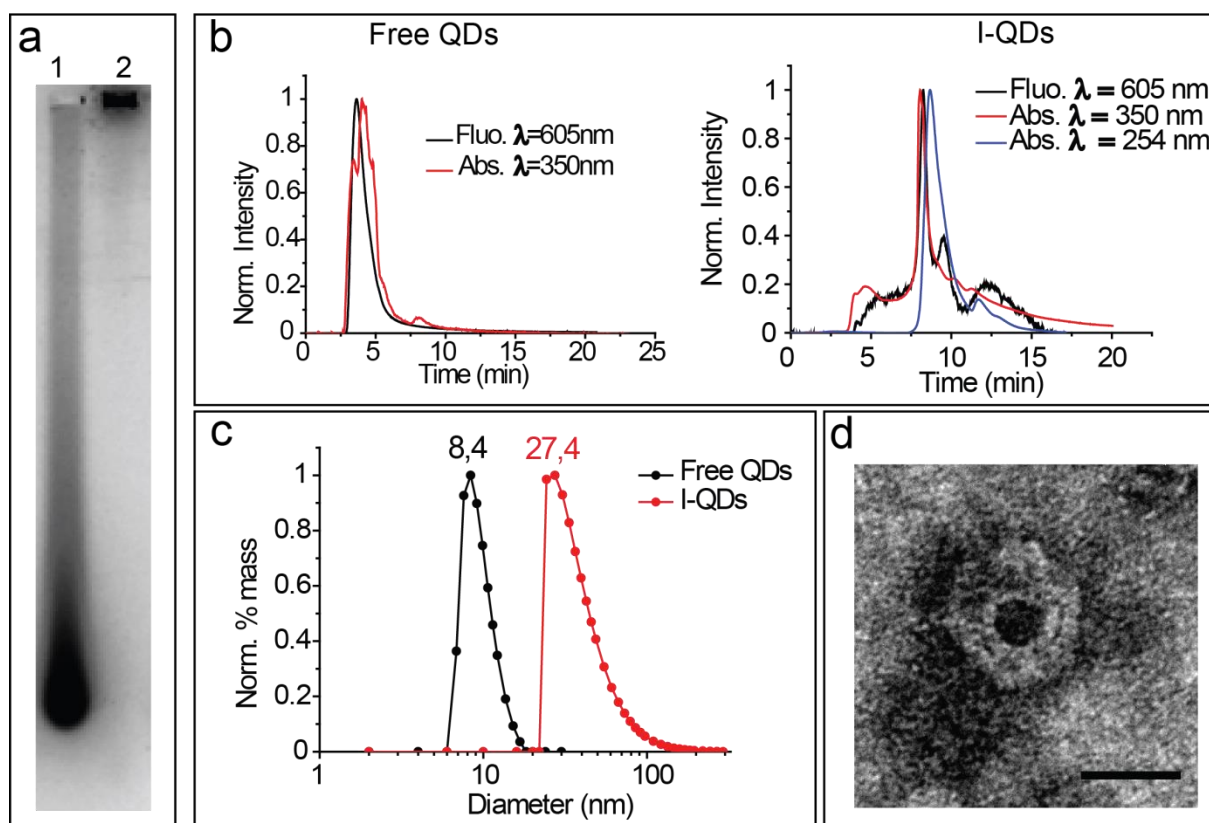


Figure V.33: a. Gel electrophoresis of free QDs (lane 1) and encapsulated QDs (I-QDs, lane 2) observed by fluorescence ( $\lambda_{\text{ex}}=350$  nm). Free QDs migrate out of the well, but the ones that are encapsulated or stuck on the icosahedra stay in the well. b. Left: Chromatogram of free QDs monitored by absorbance at 350 nm and fluorescence at 605 nm. Right: Chromatogram of free I-QDs monitored by absorbance at 254 nm and 350 nm and fluorescence at 605 nm. Free QDs elute in the void volume of the column, at 4 min. I-QDs on the other hand elute at 8 min. The absorption at 254 nm corresponds mostly to the DNA. c. Hydrodynamic diameters of I-QDs (red) measured by DLS after HPLC purification and comparison to the hydrodynamic diameter of free QDs (black). d. TEM image of a QD encapsulated in an icosahedron. Scale bar is 20 nm.

These TEM images show the hexagonal shape of the icosahedra. The QDs are located inside the icosahedra, no aggregation of QDs can be seen outside the icosahedra and the QDs seem efficiently encapsulated in the DNA nanocage.

To confirm that the I-QDs complexes are formed of QDs encapsulated within DNA capsules, a quenching experiment was performed. The fluorescence of free QDs and I-QDs was monitored after the addition of quenchers of different sizes. The quenchers will favor energy transfer from the QDs to the quencher, not allowing for radiative recombination of the exciton. The different quenchers used were: iodide anion (size: 0.5 nm), TEMPO ((2,2,6,6-Tetramethylpiperidin-1-yl)oxyl, size 1 nm) and GNPs of 2, 2.5, 3, 4 and 5 nm (the mean size and the size distribution were checked by TEM).

As the efficiencies of these quenchers are different, they need to be normalized for a fair comparison between the different quenchers. An easy way to achieve this normalization is to find the concentration of quenchers that quench 50% of the fluorescence. The Stern-Volmer plot provides a way to calculate this concentration:

$$\frac{F_0}{F} = 1 + K_{SV} \cdot [Q]$$

where  $F_0$  is the fluorescence without quencher,  $F$  is the fluorescence after the addition of quenchers,  $K_{SV}$  is the Stern-Volmer constant and  $[Q]$  is the quencher concentration. The value  $F_0/F = 2$  corresponds to 50% quenching. This method, after plotting a calibration curve, allows calculating the concentration of quenchers needed to decrease the fluorescence by 50%, thus normalizing their quenching efficiency. Each quencher is then added at its 50%-quenching concentration (corrected by a dilution factor) to solutions of free QDs and I-QDs independently. If the QDs are free or stuck outside the icosahedra, all the quenchers will be efficient in quenching the QDs (because there is no obstacle to the collision between them and the QDs) and, for all the quenchers, 50% of the initial fluorescence intensity should be observed. On the other hand, if the QDs are encapsulated inside the icosahedra, only the smallest quenchers will be able to quench them, the bigger ones being too large to diffuse into the icosahedra. Thus, there should be 50% quenching for quenchers smaller than 2.8 nm, and no quenching for quenchers larger than 2.8 nm, yielding a sigmoidal curve as a function of size of quencher (Figure V.34).

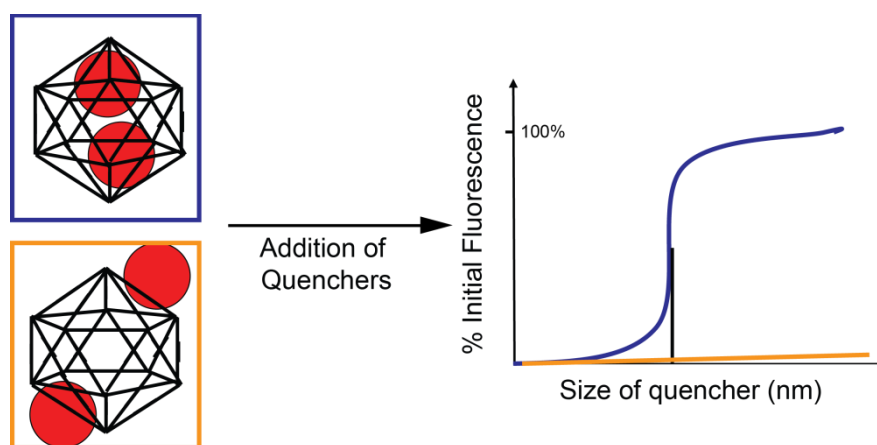


Figure V.34: Schematic of the quenching experiment principle. If the QDs are encapsulated in the DNA icosahedron (blue), they can only be quenched by quencher that can diffuse inside the cage, i.e. of size smaller than the pore size. If the QDs are stuck on the outside of the DNA cage (orange), quenchers of all sizes can quench their fluorescence as they do not need to diffuse in the cage. The black vertical bar corresponds to the size of quencher equal to the DNA-cage pore size.

The experiment was performed in a quartz cuvette. The curves representing  $F_0/F$  as a function of quencher size in the case of free QDs and in the case of isolated and purified I-QDs were compared (Figure V.35).

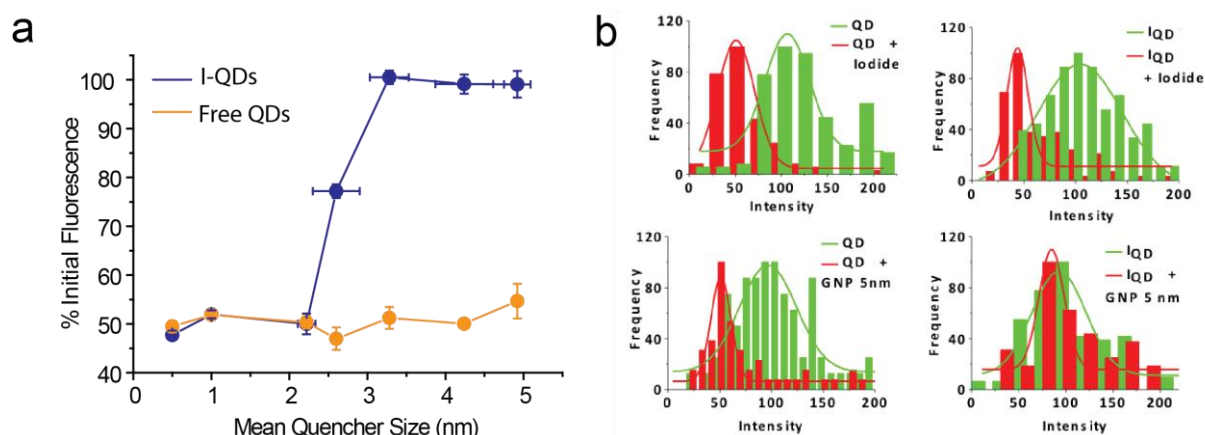


Figure V.35: a. Percentage of initial fluorescence intensity of free QDs (orange) and I-QDs (blue) after the addition of quenchers of different sizes for 50% quenching. b. Normalized frequency counts of the fluorescence intensity of free QDs (left) and I-QDs (right) after the addition of small (iodide, upper part) and large (5 nm GNPs, lower part) quenchers.

For free QDs, quenchers of any size were able to quench the fluorescence by 50% when they were added at a concentration of  $1/K_{SV}$ ; the QDs are indeed accessible to all quenchers. However, for I-QDs, only quenchers smaller than  $\sim 2.5$  nm were able to quench the fluorescence of the QDs while the quenchers larger than  $\sim 3$  nm were unable to efficiently quench the QD fluorescence. This was further confirmed at the single particle level with the measurement of the mean fluorescence intensity of  $\sim 100$  particles (QDs or I-QDs) in the presence of quenchers of different sizes. This confirms that in the I-QD complexes, the QDs are inside the DNA nanocages, and that the pore through which quenchers can diffuse inside the cage has a size between 2.5 nm and 3 nm (the calculated pore size is 2.8 nm).

The DNA icosahedron offers a wide encapsulation volume together with a small pore size. The addition of a cargo during the synthesis of the nanocage does not alter the formation of the scaffold, and cargoes of different sizes (up to 11 nm) can be encapsulated within the DNA cage. Thus, these results demonstrate that it is possible to encapsulate QDs within a DNA cage, by definition biocompatible, which can be easily functionalized in a precisely controlled manner.

## V.5.3. Monofunctionalization of DNA icosahedron

DNA has a unique molecular programmability that allows easy modifications of the oligonucleotide sequence. Besides, as the DNA nanocage is made of different sequences, some of them present only once in the nanostructure, the precise modification of one of the sequence allows introducing a given number of reactive functions for functionalization.

In order to functionalize the I-QD complexes to target a specific endocytosis pathway, it is necessary to identify the positions of the nucleotides in the DNA sequence of the icosahedron that project to the outside of the cage, so that the targeting element coupled to the DNA is displayed as efficiently as possible. For this study, a folic acid (FA) targeting element was chosen. FA drives internalization inside cells through binding to FA receptors and triggers endocytosis. It was attached at seven different positions on different icosahedra, but along the same DNA strand, so that they span a full helical turn (Figure V.36.a). The icosahedra also expressed an Alexa647 fluorescent marker (the resulting complex is called I-FA/647). A solution containing I-FA/647 was added to cells expressing folate receptors, as well as transferrin receptors. To visualize the endocytic pathway, transferrin labeled with Alexa568, Tf568, was also added (Figure V.36.b). The best uptake efficiency was obtained for the icosahedron whose FA was coupled to position 11. When the FA is moved away from those positions, the uptake is dramatically decreased (Figure V.36.c). An atomistic model confirms that position 11 is the one that project towards the outside of the cage, increasing the accessibility of FA for its receptor, explaining the higher uptake.

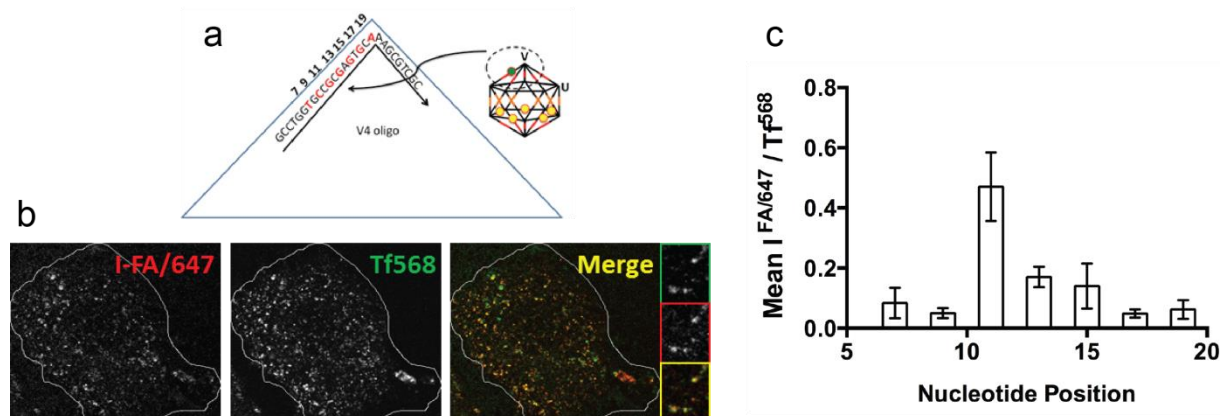


Figure V.36: a. Scheme of icosahedron monofunctionalization. Only one position on one oligonucleotide  $V_4$  has been modified to attach folic acid. The DNA nanocage is besides marked with fluorescent Alexa647. b. Fluorescence images showing colocalization of I-FA/647 and Tf568 in cells. c. Measurement of the efficiency of the uptake of I-FA/647 according to the position of the folic acid tag of the DNA  $V_4$  strand (normalized by the uptake efficiency of Tf568).

Control experiments with an excess of free FA (to compete out the binding of the FA-functionalized DNA cage), with cells that lack folate receptors or with DNA icosahedra that do

not express the FA tag showed no uptake in cells (Figure V.37). This demonstrates that the FA attached to the DNA cage is responsible, via its binding to the folate receptor, of the endocytosis via the folate receptor endocytosis pathway.

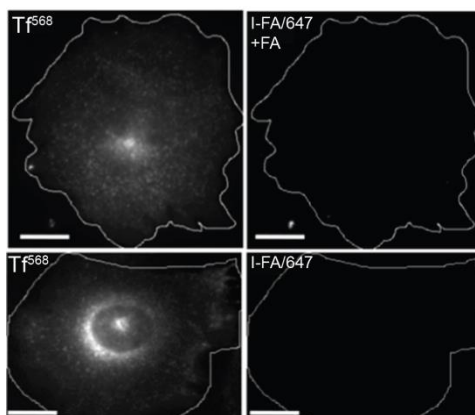


Figure V.37: Fluorescence images of cells labeled with fluorescent transferrin Tf568 and I-FA/647 with an excess of free FA which competed out the uptake of I-FA/647(top) or with cells that do not express the FA receptors (bottom). These control experiments prove that the uptake of I-FA/647 was due to the triggering of FA receptors that bind to the FA on the functionalized icosahedron.

Finally, now that the best position in the DNA sequence is known for coupling of a FA targeting element, and that the internalization process has been verified using empty cages, cells were incubated with fluorescent transferrin (Tf488) and I-QD/FA, *i.e.* DNA nanocages that contain QDs as cargoes and are monofunctionalized with one FA at position 11. In cells expressing folate receptors, free QDs did not show any uptake. Transferrin and I-QD/FA showed colocalization which confirms that correct monofunctionalization of QDs through the DNA scaffold has been achieved (Figure V.38).

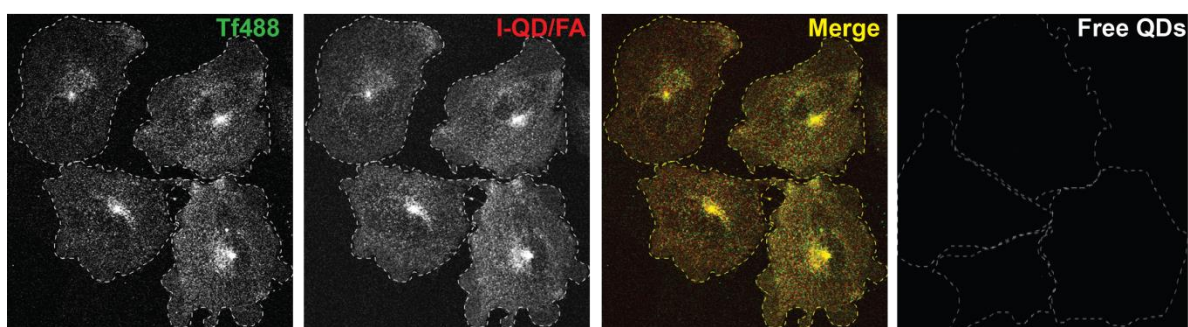


Figure V.38: Colocalization of fluorescently labeled transferrin Tf488 and I-QD/FA, *i.e.* monofunctionalized FA-labeled icosahedron at position 11. The colocalization shows that the DNA nanocage containing QDs is efficiently uptake through the FA pathway. The negative control with free QDs shows no uptake.

## V.5.4. Probing the Shiga toxin endocytosis pathway

Shiga Toxin is a protein that binds to specific receptors Gb3 on the plasma membrane of cells. After binding, a clustering of the receptors occurs and leads to the formation of invaginations that will endocytose the protein. The endosomes will carry it to the Golgi apparatus and then to the endoplasmic reticulum through the retrograde pathway, where it stops the cell protein synthesis (Figure V.39).<sup>256</sup> Monofunctionalized probes are necessary to trigger this endocytosis pathway as multivalent probes have been shown not to be delivered to the Golgi apparatus.<sup>257,258</sup>

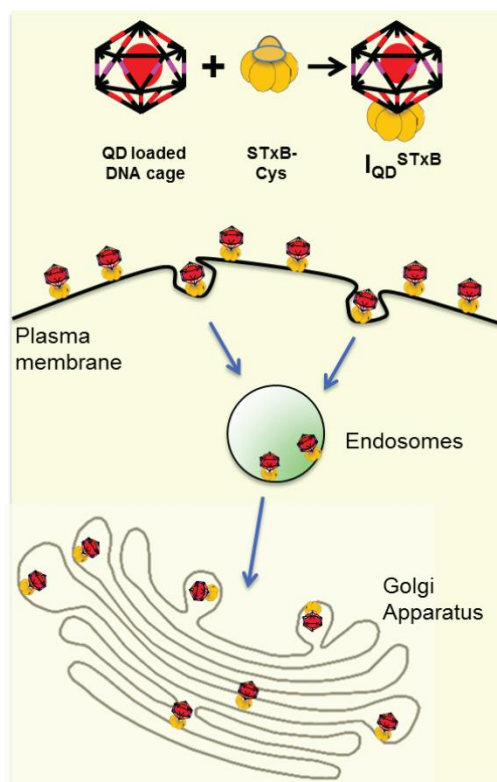


Figure V.39: Scheme of Shiga toxin B subunit labeled I-QD endocytosis pathway towards the Golgi apparatus.

The DNA icosahedron has been shown to be a great candidate for (i) encapsulation of cargoes like fluorescent probes (QDs) and (ii) perfectly controlled monofunctionalization of its surface. The endocytosis pathway of Shiga toxin can therefore be probed with a monofunctionalized DNA cage bearing one STxB (Shiga toxin B subunit, responsible for binding but non-toxic) moiety and carrying QDs.

However, the endocytosis of the DNA cage with a STxB unit has first to be shown. In order to check this, STxB was attached through a cysteine group to a DNA cage carrying a Cy3 fluorescent probe. HeLa cells were incubated with I-STxB/Cy3 and fluorescently labeled STxB, and they were found to colocalize (Figure V.40.a). Colocalization was also found when

I-STxB/Cy3 was incubated with cells expressing Rab5-GFP (GFP labeled early endosomal marker; Figure V.40.b), confirming that I-STxB/Cy3 is endocytosed in the cells and that it targets early endosomes through the STxB retrograde endocytosis pathway. Finally, a longer incubation of I-STxB/Cy3 and fluorescently labeled STxB showed colocalization in the Golgi apparatus (Figure V.40.c) (confirmed by Galt-GFP, a Golgi apparatus marker, Figure V.40.d).

This proves that the DNA nanocage coupled to one STxB follows the retrograde pathway. Furthermore, a DNA cage carrying QDs (I-QD/STxB) is found to be efficiently internalized and colocalizes with the Golgi apparatus marker (Figure V.40.e), while free QDs do not undergo endocytosis (Figure V.40.f).

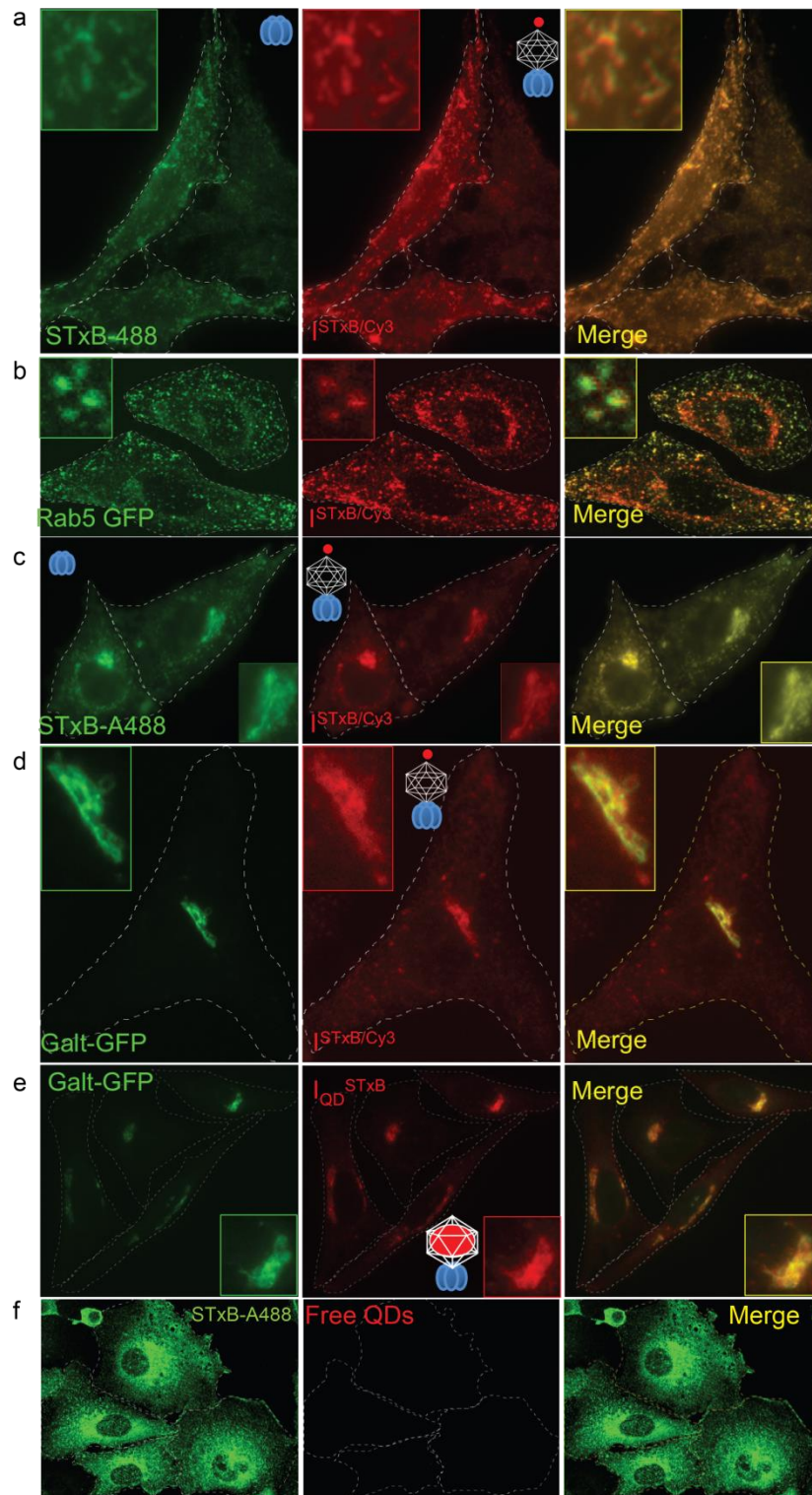


Figure V.40: a. Colocalization of fluorescently-labeled STxB and fluorescent STxB-labeled DNA icosahedron (I-STxB/Cy3). b. Colocalization of Rab5-GFP, a fluorescent marker of early endosomes, and fluorescent STxB-labeled DNA icosahedron (I-STxB/Cy3). The DNA nanocage is efficiently targeted to the early endosomes. c. Colocalization of fluorescently-labeled STxB and fluorescent STxB-labeled DNA icosahedron (I-STxB/Cy3) after 45 min of incubation. The markers are colocalized in the Golgi apparatus, which is confirmed by d. the colocalization of the same labeled icosahedron (I-

*STxB/Cy3) and Galt-GFP, a fluorescent Golgi marker. e. Similar experiment performed with QD-loaded DNA icosahedron and colocalization of Galt-GFP and I-QD/STxB. f. Control experiment: free QDs are not uptaken by the cells.*

This is the first time that the endocytosis up to the Golgi apparatus has been shown with colloidal particles, and in particular QDs. Given their photostability, Quantum Dots can be used for long term tracking where organic fluorophores bleach after a few minutes, or even seconds. It is then possible to study the dynamics of the STxB-mediated transport at a single particle precision level.

HeLa cells were labeled with a mixture of STxB-labeled DNA icosahedron carrying QDs (I-QD/STxB) and free STxB (the latter one's role was to promote internalization and ensure that I-QD/STxB were incorporated into larger clusters to facilitate their observation by Total Internal Reflection Fluorescence, or TIRF, microscopy). A bicolor imaging of I-QD/STxB and fluorescently labeled microtubules shows that the endosomes containing I-QD/STxB colocalize with the microtubules, and show active motility on them (Figure V.41). Their dynamics include bursts of active transport with pauses in between, as well as back and forth motility along one or several microtubules. A single particle tracking observation shows that a single endosome switches from confined or diffusive motion to active motions in bursts. The endosomes spend most of their time in a confined or diffusive regime but the transport to targeted organelles is performed in active bursts. The pausing events may happen for several reasons: crossing at intersections of microtubules, interaction with endoplasmic reticulum, actin meshwork and other organelles.<sup>259,260</sup> Their speed as well as their direction of motion can be observed through single particle tracking: a single endosome can move along  $2.4 \pm 1.4 \mu\text{m}$  with an average speed of about  $0.5 \pm 0.2 \mu\text{m/s}$ , changing from diffusive transport to bursts.

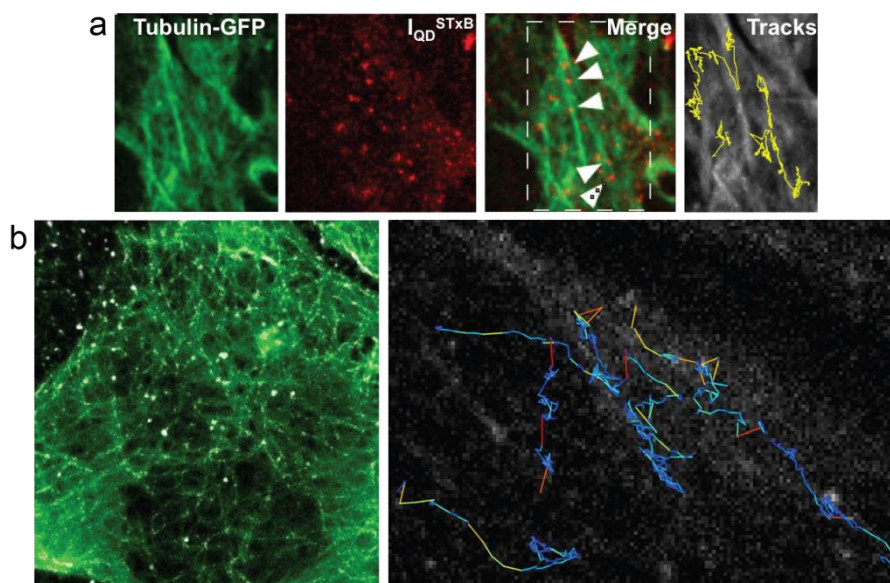


Figure V.41: Single-particle tracking by TIRF imaging. *a.* Example of tracking of Shiga-toxin labeled I-QD (red) along the microtubules (GFP-labeled, green). *b.* Example of monitoring the direction and speed (right, color coded) of the I-QD/STxB (left, white) along the microtubules (left, green).

DNA icosahedra present several advantages: they are stable, easily functionalizable, biocompatible... QDs have unique properties that make them excellent probes for biological imaging and more particularly for single particle tracking or long-term imaging. Encapsulating QDs in a DNA icosahedron does not change the properties of neither the cage nor the fluorescent probe. Given the fact that a DNA structure can be precisely controlled and simulated, it is possible to choose the best position for the coupling with a targeting moiety. Besides, this coupling can be performed in a fully controlled manner so that monofunctionalization of the DNA cage, and consequently of the QDs it contains, can be achieved. The endocytic pathway of STxB, highly sensitive to multivalent receptor binding, could thus be studied at the single particle level and information about the dynamics of the STxB-mediated endosome formation and transport were collected.

This methodology has a huge potential for biological imaging as it can be generalized to several QD-types as well as several biological tags. Another step might be the investigation of receptor-ligand interactions such as the formation of clusters: they can be studied through the finely controlled functionalization of the DNA cage (number and position of the functional groups) as different stoichiometry of associations between ligand and receptors can lead to different endocytosis pathways.

### V.5.5. Conclusion

DNA self-assemblies are robust and biocompatible hosts that offer the possibility to encapsulate different types of cargoes. Fluorescent QDs were here used as markers to probe the Shiga toxin retrograde endocytosis pathway. This pathway is sensitive to the number of receptors involved in the endocytosis process. The DNA icosahedron can be easily modified to express only one targeting group, opening the road to monofunctionalization of QDs. The encapsulation of QDs, as well as the monofunctionalization of the DNA cage, was verified. The strong and robust fluorescence signal of QDs was then used to follow the endocytosis dynamics of the QD-DNA icosahedron complex up to the Golgi apparatus.





---

## Conclusion

This 3-year doctoral work was focused on the life of CdSe/CdS nanocrystals, from their synthesis, to their optical study, to the modification of their surface chemistry, to their applications, mostly as biological fluorescent markers.

The first part aimed at improving the colloidal synthesis of non-blinking CdSe/CdS Quantum Dots. Thick-shell CdSe/CdS QDs synthesized in the lab have already been shown to decrease the blinking of individual particles. This synthesis was however done only on one type of core. The synthesis developed as part of this work yielded non-blinking CdSe/CdS on different types of CdSe cores, making it fast, versatile and robust to grow thick CdS shells on CdSe core.

These thick-shell CdSe/CdS QDs did show some remaining flickering in air, at room temperature, decreasing the overall quantum yield. Therefore, the next step of this work was to develop CdSe/CdS QDs that show no blinking and no flickering at room temperature under atmospheric pressure, with a quantum yield close to unity. In order to get closer to this perfect emitter, two important properties were combined in the same QDs: a thick shell and a gradient of composition between the core and the shell. Both these structural characteristics have been shown to decrease the blinking. Besides, previous works have claimed near-unity quantum yield for the monoexciton, but the quantum yield of the biexciton remained overall unexplored. The bulky-gradient CdSe/CdS QDs (b-QDs) synthesized here have shown the complete elimination of blinking at room temperature and in air. The measured quantum yield was ~100% for the monoexciton as well as for the biexciton. Non-radiative Auger recombinations only occurred for higher order multiexcitonic transitions, yielding at high excitation power individual white-light-emitting QDs. The lack of blinking and the high quantum yield of the mono- and biexciton make those b-QDs very interesting for applications where a high brightness and low energy consumption are required.

Another strategy was explored to decrease the blinking of CdSe/CdS QDs. Capping the QD with a gold nanoshell resulted in golden-QD with accelerated radiative recombinations. Coupling between the exciton and the surface plasmons of gold decreased the radiative lifetime by a factor of ~6 due to the Purcell effect. These faster radiative recombinations overcame Auger recombinations, which resulted in suppressed blinking of the QD. Finally, golden-QDs showed increased resistance to continuous excitation, high-

power illumination or high-energy electron beam, which makes them useful bimodal probes for several applications from lithography to biology.

Finally, the last part of this work focused on biological applications of CdSe/CdS QDs. Their electron-dense inorganic core and their unique optical properties can be taken advantage of for bimodal imaging with multiscale resolution. Voltage-dependent calcium channels (VDCCs) in *C. elegans* worms were targeted with modified CdSe/CdS QDs that exhibit antibodies at their surface. Optical imaging confirmed the specific labeling. The worms were then cut into 70-nm-thick sections that were imaged by transmission electron microscopy. The Cd-based QDs were clearly visible in the worm organism which allowed precise localization and counting of the VDCCs in 3D reconstructions of the worm synaptic area.

The coupling strategy used in this case did not allow for monofunctionalization of QDs. The study of some endocytosis pathways, however, requires the probe to bind to only one receptor. This was achieved using a novel host-cargo strategy: QDs were encapsulated in a DNA nanocage whose synthesis was perfectly controlled and oriented to present at its surface only one targeting element. This QD-DNA complex proved to be efficient for the study of Shiga-toxin mediated retrograde endocytosis pathway in cells. The dynamics of this pathway could be studied using the fluorescence of QDs.

The study of CdSe/CdS QDs over the last 30 years has increased the understanding of this model system. Although many improvements have been brought to develop bright, high-quantum-yield QDs, there is still room for innovation. QDs with a 100% quantum yield are excellent candidates for low-energy-consumption display devices. However, they have been developed only in the red spectral region, when green efficient emitters are also required. This may be achieved by QDs based on new materials or new structures. Coupling to other metal surface plasmons might also lead to high-efficiency emitters in a different spectral range.

15 years ago, the control of the shape during NC growth opened interesting perspective for the growth of even better QDs. Nanoplatelets can now be grown with high quantum yields, they can withstand long excitation powers and high temperatures, and can soon replace spherical QDs for display devices as their emission is spectrally much narrower, giving colors with even higher purity. Improvements of the synthesis of 2D systems are still underway and reaching higher emitting efficiency is now within reach.

Finally, even if CdSe/CdS Quantum Dots, due to their easy and robust synthesis, and high brightness, can be used for biological imaging in laboratory animals, their cadmium content makes them dangerous for use in humans. Besides, their emission range in the visible part of the spectrum strongly limits their use in complex organisms that require a large

penetration depth and are transparent in the infrared region. Not to mention that the European Union has now forbidden cadmium even for use in devices. Therefore, the next revolution in the QDs community will surely come from efficient, cadmium-free NCs. QDs based on III-V compounds are now under thorough investigation (InP for example), and the far infrared spectral region is yet to be explored.



---

## References

1. Lu, X., Rycenga, M., Skrabalak, S. E., Wiley, B. & Xia, Y. Chemical synthesis of novel plasmonic nanoparticles. *Annu. Rev. Phys. Chem.* **60**, 167–192 (2009).
2. Oldenburg, S., Averitt, R. & Halas, N. Metal nanoshells. (2004). at <<http://www.google.st/patents/US20040214001>>
3. Kovalenko, M. V *et al.* Prospects of Nanoscience with Nanocrystals. *ACS Nano* **9**, 1012–1057 (2015).
4. Issa, B., Obaidat, I., Albiss, B. & Haik, Y. Magnetic Nanoparticles: Surface Effects and Properties Related to Biomedicine Applications. *Int. J. Mol. Sci.* **14**, 21266–21305 (2013).
5. Ekimov, A. I. & Onushchenko, A. A. Quantum size effect in three-dimensional microscopic semiconductor crystals. *Jetp Lett.* **34**, 345–349 (1981).
6. Efros, A. L. Interband absorption of light in a semiconductor sphere. *Sov. Phys. Semicond. USSR* **16**, 772–775 (1982).
7. Brus, L. E. A simple model for the ionization potential, electron affinity, and aqueous redox potentials of small semiconductor crystallites. *J. Chem. Phys.* **79**, 5566 (1983).
8. Murray, C. B., Norris, D. & Bawendi, M. G. Synthesis and characterization of nearly monodisperse CdE (E= S, Se, Te) semiconductor nanocrystallites. *J. Am. Chem. Soc.* **115**, 8706–8715 (1993).
9. Nirmal, M. *et al.* Fluorescence intermittency in single cadmium selenide nanocrystals. *Nature* **383**, 802–804 (1996).
10. Efros, A. & Rosen, M. Random Telegraph Signal in the Photoluminescence Intensity of a Single Quantum Dot. *Phys. Rev. Lett.* **78**, 1110–1113 (1997).
11. Chen, Y. *et al.* ‘Giant’ multishell CdSe nanocrystal quantum dots with suppressed blinking. *J. Am. Chem. Soc.* **130**, 5026–7 (2008).
12. Mahler, B. *et al.* Towards non-blinking colloidal quantum dots. *Nat. Mater.* **7**, 659–64 (2008).
13. Hohng, S. & Ha, T. Near-Complete Suppression of Quantum Dot Blinking in Ambient Conditions. *J. Am. Chem. Soc.* **126**, 1324–1325 (2004).

14. Belacel, C. *et al.* Controlling spontaneous emission with plasmonic optical patch antennas. *Nano Lett.* **13**, 1516–1521 (2013).
15. Javaux, C. *et al.* Thermal activation of non-radiative Auger recombination in charged colloidal nanocrystals. *Nat. Nanotechnol.* **8**, 206–12 (2013).
16. Michalet, X. *et al.* Quantum dots for live cells, in vivo imaging, and diagnostics. *Science* **307**, 538–44 (2005).
17. Chuang, C.-H. M., Brown, P. R., Bulović, V. & Bawendi, M. G. Improved performance and stability in quantum dot solar cells through band alignment engineering. *Nat. Mater.* **13**, 1–6 (2014).
18. Tang, J. *et al.* Colloidal-quantum-dot photovoltaics using atomic-ligand passivation. *Nat. Mater.* **10**, 765–771 (2011).
19. Rizzo, A. *et al.* Blue light emitting diodes based on fluorescent CdSe/ZnS nanocrystals. *Appl. Phys. Lett.* **90**, 14–17 (2007).
20. Colvin, V. L., Schlamp, M. C. & Alivisatos, a P. Light-Emitting-Diodes Made from Cadmium Selenide Nanocrystals and a Semiconducting Polymer. *Nature* **370**, 354–357 (1994).
21. Mashford, B., Stevenson, M. & Popovic, Z. High-efficiency quantum-dot light-emitting devices with enhanced charge injection. *Nat. ...* **7**, 407–412 (2013).
22. Shirasaki, Y., Supran, G. J., Bawendi, M. G. & Bulović, V. Emergence of colloidal quantum-dot light-emitting technologies. *Nat. Photonics* **7**, 933–933 (2013).
23. Klimov, V. I. Optical Gain and Stimulated Emission in Nanocrystal Quantum Dots. *Science* **290**, 314–317 (2000).
24. Grim, J. Q. *et al.* Continuous-wave biexciton lasing at room temperature using solution-processed quantum wells. *Nat. Nanotechnol.* **9**, 891–895 (2014).
25. Brokmann, X., Giacobino, E., Dahan, M. & Hermier, J. P. Highly efficient triggered emission of single photons by colloidal CdSe/ZnS nanocrystals. *Appl. Phys. Lett.* **85**, 712–714 (2004).
26. Alivisatos, a P. Semiconductor Clusters, Nanocrystals, and Quantum Dots. *Science* **271**, 933–937 (1996).
27. Banin, U., Cao, Y., Katz, D. & Millo, O. Identification of atomic-like electronic states in indium arsenide nanocrystal quantum dots. *Nature* **400**, 542–544 (1999).
28. Klimov, V. I. *Nanocrystal Quantum Dots*. (CRC Press, 2010). at <http://books.google.fr/books?id=BYIsyk3emCEC>
29. Gross, E. F. & Kapliansky, A. A. A Spectroscopic Study of Absorption and Luminescence of Cuprous Chloride, Introduced into a Crystal of Rock Salt. *Opt. / Spektrosk.* **2**, 204–209 (1957).

30. Katzschmann, R., Rehfeld, A. & Kranold, R. Optical anomaly of small particles in glasses. *Phys. Status Solidi* **40**, K161–K161 (1977).
31. Ekimov, A. I. & Onushchenko, A. A. Quantum size effect in the optical-spectra of semiconductor micro-crystals. *Sov. Phys. Semicond.* **16**, 775–778 (1982).
32. Ekimov, A. I. & Onushchenko, A. A. Size quantization of the electron energy spectrum in a microscopic semiconductor crystal. *JETP lett* **40**, 1136–1139 (1984).
33. Brus, L. E. Electron–electron and electron-hole interactions in small semiconductor crystallites: The size dependence of the lowest excited electronic state. *J. Chem. Phys.* **80**, 4403 (1984).
34. Henglein, A. Photo-Degradation and Fluorescence of Colloidal-Cadmium Sulfide in Aqueous Solution. *Berichte der Bunsengesellschaft für Phys. Chemie* **86**, 301–305 (1982).
35. Ekimov, A. I. *et al.* Absorption and intensity-dependent photoluminescence measurements on CdSe quantum dots: assignment of the first electronic transitions. *J. Opt. Soc. Am. B* **10**, 100 (1993).
36. Borrelli, N. F. & Luong, J. C. Semiconductor Microcrystals In Porous Glass. *Proc. SPIE* **0866**, 104–109 (1987).
37. De Rougemont, F., Frey, R., Roussignol, P., Ricard, D. & Flytzanis, C. Evidence of strong Auger recombination in semiconductor-doped glasses. *Appl. Phys. Lett.* **50**, 1619–1621 (1987).
38. Hines, M. a. & Guyot-Sionnest, P. Synthesis and Characterization of Strongly Luminescing ZnS-Capped CdSe Nanocrystals. *J. Phys. Chem.* **100**, 468–471 (1996).
39. Peng, X. *et al.* Shape control of CdSe nanocrystals. *Nature* **404**, 59–61 (2000).
40. Joo, J., Son, J. S., Kwon, S. G., Yu, J. H. & Hyeon, T. Low-temperature solution-phase synthesis of quantum well structured CdSe nanoribbons. *J. Am. Chem. Soc.* **128**, 5632–5633 (2006).
41. Ithurria, S. & Dubertret, B. Quasi 2D colloidal CdSe platelets with thicknesses controlled at the atomic level. *J. Am. Chem. Soc.* **130**, 16504–16505 (2008).
42. Efros, A. L. & Rosen, M. The electronic structure of semiconductor nanocrystals. *Annu. Rev. Mater. Sci.* **30**, 475–521 (2000).
43. Klimov, V. I. *Nanocrystal Quantum Dots, Second Edition.* *Los Alamos Sci.* **112**, (2003).
44. Norris, D. & Bawendi, M. Measurement and assignment of the size-dependent optical spectrum in CdSe quantum dots. *Phys. Rev. B* **53**, 16338–16346 (1996).
45. Guyot-Sionnest, P., Shim, M., Matranga, C. & Hines, M. Intraband relaxation in CdSe quantum dots. *Phys. Rev. B* **60**, R2181–R2184 (1999).
46. Woggon, U. *et al.* Ultrafast energy relaxation in quantum dots. *Phys. Rev. B. Condens.*

- Matter* **54**, 17681–17690 (1996).
47. Efros, A. *et al.* Band-edge exciton in quantum dots of semiconductors with a degenerate valence band: Dark and bright exciton states. *Phys. Rev. B. Condens. Matter* **54**, 4843–4856 (1996).
  48. Nirmal, M. *et al.* Observation of the ‘dark exciton’ in CdSe quantum dots. *Phys. Rev. Lett.* **75**, 3728–3731 (1995).
  49. Bawendi, M. *et al.* Electronic structure and photoexcited-carrier dynamics in nanometer-size CdSe clusters. *Phys. Rev. Lett.* **65**, 1623–1626 (1990).
  50. Htoon, H., Cox, P. & Klimov, V. Structure of Excited-State Transitions of Individual Semiconductor Nanocrystals Probed by Photoluminescence Excitation Spectroscopy. *Phys. Rev. Lett.* **93**, 187402 (2004).
  51. Empedocles, S. a. & Bawendi, M. G. Quantum-confined stark effect in single CdSe nanocrystallite quantum dots. *Science* **278**, 2114 (1997).
  52. Neuhauser, R. G., Shimizu, K. T., Woo, W. K., Empedocles, S. a. & Bawendi, M. G. Correlation between fluorescence intermittency and spectral diffusion in single semiconductor quantum dots. *Phys. Rev. Lett.* **85**, 3301–3304 (2000).
  53. Anikeeva, P. O., Halpert, J. E., Bawendi, M. G. & Bulović, V. Quantum dot light-emitting devices with electroluminescence tunable over the entire visible spectrum. *Nano Lett.* **9**, 2532–2536 (2009).
  54. Brovelli, S. *et al.* Dual-Color Electroluminescence from Dot-in-Bulk Nanocrystals. *Nano Lett.* **14**, 486–494 (2014).
  55. Dekanozishvili, G., Driaev, D., Kalabegishvili, T. & Kvatchadze, V. Thermoluminescence and absorption spectra of CdSe quantum dot-doped glass irradiated by X-rays. *J. Lumin.* **129**, 1154–1157 (2009).
  56. Rodriguez-Viejo, J. *et al.* Cathodoluminescence and photoluminescence of highly luminescent CdSe/ZnS quantum dot composites. *Appl. Phys. Lett.* **70**, 2132 (1997).
  57. Mahfoud, Z. *et al.* Cathodoluminescence in a scanning transmission electron microscope: A nanometer-scale counterpart of photoluminescence for the study of II-VI quantum dots. *J. Phys. Chem. Lett.* **4**, 4090–4094 (2013).
  58. Klimov, V. & McBranch, D. *Femtosecond 1P-to- 1S Electron Relaxation in Strongly Confined Semiconductor Nanocrystals.* *Phys. Rev. Lett.* **80**, 4028–4031 (1998).
  59. Nozik, A. J. Spectroscopy and hot electron relaxation dynamics in semiconductor quantum wells and quantum dots. *Annu. Rev. Phys. Chem.* **52**, 193–231 (2001).
  60. Efros, A. L., Kharchenko, V. A. A. & Rosen, M. Breaking the phonon bottleneck in nanometer quantum dots: Role of Auger-like processes. *Solid State Commun.* **93**, 281–284 (1995).
  61. Hendry, E. *et al.* Direct Observation of Electron-to-Hole Energy Transfer in CdSe

- Quantum Dots. *Phys. Rev. Lett.* **96**, 057408 (2006).
62. Xu, S., Mikhailovsky, A., Hollingsworth, J. & Klimov, V. Hole intraband relaxation in strongly confined quantum dots: Revisiting the 'phonon bottleneck' problem. *Phys. Rev. B* **65**, 045319 (2002).
  63. Klimov, V. I. Quantization of Multiparticle Auger Rates in Semiconductor Quantum Dots. *Science* **287**, 1011–1013 (2000).
  64. Chepic, D. I. *et al.* Auger ionization of semiconductor quantum drops in a glass matrix. *J. Lumin.* **47**, 113–127 (1990).
  65. LaMer, V. K. & Dinegar, R. H. Theory, Production and Mechanism of Formation of Monodispersed Hydrosols. *J. Am. Chem. Soc.* **72**, 4847–4854 (1950).
  66. García-Rodríguez, R., Hendricks, M. P., Cossairt, B. M., Liu, H. & Owen, J. S. Conversion Reactions of Cadmium Chalcogenide Nanocrystal Precursors. *Chem. Mater.* **25**, 1233–1249 (2013).
  67. Owen, J. S., Chan, E. M., Liu, H. & Alivisatos, a. P. Precursor conversion kinetics and the nucleation of cadmium selenide nanocrystals. *J. Am. Chem. Soc.* **132**, 18206–18213 (2010).
  68. Park, J., Joo, J., Kwon, S. G., Jang, Y. & Hyeon, T. Synthesis of monodisperse spherical nanocrystals. *Angew. Chem. Int. Ed. Engl.* **46**, 4630–60 (2007).
  69. Kolosky, M., Vialle, J. & Cotel, T. Determination of trioctylphosphine oxide and its impurities by reversed-phase high-performance liquid chromatography. *J. Chromatogr. A* **299**, 436–444 (1984).
  70. Peng, Z. A. & Peng, X. Formation of high-quality CdTe, CdSe, and CdS nanocrystals using CdO as precursor. *J. Am. Chem. Soc.* **123**, 183–184 (2001).
  71. Liu, H., Owen, J. S. & Alivisatos, a. P. Mechanistic study of precursor evolution in colloidal group II-VI semiconductor nanocrystal synthesis. *J. Am. Chem. Soc.* **129**, 305–312 (2007).
  72. Chen, O. *et al.* Synthesis of metal-selenide nanocrystals using selenium dioxide as the selenium precursor. *Angew. Chem. Int. Ed. Engl.* **47**, 8638–41 (2008).
  73. Deng, Z., Cao, L., Tang, F. & Zou, B. A new route to zinc-blende CdSe nanocrystals: Mechanism and synthesis. *J. Phys. Chem. B* **109**, 16671–16675 (2005).
  74. van Sark, W. G. J. H. M. *et al.* Photooxidation and Photobleaching of Single CdSe/ZnS Quantum Dots Probed by Room-Temperature Time-Resolved Spectroscopy. *J. Phys. Chem. B* **105**, 8281–8284 (2001).
  75. Katari, J. E. B., Colvin, V. L. V. & Alivisatos, A. P. A. X-ray Photoelectron Spectroscopy of CdSe Nanocrystals with Applications to Studies of the Nanocrystal Surface. *J. Phys. Chem.* **98**, 4109–4117 (1994).
  76. Bouroushian, M. *Electrochemistry of Metal Chalcogenides. Monogr. Electrochem.*

- (Springer Berlin Heidelberg, 2010). doi:10.1007/978-3-642-03967-6
77. Spanhel, L., Haase, M., Weller, H. & Henglein, A. Photochemistry of colloidal semiconductors. 20. Surface modification and stability of strong luminescing CdS particles. *J. Am. Chem. Soc.* **109**, 5649–5655 (1987).
  78. Dabbousi, B. O. *et al.* (CdSe)ZnS Core–Shell Quantum Dots: Synthesis and Characterization of a Size Series of Highly Luminescent Nanocrystallites. *J. Phys. Chem. B* **101**, 9463–9475 (1997).
  79. Reiss, P., Protière, M. & Li, L. Core/Shell semiconductor nanocrystals. *Small* **5**, 154–68 (2009).
  80. Pedetti, S., Ithurria, S., Heuclin, H., Patriarche, G. & Dubertret, B. Type-II CdSe/CdTe Core/Crown Semiconductor Nanoplatelets. *J. Am. Chem. Soc.* **136**, 16430–16438 (2014).
  81. Verma, S., Kaniyankandy, S. & Ghosh, H. N. Charge Separation by Indirect Bandgap Transitions in CdS/ZnSe Type-II Core/Shell Quantum Dots. *J. Phys. Chem. C* **117**, 10901–10908 (2013).
  82. Kim, S., Fisher, B. & Bawendi, M. Type-II Quantum Dots : CdTe / CdSe ( Core / Shell ) and CdSe / ZnTe ( Core / Shell ) Heterostructures. 11466–11467 (2003).
  83. Mahadevu, R., Yelameli, A. R., Panigrahy, B. & Pandey, A. Controlling light absorption in charge-separating core/shell semiconductor nanocrystals. *ACS Nano* **7**, 11055–11063 (2013).
  84. Xia, X., Liu, Z., Du, G., Li, Y. & Ma, M. Wurtzite and zinc-blende CdSe based core/shell semiconductor nanocrystals: Structure, morphology and photoluminescence. *J. Lumin.* **130**, 1285–1291 (2010).
  85. Qin, W., Shah, R. a & Guyot-Sionnest, P. CdSeS/ZnS alloyed nanocrystal lifetime and blinking studies under electrochemical control. *ACS Nano* **6**, 912–8 (2012).
  86. Swafford, L. a *et al.* Homogeneously alloyed CdS<sub>x</sub>Se<sub>1-x</sub> nanocrystals: synthesis, characterization, and composition/size-dependent band gap. *J. Am. Chem. Soc.* **128**, 12299–306 (2006).
  87. Keene, J. D., McBride, J. R., Orfield, N. J. & Rosenthal, S. J. Elimination of Hole–Surface Overlap in Graded CdS x Se 1– x Nanocrystals Revealed by Ultrafast Fluorescence Upconversion Spectroscopy. *ACS Nano* **8**, 10665–10673 (2014).
  88. Boldt, K., Kirkwood, N., Beane, G. A. & Mulvaney, P. Synthesis of Highly Luminescent and Photo-Stable, Graded Shell CdSe/Cd x Zn 1– x S Nanoparticles by In Situ Alloying. *Chem. Mater.* **25**, 4731–4738 (2013).
  89. Manna, L., Scher, E. C., Li, L.-S. & Alivisatos, a P. Epitaxial growth and photochemical annealing of graded CdS/ZnS shells on colloidal CdSe nanorods. *J. Am. Chem. Soc.* **124**, 7136–45 (2002).
  90. Cihan, A. F. *et al.* Attractive versus repulsive excitonic interactions of colloidal

- quantum dots control blue- to red-shifting (and non-shifting) amplified spontaneous emission. *J. Phys. Chem. Lett.* **4**, 4146–4152 (2013).
91. Smith, A. M., Mohs, A. M. & Nie, S. Tuning the optical and electronic properties of colloidal nanocrystals by lattice strain. *Nat. Nanotechnol.* **4**, 56–63 (2009).
  92. Piryatinski, A., Ivanov, S. a, Tretiak, S. & Klimov, V. I. Effect of quantum and dielectric confinement on the exciton-exciton interaction energy in type II core/shell semiconductor nanocrystals. *Nano Lett.* **7**, 108–115 (2007).
  93. Acharya, K. P. *et al.* Elucidation of Two Giants: Challenges to Thick-Shell Synthesis in CdSe/ZnSe and ZnSe/CdS Core/Shell Quantum Dots. *J. Am. Chem. Soc.* **137**, 3755–3758 (2015).
  94. Soni, U. *et al.* Simultaneous Type-I/Type-II Emission from CdSe/CdS/ZnSe Nano-Heterostructures. *ACS Nano* **8**, 113–123 (2014).
  95. Samokhvalov, P., Artemyev, M. & Nabiev, I. Basic principles and current trends in colloidal synthesis of highly luminescent semiconductor nanocrystals. *Chem. - A Eur. J.* **19**, 1534–1546 (2013).
  96. Ithurria, S., Guyot-Sionnest, P., Mahler, B. & Dubertret, B. Mn<sup>2+</sup> as a radial pressure gauge in colloidal core/shell nanocrystals. *Phys. Rev. Lett.* **99**, 5–8 (2007).
  97. Murray, C. B., Norris, D. J. & Bawendi, M. G. Synthesis and characterization of nearly monodisperse CdE (E = sulfur, selenium, tellurium) semiconductor nanocrystallites. *J. Am. Chem. Soc.* **115**, 8706–8715 (1993).
  98. Li, J. J. *et al.* Large-scale synthesis of nearly monodisperse CdSe/CdS core/shell nanocrystals using air-stable reagents via successive ion layer adsorption and reaction. *J. Am. Chem. Soc.* **125**, 12567–75 (2003).
  99. Yang, Y. A., Wu, H., Williams, K. R. & Cao, Y. C. Synthesis of CdSe and CdTe nanocrystals without precursor injection. *Angew. Chem. Int. Ed. Engl.* **44**, 6712–5 (2005).
  100. van Embden, J., Chesman, A. S. R. & Jasieniak, J. J. The Heat-Up Synthesis of Colloidal Nanocrystals. *Chem. Mater.* **27**, 2246–2285 (2015).
  101. Abécassis, B. *et al.* Real-Time in Situ Probing of High-Temperature Quantum Dots Solution Synthesis. *Nano Lett.* **15**, 2620–2626 (2015).
  102. Reiss, P., Bleuse, J. & Pron, A. Highly Luminescent CdSe/ZnSe Core/Shell Nanocrystals of Low Size Dispersion. *Nano Lett.* **2**, 781–784 (2002).
  103. Hoogenboom, J. P., Hernando, J., van Dijk, E. M. H. P., van Hulst, N. F. & García-Parajó, M. F. Power-law blinking in the fluorescence of single organic molecules. *ChemPhysChem* **8**, 823–33 (2007).
  104. Moerner, W. E. & Orrit, M. Illuminating single molecules in condensed matter. *Science* **283**, 1670–1676 (1999).

105. Basché, T., Kummer, S. & Bräuchle, C. Direct spectroscopic observation of quantum jumps of a single molecule. *Nature* **373**, 132–134 (1995).
106. Cook, R. J. & Kimble, H. J. Possibility of direct observation of quantum jumps. *Phys. Rev. Lett.* **54**, 1023–1026 (1985).
107. Kuno, M., Fromm, D. P., Hamann, H. F., Gallagher, a. & Nesbitt, D. J. Nonexponential 'blinking' kinetics of single CdSe quantum dots: A universal power law behavior. *J. Chem. Phys.* **112**, 3117 (2000).
108. Kuno, M., Fromm, D. P., Hamann, H. F., Gallagher, A. & Nesbitt, D. J. 'On'/'off' fluorescence intermittency of single semiconductor quantum dots. *J. Chem. Phys.* **115**, 1028 (2001).
109. Jung, Y., Barkai, E. & Silbey, R. J. Lineshape theory and photon counting statistics for blinking quantum dots: a Lévy walk process. *Chem. Phys.* **284**, 181–194 (2002).
110. Margolin, G., Protasenko, V., Kuno, M. & Barkai, E. Photon Counting Statistics for Blinking CdSe–ZnS Quantum Dots: A Lévy Walk Process †. *J. Phys. Chem. B* **110**, 19053–19060 (2006).
111. Krauss, T. & Brus, L. Charge, Polarizability, and Photoionization of Single Semiconductor Nanocrystals. *Phys. Rev. Lett.* **83**, 4840–4843 (1999).
112. Peterson, J. J. & Nesbitt, D. J. Modified power law behavior in quantum dot blinking: A novel role for biexcitons and auger ionization. *Nano Lett.* **9**, 338–345 (2009).
113. Shimizu, K. *et al.* Blinking statistics in single semiconductor nanocrystal quantum dots. *Phys. Rev. B* **63**, 1–5 (2001).
114. Efros, A. L. Nanocrystals - Almost always bright. *Nat. Mater.* **7**, 612–613 (2008).
115. Fisher, B. R., Eisler, H. J., Stott, N. E. & Bawendi, M. G. Emission intensity dependence and single-exponential behavior in single colloidal quantum dot fluorescence lifetimes. *J. Phys. Chem. B* **108**, 143–148 (2004).
116. Zhang, K., Chang, H., Fu, A., Alivisatos, a P. & Yang, H. Continuous distribution of emission states from single CdSe/ZnS quantum dots. *Nano Lett.* **6**, 843–847 (2006).
117. Galland, C. *et al.* Two types of luminescence blinking revealed by spectroelectrochemistry of single quantum dots. *Nature* **479**, 203–7 (2011).
118. Frantsuzov, P. a. & Marcus, R. a. Explanation of quantum dot blinking without the long-lived trap hypothesis. *Phys. Rev. B - Condens. Matter Mater. Phys.* **72**, 1–10 (2005).
119. Frantsuzov, P. a., Volkán-Kacsó, S. & Jankó, B. Model of fluorescence intermittency of single colloidal semiconductor quantum dots using multiple recombination centers. *Phys. Rev. Lett.* **103**, 1–4 (2009).
120. Schwartz, O. & Oron, D. A present understanding of colloidal quantum dot blinking. *Isr. J. Chem.* **52**, 992–1001 (2012).

- 
121. Cragg, G. E. & Efros, A. L. Suppression of Auger processes in confined structures. *Nano Lett.* **10**, 313–7 (2010).
  122. Wang, X. *et al.* Non-blinking semiconductor nanocrystals. *Nature* **459**, 686–9 (2009).
  123. Spinicelli, P. *et al.* Bright and Grey States in CdSe-CdS Nanocrystals Exhibiting Strongly Reduced Blinking. *Phys. Rev. Lett.* **102**, 136801 (2009).
  124. Brokmann, X., Coolen, L., Dahan, M. & Hermier, J. Measurement of the Radiative and Nonradiative Decay Rates of Single CdSe Nanocrystals through a Controlled Modification of their Spontaneous Emission. *Phys. Rev. Lett.* **93**, 107403 (2004).
  125. Ghosh, Y. *et al.* New insights into the complexities of shell growth and the strong influence of particle volume in nonblinking 'giant' core/shell nanocrystal quantum dots. *J. Am. Chem. Soc.* **134**, 9634–9643 (2012).
  126. Mangum, B. D. *et al.* Influence of the core size on biexciton quantum yield of giant CdSe/CdS nanocrystals. *Nanoscale* **6**, 3712–20 (2014).
  127. Bouet, C. *et al.* Two-Dimensional Growth of CdSe Nanocrystals, from Nanoplatelets to Nanosheets. *Chem. Mater.* **25**, 639–645 (2013).
  128. Bouet, C. *et al.* Flat Colloidal Semiconductor Nanoplatelets. *Chem. Mater.* **25**, 1262–1271 (2013).
  129. Mino, L. *et al.* Low-dimensional systems investigated by x-ray absorption spectroscopy: a selection of 2D, 1D and 0D cases. *J. Phys. D: Appl. Phys.* **46**, 423001 (2013).
  130. Ithurria, S. *et al.* Colloidal nanoplatelets with two-dimensional electronic structure. *Nat. Mater.* **10**, 936–941 (2011).
  131. Mahler, B., Nadal, B., Bouet, C., Patriarche, G. & Dubertret, B. Core/Shell Colloidal Semiconductor Nanoplatelets. *J. Am. Chem. Soc.* **134**, 18591–18598 (2012).
  132. Pedetti, S. *et al.* Optimized synthesis of CdTe nanoplatelets and photoresponse of CdTe nanoplatelets films. *Chem. Mater.* **25**, 2455–2462 (2013).
  133. Ithurria, S. & Talapin, D. V. Colloidal atomic layer deposition (c-ALD) using self-limiting reactions at nanocrystal surface coupled to phase transfer between polar and nonpolar media. *J. Am. Chem. Soc.* **134**, 18585–90 (2012).
  134. Leatherdale, C. A., Woo, W., Mikulec, F. V. & Bawendi, M. G. On the Absorption Cross Section of CdSe Nanocrystal Quantum Dots. *J. Phys. Chem. B* **106**, 7619–7622 (2002).
  135. Yu, W. W., Qu, L., Guo, W. & Peng, X. Experimental Determination of the Extinction Coefficient of CdTe, CdSe, and CdS Nanocrystals. *Chem. Mater.* **15**, 2854–2860 (2003).
  136. Jasieniak, J., Smith, L., Embden, J. Van, Mulvaney, P. & Califano, M. Re-examination

- of the size dependent absorption properties of CdSe quantum dots. *J. Phys. Chem. C* **113**, 19468–19474 (2009).
137. Karel Čapek, R. *et al.* Optical Properties of Zincblende Cadmium Selenide Quantum Dots. *J. Phys. Chem. C* **114**, 6371–6376 (2010).
138. Kamal, J. S. *et al.* Size-Dependent Optical Properties of Zinc Blende Cadmium Telluride Quantum Dots. *J. Phys. Chem. C* **116**, 5049–5054 (2012).
139. Jobin Yvon. A guide to recording quantum yields.
140. Tonti, D., van Mourik, F. & Chergui, M. On the Excitation Wavelength Dependence of the Luminescence Yield of Colloidal CdSe Quantum Dots. *Nano Lett.* **4**, 2483–2487 (2004).
141. Liu, F. *et al.* Spin dynamics of negatively charged excitons in CdSe/CdS colloidal nanocrystals. *Phys. Rev. B* **88**, 035302 (2013).
142. Mahler, B., Lequeux, N. & Dubertret, B. Ligand-controlled polytypism of thick-shell CdSe/CdS nanocrystals. *J. Am. Chem. Soc.* **132**, 953–9 (2010).
143. Mohamed, M. B., Tonti, D., Al-Salman, A., Chemseddine, A. & Chergui, M. Synthesis of high quality zinc blende CdSe nanocrystals. *J. Phys. Chem. B* **109**, 10533–7 (2005).
144. Nair, G., Zhao, J. & Bawendi, M. G. Biexciton quantum yield of single semiconductor nanocrystals from photon statistics. *Nano Lett.* **11**, 1136–1140 (2011).
145. Ji, B. *et al.* Non-blinking quantum dot with a plasmonic nanoshell resonator. *Nat. Nanotechnol.* **10**, 1–6 (2015).
146. Gómez, D. E., van Embden, J., Mulvaney, P., Fernée, M. J. & Rubinsztein-Dunlop, H. Exciton-trion transitions in single CdSe-CdS core-shell nanocrystals. *ACS Nano* **3**, 2281–7 (2009).
147. Jha, P. P. & Guyot-Sionnest, P. Trion decay in colloidal quantum dots. *ACS Nano* **3**, 1011–5 (2009).
148. Klimov, V. I. Optical Nonlinearities and Ultrafast Carrier Dynamics in Semiconductor Nanocrystals. *J. Phys. Chem. B* **104**, 6112–6123 (2000).
149. Müller, J. *et al.* Air-induced fluorescence bursts from single semiconductor nanocrystals. *Appl. Phys. Lett.* **85**, 381 (2004).
150. Brovelli, S. *et al.* Nano-engineered electron-hole exchange interaction controls exciton dynamics in core-shell semiconductor nanocrystals. *Nat. Commun.* **2**, 280 (2011).
151. de Mello Donegá, C., Bode, M. & Meijerink, A. Size- and temperature-dependence of exciton lifetimes in CdSe quantum dots. *Phys. Rev. B* **74**, 085320 (2006).
152. Louyer, Y., Biadala, L., Tamarat, P. & Lounis, B. Spectroscopy of neutral and charged exciton states in single CdSe/ZnS nanocrystals. *Appl. Phys. Lett.* **96**, (2010).

- 
153. Peng, X., Schlamp, M. C., Kadavanich, A. V & Alivisatos, a P. Epitaxial Growth of Highly Luminescent CdSe/CdS Core/Shell Nanocrystals with Photostability and Electronic Accessibility. *J. Am. Chem. Soc.* **119**, 7019–7029 (1997).
  154. Steiner, D. *et al.* Determination of Band Offsets in Heterostructured Colloidal Nanorods Using Scanning Tunneling Spectroscopy. *Nano Lett.* **8**, 2954–2958 (2008).
  155. Nethercot, A. H. Prediction of Fermi Energies and Photoelectric Thresholds Based on Electronegativity Concepts. *Phys. Rev. Lett.* **33**, 1088–1091 (1974).
  156. Pandey, A. & Guyot-Sionnest, P. Intraband spectroscopy and band offsets of colloidal II-VI core/shell structures. *J. Chem. Phys.* **127**, 104710 (2007).
  157. Fisher, B., Caruge, J.-M., Chan, Y.-T., Halpert, J. & Bawendi, M. G. Multiexciton fluorescence from semiconductor nanocrystals. *Chem. Phys.* **318**, 71–81 (2005).
  158. Park, Y.-S. S. *et al.* Near-Unity Quantum Yields of Biexciton Emission from CdSe/CdS Nanocrystals Measured Using Single-Particle Spectroscopy. *Phys. Rev. Lett.* **106**, 187401 (2011).
  159. Spinicelli, P. Thèse: Contrôle des propriétés quantiques de fluorescence des nanocristaux semi-conducteurs. (2009).
  160. Xu, X. Surface recombination and charged exciton in nanocrystal quantum dots on photonic crystals under two-photon excitation. *Sci. Rep.* **4**, 1–7 (2014).
  161. Htoon, H. *et al.* Highly emissive multiexcitons in steady-state photoluminescence of individual ‘giant’ CdSe/CdS Core/Shell nanocrystals. *Nano Lett.* **10**, 2401–7 (2010).
  162. Klimov, V. I., McGuire, J. a., Schaller, R. D. & Rupasov, V. I. Scaling of multiexciton lifetimes in semiconductor nanocrystals. *Phys. Rev. B - Condens. Matter Mater. Phys.* **77**, 1–12 (2008).
  163. Jones, M., Lo, S. S. & Scholes, G. D. Quantitative modeling of the role of surface traps in CdSe/CdS/ZnS nanocrystal photoluminescence decay dynamics. *Proc. Natl. Acad. Sci. U. S. A.* **106**, 3011–6 (2009).
  164. Bartsch, G. *et al.* Positively versus negatively charged excitons: A high magnetic field study of CdTe/Cd<sub>1-x</sub>Mg<sub>x</sub>Te quantum wells. *Phys. Rev. B - Condens. Matter Mater. Phys.* **83**, 1–14 (2011).
  165. Krahne, R., Zavelani-Rossi, M., Lupo, M. G., Manna, L. & Lanzani, G. Amplified spontaneous emission from core and shell transitions in CdSe/CdS nanorods fabricated by seeded growth. *Appl. Phys. Lett.* **98**, 063105 (2011).
  166. She, C. *et al.* Low-threshold stimulated emission using colloidal quantum wells. *Nano Lett.* **14**, 2772–7 (2014).
  167. García-Santamaría, F. *et al.* Suppressed auger recombination in ‘giant’ nanocrystals boosts optical gain performance. *Nano Lett.* **9**, 3482–8 (2009).
  168. Klimov, V. I. Mechanisms for Photogeneration and Recombination of Multiexcitons in

- Semiconductor. 16827–16845 (2006).
169. Agio, M. & Cano, D. M. Nano-optics: The Purcell factor of nanoresonators. *Nat. Photonics* **7**, 674–675 (2013).
  170. Anonymous. Proceedings of the American Physical Society. *Phys. Rev.* **69**, 674–674 (1946).
  171. Sheldon, M. T. Plasmoelectric potentials in metal nanostructures. *Nat. Mater.* **9**, 193–204 (2014).
  172. Quattieri, A. *et al.* Nonclassical emission from single colloidal nanocrystals in a microcavity: A route towards room temperature single photon sources. *New J. Phys.* **11**, (2009).
  173. Canneson, D. *et al.* Influence of the cluster's size of random gold nanostructures on the fluorescence of single CdSe-CdS nanocrystals. *Gold Bull.* **46**, 329–334 (2013).
  174. Jin, Y. & Gao, X. Plasmonic fluorescent quantum dots. *Nat. Nanotechnol.* **4**, 571–6 (2009).
  175. Oldenburg, S. ., Averitt, R. ., Westcott, S. . & Halas, N. . Nanoengineering of optical resonances. *Chem. Phys. Lett.* **288**, 243–247 (1998).
  176. Habert, B. Thèse : Contrôle de la fluorescence par des nanoantennes plasmoniques. (2014).
  177. Cordero, S. R., Carson, P. J., Estabrook, R. A., Strouse, G. F. & Buratto, S. K. Photo-Activated Luminescence of CdSe Quantum Dot Monolayers. *J. Phys. Chem. B* **104**, 12137–12142 (2000).
  178. Karan, N. S. *et al.* Plasmonic giant quantum dots: hybrid nanostructures for truly simultaneous optical imaging, photothermal effect and thermometry. *Chem. Sci.* **6**, 2224–2236 (2015).
  179. Ithurria, S., Bousquet, G. & Dubertret, B. Continuous Transition from 3D to 1D Confinement Observed during the Formation of CdSe Nanoplatelets. *J. Am. Chem. Soc.* **133**, 3070–3077 (2011).
  180. Tessier, M. D., Javaux, C., Maksimovic, I., Loriette, V. & Dubertret, B. Spectroscopy of single CdSe nanoplatelets. *ACS Nano* **6**, 6751–6758 (2012).
  181. Crooker, S. a., Barrick, T., Hollingsworth, J. a. & Klimov, V. I. Multiple temperature regimes of radiative decay in CdSe nanocrystal quantum dots: Intrinsic limits to the dark-exciton lifetime. *Appl. Phys. Lett.* **82**, 2793–2795 (2003).
  182. Valerini, D. *et al.* Temperature dependence of the photoluminescence properties of colloidal CdSe/ZnS core/shell quantum dots embedded in a polystyrene matrix. *Phys. Rev. B* **71**, 235409 (2005).
  183. Tessier, M. D. *et al.* Spectroscopy of colloidal semiconductor core/shell nanoplatelets with high quantum yield. *Nano Lett.* **13**, 3321–3328 (2013).

- 
184. Chalfie, M., Tu, Y., Euskirchen, G., Ward, W. W. & Prasher, D. C. Green fluorescent protein as a marker for gene expression. *Science* **263**, 802–805 (1994).
  185. Kremers, G., Gilbert, S. G., Cranfill, P. J., Davidson, M. W. & Piston, D. W. Fluorescent proteins at a glance. *J. Cell Sci.* **124**, 157–160 (2011).
  186. Adam, V., Berardozi, R., Byrdin, M. & Bourgeois, D. Phototransformable fluorescent proteins: Future challenges. *Curr. Opin. Chem. Biol.* **20**, 92–102 (2014).
  187. Wang, Y. *et al.* Mechanism of strong luminescence photoactivation of citrate-stabilized water-soluble nanoparticles with CdSe cores. *J. Phys. Chem. B* **108**, 15461–15469 (2004).
  188. Smith, A. M., Dave, S., Nie, S., True, L. & Gao, X. Multicolor quantum dots for molecular diagnostics of cancer. *Expert Rev. Mol. Diagn.* **6**, 231–244 (2006).
  189. Resch-Genger, U., Grabolle, M., Cavaliere-Jaricot, S., Nitschke, R. & Nann, T. Quantum dots versus organic dyes as fluorescent labels. *Nat. Methods* **5**, 763–775 (2008).
  190. Wu, X. *et al.* Immunofluorescent labeling of cancer marker Her2 and other cellular targets with semiconductor quantum dots. *Nat. Biotechnol.* **21**, 41–46 (2003).
  191. Cassette, E. *et al.* Synthesis and characterization of near-infrared Cu-In-Se/ZnS core/shell quantum dots for in vivo imaging. *Chem. Mater.* **22**, 6117–6124 (2010).
  192. Medintz, I. L., Uyeda, H. T., Goldman, E. R. & Mattoussi, H. Quantum dot bioconjugates for imaging, labelling and sensing. *Nat. Mater.* **4**, 435–46 (2005).
  193. Weissleder, R. A clearer vision for in vivo imaging. *Nat. Biotechnol.* **19**, 316–317 (2001).
  194. Lacroix, L., Delpech, F., Nayral, C., Lachaize, S. & Chaudret, B. New generation of magnetic and luminescent nanoparticles for in vivo real-time imaging. *Interface Focus* **3**, 20120103 (2013).
  195. Bouccara, S. *et al.* Time-gated cell imaging using long lifetime near-infrared-emitting quantum dots for autofluorescence rejection. *J. Biomed. Opt.* **19**, 051208 (2014).
  196. Dubertret, B. *et al.* In vivo imaging of quantum dots encapsulated in phospholipid micelles. *Science* **298**, 1759–62 (2002).
  197. Gerion, D. *et al.* Synthesis and properties of biocompatible water-soluble silica-coated CdSe/ZnS semiconductor quantum dots. *J. Phys. Chem. B* **105**, 8861–8871 (2001).
  198. Darbandi, M., Thomann, R. & Nann, T. Single quantum dots in silica spheres by microemulsion synthesis. *Chem. Mater.* **17**, 5720–5725 (2005).
  199. Koole, R. *et al.* On the incorporation mechanism of hydrophobic quantum dots in silica spheres by a reverse microemulsion method. *Chem. Mater.* **20**, 2503–2512 (2008).

- 
200. Muro, E. *et al.* Small and stable sulfobetaine zwitterionic quantum dots for functional live-cell imaging. *J. Am. Chem. Soc.* **132**, 4556–7 (2010).
201. Giovanelli, E. *et al.* Highly Enhanced Affinity of Multidentate versus Bidentate Zwitterionic Ligands for Long-Term Quantum Dot Bio-imaging. *Langmuir* **28**, 15177–84 (2012).
202. Knittel, F. *et al.* On the characterization of the surface chemistry of quantum dots. *Nano Lett.* **13**, 5075–8 (2013).
203. Sitbon, G. *et al.* Multimodal Mn-doped I-III-VI quantum dots for near infrared fluorescence and magnetic resonance imaging: from synthesis to in vivo application. *Nanoscale* **6**, 9264–72 (2014).
204. Winnik, F. M. & Maysinger, D. Quantum dot cytotoxicity and ways to reduce it. *Acc. Chem. Res.* **46**, 672–680 (2013).
205. Shiohara, A., Hoshino, A., Hanaki, K.-I., Suzuki, K. & Yamamoto, K. On the cytotoxicity caused by quantum dots. *Microbiol. Immunol.* **48**, 669–675 (2004).
206. Ye, L. *et al.* A pilot study in non-human primates shows no adverse response to intravenous injection of quantum dots. *Nat. Nanotechnol.* **7**, 453–8 (2012).
207. Yong, K.-T. *et al.* Nanotoxicity assessment of quantum dots: from cellular to primate studies. *Chem. Soc. Rev.* **42**, 1236–50 (2013).
208. Yeh, Y.-C. *et al.* The role of ligand coordination on the cytotoxicity of cationic quantum dots in HeLa cells. *Nanoscale* **5**, 12140–12143 (2013).
209. Gary, D. C., Terban, M. W., Billinge, S. J. L. & Cossairt, B. M. Two-Step Nucleation and Growth of InP Quantum Dots via Magic-Sized Cluster Intermediates. *Chem. Mater.* **27**, 1432–1441 (2015).
210. Song, W. S. *et al.* Amine-derived synthetic approach to color-tunable InP/ZnS quantum dots with high fluorescent qualities. *J. Nanoparticle Res.* **15**, (2013).
211. Lewinski, N., Colvin, V. & Drezek, R. Cytotoxicity of nanoparticles. *Small* **4**, 26–49 (2008).
212. Li, H., Shih, W. Y. & Shih, W.-H. Non-heavy-metal ZnS quantum dots with bright blue photoluminescence by a one-step aqueous synthesis. *Nanotechnology* **18**, 205604 (2007).
213. Cheng, J. *et al.* Aqueous synthesis of high-fluorescence CdZnTe alloyed quantum dots. *J. Alloys Compd.* **589**, 539–544 (2014).
214. Weng, J. *et al.* Highly luminescent CdTe quantum dots prepared in aqueous phase as an alternative fluorescent probe for cell imaging. *Talanta* **70**, 397–402 (2006).
215. Liu, W. *et al.* Compact cysteine-coated CdSe(ZnCdS) quantum dots for in vivo applications. *J. Am. Chem. Soc.* **129**, 14530–14531 (2007).

- 
216. Wu, M. & Algar, W. R. Acceleration of Proteolytic Activity Associated with Selection of Thiol Ligand Coatings on Quantum Dots. *ACS Appl. Mater. Interfaces* **7**, 2535–2545 (2015).
217. Efremova, N. V, Sheth, S. R. & Leckband, D. E. Protein-induced changes in poly(ethylene glycol) brushes: Molecular weight and temperature dependence. *Langmuir* **17**, 7628–7636 (2001).
218. Kim, H. R. *et al.* Analysis of plasma protein adsorption onto PEGylated nanoparticles by complementary methods: 2-DE, CE and Protein Lab-on-chip® system. *Electrophoresis* **28**, 2252–2261 (2007).
219. Zhan, N., Palui, G., Safi, M., Ji, X. & Mattoussi, H. Multidentate zwitterionic ligands provide compact and highly biocompatible quantum dots. *J. Am. Chem. Soc.* **135**, 13786–13795 (2013).
220. Palui, G., Na, H. Bin & Mattoussi, H. Poly(ethylene glycol)-based multidentate oligomers for biocompatible semiconductor and gold nanocrystals. *Langmuir* **28**, 2761–2772 (2012).
221. de Bono, M., Tobin, D. M., Davis, M. W., Avery, L. & Bargmann, C. I. Social feeding in *Caenorhabditis elegans* is induced by neurons that detect aversive stimuli. *Nature* **419**, 899–903 (2002).
222. Rankin, C. H. From gene to identified neuron to behaviour in *Caenorhabditis elegans*. *Nat. Rev. Genet.* **3**, 622–630 (2002).
223. Fares, H. & Grant, B. Deciphering endocytosis in *Caenorhabditis elegans*. *Traffic* **3**, 11–19 (2002).
224. Hulme, S. E. & Whitesides, G. M. Chemistry and the worm: *Caenorhabditis elegans* as a platform for integrating chemical and biological research. *Angew. Chemie - Int. Ed.* **50**, 4774–4807 (2011).
225. Kirienko, N. V, Mani, K. & Fay, D. S. Cancer models in *Caenorhabditis elegans*. *Dev. Dyn.* **239**, 1413–1448 (2010).
226. Pereda, A. E. Electrical synapses and their functional interactions with chemical synapses. *Nat. Rev. Neurosci.* **15**, 250–63 (2014).
227. Howes, P. D., Chandrawati, R. & Stevens, M. M. Colloidal nanoparticles as advanced biological sensors. *Science* **346**, 1247390–1247390 (2014).
228. Algar, W. R., Stewart, M. H., Scott, A. M., Moon, W. J. & Medintz, I. L. Quantum dots as platforms for charge transfer-based biosensing: challenges and opportunities. *J. Mater. Chem. B* **2**, 7816–7827 (2014).
229. Alivisatos, P. The use of nanocrystals in biological detection. *Nat. Biotechnol.* **22**, 47–52 (2004).
230. Pierobon, P. & Cappello, G. Quantum dots to tail single bio-molecules inside living cells. *Adv. Drug Deliv. Rev.* **64**, 167–78 (2012).

231. Pericleous, P. *et al.* Quantum dots hold promise for early cancer imaging and detection. *Int. J. Cancer* **528**, 519–528 (2012).
232. Gao, X., Cui, Y., Levenson, R. M., Chung, L. W. K. & Nie, S. In vivo cancer targeting and imaging with semiconductor quantum dots. *Nat. Biotechnol.* **22**, 969–976 (2004).
233. Mérian, J., Gravier, J., Navarro, F. & Texier, I. Fluorescent Nanoprobes Dedicated to in Vivo Imaging: From Preclinical Validations to Clinical Translation. *Molecules* **17**, 5564–5591 (2012).
234. Cassette, E. *et al.* Design of new quantum dot materials for deep tissue infrared imaging. *Adv. Drug Deliv. Rev.* **65**, 719–31 (2013).
235. Pons, T. *et al.* Cadmium-free CuInS<sub>2</sub>/ZnS quantum dots for sentinel lymph node imaging with reduced toxicity. *ACS Nano* **4**, 2531–8 (2010).
236. Ma, Q. & Su, X. Near-infrared quantum dots: synthesis, functionalization and analytical applications. *Analyst* **135**, 1867–77 (2010).
237. Frangioni, J. V. In vivo near-infrared fluorescence imaging. *Curr. Opin. Chem. Biol.* **7**, 626–634 (2003).
238. Mukherjee, S., Ghosh, R. N. & Maxfield, F. R. Endocytosis. *Physiol. Rev.* **77**, 759–803 (1997).
239. Surana, S., Bhat, J. M., Koushika, S. P. & Krishnan, Y. An autonomous DNA nanomachine maps spatiotemporal pH changes in a multicellular living organism. *Nat. Commun.* **2**, 340 (2011).
240. Brenner, S. The genetics of *Caenorhabditis elegans*. *Genetics* **77**, 71–94 (1974).
241. Rostaing, P., Weimer, R. M., Jorgensen, E. M., Triller, A. & Bessereau, J.-L. Preservation of immunoreactivity and fine structure of adult *C. elegans* tissues using high-pressure freezing. *J. Histochem. Cytochem.* **52**, 1–12 (2004).
242. Fiala, J. C. Reconstruct: A free editor for serial section microscopy. *J. Microsc.* **218**, 52–61 (2005).
243. Bucurenciu, I., Kulik, A., Schwaller, B., Frotscher, M. & Jonas, P. Nanodomain Coupling between Ca<sup>2+</sup> Channels and Ca<sup>2+</sup> Sensors Promotes Fast and Efficient Transmitter Release at a Cortical GABAergic Synapse. *Neuron* **57**, 536–545 (2008).
244. Shahrezaei, V., Cao, A. & Delaney, K. R. Ca<sup>2+</sup> from one or two channels controls fusion of a single vesicle at the frog neuromuscular junction. *J. Neurosci.* **26**, 13240–13249 (2006).
245. Neish, C. S., Martin, I. L., Henderson, R. M. & Edwardson, J. M. Direct visualization of ligand-protein interactions using atomic force microscopy. *Br. J. Pharmacol.* **135**, 1943–1950 (2002).
246. Clarke, S., Tamang, S., Reiss, P. & Dahan, M. A simple and general route for

- monofunctionalization of fluorescent and magnetic nanoparticles using peptides. *Nanotechnology* **22**, 175103 (2011).
247. Carstairs, H. M. J., Lympelopoulos, K., Kapanidis, A. N., Bath, J. & Turberfield, A. J. DNA monofunctionalization of quantum dots. *ChemBiochem* **10**, 1781–3 (2009).
248. Uddayasankar, U., Zhang, Z., Shergill, R. T., Gradinaru, C. C. & Krull, U. J. Isolation of monovalent quantum dot-nucleic acid conjugates using magnetic beads. *Bioconjug. Chem.* **25**, 1342–1350 (2014).
249. Clarke, S. *et al.* Covalent monofunctionalization of peptide-coated quantum dots for single-molecule assays. *Nano Lett.* **10**, 2147–2154 (2010).
250. Howarth, M. *et al.* Monovalent, reduced-size quantum dots for imaging receptors on living cells. *Nat. Methods* **5**, 397–399 (2008).
251. Farlow, J. *et al.* Formation of targeted monovalent quantum dots by steric exclusion. *Nat. Methods* **10**, 1203–5 (2013).
252. Rothmund, P. W. K. Folding DNA to create nanoscale shapes and patterns. *Nature* **440**, 297–302 (2006).
253. Douglas, S. M. *et al.* Self-assembly of DNA into nanoscale three-dimensional shapes. *Nature* **459**, 414–418 (2009).
254. He, Y. *et al.* Hierarchical self-assembly of DNA into symmetric supramolecular polyhedra. *Nature* **452**, 198–201 (2008).
255. Bhatia, D. *et al.* Icosahedral DNA nanocapsules by modular assembly. *Angew. Chemie - Int. Ed.* **48**, 4134–4137 (2009).
256. Sandvig, K. & van Deurs, B. Endocytosis, intracellular transport, and cytotoxic action of Shiga toxin and ricin. *Physiol. Rev.* **76**, 949–966 (1996).
257. Tekle, C., Van Deurs, B., Sandvig, K. & Iversen, T. G. Cellular trafficking of quantum dot-ligand bioconjugates and their induction of changes in normal routing of unconjugated ligands. *Nano Lett.* **8**, 1858–1865 (2008).
258. van Deurs, B., Tønnessen, T. I., Petersen, O. W., Sandvig, K. & Olsnes, S. Routing of internalized ricin and ricin conjugates to the Golgi complex. *J. Cell Biol.* **102**, 37–47 (1986).
259. Zajac, A. L., Goldman, Y. E., Holzbaur, E. L. F. & Ostap, E. M. Local cytoskeletal and organelle interactions impact molecular-motor-driven early endosomal trafficking. *Curr. Biol.* **23**, 1173–1180 (2013).
260. Bálint, Š., Verdeny Vilanova, I., Sandoval Álvarez, Á. & Lakadamyali, M. Correlative live-cell and superresolution microscopy reveals cargo transport dynamics at microtubule intersections. *Proc. Natl. Acad. Sci. U. S. A.* **110**, 3375–80 (2013).



## Abstract

Colloidal Quantum Dots (QDs) are colloidal semiconductor nanocrystals with unique optical properties: narrow emission spectrum, large spectral range of excitation, high brightness. However, their applications are still limited by the blinking of their fluorescence emission at the single particle scale.

This work focuses on the improvement of optical properties of CdSe/CdS QDs, as well as on the biological applications.

The development of a synthesis of thick-shell CdSe/CdS nanocrystals allowed easy obtaining of non-blinking QDs from CdSe cores of different crystallinity. However, these QDs flicker between an on and a grey state.

The synthesis of thick-shell CdSe/CdS QDs with a composition gradient between the core and the shell produces nanocrystals whose fluorescence emission is perfectly stable with time. The quantum yields of the mono- and biexciton are 100% in air, at room temperature. Multiexcitonic recombinations are also efficient making a single QD emit white light under strong excitation.

The growth of a gold nanoshell around a QD (golden-QDs) allows the coupling of the exciton of the semiconductor and the metal plasmons. This Purcell effect speeds up all the radiative processes, decreasing the lifetime and eliminating the blinking. Besides, the gold shell acts as a barrier against photooxidation and the golden-QDs show increased resistance to high excitation powers.

The control of the shape of nanocrystals allowed the synthesis of nanoplatelets, bidimensionnal structures whose thickness is controlled to the atomic monolayer. A new synthesis of core/shell nanoplatelets leads to interesting properties due to the purity of the emission of the nanocrystals and to their resistance with temperature.

Finally, CdSe/CdS QDs, because of the low photobleaching and high brightness, are excellent fluorescent probes for biological imaging. Their fluorescence and their inorganic structure were taken advantage of to perform bimodal optical/electron imaging to precisely localize and count synaptic receptors in *C. elegans*.

Monofunctionalization of QDs, required to probe some endocytosis pathways in cells, was performed thanks to encapsulation of QDs in a DNA nanocage whose formation is perfectly controlled. This DNA cage – QD complex was used to study the dynamics of endocytosis of Shiga toxin in the retrograde endocytosis pathway, up to the Golgi apparatus.

### Keywords:

Nanocrystals, semiconductors, quantum dots, synthesis, blinking, quantum yield, biological imaging, bimodal imaging, monofunctionalization.



---

## Résumé

Les Quantum Dots colloïdaux (QDs) sont des nanocristaux colloïdaux de semiconducteurs aux propriétés optiques uniques : finesse spectrale d'émission, large gamme spectrale d'excitation, brillance élevée. Cependant, leurs applications sont encore limitées par le clignotement de leur émission de fluorescence à l'échelle de la particule unique.

Ce travail se concentre sur l'amélioration des propriétés optiques des QDs de CdSe/CdS, ainsi que sur leurs applications biologiques.

Le développement d'une synthèse de nanocristaux de CdSe/CdS à coque épaisse a permis d'obtenir facilement des QDs non-clignotants à partir de cœurs de CdSe de cristallinité différente. Cependant, ces QDs oscillent entre un état brillant et un état gris.

La synthèse de QDs de CdSe/CdS à coque épaisse avec un gradient de composition entre le cœur et la coque produit des nanocristaux dont l'émission de fluorescence est parfaitement stable au cours du temps, et donc les rendements quantiques du mono- et du biexciton sont à 100% à l'air, à température ambiante. Les recombinaisons multiexcitoniques sont également efficaces permettant à un QD unique d'émettre de la lumière blanche à forte excitation.

La croissance d'une coque d'or autour d'un QD (QDs-dorés) favorise le couplage entre l'exciton du semiconducteur et les plasmons du métal. Cet effet Purcell a pour conséquence d'accélérer les phénomènes radiatifs, diminuant le temps de vie et supprimant le clignotement du QD. De plus, la couche d'or agit comme une barrière contre la photooxydation et les QDs-dorés présentent une résistance plus élevée aux fortes puissances d'excitation.

Le contrôle de la forme des nanocristaux a permis la synthèse de nanoplaquettes, structures bidimensionnelles dont l'épaisseur est contrôlée à la monocouche atomique près. Une nouvelle synthèse de nanoplaquettes cœur/coque conduit à des propriétés intéressantes tant par la pureté de l'émission des nanocristaux que par leur résistance en température.

Enfin, les QDs de CdSe/CdS, de par leur brillance et faible photoblanchiment, sont d'excellentes sondes fluorescentes pour l'imagerie biologique. Leur fluorescence et leur structure inorganique ont permis de réaliser de l'imagerie bimodale optique/électronique pour déterminer le nombre et la localisation précise de récepteurs synaptiques dans *C. elegans*.

La monofonctionnalisation des QDs, nécessaire pour sonder certaines voies d'endocytose dans les cellules, a été réalisée grâce à l'encapsulation des QDs dans une nanocage d'ADN dont la formation est parfaitement contrôlée, à la base près. Ce complexe

cage d'ADN – QDs a permis de suivre la dynamique d'endocytose des toxines Shiga dans la voie d'endocytose rétrograde jusqu'à l'appareil de Golgi.

**Mots-clés :**

Nanocristaux, semiconducteurs, boîte quantique, synthèse, clignotement, rendement quantique, imagerie biologique, imagerie bimodale, monofonctionnalisation.





Michel NASILOWSKI

## Synthesis and Optical Spectroscopy of Thick-Shell Semiconductor Nanoparticles. Applications to Biological Imaging.

---

### Abstract

Colloidal Quantum Dots (QDs) are semiconducting nanocrystals whose applications are limited by the blinking of their emission.

The growth of a thick shell on QDs decreases the blinking. An additional composition gradient between the core and the shell completely eliminates non-radiative Auger recombinations, yielding QDs with 100% quantum yield in air and at room temperature for the mono- and the biexciton, and increased efficiency for multiexcitons. A similar result can be obtained by capping the QDs with a silica spacer and a gold nanoshell to take advantage of the Purcell effect and the coupling between the exciton and the surface plasmons. Finally, two-dimensional structures, nanoplatelets (NPLs) with thick shell have been developed to decrease their blinking.

QDs strong fluorescence and robustness make them excellent probes for biological imaging. They open the road for bimodal light/electron imaging: synaptic receptors in *C. elegans* worms were localized at the nanometer scale using QDs. The monofunctionalization issue of the probe was addressed using a perfectly controlled DNA nanocage to encapsulate the QDs and probe the Shiga toxin endocytosis pathway.

**Keywords:** Nanocrystals, semiconductors, quantum dots, synthesis, blinking, quantum yield, biological imaging, bimodal imaging, monofunctionalization.

---

### Résumé

Les Boîtes Quantiques colloïdales (QDs) sont des nanocristaux de semiconducteur dont les applications sont limitées par le clignotement de leur émission.

La croissance d'une coque épaisse sur les QDs diminue le clignotement. L'ajout d'un gradient de composition entre le cœur et la coque élimine complètement les recombinaisons Auger non-radiatives, donnant aux QDs 100% de rendement quantique à l'air et à température ambiante pour le mono- et le biexciton, et une efficacité accrue pour les multiexcitons. Un résultat similaire peut être obtenu en recouvrant les QDs d'une couche de silice et d'or, pour tirer profit de l'effet Purcell et du couplage entre l'exciton et les plasmons de surface. Enfin, des structures bidimensionnelles, les nanoplaquettes (NPLs) à coque épaisse, ont été développées pour diminuer leur clignotement.

La fluorescence intense et robuste des QDs en fait d'excellents marqueurs pour l'imagerie biologique. Elles ouvrent la voie à l'imagerie bimodale optique/électronique : des récepteurs synaptiques dans les vers *C. elegans* ont été localisés à l'échelle nanométrique en utilisant des QDs. Le problème de la monofonctionnalisation des marqueurs a été résolu grâce à des nanocages d'ADN parfaitement contrôlés pour l'encapsulation des QDs : la voie d'endocytose de la Shiga-toxine a pu ainsi être étudiée.

**Mots-clés :** Nanocristaux, semiconducteurs, boîte quantique, synthèse, clignotement, rendement quantique, imagerie biologique, imagerie bimodale, monofonctionnalisation.